HYDROLOGIC AND ECO-GEOMORPHIC RESPONSE OF TIDAL SALT-MARSH PLATFORMS TO SEA-LEVEL RISE AND PROTECTIVE BARRIER DESIGN

By

Susan Meredith Howell Taylor

Dissertation

Submitted to the Faculty of the

Graduate School of Vanderbilt University

in partial fulfillment of the requirements

for the degree of

DOCTOR OF PHILOSOPHY

in

Environmental Engineering

May, 2013

Nashville, TN

Approved:

Professor David Jon Furbish

Professor George Hornberger

Professor Steven Goodbred, Jr.

Professor James Clarke

To my mother, Patricia Spell Howell

ACKNOWLEDGMENTS

This work was made possible through the financial support of the National Oceanic and Atmospheric Administration and Vanderbilt University.

I must first acknowledge David Furbish, my advisor and mentor, for his endearing support. I will remember fondly our discussions, chalkboard debates, field excursions, and his philosophical inspiration. I will strive to continue his inspiring intellectual pursuit and enthusiasm towards earth sciences.

I am grateful for my supportive family. The support and patience of my husband Stephen and son Shepard has made this work possible. My brother Michael's enthusiastic pride has kept me motivated throughout this process. My mother's support had no bounds, and I am forever grateful that she was with me when I completed this dissertation. I will strive in my career to live out the abilities my mother was confident I possess.

I wish to also give special thanks to the people with whom I have had endless discussions pertaining to coastal processes. These people include (in semi-chronological order) Clark Alexander, Simon Mudd, Jim Morris, Don Cahoon, Steve Goodbred, Beth Weinman, Kimberly Rogers, Brooke Traynham, Chris Voss, Jim Clarke, George Hornberger, Andrew Roberts, Stacey Worman, and Aaron Covey.

TABLE OF CONTENTS

LIST OF TABLES

LIST OF FIGURES

Figure Page

CHAPTER I

INTRODUCTION

1. Background

Coastal salt marshes are areas of intertidal mud stabilized by a cover of vegetation. Salt marshes develop along back barrier bays, river mouths, estuaries, deltas, and low energy open coasts. Intertidal salt marshes occupy a broad, flat expanse of landscape, refereed to as the marsh platform, at an elevation within the intertidal zone that approximates that of the mean high tide. The type of vegetation that colonizes tidal marshes depends on the elevation within the intertidal zone and climatic controls. *Juncus* and *Spartina* are two macrophytes that are most common along the east coast of the U.S. *Spartina alterniflora* is a low marsh grass able to tolerate prolonged tidal inundation due to extensive aerenchymatous tissue that supplies oxygen to the roots. *Spartina patens* dominates the high marsh and grows best on the upper flat surface of the marsh subject to less inundation. *Juncus roemerianus* is a high marsh rush that grows tall and occurs as dense patches restricted to elevations close to spring high tide, and occasionally exists as monotypic stands along creeks banks. Whereas relief on the marsh platform is low, subtle variations in elevation cause distinct vegetation zonation. The physical environment of the marsh community is influenced by the degree to which it is protected from wave or storm action, by tidal regime, rate of sea-level rise, topography of the coastal area, sediment supply, and the nature of the substrate.

Salt marsh ecosystems play a vital role in the dissipation of wave energy, accretion of sediment, filtration of nutrients, and as habitats for commercially important fisheries. Global sea level over the past 100 years is estimated to have risen at a rate of 1 to 2 mm yr^{-1}, whereas rates over the period of 1993-2002 are greater than the past 100 years [*Holgate & Woodworth*, 2004]. The Intergovernmental Panel on Climate Change (IPCC) recognizes sea-level rise (SLR) as a significant long-term consequence of climate change. Estimates of global SLR for the 21st century range from 9 to 90 cm, but local sea-level rise may be much higher or lower due to factors such as subsidence, sediment compaction or uplift [*IPCC*, 2010]. These estimates are currently being revised to account for glacial effects, and therefore the IPCC's projections of sea-level rise (AR4) are now considered a conservative estimate. Climate change is likely to impact tidal salt marshes by sea-level rise primarily thorough thermal expansion of water due to increasing temperatures. Many coastal areas will experience increased levels of flooding, accelerated erosion, loss of wetlands and low-lying terrestrial ecosystems, and salt water intrusion into freshwater sources as a result of sea-level rise and potentially enhanced storm frequency and severity. For example, the entire marsh environment in coastal North Carolina exists within less than a meter of relief near high tide, and the high marsh environment consists of approximately 10 to 15 cm of relief. Wetland loss is also expected to be prevalent where coastal development limits the landward migration of the wetland or engineered structures change flooding and sediment exchange, thereby modifying natural adjustment to changes in sea level.

The long-term stability of tidal marshes is related to the interactions between surface slope, sedimentation, primary productivity, and the relative rate of sea-level rise, *RSLR* (land

subsidence plus the eustatic change in sea level). My research focuses on how hydrologic-sediment-biologic interactions influence platform elevation, which can ultimately be used to inform the response of wetlands to sea-level change. This coupling between biotic and physical processes is beginning to be recognized as a fundamental driver of marsh platform evolution [*Nikora*, 2009]. Salt marsh platforms are dynamic environments sustained by the input of mineralogic sediment and macrophytes that provide for accumulation of organic matter. Accumulation of material helps to maintain the platform elevation, and therefore allows a platform to keep pace with mean sea level. The elevation of the sediment surface determines the duration and frequency that marsh platforms are submerged by tides. Elevation therefore influences plant productivity, and vegetation, on the other hand, controls flow within the canopy and sedimentation, which ultimately determines the change in platform elevation. These ecogeomorphic feedbacks likely explain the ability of wetlands to withstand and adapt to environmental changes over geologic timescales. For example, *Cahoon et al*. [2006] report observations of accretion rates that are highest in regions with historically high rates of SLR. However, marsh submergence has been observed for present day conditions at several locations including Louisiana and parts of the Chesapeake Bay [*e.g*. *Reed*, 1995; *Nicholls et al*., 2007] and the sedimentary record reveals that marshes commonly recede in response to sea-level rise [*e.g*. *Marsh and Cohen*, 2008]. The question therefore remains as to what rate of sea-level rise or sediment supply conditions will result in the loss of coastal marshes for a given locale. Conceptual models of short-term marsh evolution define three generalized responses to *RSLR* as a function of sediment accumulation: 1) the marsh accretion rates are to equal the rate of SLR, resulting in marsh surface maintenance;

2) the marsh and subtidal accretion rates are greater than the rate of SLR, promoting marsh expansion; and 3) the marsh accretion rates are less than the rate of SLR, leading to marsh drowning.

Focusing now on coastal North Carolina, recent sea-level reconstructions spanning the past 2000 years suggest that the mean rate of sea-level rise in North Carolina is 2.1 mm yr^{-1}, a rate of rise that is greater than any other U.S. Atlantic coast trend during the past 2000 years [*Kemp et al.*, 2011]. Due to the low topographic slopes on the coastal plain (less than 10 cm elevation for every horizontal kilometer), much of the coastal zone of eastern North Carolina is within less than a meter of current sea level (Fig. 1). Further, the microtidal range, low salinity, and low sediment supply likely make the wetland macrophytes here vulnerable to sea-level rise, especially if changes in the barrier islands expose the sounds [*Titus and Wang*, 2008].

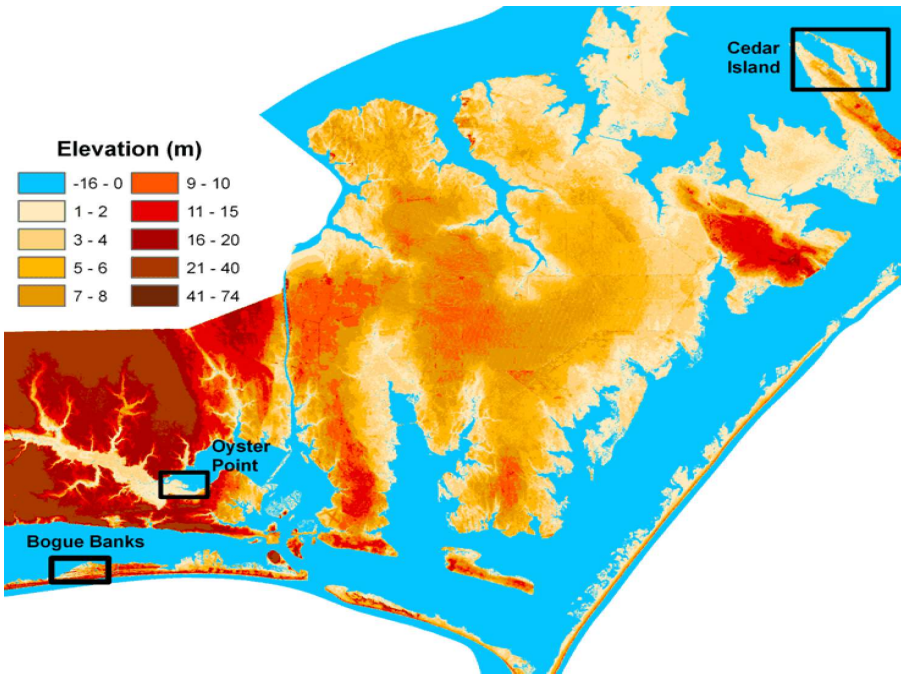

Figure 1. Digital Elevation Model of the field sites at coastal North Carolina along the Outer Banks (Source: NOAA Coastal Services Center Digital Coast).

This research consists of three primary components aimed at understanding the physical and ecological responses to inundation and engineered barriers on marsh platforms (Fig. 2). The first component of this research is focused on tidal cycle to annual scale processes, including the influence of marsh platform length-scale and biomass on the flow regime. The second focus considers reconstructed and simulated marsh platform behavior using analytical and numerical methods to forecast the effects of changes in sediment supply on the stratigraphy and carbon accumulation in coastal salt marshes. Simulations also explore the effects of organic decomposition on marsh accretion rates. The third component examines the effects of engineering an estuarine shoreline, focusing on the change in inundation duration and frequency. Analyses of these three components required collection of field data to characterize flow dynamics, ecology, and sedimentation on coastal salt marshes. The study sites for this research are located at Bogue Banks (Pine Knolls Shore) and Oyster Point, North Carolina (Fig. 1). The back barrier sound of Bogue Banks is characterized by a brackish and semi-diurnal microtidal regime. The

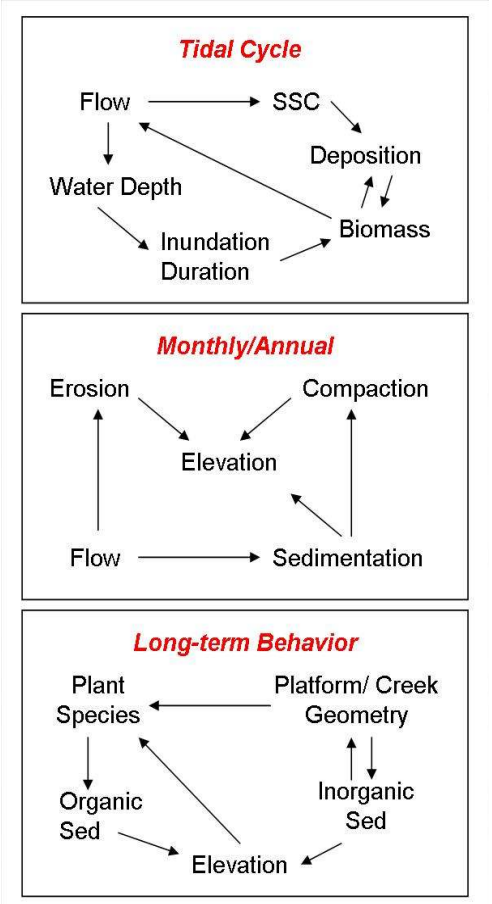

Figure 2. Time scales of field and modeling studies. Tidal cycle data, especially wetting of the marsh platform and suspended sediment concentrations, are used to understand the basic processes and inform descriptions of monthly and annual processes. Monthly and annually averaged processes include tidal cycle effects on elevation, and implicitly include changes in biomass. Although this study is focused on the tidal cycle to annual scale, it is feasible to average the monthly scale processes to simulate the response to sea-level change over time scales spanning tens to hundreds of years. Analysis of long-term behavior could contribute to parameterization of marsh platform evolution.

Bogue Banks-Pine Knolls Shore (PKS) site is primarily colonized by *Spartina alterniflora* of moderate biomass and *Spartina patens*, and *Juncus roemerianus* and *Distichlis spicata* at higher elevations. Oyster Point (OP) is located inland along the Newport River with a semi-diurnal microtidal regime; this site was selected because of the high biomass (600 to 1500 stems per m^{-2}) and macrophyte zonation. Here, *Spartina alterniflora* is present closest to the creek, and *Juncus roemerianus* at higher elevations.

2. Organization of Dissertation

This dissertation is organized such that individual chapters may be submitted for publication as separate papers. Chapters 2 through 6 cover individual topics of the research and include separate introductions, methodologies, results, and conclusions. There is a certain amount of overlap among the chapters, particularly between the review of flow resistance in Chapter 2 and the abbreviated literature reviews in Chapters 3 through 6. The objectives of this research my be summarized as follows.

1. The first objective is to develop analytical expressions to test if the total drag force resulting from flow through a canopy can be approximated as the sum of the drag on individual stems. We demonstrate that this resistance to flow can be characterized as an additive drag. A numerical model was then developed to simulate the flood and ebb of marsh platform flow representative of North Carolina marshes. The influence of marsh platform length scales and biomass are examined to inform the flow behavior under modern conditions. In particular, uniform biomass and biomass distributed as a parabola over

distance are considered.

2. The second objective is to extend application of the one-dimensional hydrodynamic model based on additive stem drag and bed stress to a two-dimensional model that incorporates various shoreline protection or barrier designs. By evaluating the effect of flow routing and inundation duration on a salt marsh platform, this approach provides the first step in determining the extent to which shoreline structures contribute to macrophyte sustainability or degradation as well as platform erosion or accretion. Macrophyte response is anticipated to be influenced by prolonged pooling of water or reduced inundation duration and frequency.

3. The third objective is to develop a description of the astronomical and wind driven signals and the separation of these two constituents. The initial conceptualization of a wind driven signal superimposed on the astronomical signal is not quite correct; rather, harmonic analysis reveals that low-frequency variations in the water level constitute a significant part of the observed record, the effect of which is to set the average water level about which the astronomical signal fluctuates. This study also examines the astronomical and wind-driven components of the tidal signal within frequency domains in order to explore the response time of the movement of water into and out of the estuary. Implications of these results, including the frequency of marsh platform wetting and drying, are then related to macrophyte productivity.

4. The fourth objective is to explore the impacts of sea-level rise on the long-term behavior of sedimentation rates, organic decomposition, and carbon sequestration. Two models of salt marsh sedimentation are presented that capture the inorganic and above- and belowground

organic processes. The analytical model is used to examine the bias introduced by organic processes into proxy records of sedimentation. The numerical model expands upon the analytical model and simulates marsh stratigraphy response to sediment supply and the rate of sea-level rise. The model was initially calibrated and tested using marsh stratigraphy and vegetation dynamics from South Carolina, and later refined using sediment profiles from North Carolina. These sediment profiles were analyzed for sedimentation rate, organic matter, and carbon content. These new data allowed me to elucidate the mass fraction of deposited organic matter that goes into the refractory pool of carbon and the sedimentation history for the site.

Much of the available literature related to inner-canopy flow and resistance has considered stem-scale processes, modified open channel flow equations, or fully turbulent flow conditions. This research aims to provide tools to simulate marsh platform flow dynamics that are sufficiently general that they can be applied to many locales. A review of flood and ebb flow is provided in Chapter II, with a focus on the significance of emergent stems, the characterization of the total drag, and the momentum balance of the flow. Resistance equations include both stem drag and bed stress, wherein the total stem drag is shown to be additive. Flood and ebb flow is modeled to elucidate the effects of length-scale controlled by both the amount of biomass and the spatial distribution of biomass. Short platform length-scales are shown to exhibit a bath-tub flooding behavior. Over longer platform length-scales a wave-like behavior can occur, where the extent of this wave-like behavior is controlled by the spatial distribution of the biomass.

A two-dimensional model is presented in Chapter III to evaluate flow routing and

inundation duration on a salt marsh platform in response to shoreline barrier design. This research provides the first steps for demonstrating implications of "protective" barrier design on macrophyte degradation or platform erosion, or conversely, resulting increased productivity and sedimentation. The impetus for this chapter is to explore the physical consequences of physical-biological coupling at "living shorelines," a relatively new approach to erosion control that aims for minimal disruption to the local habitat. Particular aspects explored in this chapter include the influence of estuarine barriers on the extent of marsh platform flooding, change in ebb flow with platform length-scale, the influence of barrier and segment gap lengths on ebb flow, and the influence of biomass on the flow behavior. Structural designs explore single continuous and segmented shoreline barriers and multiple staggered barriers of varying length and spacing. Barriers are shown to influence the distribution of water at the platform edge. Likewise, under the condition of large platform length-scale, high biomass, and long barrier length, the hydroperiod is affected at higher elevations. This research suggests that in order to maintain ambient conditions on the marsh platform it is necessary to minimize the length of barriers.

North Carolina is characterized by large open sounds subject to microtidal astronomical influences and wind tide dominated areas in the northern Outer Banks (*e.g*,. Cedar Island). Astronomical tides and the associated flooding can be described by harmonic analysis of the local tidal constituents. The flood and ebb associated with wind-driven tides, however, are stochastic and depend on the strength and direction of the wind. Chapter IV presents a description of the astronomical and wind-driven tidal signals. It is demonstrated that the mixed tidal record does not consist of a wind-driven component superimposed on

the astronomical part, wherein water is driven onto the platform by wind. Rather, the effect of wind is to increase or decrease the overall level of the water in the estuary and therefore the mean water level about which the astronomical signal fluctuates over timescales longer than semi-diurnal and diurnal. This concept is further illustrated within the frequency domain to explore the response time of estuary fill and drain. A significant conclusion from this chapter is that the highest and lowest inundation depths and durations associated with the wind driven component can not be described with a simple model, and this has implications for predicting aboveground productivity.

Chapter V presents an analytical and numerical model of salt marsh sedimentation that explicitly accounts for above- and belowground organic processes including root growth and decay of organic carbon. The analytical model demonstrates how organic processes may introduce bias into proxy records of sedimentation, namely those based on ^{137}Cs and ^{210}Pb concentrations. The numerical model simulates marsh stratigraphy response to sediment supply and the rate of sea-level rise. Carbon accumulation in marshes is shown to be nonlinearly related to the supply of inorganic sediment and the rate of sea-level rise. Further, carbon accumulation on marshes that are sediment poor are more sensitive to changes in sediment supply than sediment-rich marshes.

Chapter VI involves calibration and testing of the model in Chapter 5 using field data from Pine Knolls Shore, North Carolina. This study focuses on the ability of the analytical model to reproduce marsh stratigraphy measured in the field. Comprehensive field and laboratory data presented include biological demographics, organic matter content, grain size, sediment accretion rates, ^{210}Pb and ^{137}Cs concentrations, and organic carbon profiles. The

PKS site consists of a *Spartina* and *Juncus* platform that differ in their source of ^{210}Pb input. Further, accretion rates from the radioisotope data suggests that the marsh platform can not maintain equilibrium with sea-level rise based on current sea level rise estimates. In addition to the analytical analysis, the data from PKS provide for a description of the depositional environment.

Chapter VII concludes this dissertation and provides a brief synthesis of the contributions to coastal geomorphology from each chapter. This chapter also describes how I intend to apply the results of Chapters II through VI as well as future research needs.

3. References

Cahoon, D.R., P.F. Hensel, T. Spencer, D.J. Reed, K.L. McKee, and N. Saintilan (2006), Coastal wetland vulnerability to relative sea-level rise: wetland elevation trends and process controls, in *Wetlands and Natural Resource Management: Ecological Studies, v. 190*, edited by J.T.A. Verhoeven, B. Beltman, R. Bobbink, and D.E. Whigham, pp. 271-292, Springer, Berlin.

Holgate, S.J., and P.L. Woodworth (2004), Evidence for enhanced coastal sea level rise during the 1990s, *Geophys. Res. Lett., 31,* L07305, doi:10.1029/2004GL019626.

IPCC (2010), Workshop Report of the Intergovernmental Panel on Climate Change Workshop on Sea Level Rise and Ice Sheet Instabilities, in *IPCC Working Group I Technical Support Unit*, edited by T.F. Stocker, D. Qin, G.K. Plattner, M. Tignor, S. Allen, and P.M. Midgley, University of Bern, Bern, Switzerland, pp. 227.

Kemp, A.C., B.P. Horton, J.P. Donnelly, M.E. Mann, M. Vermeer, and S. Rahmstorf (2011), Climate related sea-level variations over the past two millennia, *Proc Nat'l Acad Sci USA, 108:27*, 11017-11022.

Marsh, P.E., and A.D. Cohen (2008), Identifying high-level salt marshes using a palynomorphic fingerprint with implications for tracking sea level change, *Review of Palaeobotany and Palynology, 148:1*, 60-69.

Morris, J.T., P.V. Sundareshwar, C.T. Nietch, B. Kjerfve, and D.R. Cahoon (2002), Responses of coastal wetlands to rising sea level, *Ecology, 83:10*, 2869-2877.

Nicholls, R.J., P.P. Wong, V.R. Burkett, J.O. Codignotto, J.E. Hay, R.F., McLean, S. Ragoonaden, and C.D. Woodroffe (2007), Coastal systems in low-lying areas, in *Climate Change 2007: Impacts, Adaptation and Vulnerability. Contribution of Working Group II to the Fourth Assessment Report of the Intergovernamental Panel on Climate Change,* edited by M.L. Parry, O.F. Canziani, J.P. Palutikof, P.J. van der Linden, and C.E. Hanson, Cambridge University Press, Cambridge, UK, 315-356.

Nikora, V. (2009), Hydrodynamics of aquatic ecosystems: An interface between ecology, biomechanics and environmental fluid mechanics, *River Research and Applications, 26:4*, 367-384.

Reed, D.J. (1995), The response of coastal marshes to sea-level rise: survival or submergence?, *Earth Surf. Processes Landforms, 20*, 39-48.

Titus, J.G. and J. Wang (2008), Maps of lands close to sea level along the Middle Atlantic coast of the United States: An elevation data set to use while waiting for LIDAR, Section 1.1, *in Background Documents Supporting Climate Change Science Program Synthesis and Assessment Product 4.1*, eds. J.G. Titus and E.M. Strange, EPA 430R07004, U.S. EPA, Washington, DC.

CHAPTER II

HYDRODYNAMICS OF MARSH PLATFORM FLOW AND IMPLICATIONS OF PLATFORM LENGTH SCALE AND STEM DRAG

Abstract

Tidal salt marsh ecosystems are partially maintained by macrophytes that regulate platform elevation by inorganic and organic sedimentation. Macrophytes modify the flow within a canopy, yet the details of the hydrodynamic influence of a marsh canopy on water flow are only partially understood. Previous studies have documented the importance of stem drag in marsh platform hydrodynamics; however, this study is focused on the role of biomass and marsh platform length-scale on marsh flow. Four areas of research are highlighted in this chapter in order to inform a hydrodynamic model of marsh platform flow— emergent stems, characterization of the total drag, the momentum balance of the flow, and the effects of stem density. A simplified one-dimensional representation of flow on salt marsh platforms is developed, with flow governed by a balance between the pressure gradient and the resistance due to vegetative drag and bed friction. The analytical expression includes the drag coefficient as a function of the Reynolds number for the total vegetative force per unit volume in a macrophyte canopy. Total force from published experimental results are evaluated against calculated total force, and it is demonstrated that the total resistence in a marsh canopy can be approximated as the sum of the drag on individual stems. This approach varies from previous studies in that it considers transitional to laminar flow

conditions, an additive model, and resistance resulting from both the macrophyte stems and the bed. The conditions of platform length-scale and macrophyte stem density under which a bathtub flood behavior versus wave-like behavior represents the observed field conditions are described. Results suggest that short platform length-scales exhibit a bath-tub flood behavior regardless of the stem density. Over longer platforms, however, a wave-like behavior can occur, which is sensitive to the stem density. The description of marsh flow provided from this work suggests that a fully coupled, dynamic model is not necessary for marsh platforms with length-scales less than 50 m. Instead, marsh platform inundation is a linear function of elevation and can be coupled with a zero-dimensional model of stem density distributed as a parabola over the length of the platform.

1. Introduction

Mean flow and turbulence characteristics in the presence of vegetation have received much attention, notably for the case of boundary-layer atmospheric flows with applications to carbon dioxide and water vapor exchanges. Similarly, the subjects of vegetative resistance to flow and the influence of vegetation on sedimentation have been of interest in studies of open channel flow for some time, most commonly for engineering of water conveyance. In recent years, however, aquatic plants are regarded less as obstructions and more as a means of ecological engineering — bank stabilization, retention of contaminants, and flood plain management [*Knutson et al.*, 1982], and models incorporating the classic equations of open channel flow have been modified for application to intermittently flooded, vegetated marsh

conditions. Indeed, an emerging area of research focuses on the interfaces between aquatic ecology, biomechanics and environmental fluid mechanics [*e.g. Nikora*, 2009]. Such an approach was also stressed by *Stazner and Borchardt* [1994] who suggested that ecosystem studies that incorporate fluid dynamics will advance general ecological theory and understanding much faster than studies that ignore principles of moving air or water.

Salt-marsh platform evolution depends on the coupled effects of flow, sedimentation, and macrophyte productivity. Mineralogic sedimentation on salt marsh platforms results from flow resistance and wave damping by vegetation. The details of the hydrodynamic impact of a marsh canopy on water flow at the marsh edge and on the platform, and the relation to sedimentation, are only partially understood. In general, the presence of vegetation reduces near bed velocity and therefore reduces local bed stress, resulting in less resuspension of sediment and increased particle retention within the canopy [*Lopez and Garcia*, 1998; *Neumeier and Ciavola*, 2004]. The hydraulic resistance to flow introduced by plants may also contribute to an increase in water depth [*e.g. James et al.*, 2001] and residence time [*e.g. Hodges*, 1997] on the marsh platform. Plants force water to follow tortuous paths around individual stems, introducing no-slip boundaries and local, spatial variations in velocity associated with non-uniform spacing of stems. Studies of flow past a single circular cylinder, representing a stem, have documented boundary layer separation and flow oscillations in the wake region behind the body, which depends on the Reynolds number.

Models of flow through vegetative canopies require a quantitative measure of the ability of plants to extract momentum by form drag. This drag is typically characterized by

a friction factor based on the characteristics of the vegetation. Many experiments of vegetative flow resistance involve cylinders [*e.g.Nepf*, 1999; *James et al*., 2004; *Tanino and Nepf*, 2008] or macrophyte stems in laboratory flumes [*e.g. Shi et al.,* 1995; *Lee et al*., 2004; *Jordanova et al*., 2006]. Much work has focused on rigid canopies [*see Tsihrintzis and Madiedo*, 2000], which simplifies characterization of the flow regime, compared to flexible, waving canopies, and is representative of marsh grasses that have been observed to exhibit only limited bending [*e.g. Knutson*, 1982]. Numerical, laboratory, and field experiments have also considered both submerged [*e.g. Righetti and Armanini*, 2002; *Wilson et al*., 2003; *Ghisalberti and Nepf*, 2005] and emergent objects [*e.g. Roig*, 1994; *James et al*., 2001; *Järvelä*, 2004]. Under emergent conditions, stem density is suggested to be the dominant parameter regardless of species or plant shape and distribution [*Fathi-Moghadam and Kouwen*, 1997]. Submergent conditions, on the other hand, involve resistence associated with water moving both through and above the vegetation.

Previous characterizations of flow resistance within an array of cylinders are commonly based on high Reynolds numbers [*e.g. Nepf*, 1999]. However, flow over vegetated salt marshes is typically transitional between laminar and turbulent regimes, with velocities much lower than those of open-channel flow [*e.g. Kadlec*, 1990; *Leonard and Luther*, 1995]. Past studies have also considered empirical roughness coefficients, including use of conventional formulas for flow resistance in open channels (*e.g.* Manning's equation). Formulations based on open channel flow, however, are poorly suited to vegetated platforms because they fail to explicitly account for the drag exerted on elements through the flow depth [*e.g. Turner et al*., 1978; *Turner and Chanmeesri*, 1984; *Kadlec*, 1990; *James et al*.,

2001; *James et al.*, 2004]. Free surface flow resistance equations are founded on the balance of the forces acting on the water, namely the downslope weight of the water, and the forces resisting the movement of water, such as the friction imposed by the bed. This conventional force balance suggests that the boundary shear stress is a function of the flow depth, and therefore velocity, rather than stem resistence.

This chapter examines the hydrodynamics of salt-marsh platform flow, informed by field sampling of macrophyte morphology and distribution, platform elevation, the length scale of salt marsh platforms, and water level records. Flow on salt marsh platforms is simulated, with flow governed by a balance between the pressure gradient and the resistance due to vegetative or form drag F_D and bed stress F_S. The form drag exerted by a single cylinder or stem in uniform flow can be parameterized through a drag coefficient C_D. The total drag can vary with canopy density N_A (stems L^{-2}) and Reynolds number Re, morphology and flexibility of stems [*e.g. Dunn et al.*, 1996], and the presence and position of neighboring cylinders [*e.g. Petryk*, 1969; *James et al.*, 2001; *Tanino and Nepf*, 2008]. Consistent with classical dimensional analysis for the form drag of an isolated cylinder, C_D has been shown to decrease with increasing Re up to $Re = O(10^3)$ (Fig. 1) and increasing stem density (or decreased stem spacing) [*e.g. Schlicting and Gersten*, 2000]. An analytical expression is developed here based on the drag coefficient as a function of the Reynolds number for the total vegetative force per unit volume F_V in an array of cylinders. This equation is evaluated using published experimental data to determine if the total resistence can be approximated as the sum of the drag on individual stems. The one-dimensional analytical model assumes that the total resistance is the sum of the form (vegetative) drag and bed stress. This approach

varies from previous studies wherein authors have neglected the influence of bed resistance, with the assumption that energy losses due to plant stems are considerably larger. It is shown here, however, that for low stem densities, the contribution due to bed resistance is essential to characterize the resistance to flow on marsh platforms. Results from the hydrodynamic model are compared with field data collected at Bogue Banks, North Carolina, and simulations demonstrate the physical behavior of salt marsh platform flow, including the influence of marsh platform length-scales and biomass. The hydrodynamic model developed for this study is based on simple principles of conservation of mass and momentum, and therefore can be applied at other study sites.

2. Background

This section provides a review of the effect of vegetation on flood and ebb flow. Previous studies have documented the importance of stem drag for marsh platform hydrodynamics. The emphasis of this study, however, is the influence of biomass and marsh platform length-scale on marsh flow. This includes the depth and residence time of water on the surface of the marsh platform. Four areas of research are discussed below in order to inform this study — the significance of emergent stems, the characterization of the total drag, the momentum balance of the flow, and the effect of stem density on marsh flow. Previous studies have considered both emergent and submerged stems. Laboratory and field studies both support the assumption of emergent stems for the model development presented below. Previous research related to stem drag informs whether the total drag due to stems can be

approximated as the sum of the drag on individual stems or whether the total drag on stems involves an interaction with neighboring stems and wake effects. This requires consideration of typical Reynolds numbers associated with marsh platform flow and the stem densities for which additive drag, referred hereafter as an additive model, and wake effects have been documented. Considering only stem density, the momentum balance simplifies to a balance between the pressure and friction. The role of stem density and bed stress is also reviewed below, wherein it is suggested that the contribution from bed stress is necessary for low stem densities.

2.1 Stem Height

Wetland studies have focused on both submerged and emergent wetland vegetation. Emergent, rigid circular cylinders (representative of macrophyte stems) are considered here. Although submerged vegetation is equally important and common, here we are focused on describing the fundamental resistance encountered during salt marsh flow. For example, flow through emergent stems is dominated by stem interactions whereas submerged canopies are separated into two flow layers. The differing profiles of mean velocity and Reynolds stress for submerged and emergent canopies was first noted by *Pethick et al*. [1990], who observed an apparent discontinuity in the mean flow profile at the top of the canopy; the authors speculated that the two layers were isolated from one another. However, recent studies suggest that the flow regime separation may be classified as flow within the canopy (the lower longitudinal exchange zone) and flow above the canopy (the upper vertical exchange zone) [*Nepf and Vivoni*, 2000]. For emergent canopies, only the lower zone of longitudinal

exchange is present, where turbulence is generated within stem wakes and the momentum budget consists of a balance between vegetative drag and the pressure gradient since the vertical turbulent transport of momentum is negligible [*Nepf and Vivoni*, 2000; *Righetti and Armanini*, 2002].

2.2 Total Drag as Sum

Under conditions of emergent stems and high stem density on a marsh platform, the total drag consists of a balance between the vegetative drag and the pressure gradient. However, conditions of low stem density on marsh platforms are common. We examine whether the total drag due to the stems can be approximated as the sum of the drag on individual stems, wherein stems are treated as being isolated, or whether the total drag cannot be treated as the sum because of interaction and wake effects. Wake sheltering describes the influence of upstream stems on the flow field around downstream stems, which can influence vortex shedding. The Reynolds number informs whether marsh flow will have vortices. When the Reynolds number is low, under laminar conditions, the flow remains attached to the cylinder.

Typical Reynolds numbers within a vegetated canopy are transitional [*e.g. Kadlec*, 1990; *Leonard and Luther*, 1995; *Leonard et al.*, 2002]. Laminar values from field experiments have been recorded by several authors, including $75 < Re_d < 600$, where Re_d is the Reynolds number with length-scale based on the stem diameter d [*Leonard et al.*, 2002]. Studies have shown that for conditions of laminar flow and dense canopies, wake sheltering behind plant stems causes the drag from the entire array to be less than the sum of the drag

from individual stems [*see Harvey et al.*, 2009]. Experiments conducted at sufficiently large Reynolds numbers, however, suggest that the drag coefficient becomes constant [*e.g. Tsihrintzis and Madiedo*, 2000]. It has also been shown that at high Reynolds numbers, the drag coefficient for a single stem can be applied when the spacing between stems is greater than the wake length [*e.g. Nepf*, 1999] and the total drag equals the sum of the drag from the individual stems.

2.3 Momentum Balance

The equation of motion for flow within a canopy is the Navier-Stokes equation. Ensemble and spatial averaging of the Navier-Stokes equation [*e.g. Raupach and Shaw*, 1982] yields a momentum balance between pressure and stress, including the Reynolds stress, viscous drag, and the form drag. As described above, conditions with minimal wake interference result in flow around an individual cylinder in an array of cylinders resembling flow past an isolated cylinder [*e.g. Nepf*, 1999]. *Tsujimoto et al.* [1991] and *Burke and Stolzenbackh* [1983] noted negligible Reynolds stresses measured with respect to the horizontal surface, which suggests that the length-scale of turbulent eddies within the canopy is small compared to the flow depth. Here we evaluate a momentum balance consisting of pressure and vegetative drag, neglecting the inertial terms in the depth integrated equations. In this regard, the total resistance to flow involves the drag provided by the vegetation and the bed stress.

2.4 Stem Density

Mean flow velocity is influenced by variations in plant morphology and stem density. *Leonard and Luther* [1995], for example, found that mean flow velocity is inversely related to stem density and distance from the creek edge. That is, flow velocity decreases as flows encounter the vegetated marsh surface and continues to decrease with an increase in stem density. In addition, the authors found that flow rates through *Juncus roemarianus* and *Spartina alterniflora* increase with height above the substrate except at elevations approximately 7 to 12 cm above the marsh surface, where leaves begin to emerge from the sheath and speeds are lowest.

Shear stress partitioning includes both the bed stress and the vegetative stress [*Raupach*, 1992]. *Schlichting* [1936] first proposed that the total force F_T applied to a rough surface can be divided into that exerted on the roughness elements F_D and that on the bed F_S,

$$F_T = F_D + F_S \tag{1}$$

Under conditions of high stem density, vegetation increases the total resistive force while decreasing the fraction of the shear force acting on the platform bed. Conversely, for conditions of sparse stem densities, one may expect the influence of bed shear on overall resistance to be the dominant contribution to resistance. Thus, the common assumption that the majority of the resistance is due to form drag does not necessarily hold for the range of natural flow depths and stem densities [*e.g. James et al.,* 2001]. Eq. (1) has also been used as an alternative approach to using a resistance equation with the drag coefficient determined from vegetation characteristics to simulate the resistance phenomena directly [*e.g. Thompson and Roberson*, 1976].

3. Analysis

An analytical expression is developed here based on the drag coefficient as a function of the Reynolds number for the total vegetative force per unit volume in an array of cylinders. The analysis first considers the relationship between the drag coefficient and Reynolds number, comparing reported drag coefficients measured from laboratory experiments versus values calculated using the laboratory parameters. Measurements of total force from laboratory experiments reported in the literature are then evaluated against calculated total force determined from the experimental setup in order to find if the total resistance can be quantified as the cumulative measured resistance for individual stems. A one-dimensional model is then developed, wherein the force balance is solved numerically.

3.1 Additive Drag

The relationships amongst Re, N_A, and C_D are evaluated below through comparisons of experimentally measured values from the literature and drag force calculations. Reynolds numbers are calculated for a characteristic velocity U as

$$Re = \frac{UL}{\upsilon} \tag{2}$$

The kinematic viscosity υ equals the dynamic viscosity μ divided by the fluid density ρ, and the characteristic length scale L may be based on either stem diameter d denoted as Re_d or the water depth h denoted as Re_h. Consistent with *Kadlec* [1990], the average stem diameter is used here since wetland vegetation is closely spaced and turbulence is generated via eddy

shedding from plant stems.

Vegetation density is reported throughout this paper as the number of stems per unit area N_A. The stem density is computed from plant demographics available in the literature and from our own sampling at Bogue Banks, North Carolina. Vegetation density is often reported as the projected plant area per unit volume a, represented by the following when modeled as cylinders [*e.g. Dunn et al.*, 1996; *Nepf,* 1999],

$$a = \frac{A}{V} = N_A d = \frac{N_A dAh}{Ah} = \frac{dh}{\Delta s^2 h} = \frac{d}{\Delta s^2} \tag{3}$$

where h is the flow depth, d is stem diameter, and $A = dh$ is the frontal area of the cylinder. The mean spacing between stems (Δs) can also be denoted as

$$\sqrt{\frac{A}{N_{A_T}}} = N_A^{-1/2} \tag{4}$$

Here N_{A_T} is the total number of stems within a canopy of area A.

Various attempts to account for the contribution of emergent vegetation to total resistance have quantified the drag force on the stems. Stem drag models have used the drag coefficient C_D as either a fitting parameter [*e.g. Nepf*, 1999] or on the basis of values for isolated cylinders as a function of the Reynolds number. The drag coefficient is the ratio of the drag force to dynamic pressure, associated with the difference between the high pressure upstream and low pressure downstream of a stem. In this paper the impact of vegetation and the drag it provides is characterized by the drag coefficient,

$$C_D = \frac{2F_D}{\rho U^2 A} \tag{5}$$

where the form drag F_D is the drag on an individual cylinder and U is fluid velocity. The total drag force per unit volume is solved for using

$$F_V = \frac{1}{2} N_A d \rho C_D U^2 \tag{6}$$

A review of experimental studies evaluating stem drag and resistance equations was undertaken and results are summarized in Appendix A. Three of these published experimental data sets were selected (Table 1) based on the availability of the data and conditions relevant to marsh stem drag conditions. That is, studies were selected where specific parameters of stem and flow properties were available and flow velocities are primarily transitional; studies using semi-empirical approaches were avoided.

Dunn et al. [1996] measure the influence of bed slope, flow velocity, and stem spacing on the drag coefficient. Reported discharge values were converted to horizontally averaged flow velocity for Reynolds number calculations. *Dunn et al*. [1996] evaluate the one-dimensional local drag coefficient by taking the derivative of the horizontally averaged Reynolds stress curve with respect to depth within the plant canopy, which is then used to parameterize the form drag exerted by an individual cylinder. We use *Dunn et al*.'s [1996] drag coefficient with Eq. (6) to calculate an additive total drag force per unit volume, which is compared to the additive model described below.

Table 1. Laboratory design and summary of conclusions for experimental drag force measurements. Parameters from the experimental setup in these studies are used with Eq (6) to determine if the total resistance can be quantified as the cumulative measured resistance for individual stems.

Source	Stem Type	Stem diameter (mm)	Stem spacing/ density	Re_d	Experimental Conclusions
Dunn et al., [1996]	Wooden, rigid cylindrical dowels	6.37	5.08 to 15.24 cm	1383-4772	The bulk drag coefficient decreases with an increase in the product of stem density and stem height, and is dependent on turbulence intensity.
James et al., [2001]	Steel rods, reeds, bull rush	Reed (*P. austrailis*): 8.4-10.8 Bulrush (*T. capensis*): 11.57	Staggered 90 mm; Transverse, 60 mm; Longitudinal, round, square, and diagonal arrangements	246-4838	Resistance is a function of N_A. Stem shape has little influence on resistance at low slopes. Foliage significantly influences C_D . For natural stems, C_D is dependent on *Re* at much higher *Re* values than for smooth circular cylinders.
Thompson [2001]	PVC, cylindrical dowels	9.5 and 24.5	d/s: 0.039 to 0.2; Arrangement is square; 10 to 60 stems m^2	4636-23880	F/U^2 is represented by a linear relationship with upstream stem area. C_D is represented by an average value over the range of flow depths investigated; however, an average C_D can not be applied for the range of flow conditions.

James et al. [2001] measured the drag force on single stems from the weight of water in a container balanced by the rotation of a frame with anchored stems. The force required to balance the rotation of the frame under the influence of drag on the stem is used by the authors to calculate the drag force. The authors assume that resistance results from the stem drag. Stems of *Phragmite austrailis* were progressively stripped of leaves and branches to determine contributions from the main stem and foliage on the drag. Flow velocities were measured at the test stem level with the stem removed. The drag coefficient is backcalculated using the equation for form drag on an isolated cylinder,

$$F_D = \frac{1}{2}\rho A C_D U^2 \tag{7}$$

The projected area A for *Phragmite austrailis* is defined by the length and diameter of the main stem. In order to reproduce values of a similar magnitude reported by *James et al*. [2001], the additive model uses stem length in place of flow depth for Reynolds number calculations (Eq. 2). Inconsistency with the published methodology and rederived calculations may be a result of undocumented corrections performed by the authors.

Thompson [2001] developed a methodology to measure the drag force on individual elements in a laboratory flume. Reported values include the drag force on individual and multiple stems. Drag force was measured using a load cell connected to a low friction linear slide, where the slide is connected to a threaded rod with a cylinder. Drag force causes linear movement on the slide and a tensile force on the load cell. *Thompson* [2001] backcalculated the drag coefficient from the time-averaged drag force which is a function of the upstream projected area and flow velocity.

Drag force is calculated here for conditions of drag on an isolated stem F_D and drag per unit volume F_V. Drag coefficients are computed from a polynomial curve-fit of *Re* and C_D for a cylindrical object [*Schlicting and Gersten*, 2000]. Sampling from the data, the polynomial curve-fit is

$$\log C_D = 0.9914 - 0.6341(\log Re) + 0.0984(\log Re)^2 \tag{8}$$

Resulting C_D and *Re* values from Eq. (8) are plotted and compared to the standard single cylinder drag data curve in Fig. (1). The polynomial fit from Eq. (8) provides a reasonable fit through the data, including the drag crisis where C_D decreases at the critical Reynolds number ($Re_{crit} \sim 2\times10^5$). The drag crisis produces a regime where the drag force decreases as the velocity increases. The fit from Eq. (8) performs well up to $Re_d \sim 10^5$, and beyond this value the polynomial overestimates C_D.

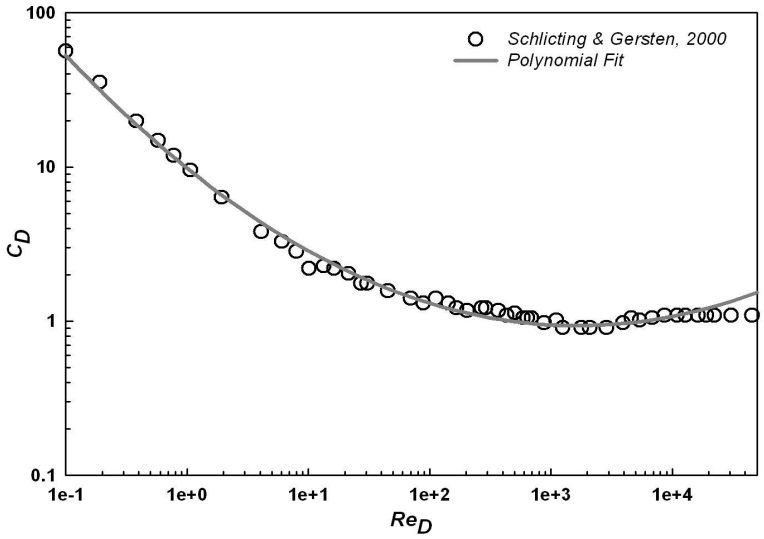

Figure 1. The standard Reynolds-Drag Coefficient curve (**o**) based on *Schlicting and Gersten* [2000] experimental data. C_D decreases as *Re* increases until turbulent conditions when C_D becomes constant. The polynomial fit from Eq. (8) (—) approximates the curve until the drag crisis, where the polynomial curve begins to overestimate C_D.

The drag coefficients measured by *Dunn et al*. [1996], *James et al*. [2001], and *Thompson* [2001] are plotted with the drag coefficient from the polynomial fit in Fig. (2), and comparisons of C_D as a function of *Re* in Fig. (3). Although the fits are only approximate one-to-one relations, suggesting experimental error over the range of Reynolds numbers in the three studies, Eq. (8) is adopted hereafter, including the variation in the Reynolds number. The range of *James et al*. [2001] values of C_D is greater than the other measured values, and is likely associated with the amount of foliage, average velocity, and/or the experimental setup. Further, the scatter observed at higher Re_d in Fig. (3) clearly represents imprecision and uncertainty with these experimental measurements.

The measured and calculated total drag force from Eqs (6) and (7) are shown in Fig. (4). Fig. (4a) suggests that the drag force can be over-predicted by the calculated method for turbulent flows. A one-to-one relationship exists for the measured and calculated total drag, for both the force per unit volume and force on an isolated cylinder, supporting the development of an additive drag model. That is, the total stem drag is well approximated as the sum of the drag on individual stems.

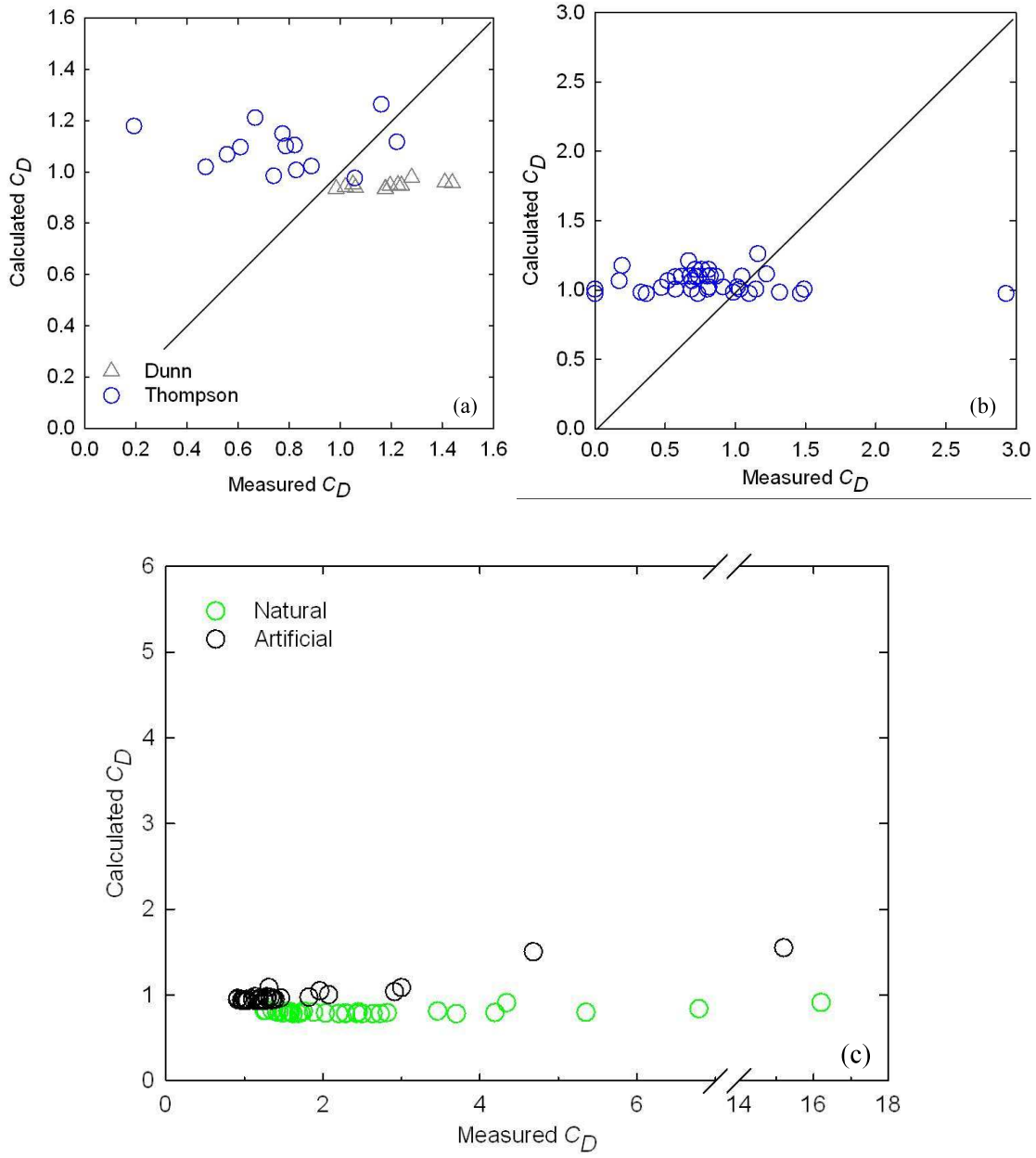

Figure 2. Drag coefficients measured from laboratory experiments in the literature and calculated here with Eq. (8) for (a) multiple cylinders [*Dunn et al.*, 1996]; (b) individual cylinders [*Thompson*, 2001]; and (c) individual cylinders and stems [*James et al.*, 2001].

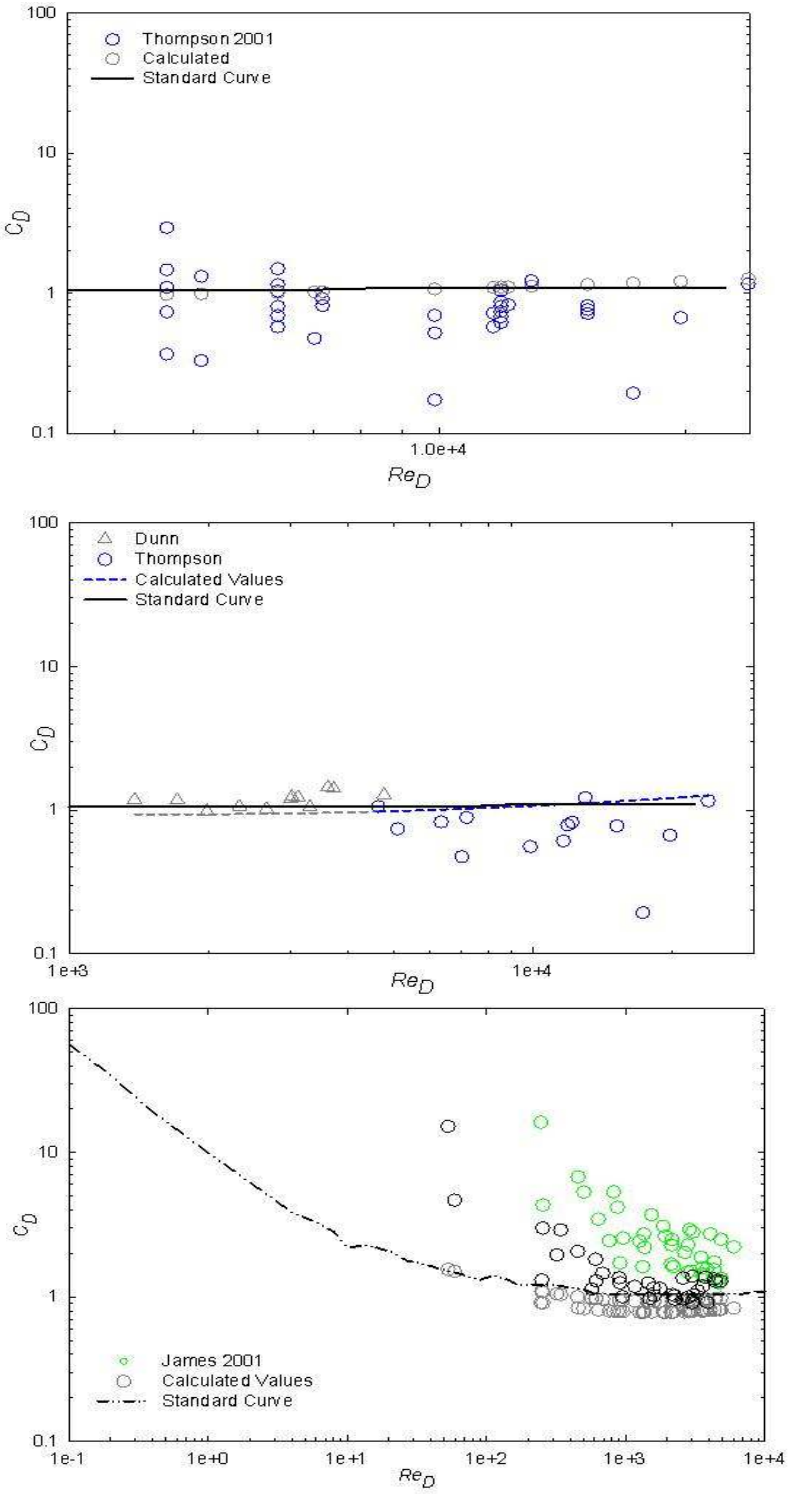

Figure 3. Drag coefficient as a function of Reynolds numbers for (*top*) multiple cylinders [*Dunn et al.*, 1996; *Thompson*, 2001]; (*middle*) individual cylinders [*Thompson*, 2001]; and (*bottom*) individual cylinders and stems [*James et al.*, 2001]. The standard drag and calculated values of the drag coefficient Eq (8) are shown for comparison.

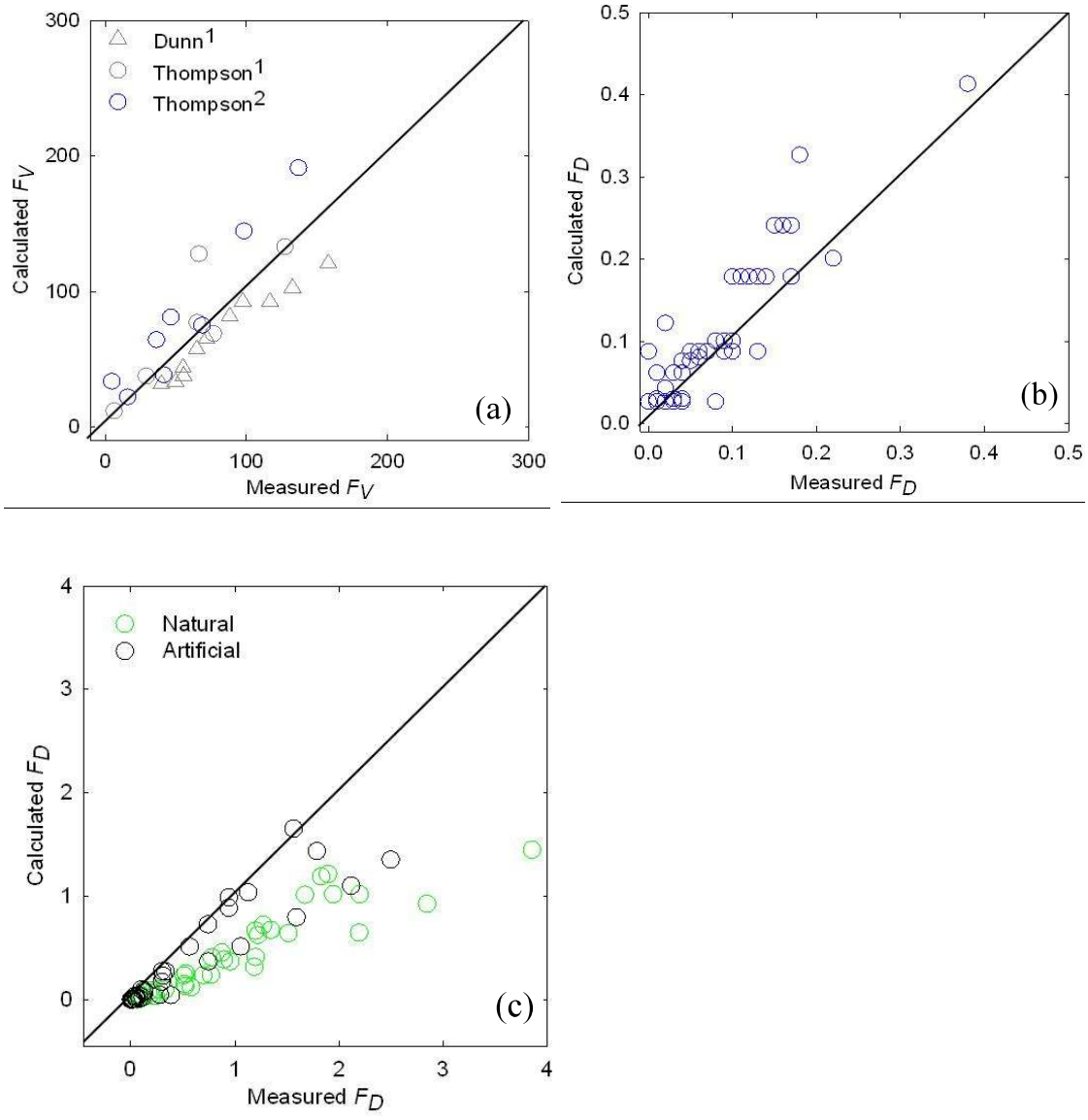

Figure 4. Stem drag from laboratory experiments and values calculated using Eqs (6) and (7). (a) Drag force per unit volume for an array of cylinders (multiple cylinders. '1' denotes *Re*d < 10,000 and '2' denotes *Re*d > 10,000 [*Dunn et al.*, 1996; *Thompson*, 2001]; (b) Individual cylinders [*Thompson*, 2001]; and (c) Individual cylinders and stems [*James et al.*, 2001].

3.2 Hydrodynamic Model

The contribution to flow resistance by stems was evaluated above to assess the use of an additive total drag for local flow velocities and stem densities. A one-dimensional, nonlinear, diffusive flow description based on conservation of mass and of momentum is presented in this section. Marsh platform flow is simulated for a range of biomass and platform length scales. The stem density on the marsh platform is simulated as uniform and as varying as a parabola over distance and therefore depth below mean high water (DBMHW). Model output is then compared to a continuous three year record at a field site in North Carolina.

There are specific conditions and assumptions under which the hydrodynamic model presented is applicable. Namely, sparse to medium stem densities are assumed, wave effects are neglected, and the total stem drag is assumed additive. The analysis is also restricted to a tidal approximation wherein a marsh canopy remains emergent. In contrast to lab experiments with uniform stem density, nonuniform biomass is considered in this study, with values sampled from the relationship of biomass and DBMHW [*e.g. Morris et al.,* 2002]. Further, there is sufficient evidence to support use of rigid stems when describing salt marsh flow [*e.g. Knutson et al., 1982*].

3.2.1 Force Balance

Consider a Cartesian *xyz* coordinate system associated with a marsh platform system (Fig. 5). The x coordinate is normal to the marsh-platform edge, positive in the landward direction, with origin ($x = 0$) at the platform edge. Let $z = \zeta$ denote the local water-surface

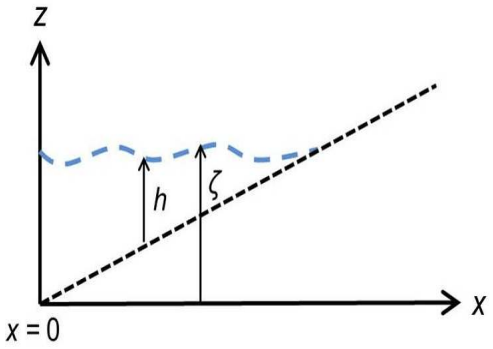

Figure 5. The marsh platform is oriented with the x coordinate normal to the marsh platform edge and the z axis is vertical. The driving force is the downstream weight component of element ρg and the slope S.

elevation, where the z axis is vertical, and let $z = \eta$ denote the local platform surface elevation such that $h = \zeta - \eta$ is the local water depth. The platform elevation is constant in time. The equation for conservation of mass is

$$\frac{\partial}{\partial x}(hU) + \frac{\partial h}{\partial t} = 0 \tag{9}$$

where U denotes the local depth-average velocity and t is time. The local momentum equation under quasi-steady flow expresses a force balance between the pressure gradient with the bed stress τ_S and stem drag τ_C. Assuming an additive stress partitioning between stems and the bed [e.g. *Schlichting*, 1936; Eq. (1)], conservation of momentum requires that

$$g\frac{\partial \zeta}{\partial x} = \frac{1}{2}C_D N_A d U^2 + \frac{1}{2}\frac{C_f}{h}U^2, \tag{10}$$

Recall that N_A is the stem density per unit area and d is the stem diameter. The bed resistence contains the Darcy-Weisbach friction factor C_f, which is calculated using a Manning's roughness coefficient relation, assumed here to be approximately equivalent to the coefficient associated with sand-bed ripples, $n = 0.02$. This roughness has been reported for *Spartina alterniflora* marshes and bare wetland surfaces [*e.g. Roig*, 1994].

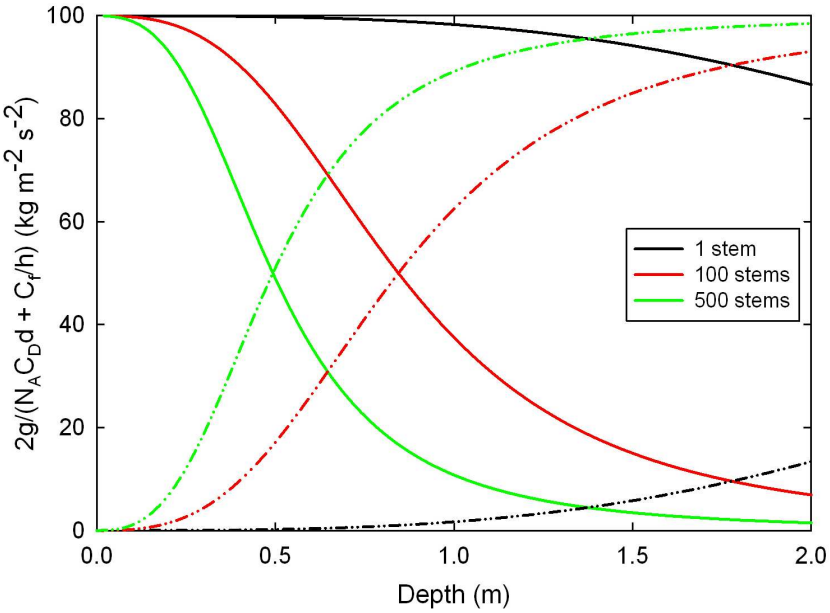

Figure 6. Resistance from Eq. (10) due to the bed (solid) and additive stem drag (dashed) for stem densities of 1 to 500 stems per unit area.

Eq. (10) is the momentum balance, where the pressure is balanced by the drag from the stems and bed stress. Two limiting states to the force balance are noted: (1) in the absence of vegetation, the contribution to resistance is due to the last term in Eq (10); and (2) for flow resistance associated with vegetation, the resistence is accounted for primarily by the middle term in Eq. (10). In the absence of stems, the shear stress increases linearly with flow depth to a maximum value at the bed, where it is balanced by the shear stress imposed by the bed on the flow (Fig. 6).

The total resistance from the partitioning of stresses in Eq. (10) is compared to *Thompson's* [2001] experiments on the total resistence with measured bed and stem drag (Fig. 7) [*see* Appendix B]. The laboratory flume used in *Thompson* [2001] includes a hot-film anemometer mounted in a movable section of the flume. Calculated bed stress τ_{OS}

values are slightly greater than those measured by *Thompson* [2001].This is likely related to the definition of the Manning's coefficient; whereas the calculated values are based on a constant Manning's coefficient $n = 0.002$, *Thompson* defines a particle drag coefficient using n and a nonlinear fit. It is likely that consideration of calculated values other than $n = 0.002$ could result in a better fit. Further, *Thompson* uses a uniform (square) configuration of stems, which may produce wake sheltering, the effect of which results in the drag from the entire array being less than the sum of the drag from that of individual stems.

3.2.2 Variation In Biomass

Within a macrophyte canopy, flow is forced to move around individual stems, resulting in spatial variations in velocity associated with non-uniform spacing of stems and the introduction of no-slip boundaries. We consider macrophytes at the canopy scale where vegetation can be described by an average morphology $A = dh$. The canopy is represented by an array of vertical, circular cylinders as a surrogate in both shape and rigidity for the stem regions of the marsh grasses *Juncus roemerainus* and *Spartina alterniflora*. Field and experimental evidence support a parabolic distribution of biomass [*e.g. Morris et al.*, 2002], wherein stem density has been shown to be a function of DBMHW and therefore elevation (Fig. 8). That is, assuming a marsh platform has a slope, stem densities are represented as a parabola with distance from the water edge.

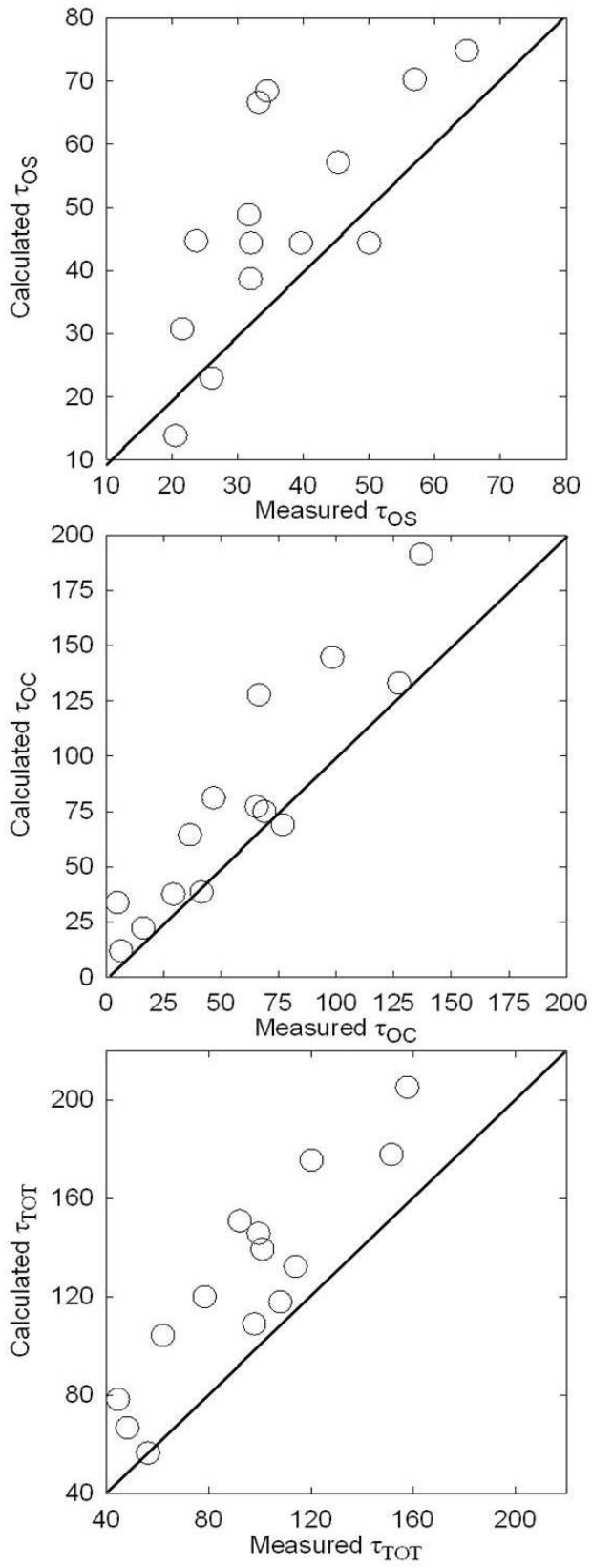

Figure 7. Comparison of measured stresses (NV^{-1}) from *Thompson* [2001] and calculated values herein for bed stress (*top*); form drag (*middle*); and total stress (*bottom*).

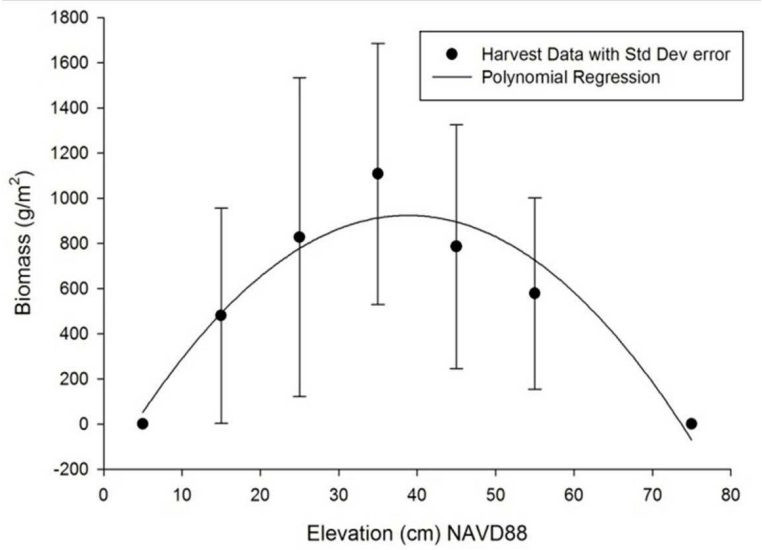

Figure 8. Parabolic distribution of *Spartina alterniflora* aboveground biomass as a function of elevation. Data from North Inlet, South Carolina [*Scott*, 2010].

3.2.3 Numerical Model

The geometry of the model is based on field data from the Pine Knolls Shore (PKS) study site, located along the back-barrier of Bogue Banks, North Carolina. Bogue Sound is characterized by a brackish and semi-diurnal microtidal regime. The tidal range at PKS is 0.96 m. PKS is colonized by *Spartina alterniflora* of moderate biomass and *Spartina patens*, *Juncus roemerianus* and *Distichlis spicata* zonation with increasing elevations. Field measurements used to estimate parametric values for the numerical simulations include platform elevation, stem density from the marsh platforms and marsh organs [*Voss*, 2009], and a three year continuous water level record (Fig. 9). The five water level recorders, In-Situ Level Troll 500 model, were established along a transect spanning monotype *Spartina alterniflora*, creek, and mixed *Spartina alterniflora* and *Juncus roemerianus*. The water

record consists of continuous sampling at 15 min intervals for three years. Biomass measurements using 25 x 25 cm quadrants were collected at sites parallel to the water level recorders transect (Table 2).

Table 2. *Spartina alterniflora* and *Juncus roemerainus* measurements from Pine Knolls Shore, N.C, used as input to the hydrodynamic model.

	Spartina alt.	***Juncus roem.***
Stem diameter (m)	0.005	0.003
Stem Density Range (stems m^{-2})	250-420*	150-250
Stem height (m)	0.17-0.6	0.8-1.3
Dry weight (g m^{-2})	18-330	350-820
Flow speed, assumed (m s^{-1})	0.005	
Re_d	<< 200	
F_v	0.020-0.055	0.007-0.025

A one-dimensional hydrodynamic numerical model was developed in Matlab, and considers tidal influence at a creek boundary that is driven by a semi-diurnal tide. The dominant harmonic signals at PKS include M_2, the lunar semidiurnal constituent, and K_1, the lunar diurnal constituent, with periods of 12.42 and 23.93, respectively [*Chapter 4*]. The marsh surface is nearly level, with a slope of 0.005 along the bank colonized with monotype *Spartina alterniflora* and a slope of 0.01 along the bank with *Spartina alterniflora* to *Juncus roemerianus* to *Distichlis spicata* zonation with increasing elevation. The platform width is greatest at the shoreline and creek mouth, reaching up to 100 m, while the landward marsh platform is approximately 50 m wide along both sides of the creek. During slack tide

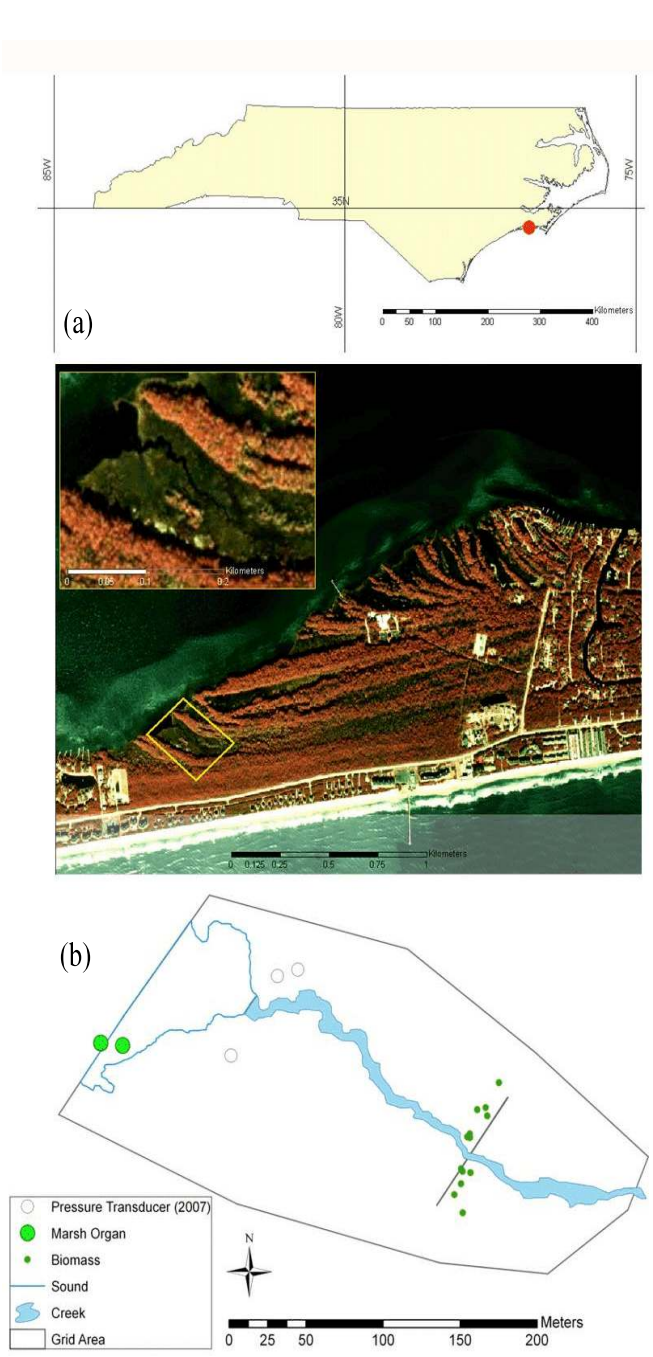

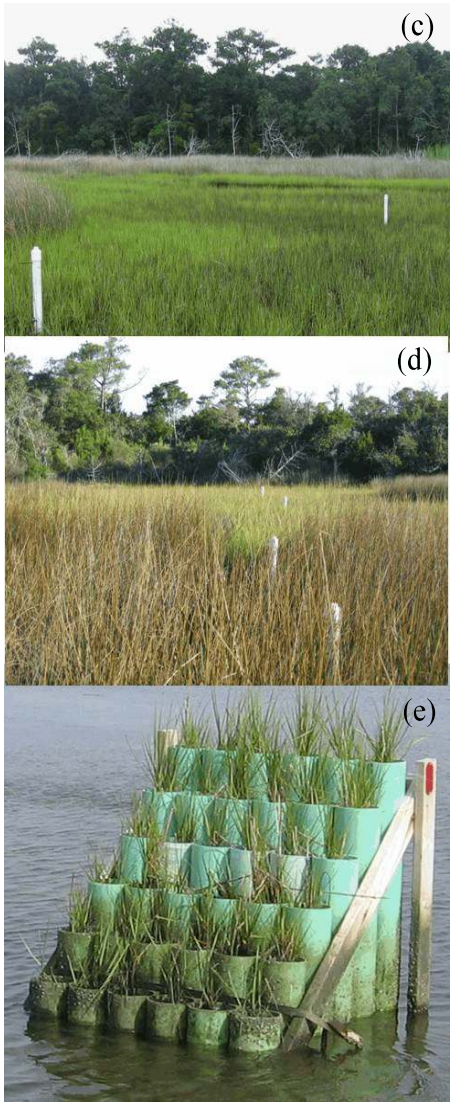

Figure 9. Location and description field measurements at the Pine Knolls Shore field site. (a) Located in North Carolina on Bogue Banks, shown with a close-up of the site with 1999 aerial photography; (b)Geometry of the site and layout of equipment. Pressure transducers were located along the transect with biomass sampling from 2005 to 2007, then moved closer to the sound; the pressure transducers are shown in (c) located in *Spartina* and (d) within *Juncus*; and (e) marsh organ planted with *Spartina*.

conditions the marsh surface is exposed and flows are confined to the tidal channel. The area colonized by *Distichlis spicata* is flooded only during spring tide conditions.

The numerical model considers inundation from a creek boundary. Using Eq. (10), the velocity is used to recursively calculate *Re* (and therefore C_D) and changes in water depth. The behavior of flood and ebb flow is modeled for low biomass (stem densities of 50 stems m^{-2}) to high biomass (stem densities up to 2000 stems m^{-2}), and for length-scales from 50 to 600 m (where slope varies from $S = 0.001$ to 0.01) (Table 3). Stem density and platform elevation are based on field surveys and studies that address similar platform conditions and tidal dynamics [*e.g. Leonard et al.*, 2002; *Valiela et al., 1978*]. The numerical model simulates the duration of inundation on a marsh platform and the geometry of platform flow. Of particular interest is the behavior resulting from the simplified hydrodynamics. Two behaviors are evaluated, (1) bathtub flooding over short distances and small biomass, and (2) wave-like behavior over long distances and large biomass.

4. Results

4.1 Model Behavior

Parameters not measured in the field include the roughness coefficient used in the bed resistance term, and lagdepth or the minimum depth of water that remains on the marsh platform during ebb and slack conditions. The roughness coefficient was determined from the literature and tested for sensitivity to model output. The model is not sensitive to

lagdepth, and a value of 0.02 m of residual water on the platform was chosen for numerical stability. This allows the water level on the marsh platform to remain positive. A given amount of standing water was observed on marsh platform surfaces between floods, likely due to microtopography. Reynolds numbers along a transect from the marsh edge to the high marsh, for the full extent of the simulated platform, range from an initial condition of 0.01 or Stokes flow to a transitional flow of 200 for all simulations. The greatest simulated flow velocities occur at the creek, and decrease with increasing distance from the marsh edge. Mean ebb flow velocities are greater than mean flood velocities. In addition, ebb velocities decrease with increasing length-scale, whereas flood velocities increase with increasing length-scale (Fig. 10). In addition to biomass influencing the distance water travels up the platform, an increase in biomass reduces the ebb velocity for length scales of 50 m and reduces both flood and ebb velocities for length scales of 200 m.

The water depth for a semidiurnal tide is plotted in terms of its exceedence probability (Fig. 11), which describes the proportion of time that water depth is greater than a specified value. The semidiurnal tide is plotted for a range of elevations to evaluate the model parameters described above. These plots demonstrate an idealized bath-tub flood geometry, where water depth with time is simply a function of platform elevation.

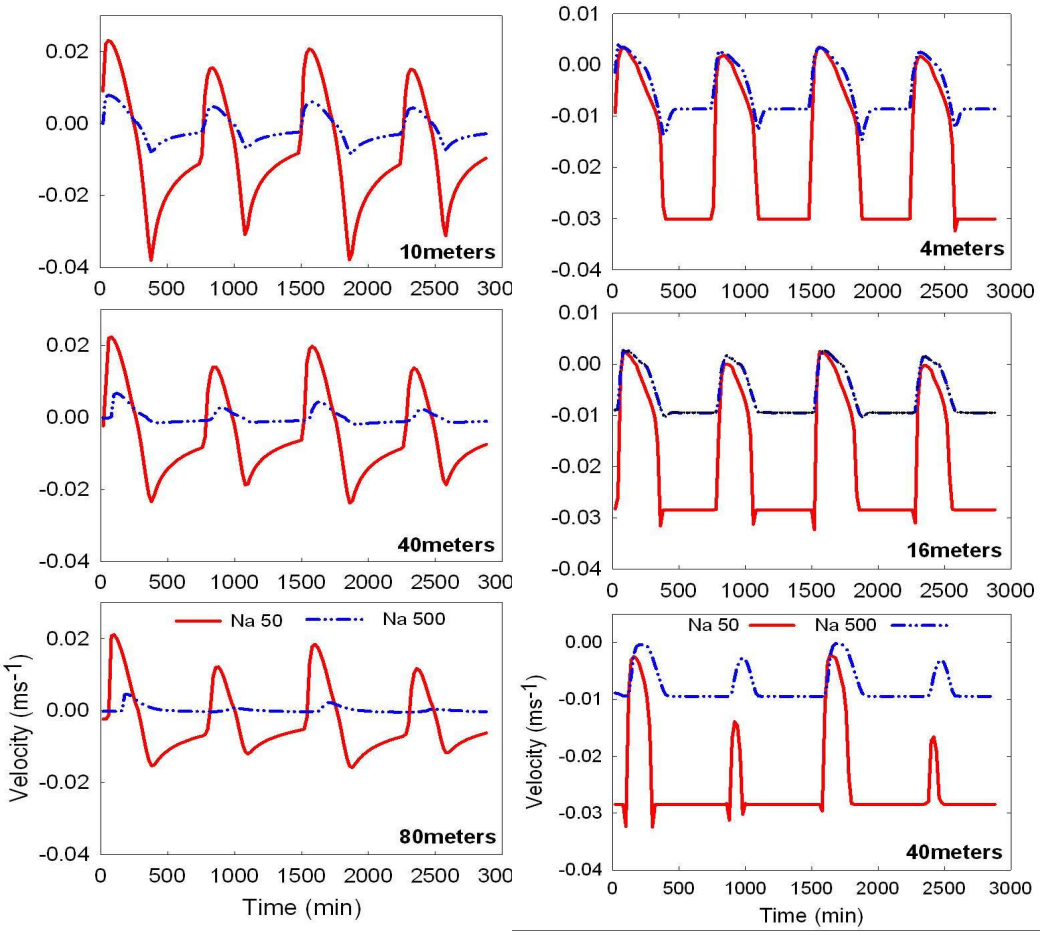

Figure 10. Velocities for length-scales of 50 m (*left*) and 200 m (*right*). Red denotes N_A = 50 and blue N_A = 500.

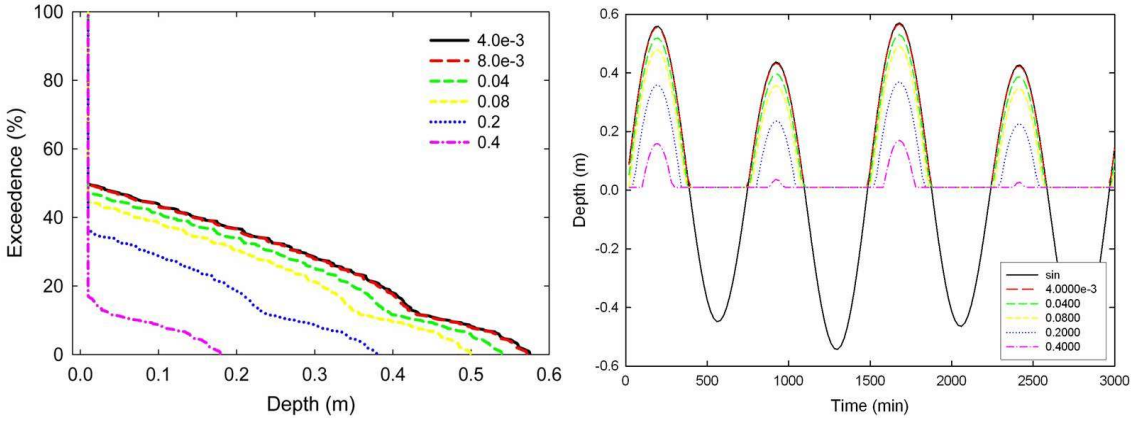

Figure 11. Semidiurnal sinusodial tide with no resistence, simulated for 100 hours. (*left)* The exceedence probability; and (*right*) Time series of the water depth demonstrating the geometry of bathtub flooding behavior.

4.2 Biomass

For uniform, sparse biomass conditions where $N_A = 50$ to 100, little difference exists in the frequency and duration of flooding along the marsh platform. The flood geometry and maximum water depths, however, differ for low stem densities compared to $N_A = 500$ for longer platform length-scales (Fig. 12). Over shorter length-scales, the entire marsh platform is able to flood and drain, and consequently, biomass values have little influence. Over greater platform length-scales, the increased resistance introduced by the stems causes the maximum depth and duration of inundation to decrease with distance from the creek for $N_A = 500$.

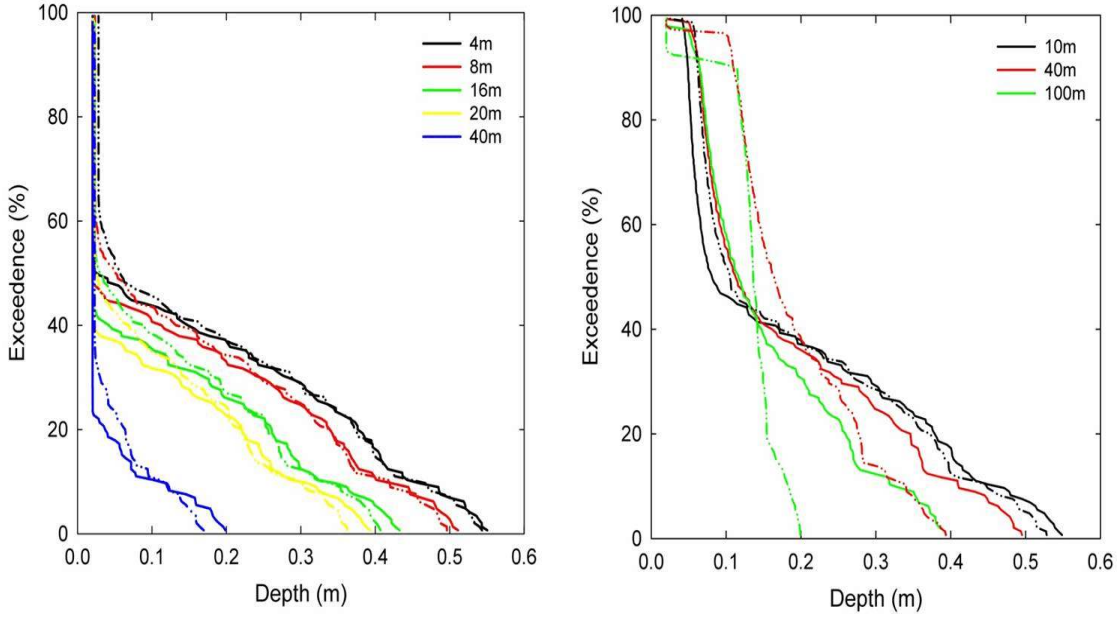

Figure 12. Exceedence probability plots for (a) length-scale of 50 m, $N_A = 50$ (—) and $N_A = 500$ (_.._); and (b) length-scale 200 m, $N_A = 50$ (—) and $N_A = 500$ (_.._).

Simulations for two parabolic biomass functions vary the maximum biomass, the elevation on the marsh platform at which the peak biomass exists, and breadth of the biomass parabola (Table 3). This parabolic biomass growth function from *Morris et al.* [2002] results from the relationship between elevation and biomass. The most favorable conditions of macrophyte primary productivity are related to the inundation duration; biomass increases with elevation up to an extent, whereafter biomass decreases due to reduced inundation duration or prolonged dryness. This inundation duration and therefore biomass parabola and its breadth result from a marsh platform having a slope. For both of the parabolic scenarios here, where the elevation of the peak biomass and breadth of biomass vary, inundation duration and frequency are not sensitive to the biomass distribution (where maximum stem densities of 100 and 500 stems m^{-2} were simulated). The influence of the biomass is observed at 40 m from the creek edge,

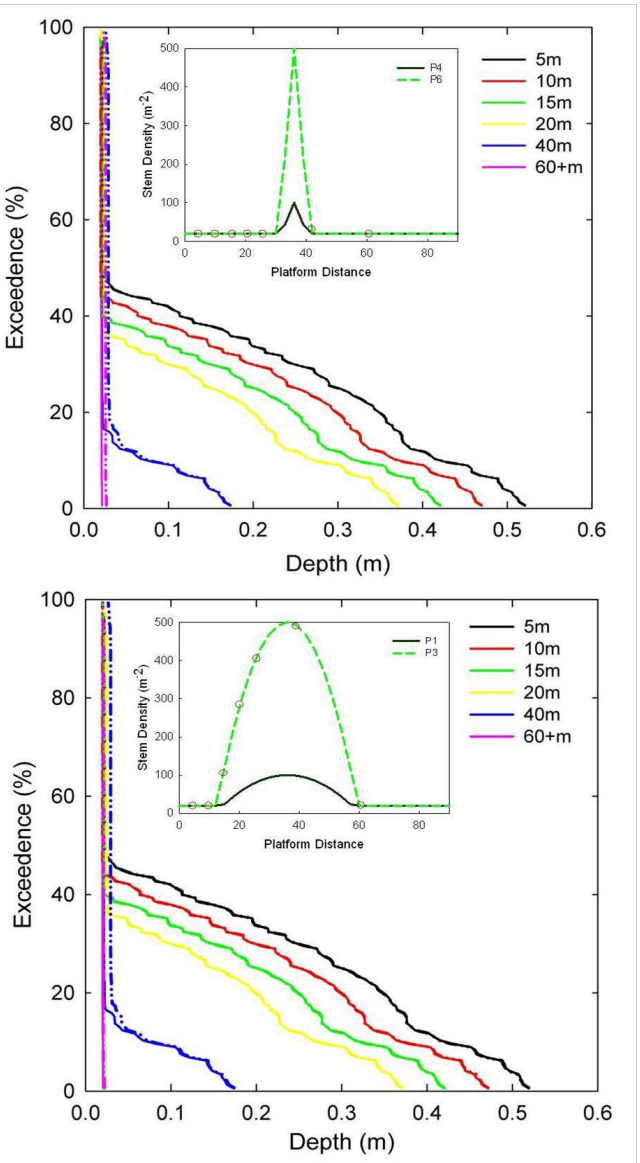

Figure 13. Exceedence probability of inundation duration for parabolic biomass. (*Top*) Run *P4* N_A = 100 (—) and Run *P6* N_A = 500 (_.._); (*Bottom*) Run *P1* N_A = 100 (—) and Run *P3* N_A = 500 (_.._). Embedded plots show stem density as a function of platform distance, with red circles marking sample points for output.

Table 3. Length-scales, biomass, and parameters for model simulations, where Y_P is the maximum stem density, Z_0 is the sea level or elevation limits where a macrophyte species can grow, and Z_p is the elevation of the maximum stem density.

Parameters	**Value**
Lag depth (m)	0.02
Slope	Length scale 50 m: 0.01 Length scale 100 m: 0.004 Length scale 200 m: 0.001
Stem density (m^{-2})	50, 100, 500
Elevation (m)	Length scale 50 m: 0-1 Length scale 200 m: 0-0.1
Manning's *n*	0.02
Tidal harmonics	M_2: 0.5; K_1: 0.08
Stem diameter (m)	0.005
Parabolic Biomass	Run P1. Y_P: 100, Z_0: 0.12, Z_P: 0.36 Run P3. Y_P: 500, Z_0: 0.12, Z_P: 0.36 Run P4. Y_P: 100, Z_0: 0.08, Z_P: 0.4 Run P6. Y_P: 500, Z_0: 0.08, Z_P: 0.4

where the peak stem density slightly reduces surface water drainage (Fig. 13). When N_A = 500, slight differences arise between the two parabolic distributions of biomass. This results from the difference in the rate of biomass increase with elevation, and therefore the amount of resistance encountered away from the creek.

Comparison between the uniform biomass and the parabolic biomass distribution suggests that greater depths and duration of flooding exist with a uniform distribution of biomass for stem densities greater than 100 stems m^{-2} (Fig. 14). Increasing the stem density to 500 stems m^{-2} results in approximately equivalent maximum water depths at 15 m and greater from the creek edge for the uniform and parabolic biomass distributions. That is,

water is able to drain faster from a platform with a parabolic biomass distribution because the average stem density is lower than the average stem density for that of a uniform biomass.

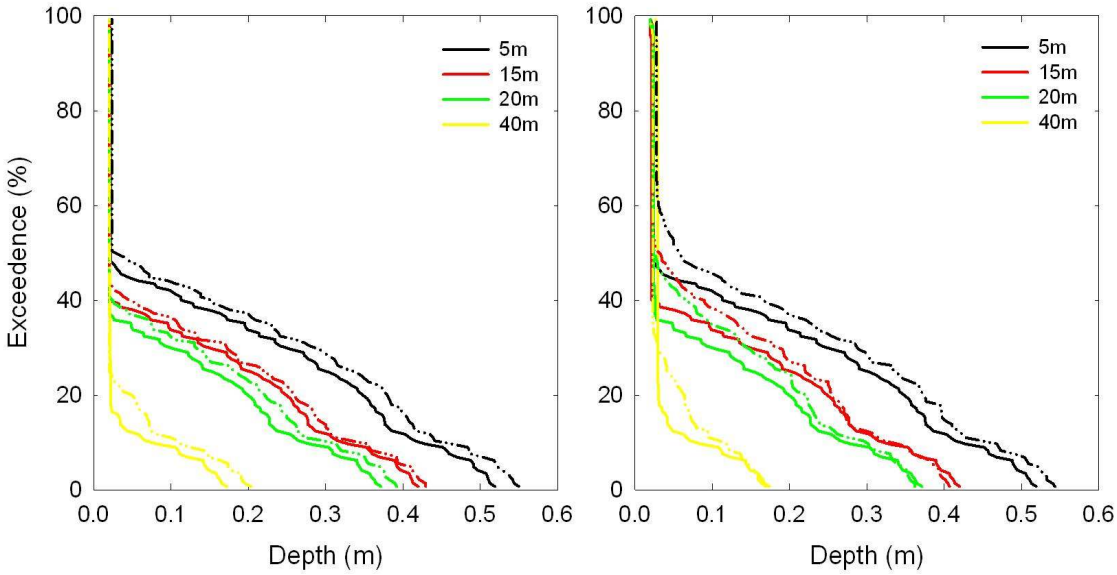

Figure 14. Inundation durations for parabolic biomass and an assumed uniform biomass. (*Left*) $N_A = 100$ with parabolic (—) and uniform (_.._); (*Right*) $N_A = 500$ with parabolic (—) and uniform (_.._).

4.3 Length Scale

Marsh platform length is varied with three slopes— $S = 0.01$ (50 m), $S = 0.004$ (150 m), and $S = 0.001$ (200+ m). For short length-scales, approximately 50 m, the marsh platform drains entirely with uniform biomass. Flooding represents a bathtub flood and ebb geometry, where the maximum water depth is a function of marsh platform elevation and lower elevations are inundated for longer durations (Fig. 15). The influence of biomass at these length-scales is shown to marginally reduce the flow depth at a given distance from the tidal creek, wherein the maximum depth and inundation duration decreases from $N_A = 50$ to

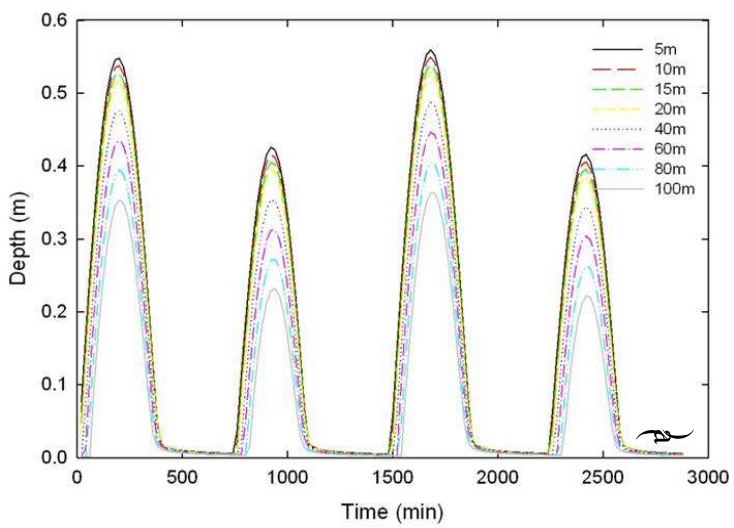

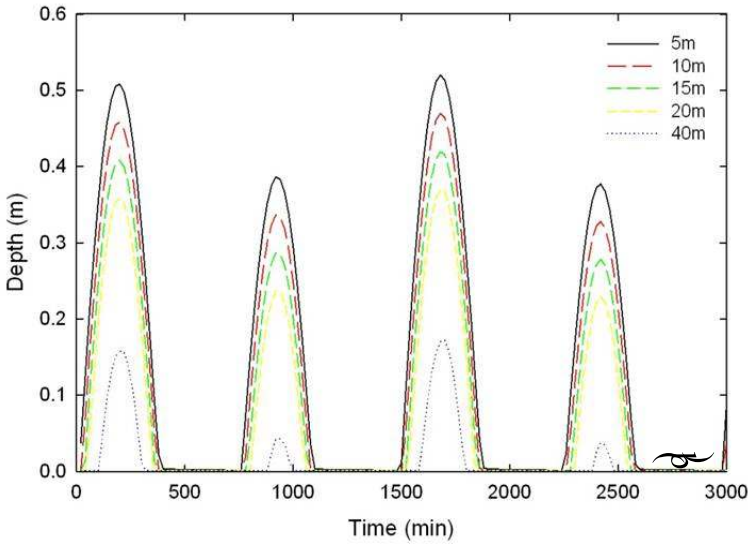

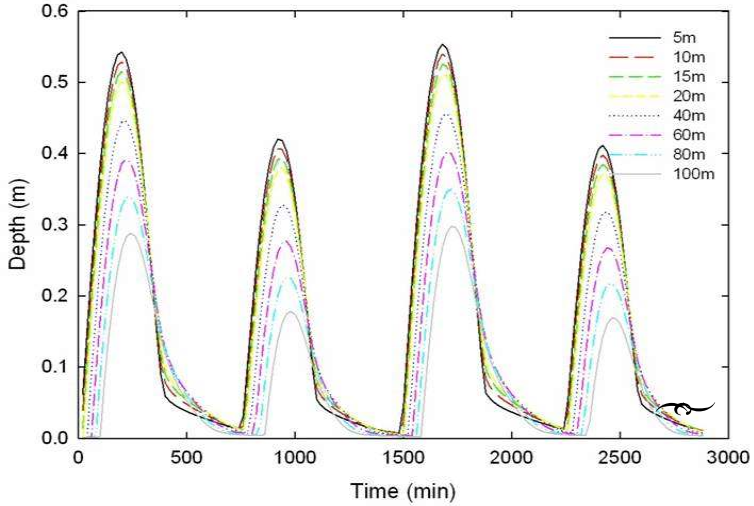

Figure 15. Time series of water depth for (a) N_A = 50 and slope = 0.002; (b) N_A = 500 and slope = 0.01; and (c) N_A = 500 and slope = 0.002.

N_A = 500. An increase in the length-scale results in a bathtub behavior at N_A = 50 and 100, and the onset of wave-like flooding when N_A = 500 (Fig. 15). At these length-scales the asymmetry in the flooding becomes evident; the water drains faster at the creek and water remains at greater platform elevations for extended periods of time. This suggests that biomass plays a more substantial role in the inundation duration over longer platform length-scales, likely attributed to reduced ebb flow rates over smaller slopes. For example, the exceedence probability plots for 2000 stems m^{-2} (Fig. 16) show the contrast in water retention on the platform, especially at 10 m and greater from the creek edge over longer length-scales. At longer platform lengths, greater water depths remain higher on the platform for longer durations.

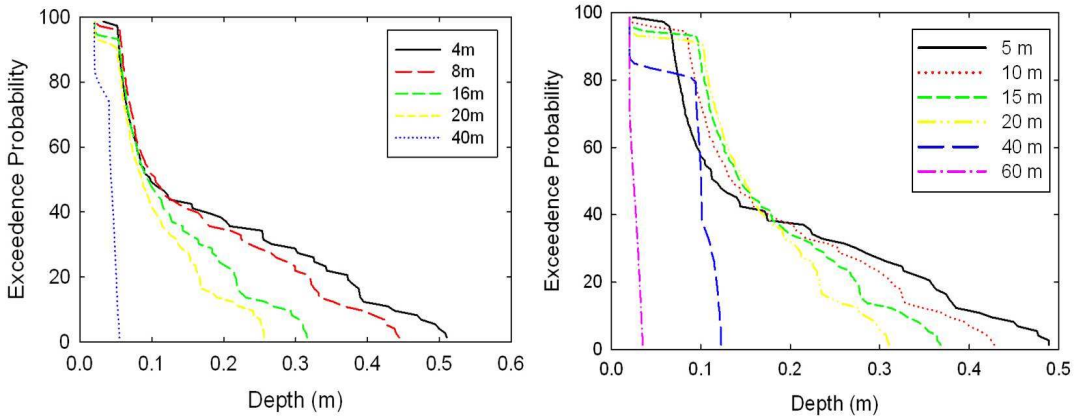

Figure 16. Exceedence probability for *NA* = 2000 at (*left*) long platform length-scales or slope = 0.004 and (*right*) short platform length-scales with slope = 0.01.

4.4 Analysis of Field Data

Field measurements at PKS include stem diameter, stem density, stem height, dry weight, and water level. Table 2 compares laboratory and field conditions from this study for *Spartina alterniflora* and *Juncus roemerianus*, the two dominant macrophytes along the eastern U.S. coast. The three year water level record from PKS suggests that instead of a complex wave flow, this salt marsh platform exhibits a simple bathtub-like flow geometry. Simulations from the idealized uniform biomass condition are compared to the three year continuous water record from PKS to evaluate modeling consistency (Fig. 17). Pressure transducers were established along a transect perpendicular to a tidal creek (Fig. 9) with the assumption that a parallel transect along a marsh platform (x) will allow for the most precise representation of a wave-form flood. The modeled and observed exceedence probability plots show the semidiurnal influence, evident by the change of slope in the plots. The observed data contain greater water depths than the simulated data, likely due to meteorological influences (*e.g.* wind, storms, precipitation; Chapter 4). The semidiurnal influence is also more evident in the observed data, whereas the simulations consider only two harmonic signals. Differences in the fit between the two graphs could also result from the natural microtopography not captured in the linear variation in platform elevation from the simulations. Additionally, the simulations do not consider the two-dimensional flow behavior on the marsh platform, where flooding may come from areas other than the creek.

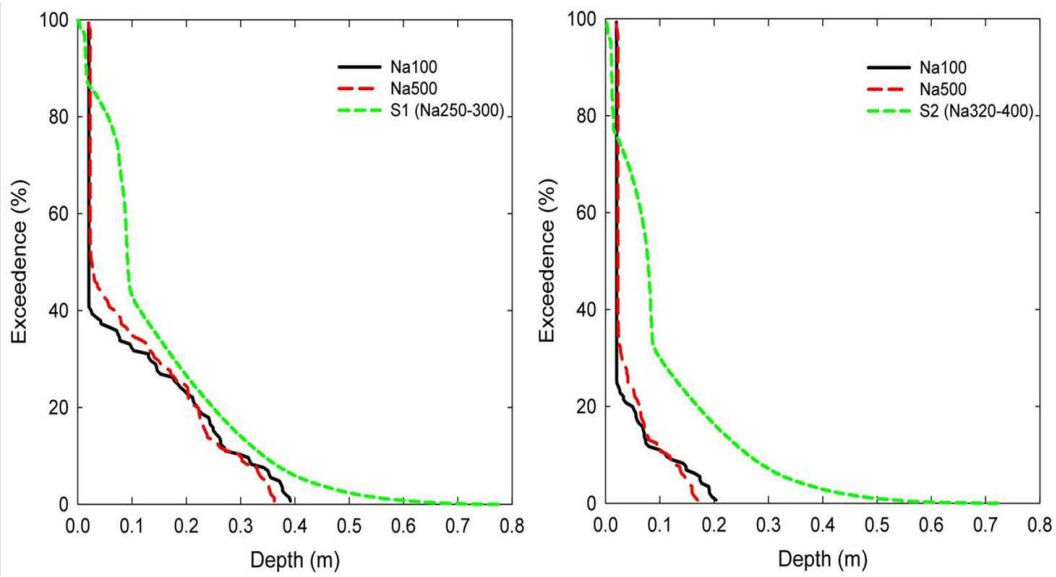

Figure 17. Exceedence probability plots for two pressure transducers located on the *Spartina alterniflora* monotype platform. Observed water levels are compared to the model output at (*left*) 20 m from the marsh edge at the location of pressure transducer "S1" and (*right*) 40 m from the marsh edge at pressure transducer "S2." The biomass range measured at each pressure transducer is provided (stems per m^{-2}).

5. Discussion of Length-scale and Biomass

This study consists of two parts — the first part demonstrates the viability of an additive model, especially with the addition of bed stress, and the second section discusses the consequence of this modeling, namely the influence of length-scale and biomass on flood and ebb behavior. Many existing models of flow through vegetative canopies have characterized drag using empirical roughness coefficients, ignored the influence of bed stress, and/or focused on high Reynolds number. However, we consider laminar to transitional flow conditions, which is commonly recorded in ecological studies. For simplicity, emergent stems are considered here as the source for form drag. Biannual measurements at our field

sites suggest that low stem densities exist, approximately between 200 to 400 stems m^{-2}. Whereas the vegetative drag has been shown as representative of the total drag for conditions of high stem density, here we examine whether the total drag due to the stems can be approximated as the sum of the drag on individual stems, wherein stems are treated as being isolated. This derives from development of an analytical expression based on C_D as a function of Re_d for the total vegetative force per unit volume in an array of cylinders. The relationship between C_D and Re_d is first examined, comparing C_D measurements from laboratory experiments with those derived from the parameters stated in the literature. A polynomial curve-fit for C_D, based on data from *Schlicting and Gersten* [2000], is used to calculate C_D. The total force F_V from laboratory experiments was next evaluated against the calculated F_V, derived from parameters provided with the experimental setup. Here conditions in which bed stress are important are demonstrated (*e.g.* low stem densities), resulting in a total force equation that partitions bed and stem drag. The one-to-one relationship of the drag coefficient, force per unit volume or stem, and stem and bed stress suggests that the total resistance may be quantified as the cumulative measured resistance for individual stems. Scatter within the plots is attributed to the imprecision and uncertainty of the experimental measurements, as well as the definition of certain parameters. For example, calculated values reported here consider a constant roughness value that has been reported for previous salt marsh studies; however, several authors derive roughness from a non-linear fit. The total resistance is then solved in a one-dimensional numerical model that determines the C_D and F_V. This one-dimensional, nonlinear, diffusive flow description is based on conservation of mass and momentum, where an additive stress is partitioned between stems

and the bed. Simulations consider a range of biomass and platform length-scale or slope. Numerical results are then compared to pressure transducer and biomass data from field sites in North Carolina.

The difference in flood durations for constant and parabolic biomass distributions highlights the importance of correctly identifying the biomass distribution for a given site. Modeling with a uniform biomass along a marsh platform is not necessarily recommended. The model is not sensitive to the peak biomass value, elevation of peak biomass, and elevation at which the biomass exists. Because biomass varies with season, Fig. (13) suggests that a mean peak stem density will suffice for model input. The slope of the platform determines the distance water travels on the marsh platform. That is, a small slope results in a wide parabolic biomass, and a steep slope produces a small parabolic biomass. This further highlights the importance of elevation and horizontal distance of a marsh platform.

This work differs from previous marsh platform hydrodynamic models wherein a wave-like flood behavior is simulated, yet the drag associated with vegetation is neglected [*e.g. D'Alpaos et al.*, 2007]. Flume experiments of flow structure and drag coefficients evaluate relationships amongst Re and N_A by horizontal averaging of the Navier Stokes equation in order to define the bulk drag associated with macrophytes [*e.g. Dunn et al.*, 1996]. This approach implicitly includes wake effects, where the bulk drag coefficient averages over the wake effects and is assumed to be constant in the plant canopy. The flow model presented above differs from previous studies in that wakes do not interact and stem densities measured in the field are sparse, such that the drag forces from the individual stems may be considered additive. The model plausibly describes the wave-like behavior during

flood and ebb flows over large length-scale platforms with moderate to high stem densities. Conversely, over short marsh platform length-scales, similar to the fringe marshes in Pamlico Sound, the marsh can be treated hydrographically like a bath-tub. Therefore, biomass can be considered simply as a function of elevation. This relationship allows for a simplified one-dimensional marsh platform hydrology model to be mapped to biomass and incorporated into landscape models.

6. Conclusion

This study begins with a review of the components needed to inform a force balance on the marsh platform, identifying the influence of emergent stems, additive stem drag, momentum balance, stem density, the role of bed stress, and the effect of platform length. Next, the conditions of length-scale and biomass under which a bathtub flood behavior represents the observed field conditions is described by a simplified one-dimensional hydrodynamic model and zero-dimensional biomass model. Model results are comparable to field studies reported in the literature, suggesting that resistance equations that includes both stem drag and bed stress, as well as the additive nature of F_V, appropriately capture the physics necessary for modeling of salt marsh platform behavior and response. In particular, we find that for low stem densities and transitional Reynolds number, the total force can be expressed using an additive model of stem drag. That is, conditions of wake sheltering are negligible. The importance of bed stress is demonstrated to be a necessary stress in the momentum balance. Additionally, short length-scales are shown to exhibit a bath-tub

flooding behavior. Over longer platform length-scales or lower slopes a wave-like behavior can occur, where the extent of this wave-like behavior is controlled by the biomass. Thus, a fully coupled dynamic model is not necessary for marsh platforms with lengths less than 50 m; rather, the platform flood and ebb is a linear function of elevation. The model presented above can be applied for platform lengths greater than 50 m. The biomass in simulations should be distributed as a parabola over the extent of platform distance.

7. Notation

a projected plant area per unit volume [L^{-1}]
A average morphology of a canopy, dh [L^2]
C_D drag coefficient [dimensionless]
d stem diameter [L]
g gravitational acceleration [ms^{-2}]
h flow depth [L]
F_D form drag [kg m s^{-2}], drag for an individual cylinder
F_S bed stress
F_V total vegetative force per unit volume [kg m^{-2} s^{-2}
n Manning's resistance coefficient [$sm^{-1/3}$]
N_A number of stems per unit area
p pressure [M L^{-1} t^{-2}]
Re Reynolds number
Re_d Reynolds number with stem diameter as length scale
S slope of the water surface
t time
U is fluid velocity [L t^{-1}]
x Cartesian coordinate parallel to downslope direction [L]
y Cartesian coordinate transverse to downslope direction [L]
z Cartesian coordinate in the bed-normal direction [L]

η platform elevation [L]
ζ water surface elevation [L]
ρ fluid density [M L^{-3}]
μ fluid viscosity [M L^{-1} t^{-1}]
τ_{tot} total stress

τ_S bed stress
τ_C stem drag
υ kinematic viscosity of water [L^2 t^{-1}]

8. References

Burke, R. and K. Stolzenbach (1983), *Free surface flow through salt marsh grass,* Tech Rep MITSG 83-16, Mass Inst of Technology, Cambridge.

D;Alpaos, A., S. Lanzoni, M. Marani, and A. Rinaldo (2007), Landscape evolution in tidal embayments: Modeling the interplay of erosion, sedimentation, and vegetation dynamics. *Journal of Geophysical Research, 112:* F01008, doi:10.1029/2006JF000537.

Dunn, C., F. Lopez, and M.H. García (1996), Mean Flow and Turbulence in a Laboratory Chennel with Simulated Vegetation, University of Illinois at Urbana-Champaig, Civil Engineering Studies, Hydraulic Engineering Series No. 51 (UILU-ENG-96-2009).

Fathi-Maghadam, M. and N. Kouwen (1997), Nonrigid, Nonsubmerged, Vegetative Roughness on Floodplains, *J. Hydraul. Eng, 123:1*, 51-57.

Ghisalberti, M. and H.M. Nepf (2005), The limited growth of vegetated shear layers, *Water Resources Research, 40: W07502*.

Harvey, J.W., R.W. Schaffranek, G.B. Noe, L.G. Larsen, D.J. Nowacki, and BlL. O'Connor (2009), Hydroecological factors governing surface water flow on a low-gradient floodplain, *Water Resources Research, 45: W03421*.

Hodges, C.C. (1997), Resistance to Flow Through Riparian Wetlands, *MS Thesis in Civil Engineering*, Virginia Polytechnic Institute and State University, Blacksburg, Virginia.

James, C.S., A.L. Birkhead, A.A. Jordanova, K.A. Kotschy, C.R. Nicolson, and M.J. Makoa (2001), Interaction of reeds, hydraulics and river morphology, *WRC Report No. 856/1/01*.

James, C.S., A.L. Birkhead, A.A. Jordanova, and J.J. O'Sullivan (2004), Flow resistance of emergent vegetation, *Journal of Hydraulic Research, 42:4*, 390-398.

Järvelä, J. (2004), Flow Resistance in Environmental Channels: Focus on Vegetation, *PhD*, Helsinki University of Technology, Espoa, Finland.

Jordanova, A.A., C.S. James, and A.L. Birkhead (2006), Practical estimation of flow resistance through emergent vegetation, *Water Management, 159:WM3*, 173-181.

Kadlec, R. (1990), Overland flow in wetlands: Vegetation resistance, *J. Hydraul. Eng., 116*, 691-707.

Knutson, P.L., R.A. Brochu, W.N. Seelig, M. Inskeep (1982), Wave damping in Spartina alterniflora marshes, *Wetlands, 2,* 87-104.

Lee, J.K, L.C. roig, H.L. Jenter, and H.M. Visser (2004), Drag coefficients for modeling flow through emergent vegetation in the florida Everglades, *Ecological Engineering, 22*, 237-248.

Leonard, L.A. and M.E. Luther (1995), Flow hydrodynamics in tidal marsh canopies, *Limnology and Oceanography, 40:8*, 1474-1484.

Leonard, L.A., P.A. Wren, and R.L. Beavers (2002), Flow dynamics and sedimentation in Spartina alterniflora and Phragmites australis marshes of the Chesapeake Bay, *Wetlands, 22:2*, 415-424.

Lopez, F. And M. Garcia (2001), Mean flow and turbulence structure of open-channel flow through non-emergent vegetation, *J. Hydraul. Eng., 127:5*, 392-402.

Morris, J.T., P.V. Sundareshwar, C.T. Nietch, B. Kjerfve, and D.R. Cahoon (2002), Responses of coastal wetlands to rising sea level, *Ecology, 83:10*, 2869-2877.

Nepf, H.M. (1999), Drag, turbulence, and diffusion in flow flow through emergent vegetation, *Water Resources Research, 35:2*, 479-489.

Nepf, H.M. and E.R. Vivoni (2000), Flow structure in depth-limited, vegetated flow, *Journal of Geophysical Research, 105:*C12, 28547-28557.

Neumeier, U. and P. Ciavola (2004), Flow resistance and associated sedimentary processes in a Spartina maritima salt-marsh, *Journal of Coastal Research, 20:2*, 435-447.

Nikora, V. (2009), Hydrodynamics of aquatic ecosystems: An interface between ecology, biomechanics and environmental fluid mechanics, *River Research and Applications, 26:4*, 367-384.

Pethick, J.S., D. Leggett, and L. Husain (1990), Boundary layers under salt marsh vegetation developed in tidal currents, in *Vegetation and Erosion*, edited by J.B. Thornes, London, John Wiley & Sons, pp. 113-123.

Petryk, S. (1969), Drag on cylinders in Open Channel Flow, *Thesis*, Colorado State

University at Fort Collins, Colorado.

Raupach, M.R. and R.H. Shaw (1982), Averaging procedures for flow within vegetation canopies, *Boundary-Layer Meteorology, 22*, 79-90.

Raupach, M.R. (1992), Drag and drag partition on rough surfaces, *Boundary-Layer Meterorology, 60,* 375-395.

Righetti, M. and A. Armanini (2002), Flow resistance in open channel flows with sparsely distributed bushes, *Journal of Hydrology, 269*, 55-64.

Roig, L.C. (1994). Hydrodynamic modeling of flows in tidal wetlands, *PhD dissertation*, University of California, Davis, Califorina.

Schlichting, H. (1936), Experimentelle untersuchungen zum rauhigkeitsproblem, *Ing. Arch., 7,* 1-34, (English transl 1937, Experimental investigation of the problem of surface roughness, *NACA tm 823*).

Schlichting, H. And K. Gersten (2000). *Boundary Layer Theory*, 8th revised edition, Springer-Verlag, Berlin, New York.

Scott, S.M. (2010), Spartina alterniflora productivity and salt marsh stability relative to marsh platform elevation, *Theses and Dissertations*, Paper 402.

Shi, Z., J.S. Pethick, and K. Pye (1995), Flow structure in and above the various heights of a saltmarsh canopy: a laboratory flume study, *Journal of Coastal Research, 11:4*, 1204-1209.

Stazner,B. and D. Borchardt (1994), Longitudinal patterns and processes along streams: modelling ecological responses to physical gradients, in *Aquatic ecology: scale, pattern and process*, edited by P.S. Giller, A.G. Hildrew, and D.G. Raffaelli, pp.113-140, Balckwell Scientific Publications, Oxford.

Tanino, Y. and H.M. Nepf (2008), Laboratory investigation of mean drag in a random array of rigid, emergent cylinders, *J. Hydraul. Eng, 134:1*, 34.

Tanino, Y. and H.M. Nepf (2009), Closure to "Laboratory investigation of mean drag in a random array of rigid emergent cylinders," *J. Hydraul. Eng, 135:8*, 693-694.

Thompson, G.T. and J.A. Robertson (1976), Theory of flow resistance for vegetated channels, *Transactions of the ASAE, 19:2*, 299-293.

Thompson, A.M. (2001), Shear stress partitioning for vegetation and erosion control blankets, *PhD,* University of Minnesota.

Tsihrintzis, V.A. and E.E. Madiedo (2000), Hydraulic resistance determination in marsh wetlands, *Water Resources Management, 14*, 285-309.

Turner, A.K., K.J. Langford, M. Win, and T.R. Clift (1978), Discharge-depth equation for shallow flow, *Proc. ASCE, 104:IR1,* 95-110.

Turner, A.K. and N. Chanmeesri (1984), Shallow flow of water through non-submerged vegetation, *Agricultural Water Management, 8*, 375-385.

Valiela, I., J.M. Teal, and W.G. Deuser (1978), The Nature of growth forms in the salt marsh grass Spartina alterniflora, *The American Naturalist, 112:985*, 461-470.

Voss, C. (2009), Responses of dominant marsh macrophytes to inundation and disturbance and assessing marsh ecosystem services, *PhD*, East Carolina University, Greenville, N.C.

CHAPTER III

DEVELOPMENT OF A TWO-DIMENSIONAL HYDRODYNAMIC MODEL TO DESCRIBE MARSH PLATFORM FLOW WITH BARRIER DESIGN

Abstract

With the high density of people living along the U.S. coast, it is common practice to modify the shoreline with erosion control structures. However, there is limited understanding of the short-term ecological impacts or the long-term effects associated with sea-level rise. A "living shoreline" is a relatively new approach that advocates the use of non-structural or soft structural control for shoreline stabilization to prevent erosion without disrupting the adjacent habitat. This chapter highlights the importance of examining the impacts of shoreline management on sheltered coastal environments, and presents an analysis of the flow regime on salt marsh platforms exposed to various barrier designs. The influence of structural design is explored with implications for primary productivity and marsh platform inundation. Single continuous and segmented barriers of varying lengths are simulated, as well as multiple (staggered) barriers. A two-dimensional hydrodynamic model is developed to evaluate flow routing and inundation duration on a salt marsh platform, providing the first steps for examining whether shoreline structures contribute to macrophyte sustainability or degradation, or contribute to platform erosion. The model consists of a force balance between the pressure gradient and additive resistance due to the form drag from vegetation and bed stress. Key points examined in the results include the extent of marsh platform flooding, the

change in ebb flow with water depth and marsh platform length, the influence of barrier length and segment gaps on ebb flow, and the influence of biomass on inundation. Results suggest that barrier length needs to be considered in order to reduce standing water depth and drainage resistance. The two-dimensional model can be coupled with a biomass distribution function to determine the range of structure lengths that will facilitate macrophyte sustainability in relation to the change in hydroperiod.

1. Introduction

Coastlines are inherently dynamic and constantly reshaping due to both natural and anthropogenic disturbances. Shoreline armoring, defined as the practice of installing protective structures for erosion control, has been shown to result in permanent loss or alteration of natural shoreline habitats [*Kraus*, 1988]. Protection of shorelines from erosion is a well-studied process. Open coasts have been the primary focus of shoreline erosion studies and stabilization, wherein structural components are needed to withstand mid to high energy wave environments. Estuaries and wetlands, however, are also subject to erosional land loss and the effects of sea-level rise. Although awareness of the value of protecting coastal marshes has increased in recent years, the effect of engineering wetlands remains largely unknown, including (1) how and to what extent waves are reduced by vegetated intertidal areas [*Meijer*, 2005]; (2) how and to what extent salt marsh platforms will evolve with changing sea-level; and (3) the influence of both engineered and natural shoreline protection on marsh platform inundation and thus platform elevation and primary

productivity. Sheltered coasts typically experience lower energy conditions that foster ecological communities not found on open coasts, suggesting the need to modify existing application of open coast engineered structures and technological approaches. Moreover, increasing pressure from coastal development has caused severe loss of shallow water habitats, such as salt marshes and seagrass beds. For example, *Seitz et al*. [2006] examined the effects of shoreline alteration in shallow habitats by contrasting the benthos of the subtidal areas adjacent to natural marsh and bulkhead shorelines. Benthic abundance and diversity were higher in subtidal habitats adjacent to natural marsh than in those adjacent to bulkhead shorelines.

Several strategies exist to stabilize shorelines, the most common response consisting of "hold the line" strategies that harden the shoreline with structures such as bulkheads and revetments. Selection of the erosion control structure and structural design depends on the local causes of erosion or inundation. Because no two shorelines are alike, any standard engineering design must be modified for the local shoreline. Shoreline hardening has been the standard for controlling shoreline erosion, yet these structures typically contribute to the problem by amplifying waves on neighboring shores, reducing available sediment necessary for marshes to maintain pace with sea level, and reducing the ability of marshes to migrate landward. The *National Academies Press* [2007] issued a call for a new shoreline management framework that addresses awareness of the choices available for erosion mitigation, improving knowledge of sheltered shoreline processes and ecological services, evaluation of cumulative consequences of erosion mitigation approaches, and improving shoreline management planning.

Estuarine shoreline erosion and accretion occur throughout North Carolina marshlands and tidal creeks in response to both natural changes within the watersheds and anthropogenic disturbances. To protect coastal property, North Carolina permits homeowners to armor the waterward boundary of estuarine shorelines with vertical and sloped structures. Although the State continues to modify coastal management policy, current regulations do not consider shoreline specific habitats and structural impacts. Research conducted along estuarine shorelines throughout North Carolina demonstrates average erosion rates greater than 1 m yr^{-1} [*Corbett et al*., 2008]. *Corbett et al*. [2008] also report that nearly 30% of the shoreline along the Neuse River Estuary in Pamlico Sound has been modified with stabilization structures, with little understanding of the short-term ecological impacts or the long-term effects associated with on-going climate change and sea-level rise.

The influence that a shoreline structure will have on the local ecology has become an important consideration for engineering practices worldwide. Vegetation, present at the foreshore, provides resistance to waves and currents, and macrophyte roots provide strength to the substrate and capture sediment [*e.g. Christiansen et al*., 2000]. The marsh edge also provides fishery habitat, including nursery, food and refuge [*Currin et al.,* 2008]. The concept of "living shorelines" is becoming popular and is a recently recognized approach to erosion control, most commonly applied to areas with low- to medium-wave energy. The living shoreline idea advocates the use of "non-structural" or "soft structural" control for shoreline stabilization to prevent erosion without disrupting shoreline habitat. Within this contribution, living shoreline projects are defined as those that consider the importance of ecological and physical processes in maintaining healthy ecosystems along the shoreline. Use

of living shoreline techniques is an evolving field. There has been little scientific investigation of living shoreline erosion control structures to determine the benefits or possible adverse impacts. For example, oyster reefs are hypothesized to contribute to shoreline stabilization by providing a coarse material to reduce wave and other erosive energies along eroding marsh and estuarine shorelines. Use of shells as a stabilization technique has been on a site-by-site basis, and monitoring the success of this technique versus traditional methods has been inadequate. Ecologists recognize that a habitat's physical structure will influence population biology and species interactions [*e.g. Bell et al.*, 1991], yet a focus on the consequences of physical-biological coupling is lacking. Quantifying the effect of physical-biological coupling on plant biomass and sedimentation will allow for the creation of models useful to support marsh platform sustainability. As an example, oyster shells provide juvenile spat attachment, thus providing the foundation for future generations of shellfish. In areas of significant oyster resources, boat wakes have caused shells to accrete as narrow ridges and washover deposits, which are locally called "washed shell" and are ubiquitous along the Atlantic Intracoastal Waterway [*Anderson et al.*, 1979]. These semi-natural barriers are thought to provide shoreline stabilization, yet it is unknown if the oyster shells are an impermeable barrier and therefore prevent tidal flood and ebb.

Structures built to withstand storm events are based on engineering principles that are well-tested. However, integrating other variables such as macrophyte productivity into these applications may lead to less effective erosion control. There has been little effort focused on the possible techniques involved in the living shoreline approach in contrast to armored shoreline techniques. Nor has there been much development of guidance on the approaches

that work best within different ecological settings [*Smith, pers. comm.* and 1999]. The use of gaps or tidal gates in sills — a shore parallel structure designed to reduce wave energy and preserve or create marsh grass fringe — is hypothesized to be an effective means for supporting habitat and maintenance of shoreline processes if designed and installed correctly. The sill breaks enhance tidal flushing, though to date no studies quantify gate effectiveness.

This study highlights the importance of examining the impacts of shoreline management on sheltered coastal environments, and presents an analysis of the flow regime on simulated salt marsh platforms exposed to conventional and alternative stabilization strategies. Although engineered barriers are commonly used as a means for erosion control, here the influence of structural design on the hydroperiod is explored with implications for primary productivity and platform inundation. In particular, this study focuses on the structural design of barriers at the marsh edge and on the marsh platform. Extending application of the one-dimensional hydrodynamic model presented in Chapter 2, a two-dimensional hydrodynamic model is developed here so that single and multiple (staggered) barriers may be simulated using enforced no-flow boundaries. By evaluating the effect of flow routing and inundation duration on a salt marsh platform, this approach provides the first step to determining if shoreline structures contribute to macrophyte sustainability or degradation, the latter resulting from either prolonged pooling of water or lack of inundation, or contributes to platform erosion.

2. Background

2.1. Types of Structures

Traditional and common erosion control practices use hardened structures that armor and stabilize the shoreline landward of the structure, particularly in high energy environments (Table 1). The presence of structures in low energy environments has been shown to impede the natural proliferation of fringe marshes, and naturally vegetated shorelines tend to be more stable than hardened shorelines [*National Academies Press,* 2007].

Table 1. Evaluation of hardened coastal protection measures [Modified from *Fulton-Bennett and Griggs*, 1986].

Type	Materials	Placement	Comment
Rip Rap	Large 1 to 5 ton rocks	Sloping landward or piled in trapezoidal rubble mound	Initial short-term toe scour
Seawalls/ Bulkheads	Continuous, rigid structures	Vertical or concave faces reflect wave energy upward, downward, and back out to sea	Undermining and overtopping
Gunite	Concrete sprayed over a steel mesh and/or reinforced rod frame	At steep, erodible slopes	Protect terrace deposits and erodible bedrock from wave splash and spray

Soft stabilization or living shoreline measures consist of restoration practices designed to reduce or prevent erosion by means of plantings or organic material to restore, protect or enhance the natural shoreline environment. Examples include fiber logs, beach nourishment, and vegetation plantings consisting of macrophytes, submerged aquatic vegetation, or dune grass (Table 2). Design criteria for living shorelines often consider the fetch, elevation, slope, and hydrology for erosion control [*Priest*, 1999]. Vegetative plantings

pose challenges to successful shoreline protection because highly erosive events may overcome the resilience of the plantings [*Williams*, 1993]. *Luscher and Hollingsworth* [2005] suggest non-structural and vegetative treatments are applicable where the fetch or distance across open water is narrow, average erosion is moderate, and the water depth near the shoreline is shallow. *Berman et al*. [2005] analyzed the spatial covariance between fringe marshes and shoreline stability for a county with approximately 300 miles of tidal shoreline, and showed that fringing marshes account for more than half of the low erosion occurrences whereas only 20% of the shorelines classified as low erosion had been hardened with either riprap or bulkheads. Shoreline orientation and boat wakes also influence the structural design of barriers. Estuarine shoreline erosion has been attributed to boat generated waves, exhibited by dislodged *Spartina* root systems [*Anderson, 1977*]. The use of natural core fiber logs has been shown to reduce boat-wake erosion, suggesting a 60% reduction of wake energy by the barrier [*Ellis et al*., 2002].

Hybrid stabilization strategies combine structural and non-structural designs to facilitate habitat creation or restoration without substantial impacts to tidal flow. The benefits of hybrid stabilization are similar to soft stabilization, and this approach may be used in a wider variety of habitats, typically with higher wave energy. Examples of this approach include, (1) vegetative planting with low-profile rock, rubble, or oyster shells; or (2) beach nourishment with a low profile breakwater composed of limestone set with oysters (*i.e*. living break water). A successful hybrid stabilization project was completed in 2009 in Hail Cove, Maryland by the Fish and Wildlife Services and Ducks Unlimited, where the isthmus that separated Hail Cove from the Chester River was narrowing. The shoreline was restored with

installation of low profile segmented headland breakwaters, an oyster reef, and native marsh grass transplants.

Table 2. Examples of soft and hybrid stabilization techniques.

Type	Materials	Placement
Fiber Logs	Manufactured, biodegradable logs	In front of or behind marsh vegetation to trap or retain sediments and reduce erosion, facilitating establishment of young plants
Marsh Toe Revetment and Sills	Low profile revetment backfilled with sand	Long continuous structure or with gaps; used to create intertidal marsh
Marsh with Groins	Graded sand fill stabilized by small stone containment groins	Perpendicular to the shoreline; used to promote fringe marsh creation
Living Breakwater	Breakwater with vegetation planted behind the structure, or colonized by oysters	Offshore
Oyster Reef	Bagged or unconstrained oyster shell	Along a marsh edge or in shallow water close to shore

2.2 Oyster Reefs

Although many approaches and combinations of soft stabilization exist, oyster shells as semi-natural barriers are the focus of this study. Supra-tidal oyster bars are a natural occurrence in macro tidal settings [*Howell et al.,* 2005*; Alexander*, 2008]. Several states along the eastern U.S. coast have invested in experimental living shoreline applications, focused primarily on the success of oyster shells and marsh plantings (*e.g. Maryland Living Shoreline Act of 2008*). An oyster reef is hypothesized to contribute to shoreline stabilization by providing a coarse material to reduce wave and other erosive energies along eroding marsh and estuarine shorelines. Likewise, an oyster reef produces a crystallizing cement of

calcium carbonate, which allows shells to bond together and expand spatially [*Harper, 1997*]. These reefs prove to be self-sustaining [*Meyer and Townsend*, 2000], as opposed to heavier shoreline protection structures (*e.g.*, riprap or limestone breakwaters) that necessitate placement of additional materials to maintain effectiveness. The eastern oyster *Crassostrea virginica* is the most common species along the eastern U.S. coast and provides a foraging substrate for other species. Oysters are also recognized as important for the fishing industry, water quality, and as habitat colonizers.

Experimental studies typically place bagged shell material known as oyster clutches close to the shoreline [*e.g. Meyer et al.,* 1997]. In Sister Lake, Louisiana, *Piazza et al.* [2005] found that shoreline erosion was reduced in clutched low-energy environments compared to the control low-energy shorelines, yet oyster clutches did not prevent further erosion at high-energy environments. *Piazza et al.* [2005] also report greater shoreline erosion at sites with the clutched oysters after storm events, compared to natural marshes, likely due to scour and water trapping behind the reef. Scouring may result from the force of breaking waves on the platform, resuspension of sediment, or changes in current velocity and patterns. Studies have also examined submerged reefs, which facilitate shoaling and breaking of waves, and thereby dissipate wave energy over the reef crest. For example, *Stabule and Tabar* [2003] examined six submerged and narrow-crested break waters, and provide evidence of scour at the landward edge of the breakwater, as well as settlement of the structures due to toe scour. In one third of the cases with individual and continuous reefs, this interaction caused scour and erosion of the beach behind the structure.

3. Two-dimensional Hydrodynamics

Shoreline stabilization methods have traditionally been designed to reduce erosion and therefore incorporate fetch with the design. However, this study focuses on the influence of stabilization structures on tidal flow and the ecological implications. The one-dimensional hydrodynamic model presented in Chapter 2 is further developed into a two-dimensional hydrodynamic model here in order to simulate the effects of barriers at the shoreline. Few studies have considered the structural design of barriers at low-energy coasts or along marsh platforms; one field study, however, examined 25 m stretches of reef placement along a shoreline [*Piazza et al*., 2005]. Barrier segments described within this chapter were selected to represent small, equal, and large barrier length-scale and spacing between barriers. Models simulations presented below consider, (1) simulations with no barriers in order to describe the flow structure and inundation duration on a natural, unstabilized marsh; (2) a single barrier at the shoreline for conditions of a continuous barrier and segmented barriers. A continuos barrier design is typically applied to residential estuarine shorelines, and here we explore the influence of the barrier length. Likewise, natural oyster bars typically form as a continuous structure; implementing segments in the design will inform if breaks are advantages in relation to flooding and draining; and (3) a staggered approach, or two offset barriers. The staggered design is motivated by the need to dissipate erosive waves, but permits flooding onto and off of the marsh platform.

Consider a Cartesian *xyz* coordinate system associated with a marsh platform system (Fig. 1). The horizontal *x* coordinate is normal to the marsh-platform edge, positive in the

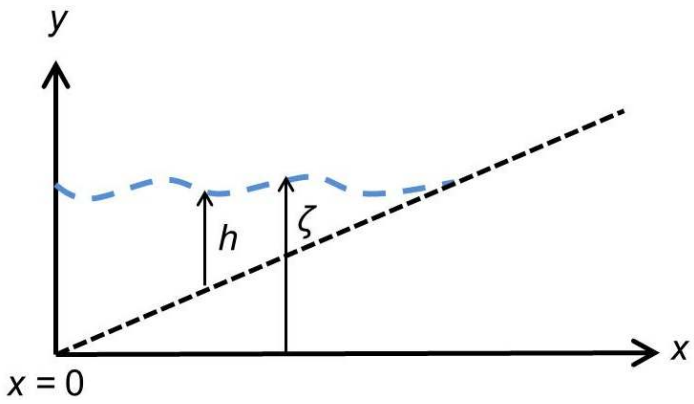

Figure 1. Definition diagram for marsh platform coordinates and water depth, where the x-axis is normal to the marsh platform edge with origin (x=0) at the platform edge. The horizontal y-axis is parallel to the platform edge and the z-axis is vertical. The local water surface elevation is $z = \zeta$, and $z = \eta$ denotes the local platform surface elevation such that $h = \zeta - \eta$.

landward direction, with origin ($x = 0$) at the platform edge. The horizontal y axis is parallel to the platform edge, with origin ($y = 0$), and the z axis is vertical. Let $z = \zeta$ denote the local water-surface elevation and let $z = \eta$ denote the local platform surface elevation such that $h = \zeta - \eta$ is the local water depth. Further, let $\mathbf{U} = \mathbf{i}U + \mathbf{j}V$ denote the local depth-averaged velocity, where $\mathbf{i}$ and $\mathbf{j}$ denote unit vectors parallel to x and y, respectively. The magnitude of the velocity is

$$|\mathbf{U}| = \sqrt{U^2 + V^2} \tag{1}$$

Conservation of mass requires that

$$\frac{\partial \zeta}{\partial t} = -\frac{\partial}{\partial x}(hU) - \frac{\partial}{\partial y}(hV) \tag{2}$$

Assuming hydrostatic conditions and slowly varying flow conditions, the force balance consists of the pressure gradient and the two ingredients of flow resistance– the resistance due to drag on plant stems and the resistance due to the bed stress. Further assuming an additive stress partitioning between stems and the bed [*e.g. Chapter 2*], conservation of momentum requires that

$$\frac{1}{2}|\mathbf{U}|U\left(N_A C_D d + \frac{C_f}{h}\right) = -g\frac{\partial \zeta}{\partial x} \tag{3}$$

$$\frac{1}{2}|\mathbf{U}|V\left(N_A C_D d + \frac{C_f}{h}\right) = -g\frac{\partial \zeta}{\partial y} \tag{4}$$

Here, N_A is the number of stems per unit area [L^{-2}], C_D is the stem drag coefficient [dimensionless], d is the stem diameter [L], C_f is the Darcy-Weisbach friction factor, g is the gravitational acceleration [LT^{-2}], and the magnitude of the velocity vector $(|\mathbf{U}|)$ preserves direction. The left hand side of the parenthetical quantity in (3) and (4) results from the stem drag per unit volume. Comparison of measured and calculated stem drag suggests that the stem drag per unit volume can be approximated as the sum of the drag on individual stems [*Chapter 2*]. This additive vegetative drag assumption applies to sparse stem densities and laminar to transitional flow regimes, wherein wake sheltering does not influence the impact velocity of downstream plant stems. The right hand side of the parenthetical quantity consists of the bed stress, where the Darcy-Weisbach friction factor is related to the Chézy coefficient C [$L^{1/2}$ T^{-1}] by $C_f = \frac{2g}{C^2}$. In the simulations below, the Chézy coefficient assumes a

Mannings roughness coefficient n on the order of sand-bed ripples, $n = 0.02$ [*e.g. Chow*, 1959; *Roig*, 1994]. Because the Chézy coefficient is a function of depth, the Darcy-Weisbach factor decreases as depth increases. That is, stress increases linearly with flow depth to a maximum value at the bed, where it is balanced by the shear stress imposed by the bed on the flow. The partitioning of stresses in Eqs. (3) and (4) contains two limiting states,

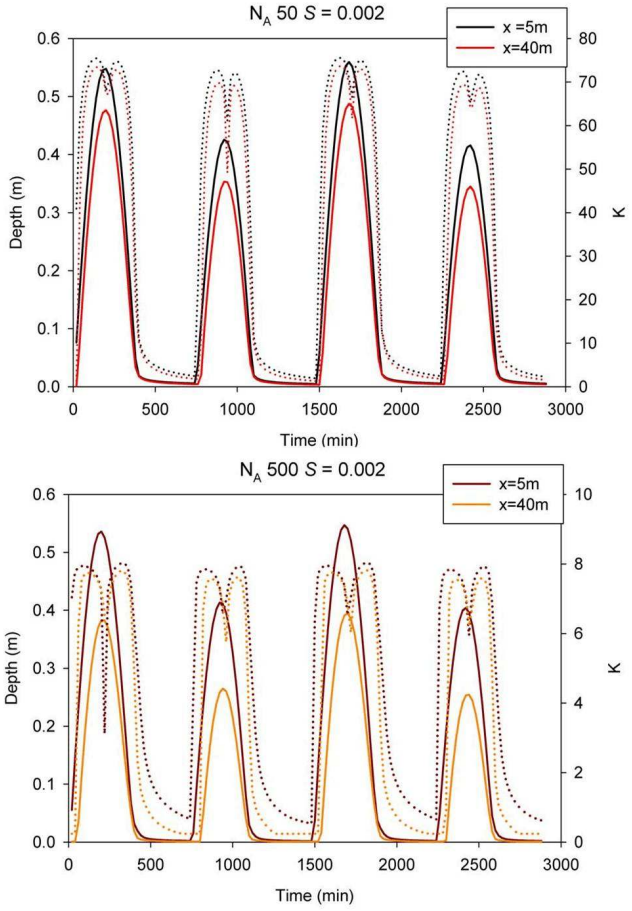

Figure 2. The depth and sum of the additive drag and bed stress (denoted as K) with time for two stem density values. Depth denoted by solid lines and K values as doted lines. The resistance term K is from Eqs (3) and (4), where $K = 2g/(N_A C_D d + C_f/h)$ [$kgm^{-2}s^{-2}$].

(1) for the case of no vegetation ($N_A = 0$), wherein the contribution to resistance is due to the second term; and (2) for flow resistance associated entirely with vegetation (Fig. 2).

The drag coefficient is computed from a polynomial curve-fit of the Reynolds number Re and C_D for a cylindrical object [*Chapter 2*]. Sampling from *Schlicting and Gerstens* [2000] data that comprises the standard drag curve, and focusing on low-Re values associated

with salt marsh platforms, the polynomial curve-fit is defined as

$$\log C_D = 0.9914 - 0.6341(\log Re) + 0.0984(\log Re)^2 \quad (5)$$

where the Reynolds number is defined here as a function of the stem diameter,

$$Re = \frac{|U|d}{\upsilon} \quad (6)$$

The kinematic viscosity υ equals the dynamic viscosity μ divided by the fluid density ρ. Laminar to transitional flow on salt marsh platforms have been recorded by several authors, including $75 < Re_d < 600$ [*Leonard et al.*, 2002].

3.1 Model Domain

Parameters were selected to represent salt marsh platforms ranging from small, tidally influenced fringe marshes to large, wind dominated marshes (Table 3). *Spartina alterniflora* and *Juncus roemerianus* biomass values are based on measurements from the Pine Knolls Shore and Cedar Island, NC field sites, and include samplings from both the growth and winter seasons. The wind dominated site is characterized by large, gently sloping marsh platform expanses colonized by *Juncus roemerianus*, and is simulated with a platform slope of $S = 0.002$. The fringe marshes have steep platforms dominated by monotype *Spartina alterniflora*, typically 50 m in width from marsh edge to the maritime forest.

Simulations consider zero, one, and two staggered barriers. The model is first run without barriers to describe the flow structure and inundation duration on a natural, unstabilized marsh. The barrier designs include, (1) continuous and segmented barriers along the marsh edge (described in 3.2); and (2) three proportional barrier lengths. The three

Table 3. Marsh platform and barrier design parameters used in simulations. Barrier length refers to the length of structure for "*short length-scale, long length-scale*." Stem diameter for all simulations is 0.005 m, representative of *Spartina alterniflora*.

Parameter	Variables					
Biomass (N_A)	50	100	500			
Slope (m)	0.002	0.004	0.007	0.01		
***x*-length [m]**	100	120	150	200	250	270
***y*-length [m]**	40	80	100			
# Structures	0	1	2			
Barrier Extent	< Half	Half	> Half			
Barrier Length [m]	12, 28	20, 44	28, 60			

lengths for single barriers at the marsh edge are referred to "*Half*," where "*Half*" refers to the *y*-axis equal to 40 m. The three simulated barrier lengths include 12 m (< *Half*), 20 m (= *Half*), and 28 m (> *Half*) (Fig. 3). For the shortest barrier length (< *Half*), the opening between barrier segments is greater than two times the length of the structure. The medium length barrier was chosen to explore between-barrier spacing equal to the length of the barrier segments, and the longest barrier length is based on previous living shoreline studies [*e.g. Piazza et al.*, 2005], wherein the majority of the shoreline is protected and gaps between segments are 12 m. The marsh platform length along the *y-axis*, parallel to the shoreline, is also doubled from y = 40 m shoreline length within the model domain to y = 80 m. The proportionality of the barriers is preserved, such that the length of the barrier is doubled. The design for two offset and staggered barriers consists of the structure lengths used in the one barrier configuration, and the length of the platform parallel to the shoreline is doubled as

well. The design for a short barrier along the marsh edge consists of a larger barrier displaced 10 m landward along *x*; likewise, a larger front barrier design is placed with a short offset barrier displaced 10 m landward (Fig. 3).

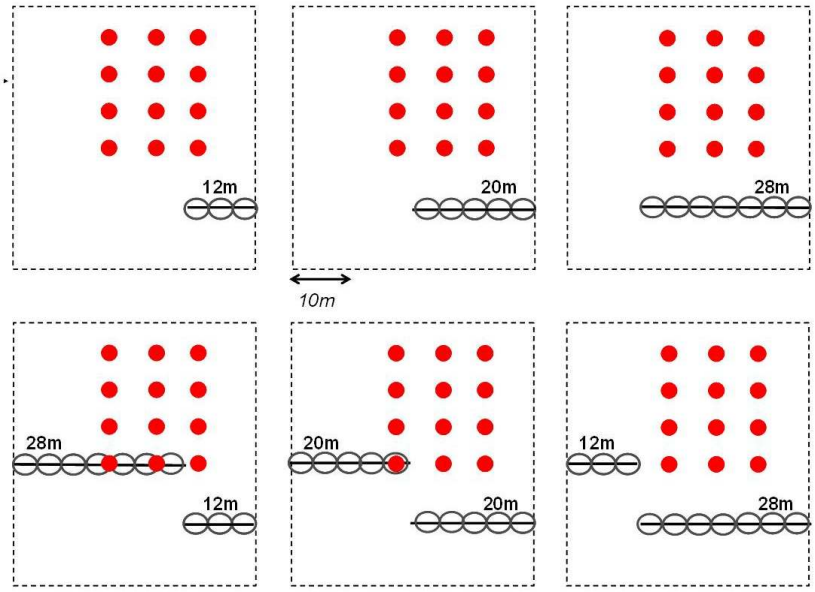

Figure 3. Description diagram of the simulated length-scales for the single (*top*) and staggered (*bottom*) barriers for y = 40 m. Length-scales include 12 m or < *Half* (*left*), 20 m or *equal to Half* (*middle*), and 28 m or > *Half* (*right*), where "*Half*" is based on the y-domain of 40 m length. Red circles denote the x,y position where data is recorded during simulations.

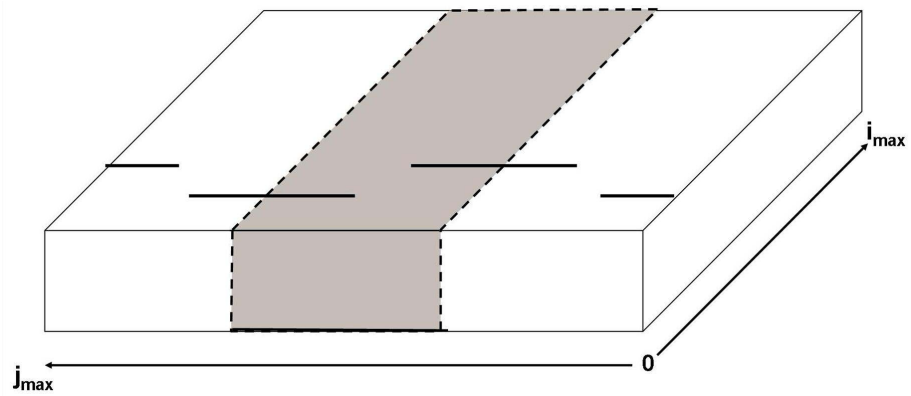

Figure 4. Description diagram for reflections used in the numeric scheme. The shaded area represents the domain simulated, with no-flow boundaries shown as dashed lines. Values are calculated adjacent to no-flow boundaries and reflected across these boundaries. The barriers are represented by solid black lines.

3.2 Numerical Expression

The analytical expression for two-dimensional flow is modeled by a finite differencing scheme coded in Matlab. Inundation is driven by a semi-diurnal microtidal amplitude and period, based on the two dominant harmonic signals at the Pine Knolls Shore site. These harmonics include the lunar semidiurnal constituent M_2 with a period of 12.42 hrs and amplitude of 0.05 m, and the lunar diurnal constituent K_1 with a period of 23.93 hrs and amplitude of 0.08 m [*Chapter 4*]. The boundary conditions consist of no-flow boundaries, or areas of zero flux, at the model domains along the *y-axis* and at the maximum distance parallel to the *x-axis* (representative of the upland maritime forest). Calculations are performed within the model area, yet the numeric scheme involves reflection across the no flow boundaries. Thus, the barrier design is repeated along the shoreline (Fig. 4). This approach reduces computation to a reasonable time-frame. The barriers are implemented by imposing no-flow boundaries along the barrier length, and reflections across the barriers along the *x*-coordinate. Conditions on the marsh platform consist of varying stem density, slope, and platform length. See Appendix C for further clarification of the analytical and numerical scheme.

4. Results of Simulations

A description of all model runs is provided in Appendix D. Model output includes animations of the flood and ebb flow as well as runs of extended time periods to capture the

semidiurnal effect and month long influence of standing water. Flow depth and velocities (U,V) are recorded at 20 minute intervals at points behind the barrier (x = 10 m) and on the marsh platform. These data logging nodes are spaced along the *y-axis* to the barrier edge or opening (Table 4, Fig. 3).

Table 4. Nodes tagged to record data at 20-minute intervals. Long length-scale preserves the spacing and lengths of the short length-scale.

Short [m]		Long [m]	
x	***y***	***x***	***y***
10	8	10	24
25	16	25	40
40	24	40	56
60		60	

4.1 No Structures

Simulations are performed without barriers to provide a control with which to compare simulations with barriers. Results consider the influence of marsh platform length-scale or slope and stem density on inundation. For short platform length-scales, approximately 50 m from the creek edge to high marsh, flooding represents a bathtub approximation regardless of the stem density. Water depth and inundation duration are therefore a function of elevation (Fig. 5). An increase in platform length-scale results in the onset of a weak wave-like flow behavior when N_A = 100 and a distinct wave-like form when N_A = 500 (Figs. 5 and 6). Here the water surface slope increases with biomass during both the flood and ebb, yet the water surface relief is on the order of a decimeter over

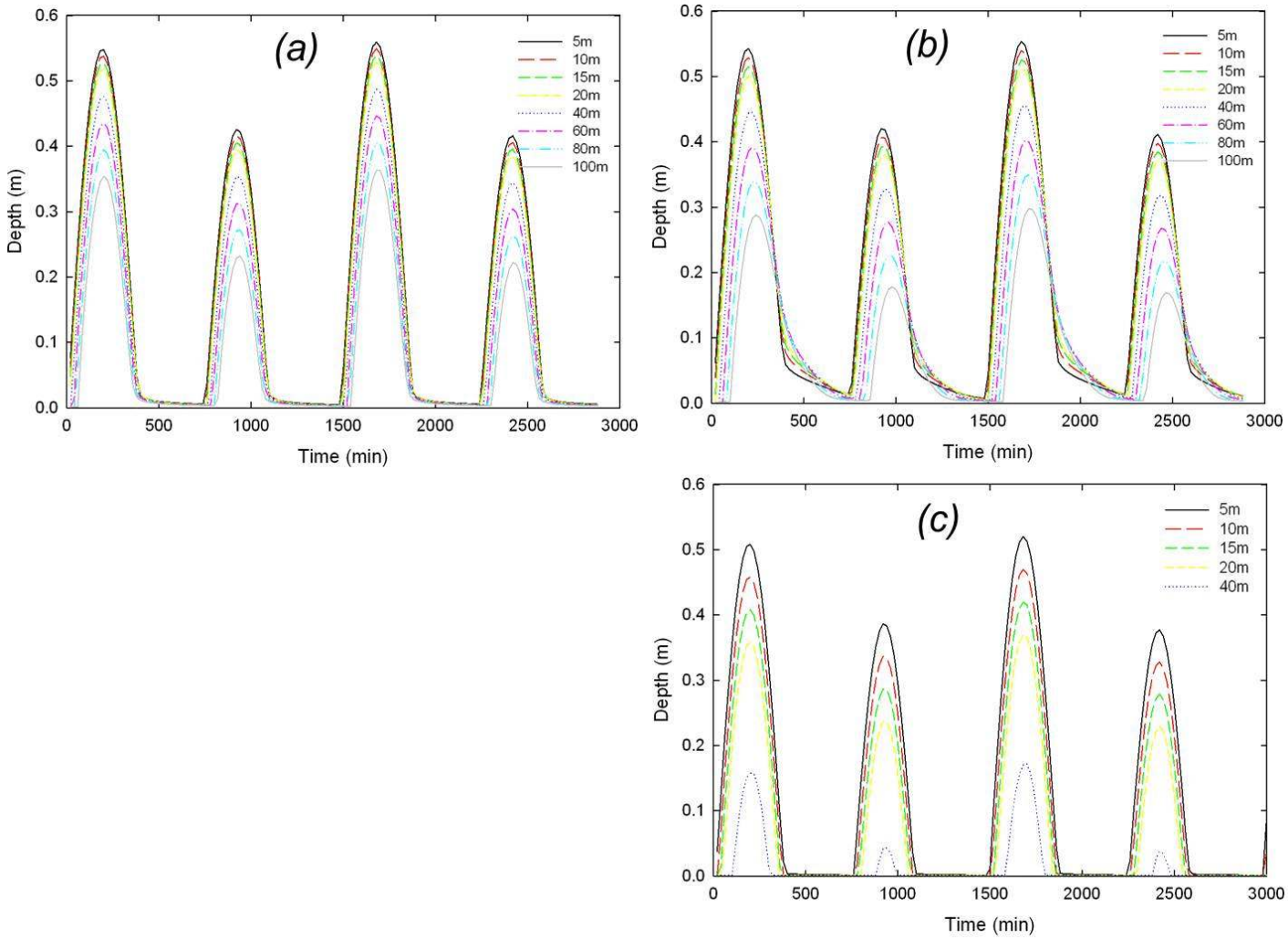

Figure 5. Time series of water depth for (a) N_A = 50 and slope = 0.002; (b) N_A = 500 and slope = 0.002; and (c) N_A = 500 and slope = 0.01.

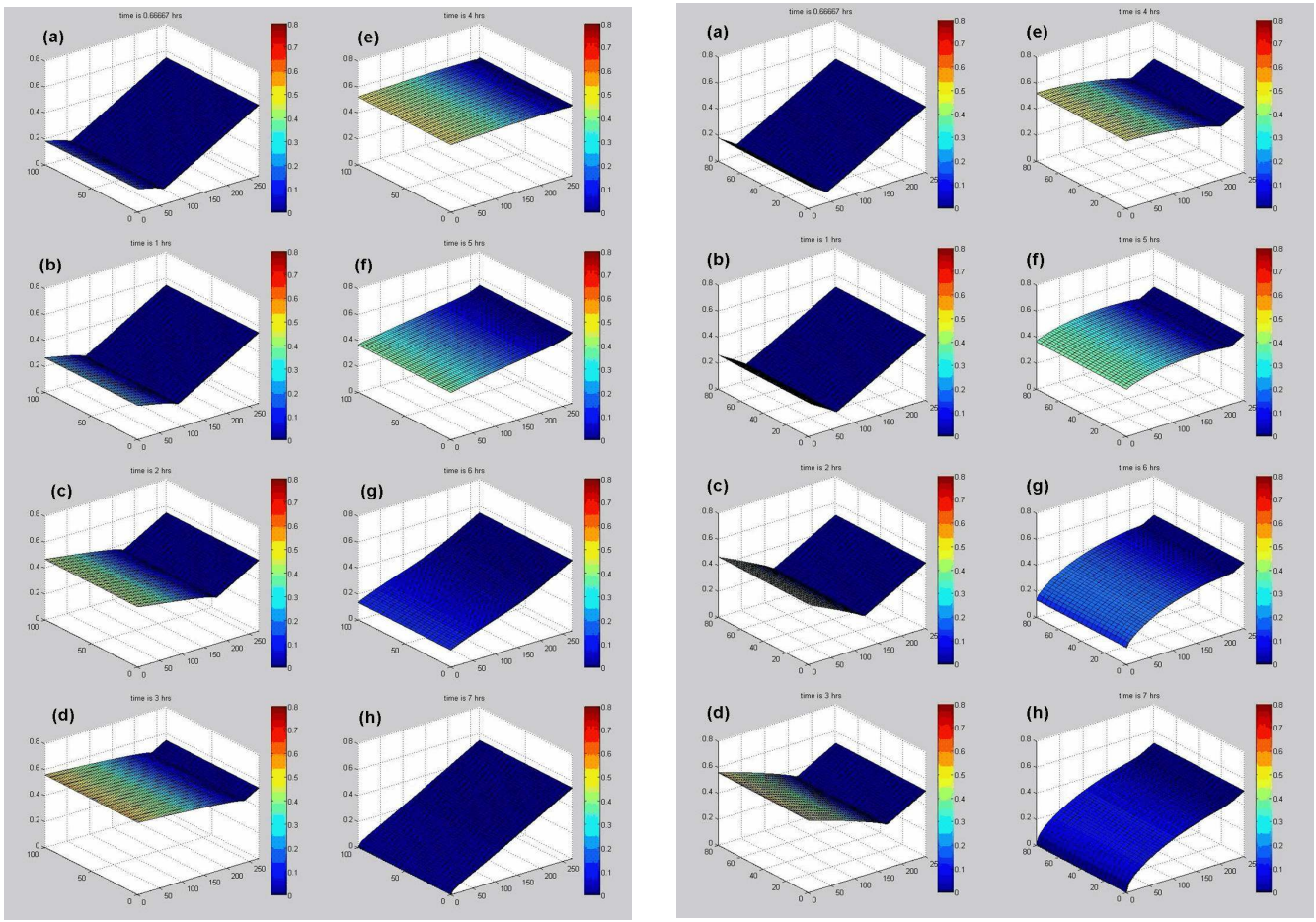

Figure 6. Marsh platform flow for zero structures with $S = 0.002$. Color denotes the water depth on the platform h and the z-axis reflects the water surface elevation for (*left*) $N_A = 100$ and (*right*) $N_A = 500$. Recorded values shown at (a) 0.5 hrs, (b) 1 hr, (c) 2 hrs, (d) 3 hrs, (e) 4 hrs, (f) 5 hrs, (g) 6 hrs, and (h) 7 hrs.

distances of 100 m. This tidal asymmetry observed with $N_A = 500$ is further illustrated with velocity over an isolated interval of time (Fig. 7). In addition, the time required for a marsh platform to drain at low slopes ($S = 0.002$) is sensitive to stem density, wherein $N_A = 100$ drains within approximately 7 hours and $N_A = 500$ drains within approximately 12 hours. Therefore, longer marsh platform length-scales appear more sensitive to changes in biomass, whereas shorter length-scales, by nature of their length, result in a flooded platform regardless of biomass.

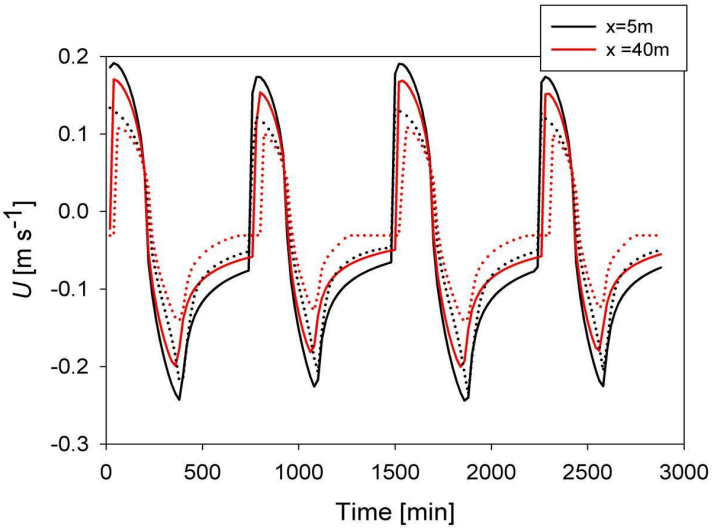

Figure 7. Tidal asymmetry demonstrated by velocity parallel to x as a function of stem density, recorded at the marsh edge and 40 m from the edge. Solid denotes $N_A = 50$ and dotted denotes $N_A = 500$.

4.2 One Structure

Simulations with one structure consider the influence of three barrier lengths along the span-wise (y) direction of flow. Barrier influence on the hydroperiod along the x-coordinate, or with increasing elevation on the marsh platform, extends to $x = 25$ m under conditions of $N_A = 500$, long length-scale (y = 80 m), and barrier extent equal to or greater

than half. As water depth (h) increases during the flood period, barrier presence has less influence on resistence to flooding. Likewise, the bed resistance term becomes negligible with increasing water depth and because the drag coefficient is a function of Reynolds number, C_D decreases with increasing velocity.

Similar to the flood and ebb observed with no obstructions, biomass delays the rate of drainage; however, barrier length also influences whether the platform is able to completely drain. For both platform lengths and barrier lengths of $< ½$ and $= ½$, water drains 90% of the time behind the barrier at the marsh edge; however, $N_A = 100$ drains faster than $N_A = 500$. Increased platform length and barrier length lead to an asymmetrical flow geometry because water must travel longer distances to move around the barrier. This effect is exaggerated with increased stem density, which influences drainage and holds water at higher elevations on the platform. Additionally, converging flow is strongest when the barrier length is greater than the spacing between the barriers and when the y-coordinate or length of the barrier is doubled (*i.e.* the barrier length is 60 m) (Fig. 8). As the volume of water flowing off the platform increases, the water surface slope steepens to accommodate the converging flow. The degree of convergence increases with both biomass and barrier length.

Results from the exceedence probability of the water depth directly behind the barrier ($x = 10$), or analysis of the proportion of time that water depth is greater than or equal to a given water depth, are shown in Table 5. Residual depth refers to the depth of standing water that does not drain. Note, however, for numerical stability, a residual depth of 0.01 m is present on the marsh platform at all times. Durations of inundation suggest that the maximum water depth during a tidal cycle is less for $N_A = 500$ and barrier length greater than

"Half." Likewise, for these conditions, the water depth is greater than or equal to 0.13 m for half of the tidal cycle period; this depth is greater than that observed at any other location compared to all other model runs, and likely results from slow platform drainage. Further, residual depth along the *x*-coordinate increases in spatial extent and at the barrier edge with an increase in barrier length.

4.3 Two Structures

The introduction of staggered barriers, separated upslope by 10 m, results in delayed flooding with respect to distance along the *x*-axis and *y*-axis (Fig. 9). Water is stored behind the seaward barrier at $x = 10$ m and depths are greatest at barrier openings. Standing water is present higher on the marsh platform for long length-scales and stem density equal to 500 stems m^{-2}. Drainage for long length-scales and $N_A = 500$ is shown for the three barrier length configurations in Figure 10. Here, a long front barrier and short back barrier result in more water being stored close to the shoreline; a short front barrier and long back barrier results in more water stored higher up on the platform; and where the front and back barrier are equal in length, water converges from both directions. Similar changes to the flood routing but with lower water depths also occurs for the short marsh platform length-scale ($x = 40$m).

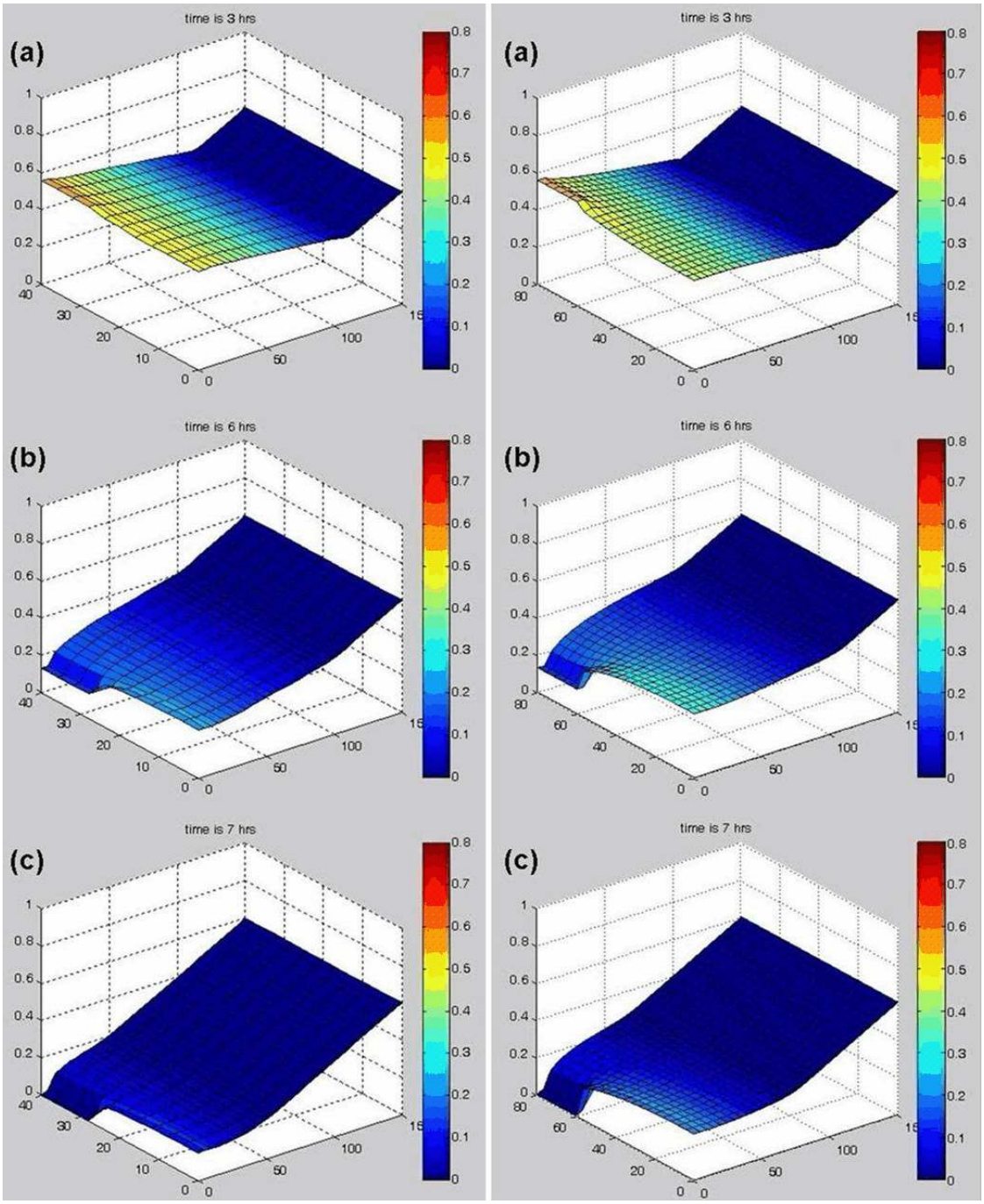

Figure 8. Converging flow shown for one-structure design with $N_A = 500$, $S = 0.004$, and barrier length-scale > *than Half*. (*left*) Barrier is 28 m with $y = 40$ m; and (*right*) Barrier is 60 m with $y = 80$ m. Recorded values shown at (a) 3 hrs, (b) 6 hrs, and (c) 7 hrs.

Table 5. Exceedence probability for one structure at x =10 m, immediately behind the barrier. Length-scale values are denoted in cells as "*short,long*." Bold cells reflect the y position for the barrier end.

		Short length-scale, Long length-scale					
		Na 100			**Na 500**		
Along Shoreline [m]		**y=12,28**	**y=20,44**	**y=28,60**	**y=12,28**	**y=20,44**	**y=28,60**
Barrier <1/2	***Residual Depth***	**0.012, 0.015**	0.006, 0.003	0.003, 0.001	**0.013, 0.016**	0.005, 0.003	0.002, 0.001
	50%	**0.015, 0.02**	0.007, 0.008	0.006, 0.006	**0.035, 0.06**	0.026, 0.03	0.025, 0.025
Barrier =1/2	***Residual Depth***	0.008, 0.001	**0.015, 0.02**	0.007, 0.004	0.001, 0.001	**0.01, 0.01**	0.006, 0.004
	50%	0.024, 0.05	**0.023, 0.03**	0.01, 0.01	0.06, 0.10	**0.05, 0.08**	0.03, 0.04
Barrier >1/2	***Residual Depth***	0.001, 0.001	0.008, 0.001	**0.015, 0.023**	0.001, 0.001	0.001, 0.001	**0.01, 0.01**
	50%	0.035, 0.06	0.033, 0.06	**0.028, 0.04**	0.07, 0.13	0.07, 0.13	**0.06, 0.10**

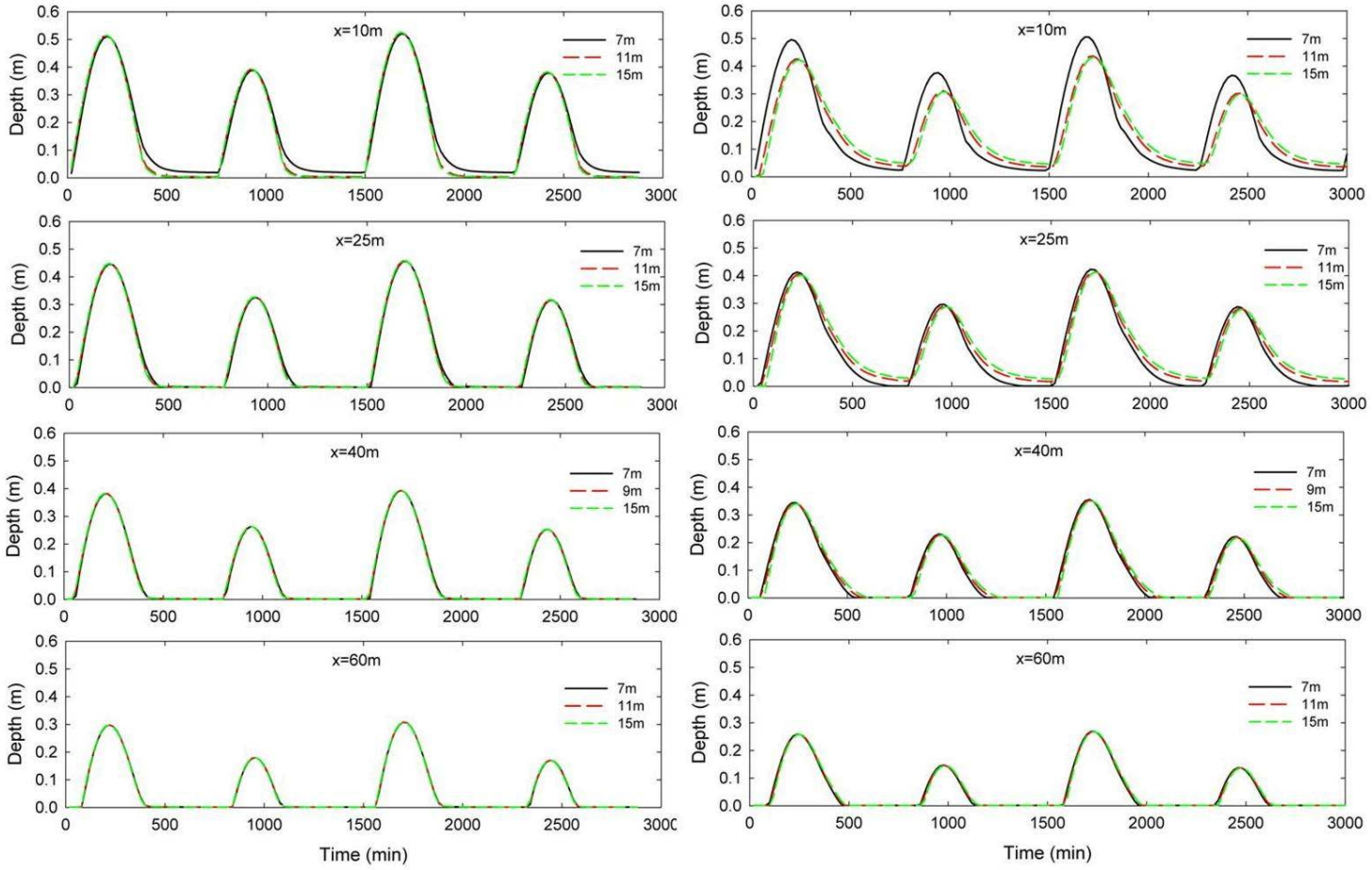

Figure 9. Water depth asymmetry for (*left*) one structure and (*right*) two structures. Simulations represent long platform length-scale, barrier < *Half* (seaward barrier is 28 m and back barrier is 56 m length), and N_A = 500. Boxes contain water depth measurements along the *y*-coordinate with distance from the marsh platform edge along *x*.

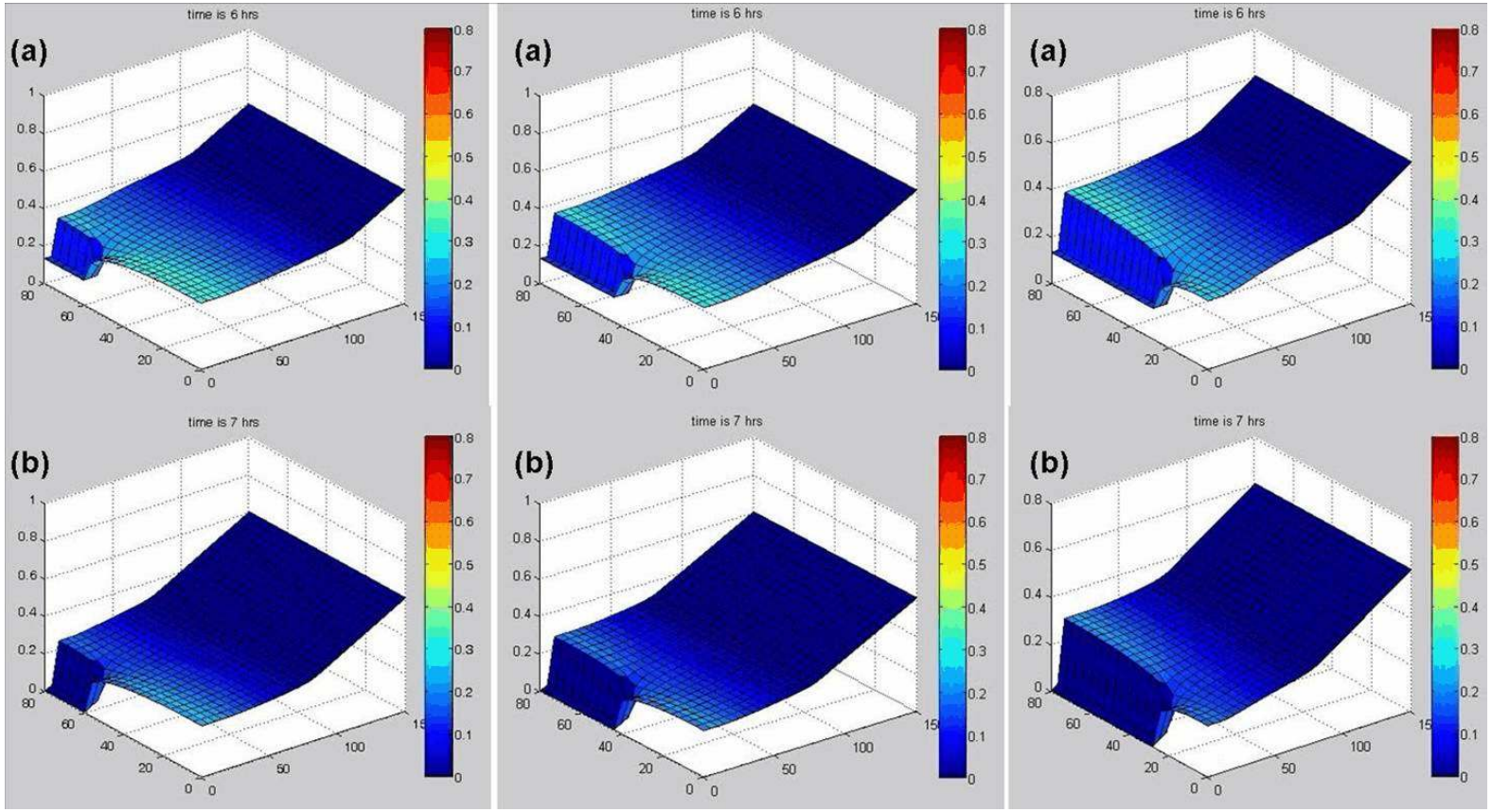

Figure 10. Ebb flow for two-structure barrier design at long platform length-scales shown at (a) 6 hrs and (b) 7 hrs. Simulations shown in decreasing seaward barrier size, (*left*) seaward barrier = 60 m and back barrier = 20 m; (*center*) seaward barrier = 40 m and back barrier = 40 m; and (*right*) seaward barrier = 28 m and back barrier = 56 m.

5. Central Points

Four generalizations are identified to describe the characteristics and change in marsh platform flow with and without obstructions to flow: (1) the distance that water travels up the marsh platform for simulated barrier design and marsh platform length-scale, (2) the change in ebb flow with water depth and marsh platform length, (3) the influence of longer barrier and segment gaps on ebb flow, and (4) the influence of biomass. These central points, discussed below, provide the first steps towards commenting on the role of shoreline structures and macrophyte sustainability.

5.1 Marsh platform flooding

The introduction of barriers alters the depth and extent of marsh platform flooding (Table 6). The maximum extent and depth of flooding from the marsh edge to the maritime forest or high marsh does not differ within a given length-scale (*i.e.* $y = 40$ m and $y = 80$ m) for the staggered barrier configurations. The extent of platform flooding for the one structure design, however, is sensitive to barrier length at long platform length-scales; here, the distance water travels onto the marsh platform decreases with increasing barrier length. That is, less water is allowed onto the marsh platform. The distance and depth is greatest in the absence of structures and with sparse stem densities.

Table 6. Maximum depth and distance of flooding for structure design and structure length. Table results are from simulations with biomass of 500 and short and long length-scales.

		y = 80m		*y* =40m	
		Distance [m]	**Depth [m]**	**Distance [m]**	**Depth [m]**
No Structures	Na 100	135	0.54		
	Na 500	130	0.52		
One Structure, Na500	Barrier < ½	130	0.52	130	0.53
	Barrier = ½	125	0.51	130	0.52
	Barrier > ½	120	0.49	130	0.52
Two Structures, Na500	Barrier < ½	120	0.48	125	0.51
	Barrier = ½	120	0.48	130	0.52
	Barrier > ½	120	0.48	130	0.52

5.2 Change in ebb flow with water depth and marsh platform length

Ebb flow drainage differs for the stabilized shoreline simulations; the asymmetry of the ebb flow on engineered platforms suggests that there is increased resistance to drainage as water depths decrease towards the end of the ebb period. For example, consider water depth over two tidal cycles at a point directly behind the end of a single barrier with length and spacing equal in distance (Fig.11). Although ebb flow is delayed for greater stem densities, the marsh platform is able to drain when marsh platform lengths are small. As length-scales increase, water is unable to drain from behind the barrier and water continues to pile at the barrier edge as upslope water drains. Long durations of inundation at low water depths for large marsh platforms results in greater resistance from the bed, and is likely associated with the decelerated drainage rates.

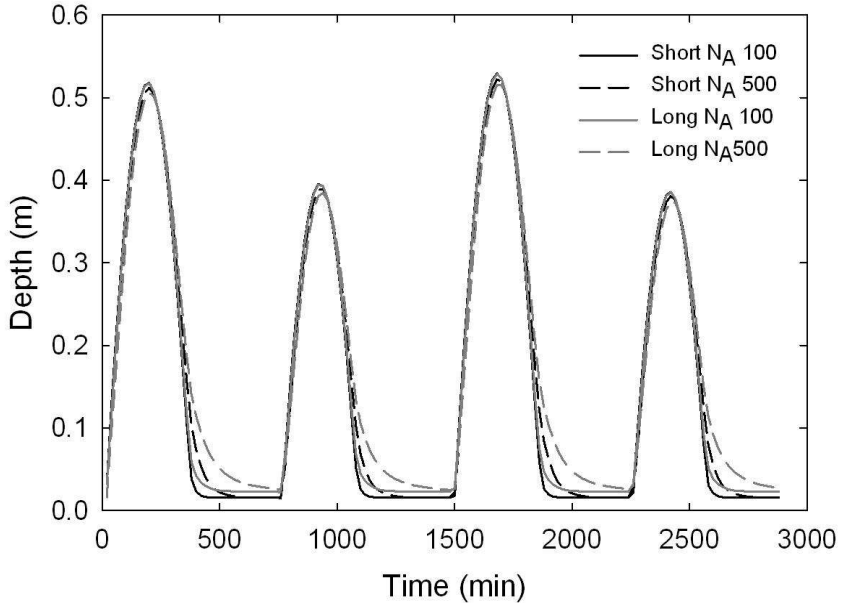

Figure 11. Ebb flow asymmetry for barrier size equal to half of the *y*-domain. N_A = 100 [solid] and 500 [dashed], short length-scales with *y* = 40 m and barrier size = 20 m [black], and long-length scales with *y* = 80 m and barrier size = 40 m [grey].

5.3 Influence of the longer barrier and segment gaps on ebb flow

For a single barrier configuration, greater amounts of standing water are present behind the barrier as the length of the barrier increases (Fig. 12). The residual water is greatest at the barrier end. Additionally, the length of the gaps between barrier segments influences the strength of converging flow (Fig. 8). Converging flow is strongest when the barrier length is greater than the spacing between the barriers and when the *y*-coordinate or length of the barriers is doubled.

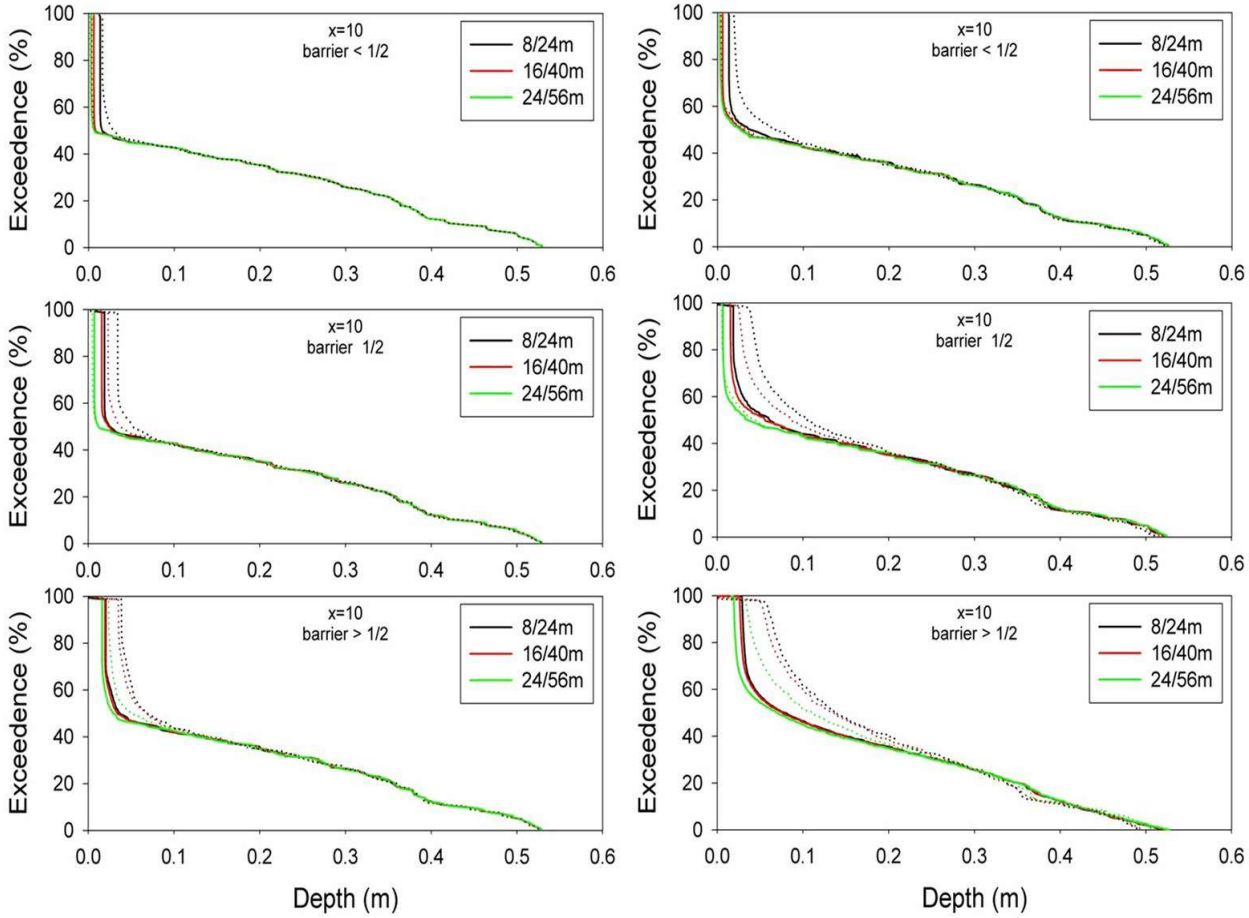

Figure 12. Exceedence probability for the proportion of time that a given depth is inundated at a given depth or greater. Inundation durations shown for one structure configuration at $S = 0.004$ for (*left*) $N_A = 100$ and (*right*) $N_A = 500$. Solid lines denote short length-scales where $y = 40$ m and dashed lines denote long length-scales with $y = 80$ m. Durations of inundation are recorded directly behind the barrier at $x = 10$ m.

5.4 The influence of biomass

Biomass influences flood and ebb flow regardless of the platform length, including ebb drainage, water surface slope during flooding, and extent of flooding onto the platform (Fig. 13). Consider a short length-scale single barrier with length less than *Half* and S = 0.004. Here, an increase in stem density from 50 to 500 stems m^{-2} leads to a greater water surface slope during the flood tide and delayed ebb flow. This effect is exaggerated at larger length-scales without barriers (Fig. 6). In addition, there is an increase in the amount of standing water and the rate of ebb flow for the staggered barrier design, largely influenced by stem density (Fig. 14).

6. Discussion

The ideal marsh shoreline protection design should be informed by the principles of ecology and sedimentology. The results presented above suggest that barrier length needs to be considered in order to reduce standing water depth. Decreased barrier size will also minimize drainage resistance, namely the increased water surface slope that results at the barrier end due to water convergence. This convergence results from upslope water drainage that is forced to exit through a specific area, and has important implications for erosion. Water passing the ends of a structure is partially slowed, causing a current that wraps around the end of the structure and may result in bed scour. This scour has been shown to cause accelerated erosion immediately behind the ends of structures such as seawalls, breakwaters and reefs [*Hughes and Schwichtenberg*, 1998].

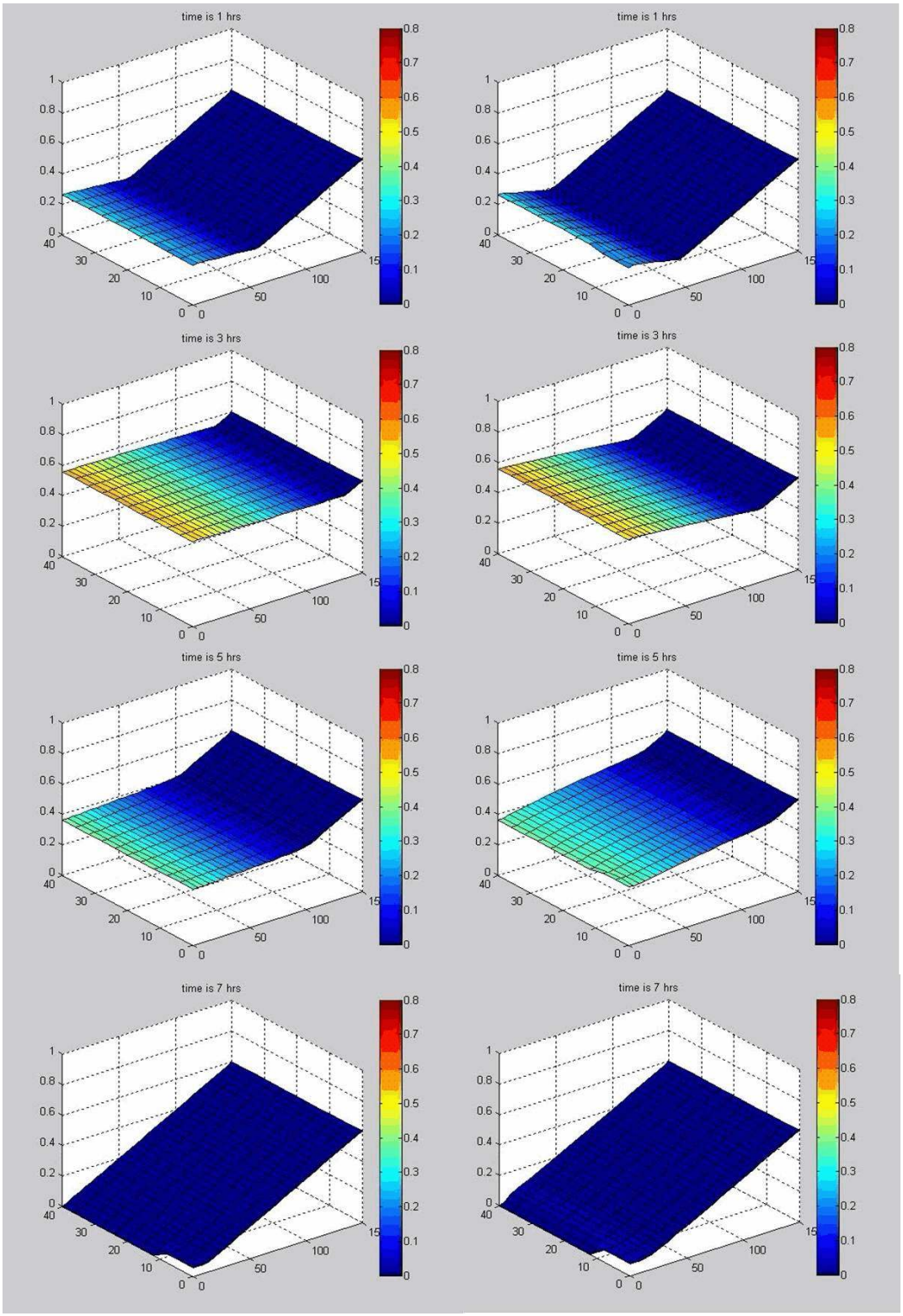

Figure 13. Biomass influence on the water surface slope shown for one structure, short length-scale, barrier length < *Half*, and $S = 0.004$. (*left*) $N_A = 100$ and (*right*) $N_A = 500$.

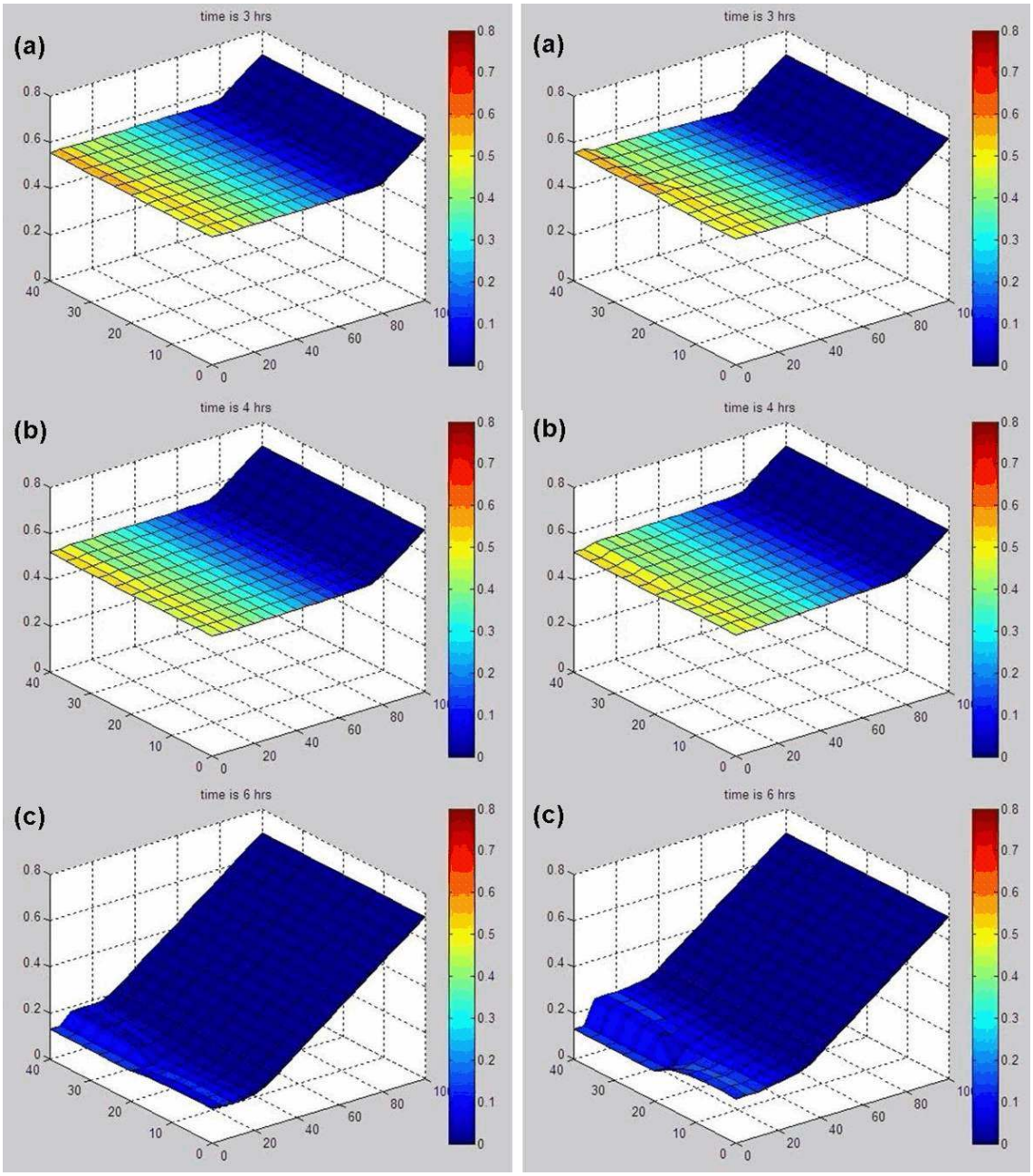

Figure 14. Influence of stem density and staggered barrier design on the amount of standing water behind barriers during ebb flow. Output is for simulations of short length-scale, equal barrier length, and representative fringe marsh slopes with $S = 0.007$. (*left*) $N_A = 100$ and (*right*) $N_A = 500$. Output shown for (a) 3 hrs, (b) 4 hrs, and (c) 6 hrs.

Turning now to the ecological implications, it is well established that plants less tolerant of inundation and/or salinity are found at higher elevations. The design of the larger back barriers for two offset structures results in greater amounts of standing water for longer durations of time regardless of platform length-scale and biomass. Therefore, when trying to protect a healthy marsh, the results from the two-dimensional hydrodynamic model presented here indicate that a short landward barrier is ideal. Exceedence probability from the model output can be used with a parabolic distribution of biomass over the distance of a marsh platform [*Morris et al*., 2002] to determine the range of structure lengths that will facilitate healthy stem densities. Field experiments by *Morris et al*. [2002] suggest a parabolic growth curve for *Spartina alterniflora*, where primary productivity is a function of inundation duration [Fig. 15]. The lower elevation limit is likely controlled by hypoxia and the upper limit determined by salinity stress, desiccation, and/or competition pressure from

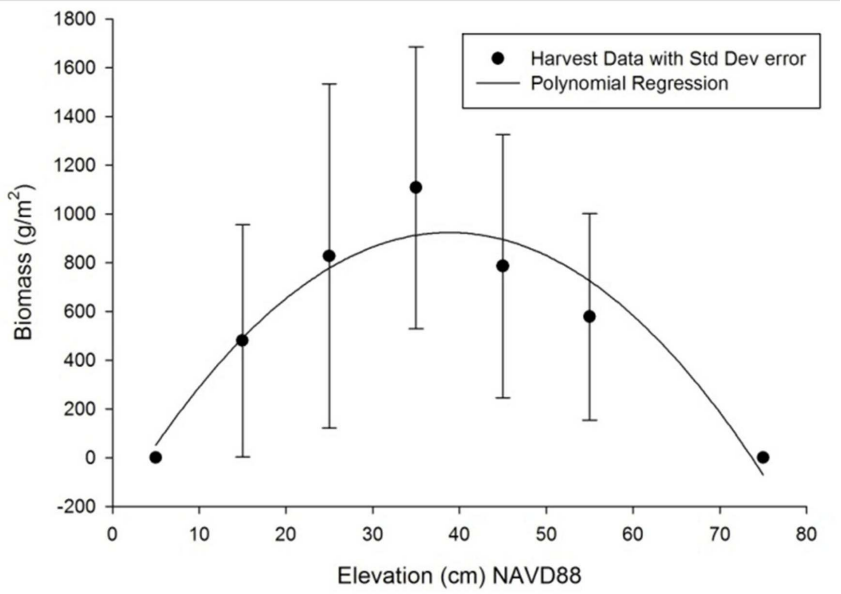

Figure 15. *Spartina alterniflora* aboveground biomass as a function of elevation. Data from North Inlet, South Carolina fit by a polynomial regression [*Scott,* 2010].

other species. A significant shift in the hydroperiod associated with barrier configuration will likely shift the predicted biomass curve. For example, if macrophytes behind a barrier are located on the left side of the parabola, an increase in inundation due to the barrier will result in a greater inundation and therefore decreased primary productivity. Conversely, if macrophytes exist on the right side of the "optimal" elevation, then the increase in inundation will increase the primary productivity. *Currin et al*. [2008] conducted initial estuarine shoreline stabilization studies at sites approximately 1 km from the PKS study area. The platform elevation was measured at a natural fringe marsh and at a nearby marsh protected with a marsh sill. Results suggest that the elevation of the natural marsh shoreline decreased while the marsh edge at the engineered shoreline increased in elevation. However, the *Spartina alterniflora* biomass remained stable at upper elevations of the natural marsh, approximately 10 to 20 m from the shoreline, while biomass decreased at the upper elevations of the protected marshes. Although an inundation analysis has not been conducted for this study, the observations suggests that the increase in elevation for the protected marsh does not support the vegetation. That is, the vegetation at higher elevations is now at a greater DBMHW.

Barrier design influences the sensitivity of marsh platform flow to biomass and platform length-scale. Consider the design example for the two barrier configuration in Fig. 10 for long platform length and a healthy marsh, $N_A = 500$. A structural design consisting of a larger seaward barrier will capture water at the marsh edge, compared to a shorter seaward barrier and larger secondary barrier where water pools at higher elevations on the marsh. The equally long seaward and offset barriers result in water pooling behind both obstructions, and

convergence of flow from both directions. All three designs produce new flow routes due to water surface slope changes. Similar conditions exist for each design at smaller platform length scales, yet with lower water depths and velocities. The amount of remnant water behind the one barrier design is a function of both length scale and biomass, where standing water increases with an increase in platform length scale and biomass. Stem density influences the slope of the ebb flow, as seen in the case of no structures (Fig. 6). For low N_A, the effect of platform length scale is reduced.

7. Conclusion

Simulations from the two-dimensional hydrodynamic model presented here illustrate how stem density influences the ability of water to flood and drain a salt marsh platform. This model demonstrates a bathtub flow geometry for short fringe marsh length-scales and sparse stem densities. The introduction of barriers influences the distribution of water at the platform edge, and large platform length-scale, biomass, and barrier length are shown to influence the hydroperiod at higher elevations. To maintain ambient conditions, it is necessary to reduce the length of the barriers. If the exchange of water is not facilitated, areas landward of the barrier may become dead zones for aquatic species. Additionally, a significant shift in the hydroperiod associated with barrier configuration will likely shift the predicted biomass curve. For plants situated at elevations on the left side of the parabola, an increase in inundation due to the barrier will result in a greater inundation and therefore decreased primary productivity. Macrophyte species on the right side of the "optimal"

elevation will experience an increase in primary productivity, however, with the associated increase in inundation. This initial characterization of the physical-biological coupling focused on marsh inundation and plant productivity supports the development of generalized barrier design based on model input of marsh platform length, slope, and biomass distribution.

8. Notation

C Chézy coefficient
C_D Drag coefficient [dimensionless]
C_f Darcy-Weisbach friction factor
d stem diameter
F_V the total stem drag
g gravitational acceleration
h water depth
i denotes unit vector parallel to x
j denotes unit vector parallel to y
K denotes the parenthetical terms for the summation of stem drag and bed stress
n Manning's coefficient [dimensionless]
N_A stems per unit area
Re Reynolds number based on stem diameter length-scale
t time
U denotes the local depth-averaged velocity
$|\mathbf{U}|$ magnitude of the velocity vector
U velocity parallel to x
V velocity parallel to y
x coordinate normal to the marsh platform edge
y coordinate parallel to the platform edge
z coordinate vertical

υ kinematic viscosity
μ dynamic viscosity
ζ denotes the local water-surface elevation
η denotes the local platform surface elevation
ρ fluid density

9. References

Alexander, C.R. (2008), *Rates and Processes of Shoreline Change at Ft. Pulaski National Monument*, Final Report to the National Park Service, 58 p.

Anderson, W.D. (1997), *Utilization of Oyster Shell to Suppress Estuarine Shoreline Erosion. Charleston Harbor Project*, Final Report: Contract #EQ-7-534.

Bell, S.S., E.D. McCoy, and H.R. Mushinsky, editors (1991), *Habitat structure: the physical arrangement of objects in space*, Chapman & Hall, London, UK.

Bennett, K.F., and G.B. Griggs (1986), *Coastal Protection Structures and their Effectiveness*, University of California at Santa Cruz, 50pp.

Berman, M.R., H.E. Berquist, and P. Mason (2005), Building arguments for living shorelines, *Proceedings of the 14th Biennial Coastal Zone Conference,* New Orleans, Louisiana, July 17-21.

Chow, V.T. (1959), *Open-Channel Hydraulics*, McGraw-Hill, New York.

Christiansen, T., P.L. Wiberg, and T.G. Milligan (200), Flow and sediment transport on a tidal salt marsh surface, *Estuarine, Coastal and Shelf Science, 50,* 315-331.

Committee on Mitigating Shore Erosion along Sheltered Coasts, National Research Council (2007), "4 Mitigating Eroding Sheltered Shorelines: A Trade Off in Ecosystem Services," *Mitigating Shore Erosion along Sheltered Coasts*, Washington, DC: The National Academies Press.

Corbett, R.D, J.P. Walsh, L. Cowart, S.R. Riggs, D.V. Ames, and S.J. Culver (2008), *Shoreline Change Within the Albemarle-Pamlico Estuarine System, North Carolina*, East Carolina University Press, 10 pgs.

Currin, C.A., P.C. Delano, and L.M. Valdes-Weaver (2008), Utilization of a citizen monitoring protocol to assess the structure and function of natural and stabilized fringing salt marshes in North Carolina, *Wetlands Ecol Manage, 16,* 97-118.

Ellis, J.T., D. J. Sherman, B.O. Bauer, and J. Hart (2002), Assessing the Impact of an Organic Restoration Structure on boat Wake Energy. *Journal of Coastal Research, Special Issue 36*, 256-266.

Harper, E.M. (1997), Attachment of mature oysters (*Saccostrea cucullata*) to natural

substrata, *Marine Biology, 127*, 449-453.

Howell, S.M., C.R. Alexander, and C. Van Westendrop (2005), Rates and processes of shoreline change at Fort Pulaski National Monument, Georgia, GSA *Abstracts with Programs*, 37:7, p. 489.

Hughes, S.A., and B.R. Schwichtenberg (1998), Current-induced scour along a breakwater at Ventura Harbor, CA- experimental study, Coastal Engineering, 34.

Kraus, N.C. (1988), The Effects of Seawalls on the Beach: An Extended Literature Review, *Journal of Coastal Research, Spec Iss 4*, 1-28.

Leonard, L.A., P.A. Wren, and R.L. Beavers (2002), Flow dynamics and sedimentation in Spartina alterniflora and Phragmites australis marshes of the Chesapeake Bay, *Wetlands, 22:2*, 415-424.

Luscher, A. And C. Hollingsworth (2005), *Shore Erosion Control: The Natural Approach*, Publication of the Maryland Coastal Zone Management Program, Dept. Natl. Res., 12pp.

Meijer, M.C. (2005), Wave attenuation over salt marsh vegetation, a numerical implementation of vegetation in SWAN, *Thesis project*, Delft University of Technology, The Netherlands.

Meyer, D.L., E.C. Townsend, and G.W. Thayer (1997), Stabilization and erosion control value of oyster clutch for intertidal marsh, *Restoration Ecology, 5:1*, 93-99.

Meyer, D.L., and E.C. Townsend (2000), Faunal utilization of created intertidal eastern oyster (*Crassostrea virgnica*) reefs in the southeastern United States, *Estuarines, 23*, 34-45.

Morris, J.T., P.V. Sundareshwar, C.T. Nietch, B. Kjerfve, and D.R. Cahoon (2002), Responses of coastal wetlands to rising sea level, *Ecology, 83:10*, 2869-2877.

Piazza, B.P., P.D. Banks, and M.K. LaPeyre (2005), The potential for created oyster shell reefs as a sustainable shoreline protection strategy in Louisiana, *Restoration Ecology 13:3,* 499-506.

Priest, G.R. (1999), Coastal shoreline change study, northern and central Lincoln County, Oregon, *Journal of Coastal Research, Special Iss #28*, p.140-157.

Roig, L.C. (1994). Hydrodynamic modeling of flows in tidal wetlands, PhD dissertation, University of California, Davis, California.

Schlichting, H., and K. Gersten (2000). *Boundary Layer Theory*, 8th revised edition,

Springer-Verlag, Berlin, New York.

Scott, S.M. (2010), Spartina Alterniflora productivity and salt marsh stability relative to marsh platform elevation, *Theses and Dissertations*, Paper 402, University of South Carolina.

Seitz, R.D., R.N. Lipcius, N.H. Olmstead, M.S. Seebo, and D.M. Lambert (2006), Influence of shallow-water habitats and shoreline development on abundance, biomass, and diversity of benthic prey and predators in Chesapeake Bay, *Mar Ecol Prog Ser 326*, 11-27.

Smith, K. (1999), Integrating habitat and shoreline dynamics into living shoreline applications, in *Evaluation of Living Shoreline Techniques: Living Shoreline Summit Conference Proceedings*, 36-37.

Stauble, D.K., and J.R. Tabar (2003), The use of submerged narrow breakwaters for shoreline erosion control, *Journal of Coastal Research, 19*, 684-722.

Williams, S.L. (1993), Shoreline erosion at Mad Island Preserve, Matagorda City, Texas, *Texas Journal of Science, 45*, 299-309.

CHAPTER IV

STOCHASTIC DESCRIPTION OF SALT-MARSH INUNDATION FROM MIXED ASTRONOMICAL AND WIND-DRIVEN TIDES, WITH IMPLICATIONS FOR MACROPHYTE GROWTH

Abstract

Irregularly flooded marshes or high-elevation macrophytes along the east coast of the U.S. are inundated during spring tides and when there are storm-induced changes in water level. This irregular flooding may affect the vertical distribution of marsh vegetation, which has been shown to be sensitive to platform elevation, mean sea level, salt stress, and competitive pressure. In this paper, we present a description of tidal signals and the separation of astronomical and wind-driven flooding. Using Least Squares Regression, we explore the number of tidal constituents necessary to simulate the predicted tidal signal, finding that the astronomical signal at Bogue Banks, North Carolina is dominated by two primary constituents. We demonstrate that the mixed tidal record does not consist of a wind-driven component superimposed on the astronomical part. Rather, harmonic analysis reveals that low-frequency variations in the water level constitute a significant part of the total variance of the observed record, the effect of which is to set the average water level about which the semi-diurnal and diurnal signals fluctuate. A simplified model is presented to illustrate the basic ingredients of how the low-frequency part of the water level signal arises from movement of water into and out of the estuary. The effect of wind in setting the overall water level in an estuary is also considered with inundation frequencies of the observed and

predicted water records and productivity of *Spartina alterniflora* and *Juncus roemerianus* at measured elevations. Inundation due to the predicted astronomical influence is less than the observed water levels, which results in wet and dry periods for given habitat zones on the marsh platform that do not necessarily match those based on the observed astronomical plus wind-driven tides. Plant productivity is also compared with continuous wet-to-dry ratios over an annual water record to further constrain the favorable conditions for macrophyte growth.

1. Introduction

Coastal salt marshes are areas of intertidal mud, wherein marsh platforms are stabilized by the input of mineralogic sediment and by macrophytes that provide for accumulation of organic matter. Sea-level rise (SLR) and sedimentation interact to control productivity since the elevation of the platform relative to mean sea level (MSL), the point between mean high tide and mean low tide, influences flooding frequency, redox potential, and soil salinity. The type of vegetation that colonizes tidal marshes depends primarily on the elevation within the intertidal zone, and the elevation of the sediment surface determines the duration and frequency that marsh platforms are submerged by tides. Physiochemical factors, such as salinity and flooding, are often considered to control the establishment and zonation patterns of species in salt marsh environments. It has been suggested that sea-level rise can proceed at a rate that is rapid enough to drown marsh vegetation [*Reed*, 1995; *Morris et al*., 2002; *Cahoon et al*., 2006; *Kirwan et al*., 2010]. Irregularly flooded marshes or high elevation marshes along the east coast of the U.S. are inundated during spring tides and

storm-driven tides. This intermittent and irregular inundation of marshes may affect the accumulation rates of inorganic sediment, the accumulation and decomposition of organic matter, and the distribution of marsh vegetation. Studies typically make use of astronomical tidal records to express biomass productivity as a function of depth below mean high water (DBMHW) [*e.g. Morris et al.,* 2002; *Mudd et al,.* 2004], where DBMHW is a surrogate for inundation duration. However, macrophyte biomass is a function of the frequency and timing of flooding rather than simply the mean water level for a given elevation, and wind driven flooding is important for the hydroperiod and the total time of inundation. Although astronomical records have been used to determine the frequency and timing of marsh platform flooding, water level anomalies— the difference between observed water level and that predicted by harmonic analysis of tides— have been shown to be as large as the tidal range [*Cox et al.,* 2002].

Astronomical tides and the associated flooding are described by harmonic analysis of the local tidal constituents, using a finite number of sinusoidal functions with known frequencies. Flood and ebb events associated with wind-driven tides, however, are stochastic and depend on the strength and direction of the wind. The wind-driven component is often regarded as noise in harmonic analysis, yet has been shown to influence the amplitude and phase of estimated tidal constituents and their overall variance [*e.g. Leffler and Jay*, 2008]. Whereas this noise, or wind influence, is typically removed from the tidal signal, we suggest that this wind-driven inundation may be an important ingredient of modeling plant productivity on salt marsh platforms, including the total hydroperiod, particularly in microtidal environments.

In this paper, we present a description of tidal signals and the separation of tidal from non-tidal constituents. We demonstrate that the mixed tidal record does not consist of a wind-driven component superimposed on the astronomical part, wherein water is driven onto the platform by wind [*e.g. Pasternack and Hinnov*, 2003]. Rather, the effect of wind is to increase or decrease the overall level of the water in the estuary that bounds the tidal marsh platform, and therefore the mean water level about which the astronomical signal fluctuates over timescales longer than semi-diurnal and diurnal. Models accounting for purely astronomical signals are unable to capture the high and low observed water levels, nor the cumulative inundation near these levels. This stochasticity suggests that wind should be accounted for as modulating the water level, and that the influence of wind is necessary to relate to timing of inundation on salt marsh platforms. We illustrate the basic ingredients within frequency domains and explore the response time of estuary fill and drain. A frequency response function is used to demonstrate that the theoretical gain function may be considered a low-pass filter. To illustrate the effect of wind in setting the overall water level in an estuary, frequency distributions of inundation from both tidal and tidal-plus-non-tidal signals are compared to productivity of *Spartina alterniflora* and *Juncus roemerianus*. We demonstrate that the frequency of marsh platform wetting and drying likely contributes to aboveground productivity.

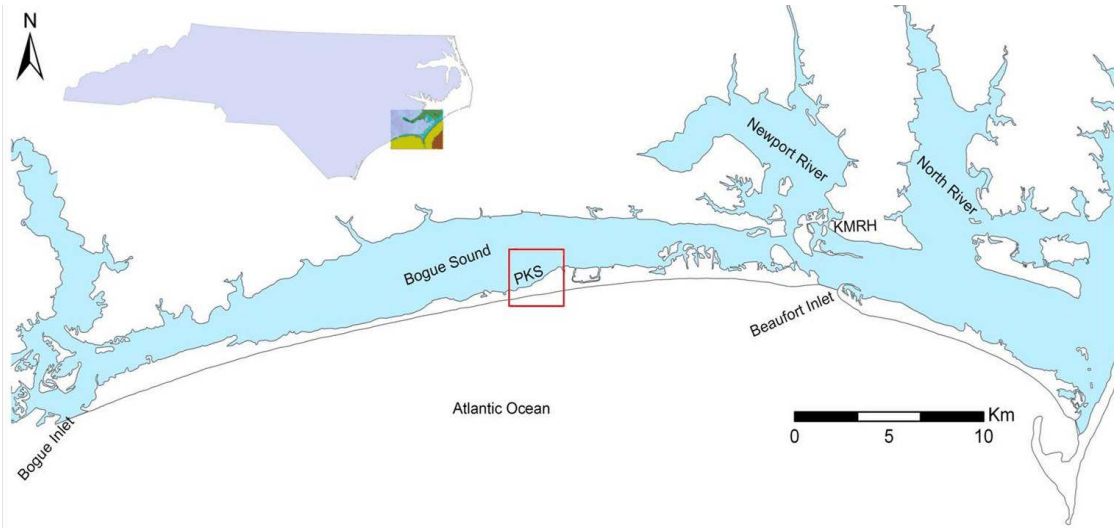

Figure 1. Location of field site and referenced water bodies. The wind station is labeled *KMRH*.

2. Description of Tidal and Wind Signals

2.1. Site Description

Field data for this study consists of water level, wind magnitude, and macrophyte biomass from Pine Knolls Shore (PKS), North Carolina, located on Bogue Banks (Fig. 1). Bogue Sound extends 35 km westward from Beaufort Inlet to Bogue Inlet, and is 3 km wide midway of its length and narrows toward each inlet. This shallow sound is characterized by a brackish and semi-diurnal microtidal regime, separated from the Atlantic Ocean by Bogue Banks, a 0.1 to 1.5 km wide barrier island. The PKS site is approximately 12 km west of Beaufort Inlet to the east and approximately 15 km from Bogue Inlet to the west. The tidal range at PKS is 0.87 to 0.96 m, and MSL from a nearby benchmark is at -0.118 m relative to NAVD88. Mean high high water (MHHW), determined from frequency distributions of water elevation, is 0.47 m. The back-barrier of Bogue Banks is colonized by *Spartina*

alterniflora of moderate biomass and *Spartina patens*, *Juncus roemerianus* and *Distichlis spicata* at higher elevations.

We use 11 months of a three year continuous water level and wind record covering the duration of May 2006 to April 2007. Five Level Troll 500 Pressure Transducers were installed along a transect spanning monotypic stands of *S. alterniflora*, creek, and *J. roemerianus* at PKS. A HOBO pressure transducer was also installed at the PKS Aquarium dock and surveyed to a nearby benchmark by the National Geodetic Survey [*Voss*, 2010]. Water level for PKS was recorded at 6-minute intervals and resampled as hourly records. Wind records obtained from the Beaufort-Smith Field, NC, were converted into North-South (+/-) and East-West (+/-) magnitudes [*SCONC*, 2010].

Macrophyte growth experiments were conducted using "marsh organs" with six elevations that are correlated with surveyed plots on the adjacent marsh platform [*Morris*, 2007; *Voss*, 2010]. Elevations from marsh organ experiments span -0.45 m and 0.56 m, and platform elevations include -0.32 m to 0.0985 m for *Spartina* and -0.007 m to 0.14 m for *Juncus*. Marsh organs reveal the relationships between elevation, inundation, and primary productivity for *Juncus* and *Spartina*, including competition experiments between *Spartina* and *Juncus*. Stem height and count were measured in the field and above- and below-ground productivity were determined in the laboratory [*Chapter 6; Voss*, 2010]. The total time of inundation during the harvest period for a given elevation is determined for both marsh organs and the adjacent marsh platform plots.

2.2. Harmonic Analysis

Harmonic tidal analysis and prediction originates from the approaches of *Doodson* [1921] and *Godin* [1972], wherein the astronomical forcing of tides are modeled as a linear combination of sinusoidal terms and shallow water tides stemming from nonlinear interactions of astronomical tides. Due to the large number and site-specific tidal frequencies, it is infeasible to consider all tidal constituents in harmonic analysis. *Godin* [1972] addressed this by defining constituent clusters— specified by frequencies arising from planetary motions— and restricting the number of constituents included in the analysis based on the record length. Drawbacks to harmonic analysis include availability of time series, where 19 years is needed to resolve the required frequencies, and the assessment of resulting sinusoids as being truly tidal or a product of statistical fitting to the non-tidal component [*Pawlowicz et al*., 2002]. Because it is subjective to remove nontidal effects from the data and infeasible to include all tidal constituents, we present a simple method of least squares regression (LSR) to test the number of tidal constituents needed to effectively model the astronomical forcing on a salt marsh platform as well as capture the wind- and storm-driven influence. Using empirical water level observations, we determine predicted water levels using two approaches. The first approach considers the recommended NOAA-NOS 37 harmonics for Beaufort, NC (Table 1). The second approach assumes a sinusoidal tide and uses LSR to determine the minimum harmonic constituents needed to adequately describe the system.

Table 1. Recommended NOAA-NOS 37 harmonics for Beaufort, NC [*NOAA, 2010*]. Units reported include amplitude in meter and phase in degree, both referenced to MLLW.

Harmonic	Amplitude	Period	Harmonic	Amplitude	Period
M2	0.44	12.421	MM	0	661.309
S2	0.71	12	SSA	0.036	4382.905
N2	0.101	12.658	SA	0.066	8765.821
K1	0.08	23.934	MSF	0	354.367
M4	0	6.21	MF	0	327.859
O1	0.061	25.819	RHO	0.003	26.723
M6	0.009	4.14	Q1	0.012	26.868
MK3	0.003	8.177	T2	0.007	12.016
S4	0.005	6	R2	0.004	11.984
MN4	0	6.269	2Q1	0.002	28.006
NU2	0.02	12.626	P1	0.027	24.006
S6	0	4	2SM2	0	11.607
MU2	0.011	12.872	M3	0.005	8.28
2N2	0.014	12.9	L2	0.023	12.192
OO1	0.003	22.306	2MK3	0.005	8.386
MLAM2	0.007	12.222	K2	0.019	11.967
S1	0.009	24	M8	0	3.105
M1	0.004	24.833	MS4	0.005	6.103
J1	0.005	23.098			

2.2.1 Spectral Analysis

Spectral analysis reveals the cyclic behavior of the dominant harmonic constituents or periods in the water level record. The contribution of each harmonic to the average power is displayed in peridograms that plot the average power of the harmonic with the frequency of the harmonic [*e.g,. Jenkins and Watts*, 1968]. Periodograms of the observed and the predicted values based on the 37 NOAA-NOS harmonics are shown in Figure (2), and are characterized by a broad low-frequency maximum and sharp peaks near diurnal and semi-diurnal frequencies. Tidal forcing at PKS is semidiurnal and consists of dominant influences from the M_2 (12.42hr), K_2 (11.97hr), N_2 (12.66hr), K_1 (23.93hr), and O_1 (25.819hr)

constituents. The periodograms reveal repetitive short time-scale phenomena (*e.g.*, effects of diurnal sea breeze). Figure (2) also shows power spectra of the wind magnitudes oriented North-South and East-West. The variance is greatest at low frequencies for both the N-S and E-W wind magnitudes, suggesting events on longer time-scales (*e.g.*, sustained winds) are significant.

2.2.2 Least Squares Regression

In this section, we explore the number of tidal constituents needed to simulate the essence of marsh platform flooding. Using LSR, the cyclical components from the observed water level are fit to the frequencies of the primary diurnal and semidiurnal constituents. The amplitude of a signal, composed of two sinusoids A and B, is $R = \sqrt{A^2 + B^2}$ and the phase is ϕ = arctan ($-B/A$). The semidiurnal periods are denoted T_1 and T_2. The sum of the squared deviations for the predicted signal (z) and observed signal $(\hat{z})$ for two harmonics is

$$s = \sum [\hat{z}_i - A_1 \cos\omega_1 - B_1 \sin\omega_1 - A_2 \cos\omega_2 - B_2 \sin\omega_2]^2 \qquad (1)$$

where $\omega_i = \frac{2\pi}{T_i} t$ and t is time. The model is linear in A and B, and the sum of squares in Eq. (1) can be minimized. As an example, consider a scenario of one sinusoid composed of constituents A and B, where from Eq. (1),

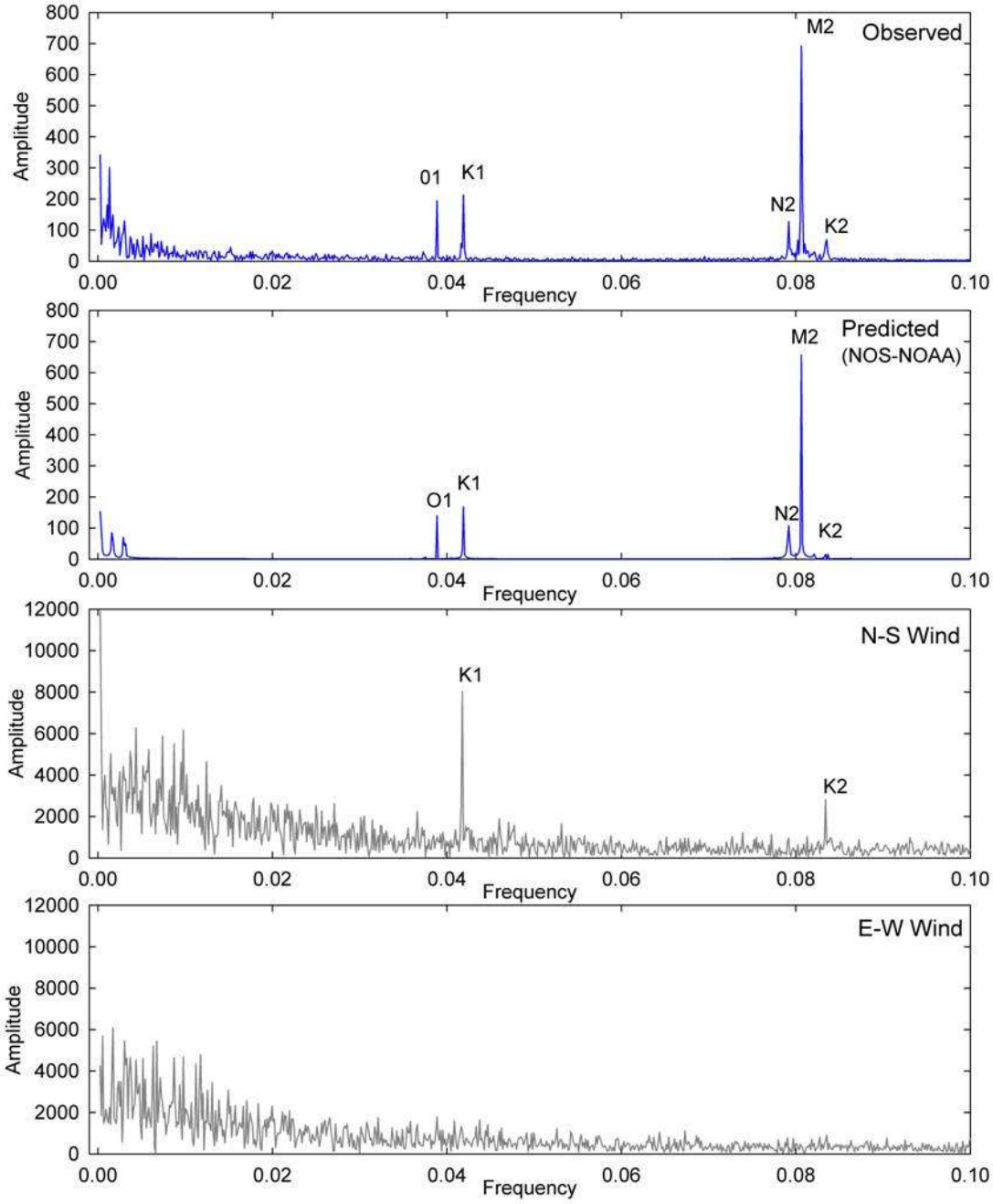

Figure 2. Periodograms for the observed water level record at PKS, predicted NOAA-NOS 37 harmonics, and the observed wind records. Power is reported as amplitude versus frequency. Units of spectral power are not comparable among the wind and water data.

$$A = \frac{\sum \cos_i \omega \hat{z}_i - B \sum \cos_i \omega \sin_i \omega}{\sum \cos_i^2 \omega} \tag{2}$$

$$B = \frac{\sum \sin_i \omega \hat{z}_i - A \sum \cos_i \omega \sin_i \omega}{\sum \sin_i^2 \omega} \tag{3}$$

Let $a_0 = \sum \cos_i \omega_i \hat{z}_i$ and let $a_1 = \sum \cos_i \omega_i \sin_i \omega_i$. That is, let a_0 represent the sum of the observed values at period i and a_1 the sum of the predicted values from period i. Similarly, the observed and predicted terms in Eq. (3) are denoted b_0 and b_1, and rearranging Eqs. (2) and (3),

$$\begin{aligned} A + a_1 B - a_0 &= 0 \\ b_1 A + B - b_0 &= 0 \end{aligned} \tag{4}$$

The linear form in Eq. (4) can then be solved to determine the amplitudes,

$$\begin{bmatrix} 1 & a_1 \\ b_1 & 1 \end{bmatrix} \begin{bmatrix} A \\ B \end{bmatrix} = \begin{bmatrix} a_0 \\ b_0 \end{bmatrix} \tag{5}$$

Least Squares Regression is performed using 2, 3, 4, and 6 harmonics (Table 2). The predicted values (Fig. 3) from these analyses were used to filter the diurnal and semidiurnal constituents, and the residuals contain the observed signal not accounted for by the predicted values (Fig. 4).

Table 2. Tidal harmonics used in the reported Least Squares Regression results and the variances.

Harmonics	R^2
$M_2\ K_1$	0.0307
$M_2\ O_1$	0.0297
$M_2\ K_1\ O_1$	0.0346
$M_2\ N_2\ K_1\ O_1$	0.0366
$M_2\ N_2\ K_1\ S_2\ O_1\ P_1$	0.0380

Table 3. Percent of the astronomical signal captured by the predicted signal, and the percent change from the observed to the residual.

Period	Observed	Predicted		Difference (% Predicted)		Residuals		Remaining Signal	
		37	2	37	2	37	2	37	2
K_2 (11.98)	69	16	—	54 (23%)	69 (0%)	71	71	102%	102%
M_2 (12.40)	692	656	709	36 (95%)	17 (102%)	247	142	36%	20%
N_2 (12.63)	127	108	—	19 (84%)	127 (0%)	54	125	42%	98%
K_1 (23.89)	213	168	214	45 (79%)	2 (100%)	228	428	107%	201%
O_1 (25.75)	194	140	—	55 (71.9%)	194 (0%)	108	194	55%	100%

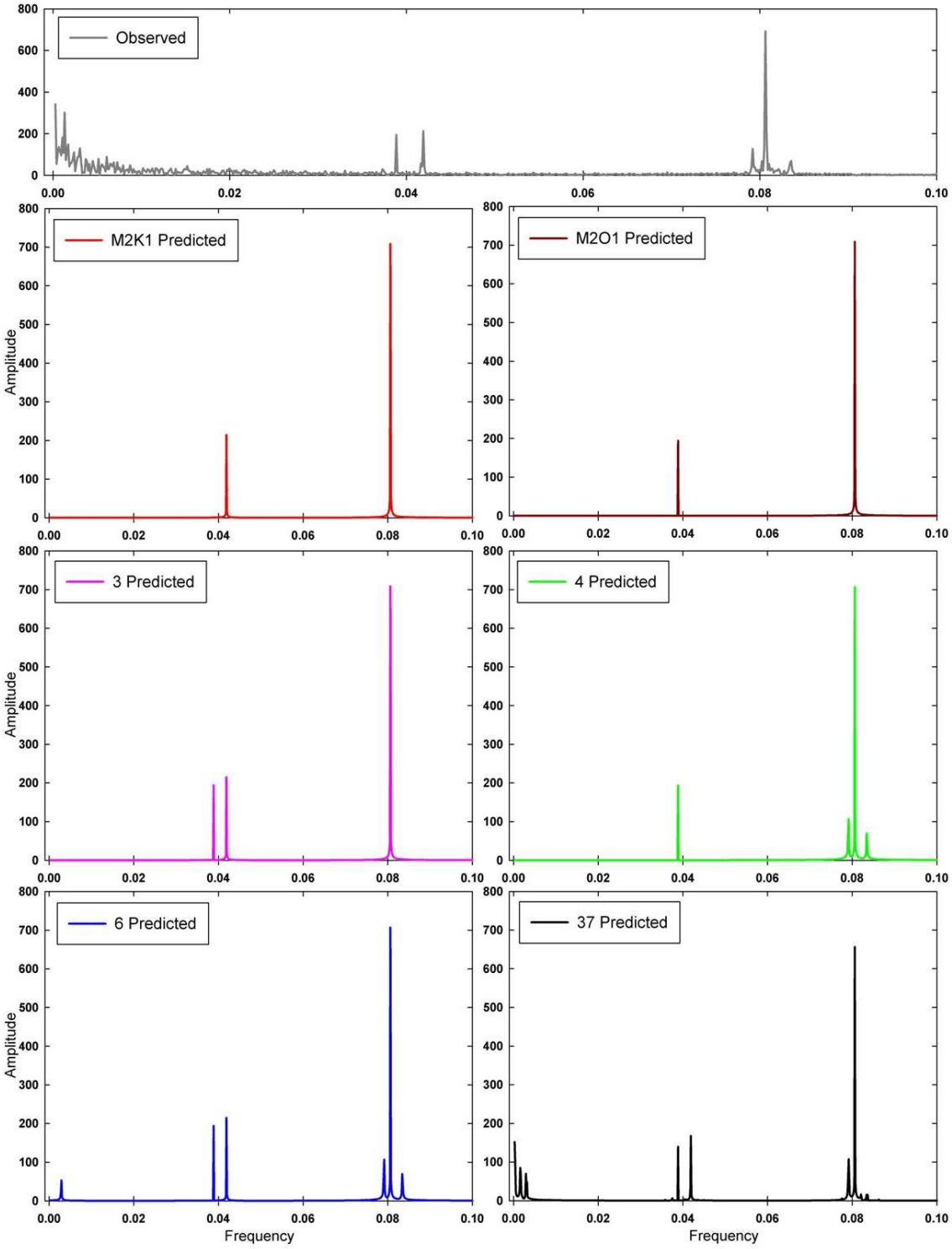

Figure 3. Predicted values from least squares regression of 2, 3, 4, 6 and 36 harmonics, plotted as peridograms.

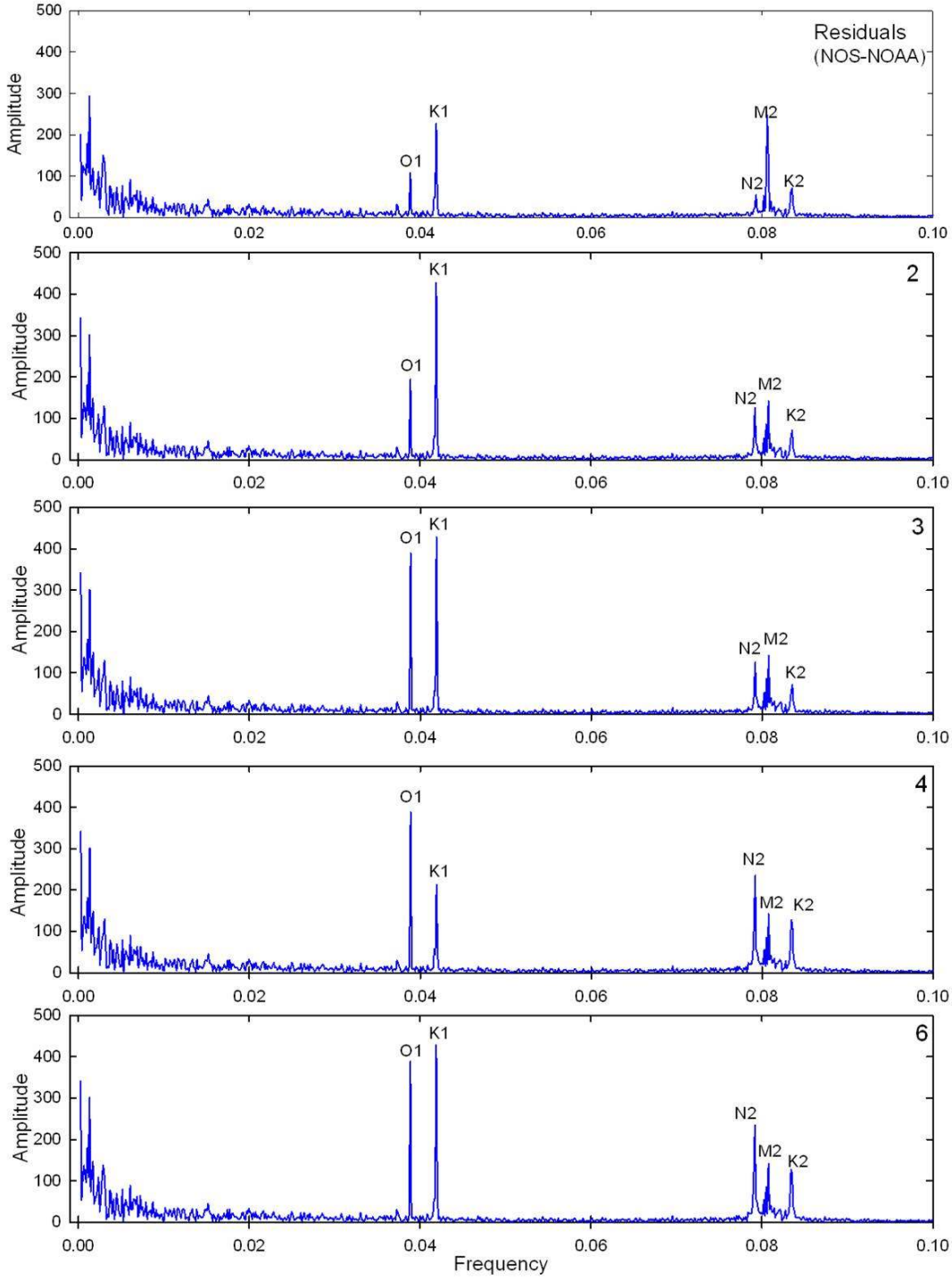

Figure 4. Periodograms of the residuals from the harmonic analysis, with number of harmonic constituents noted in the top right of graphs.

The observed data indicate that the dominant astronomical- and wind-driven signals at PKS are driven by the M_2 and K_1 signals. The 2 harmonic analysis is able reproduce these signals as well as the NOS37 analysis. The predicted spectrum using 37 harmonics (referred to hereafter as NOS37) captures at least 70% of the variance for the M_2, N_2, K_1, and O_1 tidal harmonics (Table 3). Output from simulations of two harmonics M_2 and K_1 have similar amplitudes as the observed spectrum, with slight over predictions (+2%). Residuals from the NOS37 harmonics show removal of the majority of the M_2 and N_2 tidal signals, and residuals from the two harmonic analysis using M_2 and K_1 suggest that M_2 is effectively represented.

The North-South oriented wind record has peaks corresponding with the frequencies K_2 (11.98 hours) and K_1 (23.9 hours). Remaining signals in the power spectra for the North-South and East-West winds are centered between 56 to 582 hours or 2 to 24 days. The diurnal K_1 signal for the North-South spectra is likely a result of daily sea-breeze, and the powers from approximately 10 to 24 days in both the water residual and wind magnitude spectrums suggest storm front events as described below. Similar studies have found evidence for wind forcing in the synoptic weather band, with peaks in the record at approximately 2 days to a week, in the nearby Pamlico Sound-Neuse River Estuary [*Luettich et al*., 2002]. Additionally, water level variations at time scales of less than 20 days in the Chesapeake Bay area have been attributed to astronomical tides and non-tidal wind forcing [*Pasternack and Hinnov*, 2003].

Residuals from both the NOS37 and 2 harmonics retain K_1 as a distinct constituent. Although both of the predicted models capture more than 80% of the observed K_1, the

residual K_1 is nearly equal to the observed for NOS37 output and two times greater than the observed power for the M_2 and K_1 simulation. We consider several explanations for this. First, if we assume that wind contributes to the change in water level adjacent to the marsh platform through wind stress on the water surface, then the K_1 peak in the observed water record is a remnant non-tidal effect. The spectral analysis assumes that water level is stationary about some mean water level, set by the astronomical signal, and the residual values inherit the offset in the mean water level datum from the predicted values. This difference in mean water level datum is due to the effect of wind that increases or decreases the overall level of the water in the estuary that bounds the tidal marsh platform. The K_1 peak is also attributed to daily sea breeze. *Reynolds-Fleming and Luettich* [2004] similarly reported diurnal variability in wind along the nearby Neuse River Estuary, supported by salinity and water level response. The authors attribute the diurnal variability to changes in daytime-nighttime wind strength as well as baroclinic seiches across the estuary with a period of approximately 20 hours. Comparing observed and predicted water levels with meteorological records, the influence of storms and wind is shown to modulate the water depth near the PKS site (Fig. 5). To describe these water level anomalies and mechanisms for water level change within the sound, we now turn to the low-frequency variations in the wind record and use a transfer function model to compare resultant water levels under the influence of sustained winds and tidal variations.

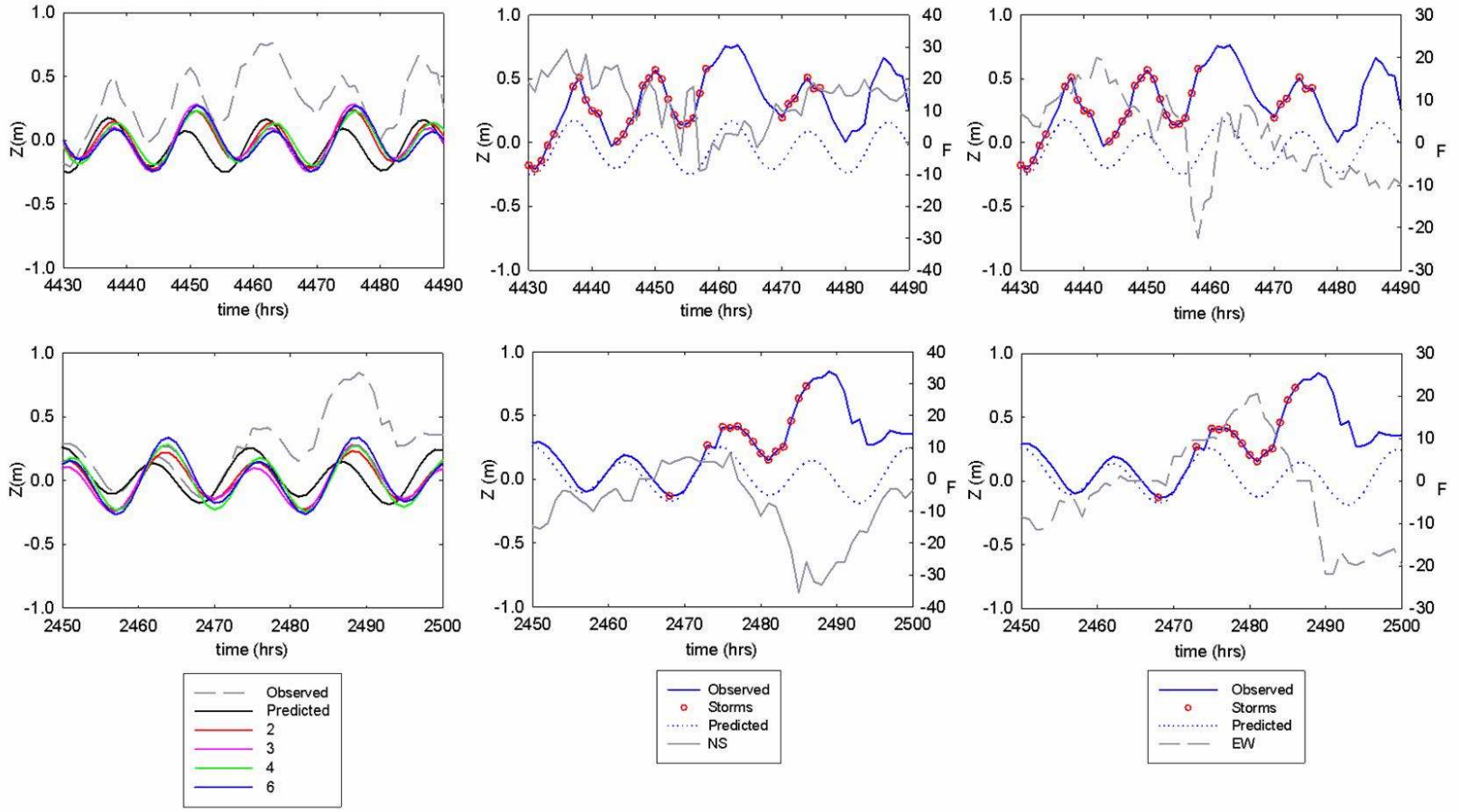

Figure 5. Two storm events recorded at the KMRH station near PKS; storms shown separately in top and bottom figures. Time series of water level is shown in the left figure; observed and NOS-37 predicted water levels are shown with the N-S (+/-) winds in the middle and E-W (+/-) winds on the right. The water level here is z, F is the wind magnitude, and t is time.

3. Model of Low-Frequency Wind-Driven Signal

Our harmonic analysis clearly reveals that low-frequency variations in the water level constitute a significant part of the total variance of the observed record (Fig. 2), the effect of which is to set the average water level about which the semi-diurnal and diurnal signals fluctuate (Fig. 5). Part of this low-frequency variance may be attributable to nonlinear hydrodynamic interactions among tidal constituents as water moves into and out of the shallow estuary that bounds the PKS site. We suggest, however, that because the astronomical part of the signal is dominated by only two primary constituents, and because the low-frequency part of the water-level spectrum does not exhibit any clear peaks or any apparent relation to the astronomical signal, this part of the spectrum more likely reflects fluctuations in water level within the estuary associated with wind and storm events that move water into and out of the estuary over timescales longer than the semi-diurnal and diurnal signals. To describe this behavior in detail would require a full hydrodynamic model of estuarine flow coupled with bathymetric, tidal and wind-stress components. Here, instead, we present a simplified model to illustrate the basic ingredients of how the low-frequency part of the water level signal arises from movement of water into and out of the estuary.

Consider an idealized estuary of area A that is separated from a larger water body by an inlet (Fig. 6). The water level within the estuary is denoted by ζ. We assume that the water level γ of the larger water body next to the inlet varies in response to tidal forcing and to sustained winds that stress its surface. Studies have concluded that wind stress comprises the primary forcing mechanism for water level fluctuations in the Neuse River Estuary and

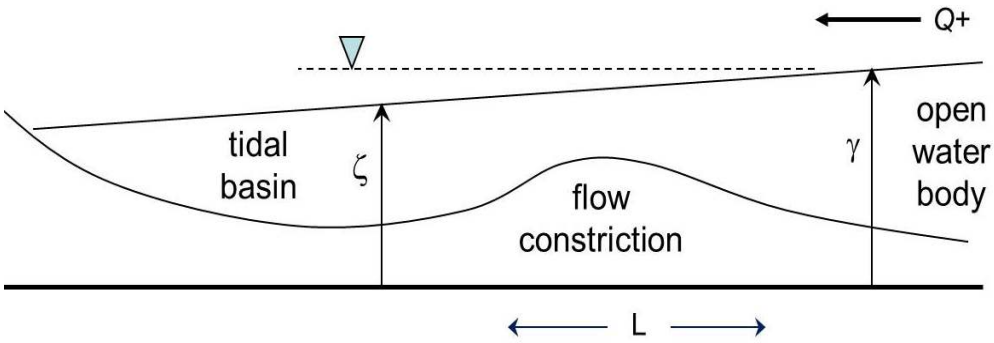

Figure 6. Definition diagram for an idealized estuary.

Pamlico Sound north of PKS [*e.g. Reed et al.*, 2008], and seiches in Pamlico Sound [*Luettich et al.*, 2002]. A similar occurrence and influence of wind is also likely in Bogue Sound given the large fetch oriented parallel to the E-W wind direction. Further, studies of tide inflow through the Beaufort Inlet and Channel show that water level at the mouth of the inlet responds to changes in wind stress direction, which affects the durations of the flood and ebb potions of the tidal cycle [*Churchill et al.,* 1999; *Blanton et al*, 1999].

Following *Fagherazzi and Furbish* [2001], by conservation of mass,

$$A\frac{d\zeta}{dt} = Q = whu \tag{6}$$

where Q is the discharge of water into the estuary through the inlet, w and h are the width and depth of the inlet, and u is the width-depth-averaged flow velocity. We assume here for simplicity that the area of the estuary A is approximately constant.

Assuming a Chézy relation for the flow velocity, $u = Ch^{1/2}S^{1/2}$, where C [$L^{1/2}$ t^{-1}] is the Chézy coefficient and S is the water-surface slope. Because of the bi-directional flow between the estuary and adjacent water body, we may write this relation as

$$u = C\sqrt{\frac{h}{|S|}}\,\frac{\gamma - \zeta}{L} \tag{7}$$

where L is the nominal length of the inlet and $S \approx (\gamma - \zeta)/L$. Substituting (7) into (6) then gives

$$\frac{d\zeta}{dt} = \frac{wC}{AL}h\sqrt{\frac{h}{|S|}}\,(\gamma - \zeta) \tag{8}$$

We now write h, $|S|$, γ and ζ as

$$h = h_0 + h_1, \qquad |S| = |S|_0 + |S|_1, \qquad \gamma = \gamma_0 + \gamma_1 \qquad \text{and} \qquad \zeta = \zeta_0 + \zeta_1 \tag{9}$$

Here, the subscript "0" denotes a time-averaged value and the subscript "1" denotes a fluctuation about the average. Note that $|S|$ is the magnitude of the water surface slope, and therefore the time-averaged value can not equal zero. Note also that $\zeta_0 = \gamma_0$. Substituting the expressions in (9) into (8) then leads to

$$\frac{d\zeta_1}{dt} = \frac{wC}{AL}\frac{h_0^{3/2}(1 + h_1/h_0)^{3/2}}{|S|_0^{1/2}(1 + |S|_1/|S|_0)^{1/2}}\,(\gamma_1 - \zeta_1) \tag{10}$$

Expanding the parenthetical quantities involving h_1 and $|S|_1$ in (10) as binomial series,

$$\frac{d\zeta_1}{dt} = \frac{wC}{AL}\frac{h_0^{3/2}}{|S|_0^{1/2}}\left(1 + \frac{3}{2}\frac{h_1}{h_0} + \ldots\right)\left(1 - \frac{1}{2}\frac{|S|_1}{|S|_0} + \ldots\right)(\gamma_1 - \zeta_1) \tag{11}$$

Assuming the Chézy coefficient C is approximately constant, then at lowest order

$$\frac{d\zeta_1}{dt} \approx \frac{wC}{AL}\frac{h_0^{3/2}}{|S|_0^{1/2}}(\gamma_1 - \zeta_1) \tag{12}$$

or,

$$\frac{d\zeta_1}{dt} \approx \frac{1}{T}(\gamma_1 - \zeta_1) \tag{13}$$

where the system response time constant T,

$$T = \frac{AL}{wC}\frac{|S|_0^{1/2}}{h_0^{3/2}} \tag{14}$$

Thus, the rate of change in the water surface of the estuary, $d\zeta/dt = d\zeta_1/dt$, is approximately proportional to the difference in the water-surface elevations of the estuary and adjacent water body, $\gamma - \zeta = \gamma_1 - \zeta_1$. The response time for the sound to drain and fill increases with the estuary area-to-inlet-width ratio A/w and the inlet length L, and decreases with the Chézy coefficient C, which is inversely proportional to the hydraulic roughness of the inlet. The ratio $|S|_0^{1/2}/h_0^{3/2}$ in (14), representing time-averaged conditions of flow through the inlet, modulates the water-surface difference $\gamma_1 - \zeta_1$. We consider two exploratory scenarios of varying width and length-scales of the estuary and inlet for PKS listed in Table 4 and defined in Fig. 7. Under these conditions, the Chézy coefficient and flow velocity increase for Scenario 1 (W_1) where the width of the inlet is reduced, resulting in greater resistence to flow with estuary size. The response time for greater A/w, L, and C in Scenario 1 is 39 hrs compared to Scenario 2, which has a response time of 19 hrs.

Table 4. Two scenarios, *W1* and *W2*, describe the sensitivity of *T* (14) to parameters, defined below. The subscript "e" denotes estuary and the subscript "i" denotes inlet. *CSA* is the cross sectional area, *wp* the wetted perimeter, and *hr* the hydraulic roughness.

	W1	**W2**
w_e	2500	2500
l_e	40,000	35,000
w_i	400	1100
l_i	6000	3000
A_e	1.0E+08	8.7E+07
CSA_i	800	2200
u (m/s)	5.21	1.66
wp_i	404	1104
hr_i	1.98	1.99
C	116	37
T (hrs)	39	19
A_e/ W_i	2.5E+05	7.9E+04

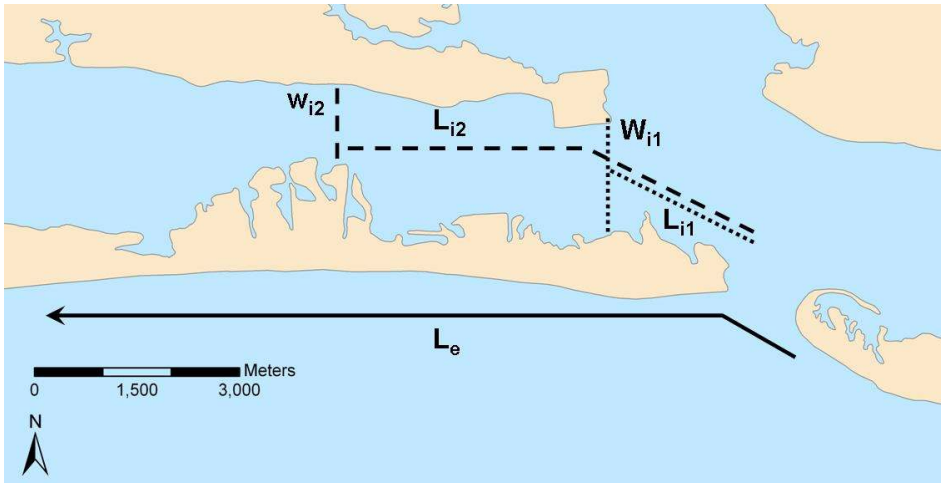

Figure 7. Schematic of the estuary area-to-inlet-width relations for scenarios *W1*, denoted with subscript "1" and *W2*, denoted with subscript "2." Values defined in Table 4.

Assuming for simplicity that the water level ζ_1 responds only to the level γ_1, then a general solution of (13) for an arbitrary signal $\gamma_1(t)$ is

$$\zeta_1(t) = \int_0^\infty h(\tau)\gamma_1(t-\tau)\,d\tau \tag{15}$$

where τ is a time lag term used to weight the value of γ and $h(t)$ is the impulse response function, namely

$$h(t) = \frac{1}{T}e^{-t/T} \tag{16}$$

Thus, the water level $\zeta_1(t)$ within the estuary at time t obtains an exponentially weighted value (convolution) of previous levels $\gamma_1(t)$ in the adjacent water body.

We now turn to the frequency domain to illustrate the use of wind magnitude series as a means to develop a transfer function model that includes T. The frequency response function $H(f)$ of the system is the Fourier transform of the impulse response function (16), namely

$$H(f) = \frac{1}{1 + i2\pi fT} \tag{17}$$

where f is the frequency and the imaginary number i is defined by $i^2 = -1$. This contains both gain and phase information. Of particular interest here is the gain function $G(f)$ of the system, obtained as the magnitude of $H(f)$. Thus,

$$G(f) = \frac{1}{[1 + (2\pi fT)^2]^{1/2}} \tag{18}$$

which may be interpreted as follows. We envision the input signal γ_1 and the output signal

ζ_1 each as consisting of the sum of a set of sinusoids of varying frequency and amplitude — in the sense of a Fourier spectrum. Then, the gain $G(f)$ is the ratio of the amplitude $A_\zeta(f)$ of the sinusoidal output signal ζ_1 with frequency f to the amplitude $A_\gamma(f)$ of the sinusoidal input signal γ_1 with frequency f. Thus, $A_\zeta(f) = G(f)A_\gamma(f)$.

The gain function (16) may be considered a low-pass filter (Fig. 8) wherein low-frequency inputs — where γ_1 varies slowly over long periods $T \sim 1/f$ — are "passed" with minimal attenuation ($G \rightarrow 1$) whereas high-frequency inputs are attenuated. We consider increases or decreases in the water level record as resulting from these low-frequency wind inputs, rather than the high-frequency events in which there is not enough time to move water over significant distances.

Coherency plots for wind magnitude and water level as a function of frequency show several periods of coupling (Fig. 9). Water level and the E-W wind component display coupling over long durations, periods of approximately 13 to 80 days, as well as shorter periods of 11 and 14 hrs. For the N-S component, coherency is strongest at frequencies less than 1 cycle per day, approximately 2 days and 21 hours. Similar studies of coherency between wind direction and water level have shown significant coupling at 1 to 10 days [*Blanton et al.*, 1999; *Pasternack et al.*, 2003]. *Blanton et al.* [1999] also show changes in salinity with wind direction within the Beaufort Inlet, consistent with the change in water level with wind stress reported here. Wind plots and wavelet power spectra from the Neuse River Estuary over shorter study periods found seiches to be excited by variability in the wind field and magnitude, and suggest that the weaker semi-diurnal oscillations present throughout time-series plots represent seiches and not the astronomical tide [*Luettich et al.*,

2002].

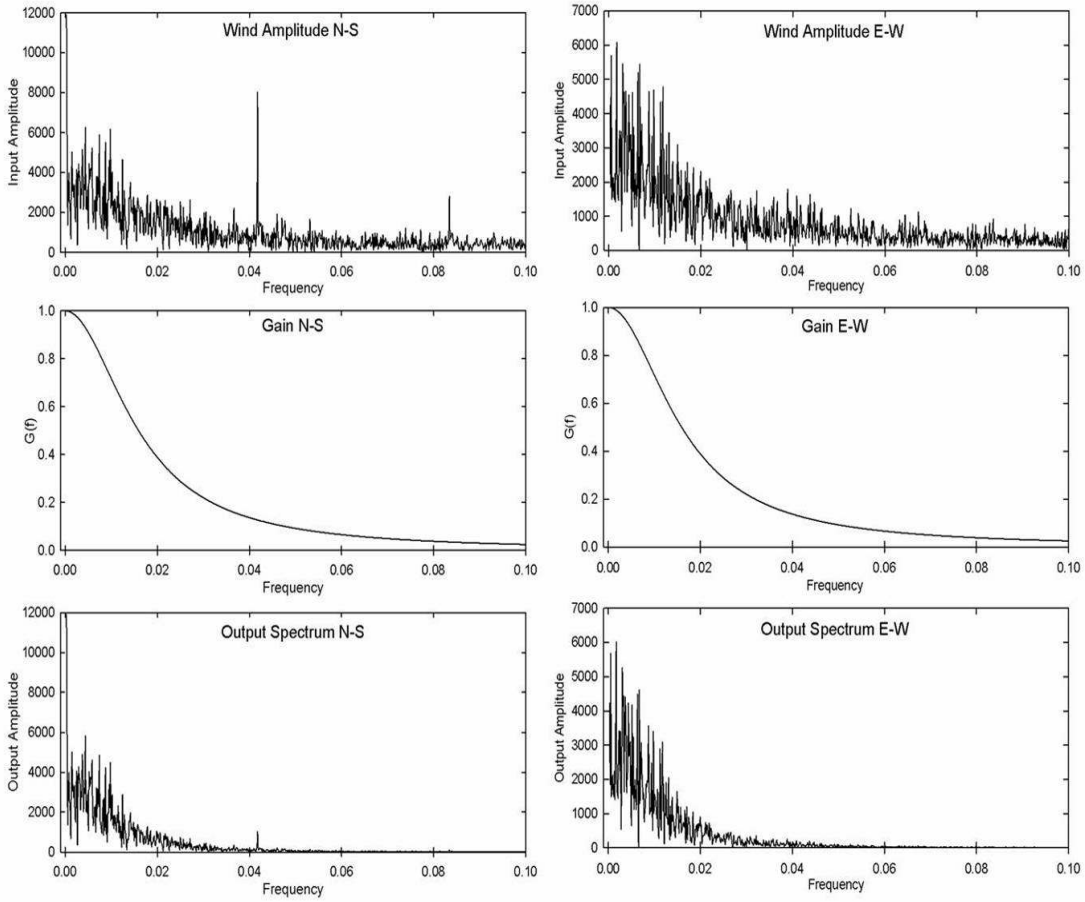

Figure 8. Gain function output for respective wind magnitudes, where the response time constant T is set at 10 hours.

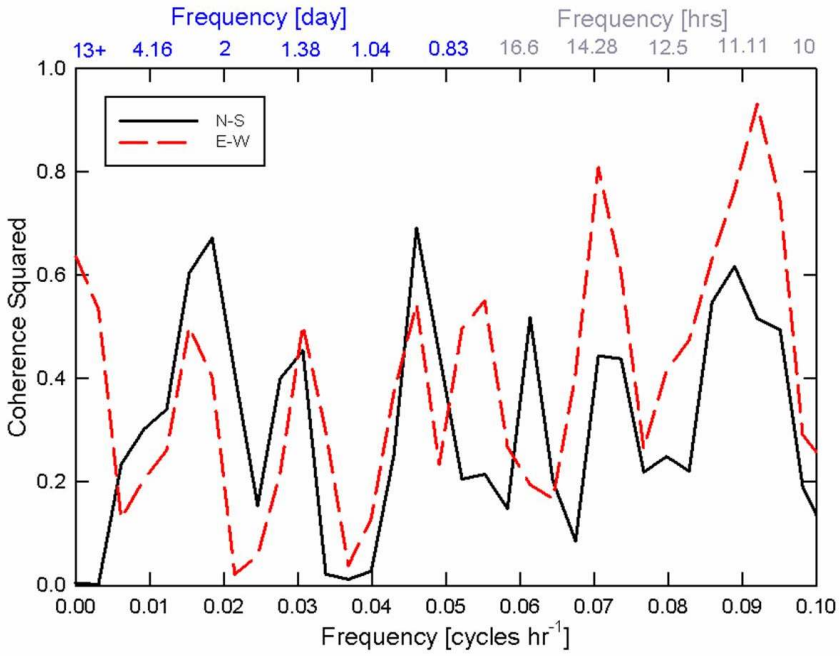

Figure 9. Coherency of the observed water level and wind magnitude.

4. Primary Productivity and Tidal Records

The Pine Knolls Shore site is dominated by a sequence of *Spartina alterniflora, Spartina patens*, to *Juncus roemarianus* with increasing elevation. *S. alterniflora* is a low marsh grass able to tolerate prolonged tidal inundation due to extensive aerenchymatous tissue that supplies oxygen to the roots. The upper flat surface of the high marsh, subject to less inundation, is colonized by *S. patens*. *J. roemerianus* is a high marsh rush that grows tall and occurs as dense patches restricted to elevations close to spring high tide and occasionally as monotypic stands along creek banks. Previous work has reported primary productivity of *Spartina alterniflora* as a function of the relative elevation or depth below MHHW [*Wilsey et al. 1992; Morris et al.*, 2002], which is a surrogate for the duration of inundation. The

frequency of marsh platform wetting provides for the inundation signal that, in part, controls the details of productivity.

To illustrate the effect of wind in setting the overall water level in an estuary, the frequency distribution of inundation using the predicted astronomical tidal record (NOS37) and the observed record containing tidal and non-tidal effects is plotted in Fig. (10). Frequency distributions for the tidal and tidal-meteorological data contain similar inundation durations at water depths of approximately 0.1 to 0 m, yet water level and cumulative inundation time differ for the high and low water depths. The astronomical simulations result in water levels between 0.4 m and -0.2 m during the study period;

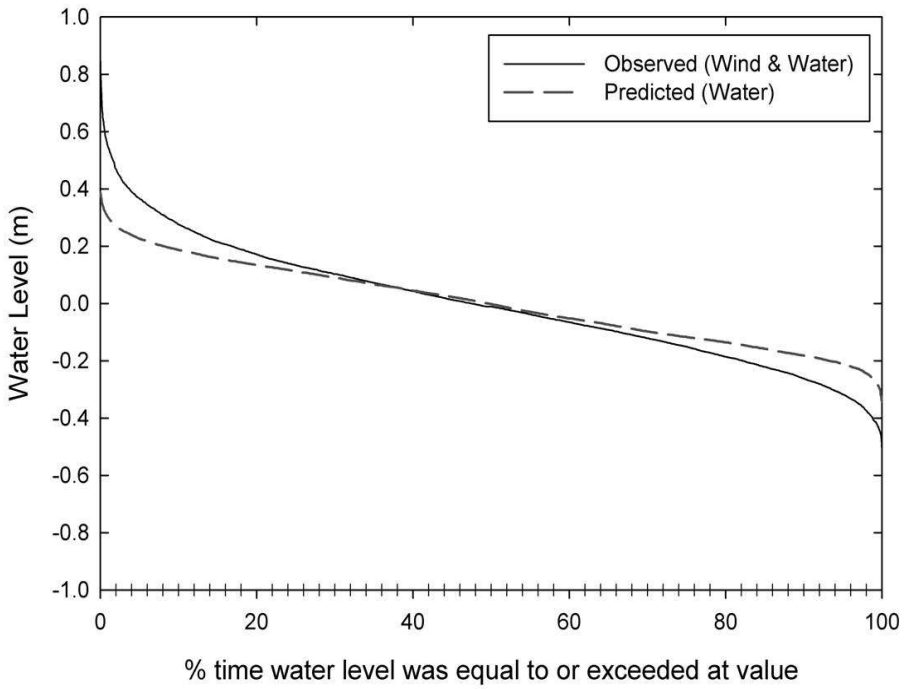

Figure 10. Frequency distribution of the observed and predicted astronomical water levels. Predicted values are based on the NOS37 harmonics.

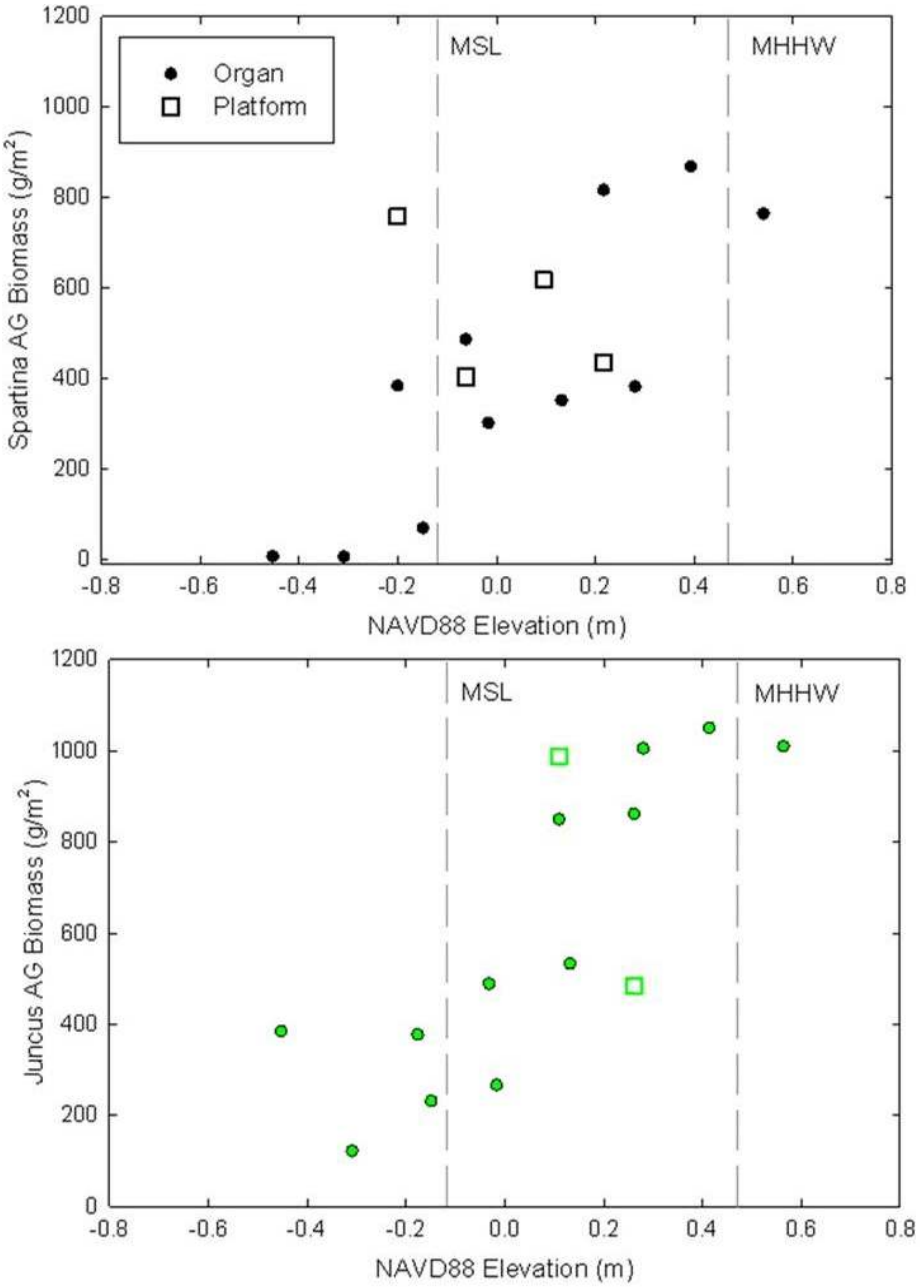

Figure 11. Aboveground biomass as a function of elevation for *Spartina alterniflora* (black) and *Juncus roemerianus* (green) at PKS.

however, the observed record establishes that water depths reached 0.8 m and minimum values of -0.4 m. That is, the observed water record suggests that water depths are higher and lower, likely due to the wind stressing the water surface, which will affect the duration that a particular elevation is inundated. These durations of inundation are applied to the *Spartina* and *Juncus* biomass measurements at PKS. *Spartina* above-ground biomass from the marsh organs at PKS is greatest from 0.30 to 0.40 m (Fig. 11), which corresponds to 0% inundation time following the purely tidal record, and 5 to 15% cumulative inundation for the observed record (Fig. 12). *Juncus* above-ground biomass is greatest at 0.4 and 0.5 m, the two highest organ elevations, with cumulative inundation ranging from 1 to 3% from the observed record and 0% flooding time for the predicted record.

Much work has focused on *Spartina* to determine conditions for the greatest productivity and the factors contributing to the zonation between *Spartina* and *Juncus* [*Delaune et al*., 1987; *Delaune et al*., 1990]. Plant productivity at PKS is compared here with the cumulative inundation time and average continuous wet-to-dry ratio for a given elevation. The average continuous wet-to-dry ratio is calculated from the 13-month observed record. *Spartina* has the greatest biomass when wet for durations of 3 to 4 hours at a time, and elevations that are dry for extremely short periods of time have the lowest biomass (Fig. 13). Elevations corresponding to sustained wet periods of 3 to 4 hours range from 0.22 to 0.39 m. Results are likely biased since the marsh organs from this experiment were installed at low elevations relative to mean sea level (< -0.19 m) and exposed to wave activity. Elevations less than -0.19 m were subject to greater average sustained wetting periods (from

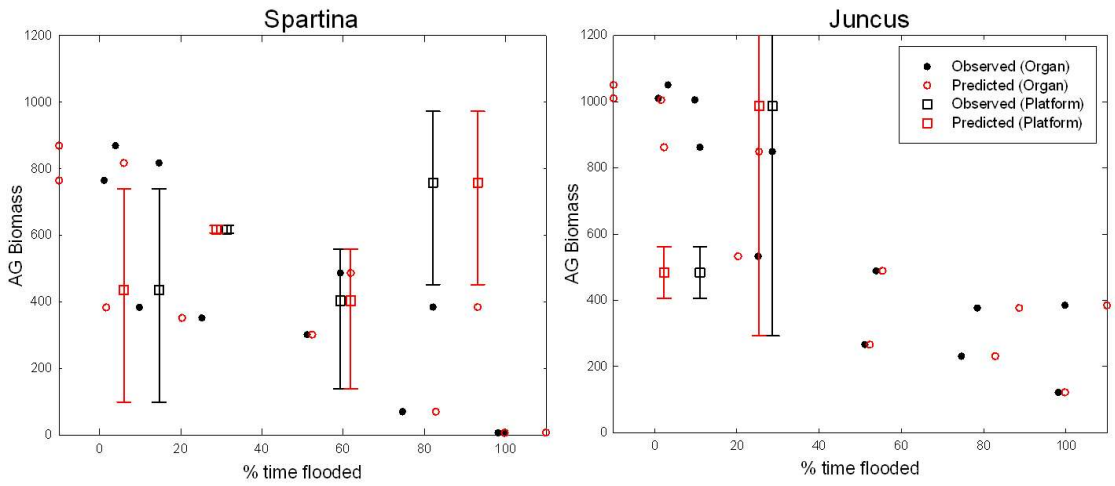

Figure 12. Observed and predicted cumulative time flooded for measured aboveground biomass at PKS.

20 to 100 hours) with 2 hours of average dry periods. Above-ground biomass from marsh organs and the platform verify a decrease in *Juncus* above-ground productivity with greater cumulative inundation time during the study period (Fig.12). Juncus productivity increases with shorter sustained wetting periods and long sustained dry periods. The two highest marsh organ elevations, 0.41 m and 0.56 m, were both subject to 2.8 hrs of sustained wetting, yet sustained dry periods increased from an average of 143 hrs to 500 hrs with increasing elevations. The elevation range where *Juncus* inhabits the vegetated marsh platform, from 0.11 to 0.26 m, is narrower than the organs. This may be due to the fact that the marsh organs reveal the "fundamental" distribution while the marsh landscape gives the realized distribution (resulting from factors such as accretion, interspecific competition, etc.). Nonetheless, *Spartina* productivity, stem density, and stem height have been previously shown to vary as a parabolic function of marsh surface elevation [*Morris et al., 2002*]. At low elevations where anoxic conditions exist, aerobic root respiration and root alcohol fermentation become the primary energy source, and lower productivity results from limited

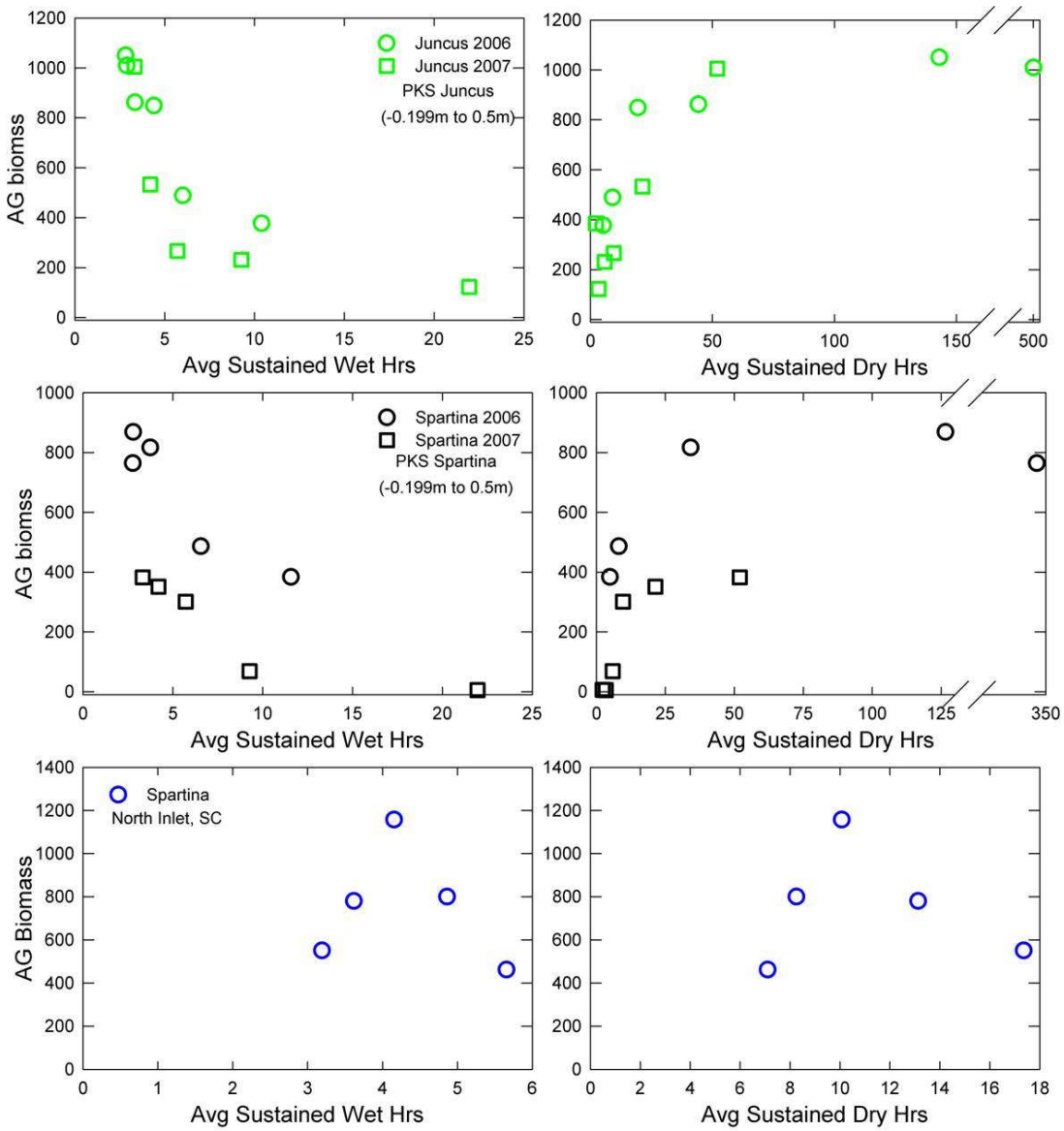

Figure 13. Average calculated sustained durations of wet and dry periods for *Spartina* and *Juncus* at PKS as well as *Spartina* at North Inlet, SC (*bottom*). PKS *Spartina* plot excludes elevations less than -0.19 m, which were subject to inundation greater than 12 hours on average.

nutrient uptake during hypoxic conditions [*Bradley and Morris*, 1990*; Morris and Dacey*, 1984]. Competition at higher elevation likely results from osmotic and salt stress.

We turn to recent field studies by *Scott* [2010] based on marsh platform studies at North Inlet-Winyah Bay, South Carolina, as an additional field site to apply this inundation-productivity model. *Scott* [2010] reports *Spartina alterniflora* demographics at elevations ranging from 0.18 to 0.54 m relative to NAVD88, where elevations are based on LiDAR. Water level data from the Oyster Landing station located at North Inlet, South Carolina, were obtained for January 2009 to January 2010. Similar to PKS, North Inlet water input to the estuary is through one main inlet and is semi-diurnal. Mean tidal amplitudes at this site reach 1.4 m, and MHW and MHHW are 0.72 m and 1.07 m, respectively. The total aboveground *S. alterniflora* biomass ranged from 0 to 2381.12 gm^2, compared to the 0 to 500 gm^2 biomass measured at PKS [*Chapter 6; Voss*, 2010]. *Spartina* aboveground biomass is fit to the marsh elevation using a parabolic function, predicting maximum standing biomass at 0.35 m NAVD88; observed maximum stem density and stem height occur at 0.40 m NAVD88. Cumulative inundation times for 2009 at this site are 30% and 20% at 0.35 m and 0.40 m, respectively. Events of sustained wet and dry marsh surface for the one year period were averaged for a given elevation on the marsh platform ranging from 0.15 m to 0.55 m. Aboveground biomass and average sustained wet and dry events vary parabolically (Fig. 13). The "optimal" elevation for *Spartina* at this site is subject to 4 hours of sustained wet hours and approximately 10 hours of sustained dry periods.

5. Discussion and Conclusions

Tidal predictions based on harmonic analysis have many applications; this study uses harmonic analysis of wind and astronomical water records in order to relate inundation and marsh platform productivity. Given the subjective nature of determining tidal constituents needed for a site as well as the filtering of non-tidal signals, recent approaches attempt to resolve harmonic constituents with weighting functions [*e.g. Leffler and Jay*, 2009]. This approach reduces the influence of large residuals and, therefore, non-tidal variation in the tidal record. To understand how coastal environments will respond to sea-level rise and the relationship between biomass and inundation, we suggest that it is necessary to include the modulated water surface within an estuary due to storm and wind influences. In shallow estuaries such as PKS, wind-influenced water movement drives hourly to daily water level variability [*Reed et al.*, 2008]. Longer scale periodicities in water level and wind are related to seasonality, including the influence of thermal expansion. Precipitation may also contribute to seasonal water level variability, where for example, at PKS, one-third of the annual average 139.7 cm of rain falls during July, August, and September, with measurable precipitation on 4 to 7 days per month.

Our harmonic analysis reveals the primary astronomical signals at PKS, including the M_2, K_2, N_2, K_1, and O_1. The North-South wind influence at PKS is close to the K_2 and K_1 frequencies, and both North-South and East-West spectrums reveal low frequency influence. The PKS site is shown to be dominated by two tidal constituents, the M_2 and K_1 signals. We illustrate a plausible model for the low-frequency portion of the water level signal that arises

from movement of water into and out of the estuary. The gain function illustrates the correlation between water level change and wind, where water level is driven by the wind.

Analysis of the observed and predicted water record suggests that macrophyte primary productivity cannot be related to simply DMHW when water level is predicted using only the astronomical signal. Macrophyte biomass is a function of the frequency and timing of flooding rather than the mean water level for a given elevation. We suggest that— because the astronomical signal is dominated by only two primary constituents, and because the low-frequency part of the water-level spectrum does not exhibit any clear peaks or apparent relation to the astronomical signal— this part of the spectrum more likely reflects fluctuations in water level within the estuary associated with wind and storm events that move water into and out of the estuary over timescales longer than the semi-diurnal and diurnal signals. These low-frequency variations in the water level constitute a significant part of the total variance of the observed record, the effect of which is to set the average water level about which the astronomical signals fluctuate. This is further illustrated with observed macrophyte biomass, platform elevation, and water records. *Spartina alterniflora* biomass from North Carolina and South Carolina is greatest at 0.3 to 0.4 m elevation relative to NAVD88, which according to the predicted exceedence probability is wet for less than 2% of the annual record. The observed record, however, suggests inundation durations of 15 to 30% of the annual time period. The predicted water levels based on the astronomical signal suggest that macrophytes are subject to wet and dry periods contrary to their known habitat zones. The continuous wet to dry ratios over an annual water record further constrain the favorable conditions for macrophyte productivity.

6. Notation

a_0, b_0 constituent for Cholesky matrix, sum of the observed period
a_1, b_1 constituent of Cholesky matrix, sum of the predicted values for a given period
A area
C [$L^{1/2}$ t^{-1}] Chézy coefficient
f frequency
G theoretical gain
h depth
H impulse response function
L length
Q discharge
R amplitude
s sum of the square deviations
S water-surface slope
t time
T period
τ time lag
u width-depth-averaged flow velocity
w width
z predicted signal
$\hat{z}$ observed signal

γ water level (large water body)
ϕ phase
ζ water level (estuary)

7. References

Blanton, J.O, J. Amft, R.A. Luettich, J.L. Hench, and J.H. Churchill (1999), Tidal and subtidal fluctuations in temperature, salinity and pressure for the winter 1996 larval ingress experiment, Beaufort, NC, *Fish. Oceanogr. 9:2*, 134-152.

Bradley, P.M. and J.T. Morris, (1990), Influence of oxygen and sulfide concentration on nitrogen uptake kinetics in Spartina alterniflora, *Ecology, 71*, 282-287.

Cahoon, D. R., P.F. Hensel, T. Spencer, D.J. Reed, K.L. McKee, N. Saintilan (2006), Coastal wetland vulnerability to relative sea-level rise: wetland elevation trends and process controls, in *Wetlands and Natural Resource Management*, edited by T.A. Verhoeven, B. Beltman, R. Bobbink, D.F. Whigham, pp 271-292, Springer, Berlin.

Churchill, J.H., J.O. Blanton, J.L. Hench, and F.E. Werner (1999), Flood tide circulation near Beaufort Inlet, North Carolina: implications for larval recruitment, *Estuaries, 22:4*, 1057-1070.

Cox, D.T., P. Tissot, and P. Michaud (2002), Water Level Observations and Short-Term Predictions Including Meteorological Events for Entrance of Galveston Bay, Texas, *Journal of Waterway, Port, Coastal and Ocean Engineering 128:1*, 21-29.

DeLaune, R.D., S.R. Pezeshki, and W.H. Patrick (1987), Response of coastal plants to increase in submergence and salinity, *Journal of Coastal Research, 3,* 535-546.

DeLaune, R.D., S.R. Pezeshki, J.H. Pardue, J.H. Whitcomb, and W.H. Patrick (1990), Some influences of sediment addition to a deteriorating salt marsh in the Mississippi River Deltaic Plain: A pilot study, *Journal of Coastal Research, 6*, 181-188.

Doodson, A.T. (1921), The harmonic development of the tide-generating potential, *Proc. Roy. Soc. Series A, 100*, 306-323, Re-issued in the *International Hydrographic Review*, May 1954.

Fagherazzi, S., and D.J. Furbish (2001), On the shape and widening of salt marsh creeks, *Journal of Geophysical Research 106:C1*, 991-1003.

Godin, G. (1972), *The Analysis of Tides*, University of Toronto Press.

Jenkins, G., and D. Watts (1968), *Spectral Analysis and Its Applications*, New York, Holden-Day.

Kirwan, M.L., G. R. Guntenspergen, A. D'Alpaos, J.T. Morris, S.M. Mudd, S. Temmerman (2010), Limits on the adaptability of coastal marshes to rising sea level, *Geophysical Research Letters, 37*, L23401, DOI:10.1029/2010gl045489.

Leffler, K.E. and D.A. Jay (2008), Enhancing tidal harmonic analysis: Robust (hybrid L^1/L^2) solutions, *Continental Shelf Research*, doi: 10.1016 /j.csr.2008.04.011.

Luettich Jr, R.A., S.D. Carr, J.V. Reynolds-Fleming, C.W. Fulcher, and J.E. McNinch (2002), Semi-diurnal seiching in a shallow, micro-tidal lagoonal estuary, *Continental Shelf Research, 22,* 1669-1681.

Morris, J.T., P.V. Sundareshwar, C.T. Nietch, B. Kjerfve, D.R. Cahoon (2002), Responses of coastal wetlands to rising sea level, *Ecology, 83*, 2869-2877.

Morris, J.T. (2007), Estimating net primary production of salt-marsh macrophytes, in *Principles and Standards for Measuring Primary Production*, edited by T.J. Fahey, and A.K Knapp, Oxford University Press, pp. 106-199.

Morris, J.T. and J. Dacey (1984), Effects of O2 on ammonium uptake and root respiration by Spartina alterniflora, *Amer. J. Bot., 71*, 979-985.

Mudd, S.M., S. Fagherazzi, J.T. Morris, and D.J. Furbish (2004), Flow, sedimentation, and biomass production on a vegetated salt marsh in South Carolina: Toward a predictive model of marsh morphologic and ecologic evolution, in *the Ecogeomorphology of Tidal Marshes, Coastal Estuarine Stud.*, vol. 59, edited by S Fagherazzi, M. Marani, and L.K. Blum, pp. 165-187, AGU, Washington, D.C.

National Oceanic and Atmospheric Administration, (2010), Tides and Currents, www.tidesandcurrents.noaa.gov.

Pasternack, G.B., and L.A. Hinnov (2003), Hydrometeorological controls on water level in a vegetated Chesapeake Bay tidal freshwater delta, *Estuarine, Coastal and Shelf Sciences, 58*, 367-387.

Pawlowicz, R., B. Beardsley, and S. Lentz (2002), Classical tidal harmonic analysis including error estimates in MATLAB using T_TIDE, *Computers & Geosciences, 28*, 929-937.

Reed, R.E., D.A. Dickey, J.M. Burkholder, C.A. Kinder, and C. Brownie (2008), Water level variations in the Neuse and Pamlico Estuaries, North Carolina due to local and remote forcing, *Estuarine, Coastal and Shelf Science, 76*, 431-446.

Reynolds-Felmeing, J.V., and R.A. Luettich (2004), Wind-driven lateral variability in a partially mixed estuary, *Estuarine, Coastal, and Shelf Science, 60*, 395-407.

Scott, S.M. (2010), Spartina Alterniflora Productivity and Salt Marsh Stability Relative to Marsh Platform Elevation, *Theses and Dissertations*, Paper 402, University of South Carolina.

State Climate Office of North Carolina: NC CRONOS Database (2010), Climate Retrieval and Observations Network of the Southeast Database, www.nc-climate.ncsu.edu/cronos.

Voss, C. (2010), Responses of dominant marsh macrophytes to inundation and disturbance and assessing marsh ecosystem services, *PhD Dissertation*, East Carolina University.

Wilsey, B.K. McKee, and I. Mendelssohn, (1992), Effects of increased elevation and macro- and micronutrient additions Spartina alterniflora transplant success in salt-marsh dieback areas in Louisiana, *Environmental Management 16*: 505-511.

CHAPTER V

CARBON I: IMPACT OF DYNAMIC FEEDBACKS BETWEEN SEDIMENTATION, SEA-LEVEL RISE, AND BIOMASS PRODUCTION ON NEAR-SURFACE MARSH STRATIGRAPHY AND CARBON ACCUMULATION

Published as: Mudd, S.M., S.M. Howell, and J.T. Morris (2009), Impact of dynamic feedbacks between sedimentation, sea-level rise, and biomass production on near-surface marsh stratigraphy and carbon accumulation, *Estuarine, Coastal and Shelf Science*, 82(3):377-389, doi:10.1016/j.ecss.2009.01.028.

Abstract

Salt marshes accrete both organic and inorganic sediments. Here we present analytical and numerical models of salt marsh sedimentation that, in addition to capturing inorganic processes, explicitly account for above- and belowground organic processes including root growth and decay of organic carbon. The analytical model is used to examine the bias introduced by organic processes into proxy records of sedimentation, namely ^{137}Cs and ^{210}Pb. We find that accretion rates estimated using ^{210}Pb will be less than accretion rates estimated using the ^{137}Cs peak in steadily accreting marshes if (1) carbon decay is significant and (2) data for ^{210}Pb extend below the ^{137}Cs peak. The numerical model expands upon the analytical model by including belowground processes such as compaction and root growth, and by explicitly tracking the evolution of aboveground biomass and its effect on sedimentation rates. Using the numerical model we explore how marsh stratigraphy responds to sediment supply and the rate of sea-level rise. It is calibrated and tested using an extensive data set of

both marsh stratigraphy and measurements of vegetation dynamics in a *Spartina alterniflora* marsh in South Carolina, USA. We find that carbon accumulation in marshes in nonlinearly related to both the supply of inorganic sediment and the rate of sea-level rise; carbon accumulation increases with sea-level rise until sea-level rise reaches a critical rate that drowns the marsh vegetation and halts carbon accumulation. The model predicts that changes in carbon storage resulting from changing sediment supply or sea-level rise are strongly dependent on the background sediment supply: if inorganic sediment supply is reduced in an already sediment poor marsh the storage of organic carbon will increase to a far greater extent than in a sediment-rich marsh, provided that the rate of sea-level rise does not exceed a threshold. These results imply that altering sediment supply to estuaries (*e.g.*, by damming upstream rivers or altering littoral sediment transport) could lead to significant changes in the carbon budgets of coastal salt marshes.

1. Introduction

Salt marsh ecosystems play a vital role in the dissipation of wave energy, accretion of sediment, filtration of nutrients, and as habitats for commercially important fisheries. Global eustatic sea-level over the past 100 years is estimated to have risen at a rate of 1-2 mm yr^{-1}, yet rates over the period of 1993-2002 are greater than the global average [*Holgate and Woodworth*, 2004]. Early studies of salt marsh accretion recognized positive feedbacks between inorganic sedimentation and marsh accretion [*e.g., Krone*, 1987; *French*, 1993; *Allen*, 1995]. For example, increasing the rate of sea-level rise will increase the duration of

inundation on the marsh, thus increasing sedimentation due to settling of inorganic sediment. In contrast, reduced rates of sea-level rise will result in decreased inundation and decreased sedimentation. It has been long recognized that many marshes are able to keep pace with sea-level rise [*Friedrichs and Perry*, 2001], and that ability depends on the complex interplay between marsh hydrodynamics, vegetation, and sedimentation. In addition, many authors have found that marsh vegetation is most productive at an optimum elevation relative to sea level [*e.g., Redfield*, 1972; *Orson et al*., 1985]. *Morris et al*. [2002] found that current rates of sea-level rise in South Carolina, USA will eventually result in drowning of local *Spartina* marshes. This finding underlines the need to better understand the relationship between vegetation, sedimentation, and sea-level rise.

A number of modeling studies have incorporated the feedbacks between vegetation, sedimentation and sea-level rise [*e.g., Mudd et al*., 2004; *D;Alpaos et al*., 2007; *Kirwan and Murray*, 2007], but these models have yet to incorporate sediment compaction and belowground biomass production. It is becoming clear, however, that belowground biomass production plays a key role in maintaining marsh surface elevations [*e.g., Nyman et al*., 2006; *Mckee et al*., 2007; *Neubauer*, 2008]. In addition, while inorganic sediments are relatively incompressible over time, this is not the case for organic sediment: in some marshes the volume of void spaces and water associated with organic material is 90% [*Turner et al*., 2001]. Early diagenetic models [*e.g. Westrich and Berner*, 1984] addressed decomposition of organic sediments but lacked descriptions of other processes such as root growth and compaction. The next generation of models quantified different suites of belowground processes [*Morris and Bowden*, 1986; *Rybczyk et al*., 1998; *Day et al*., 1999; *Rybczyk and*

Cahoon, 2002], but these models have not included the explicit feedbacks between sedimentation, sea level, and biomass dynamics first reported by *Morris et al*. [2002].

In addition to influencing marsh accretion rates, organic sedimentation allows marshes to serve as carbon sinks [*e.g., Chmura et al*., 2003]. The peraquaic moisture regime and prevalence of anaerobic decomposers in coastal marsh ecosystems reduce the efficiency of organic matter decomposition and promote the sequestration of carbon [*Hussein et al*., 2004]. Finally, carbon decay can influence the interpretation of two radioisotopes commonly used in dating of marsh sediments: ^{210}Pb and ^{137}Cs [*Appleby and Oldfield*, 1992]. *Turner et al*. [2006] observed differences between accretion rates from ^{210}Pb and ^{137}Cs and hypothesized that these differences could be the result of organic matter compaction or decomposition. Despite the importance of organic decomposition in making estimates of accretion rates using ^{210}Pb and ^{137}Cs, which are frequently used to estimate marsh accretion on decadal scales, there has been no study that combines an explicit representation of belowground processes such as organic decay and root growth, and their dependence on aboveground processes, with radioisotope deposition. This study addresses this important issue.

Here we present two models to understand both the influence of organic deposition on the interpretation of dating methods and also to examine the relative balance and feedbacks between organic versus inorganic sedimentation on coastal salt marshes. These two models are the first to couple the feedback between biomass production, sedimentation and sea-level rise first outlined by *Morris et al*. [2002] with an explicit representation of belowground processes. The resulting models allow us to predict sediment characteristics as

a function of depth on a salt marsh. We have specifically designed the models to predict characteristics that are likely to be measured in the field, *e.g.* carbon content, porosity, and the concentration of radioisotopes. The first model is a simplified analytic model that captures some essential features of marsh sedimentation. The second model is a numerical model that can account for sediment compaction, depth-dependent root growth, feedbacks between biomass and sedimentation, and belowground decay of organic carbon. This numerical model, which is tested using data from a well-studies site on the Atlantic coast of the United States, is used to examine fundamental relationships between carbon accumulation and storage as they are affected by changes in sea-level rise and changing sediment supplies. We call these models OIMAS-A and OIMAS-N (Organic-Inorganic Marsh Accretion and Stratigraphy-Analytical and Numerical, respectively).

2. OIMAS-A: a simplified analytical model

In this section we construct a mathematical model (OIMAS-A) that is highly simplified yet can be used to illustrate some of the essential features of the competition between organic and inorganic sedimentation on salt marshes. Organic sediment consists of refractory (it does not decay) and labile (it does decay) fractions. In the OIMAS-A model we consider a situation in which the decay rate of labile organic matter does not depend on its depth below the marsh surface. Although labile carbon is present near the surface, and contributes to the carbon storage in the marsh sediment, it does not contribute to marsh accretion or carbon sequestration because any labile carbon deposited decays from the system

after a given amount of time (by definition).

Numerous authors have documented a series of feedbacks that allow salt marshes under a range of conditions to keep pace with sea-level rise [*e.g., Pethick*, 1981; *Krone*, 1987; *Chmura et al*., 1992; *French*, 1993; *Allen*, 1995; *Morris et al*., 2002]. Here we consider a point on the marsh surface that is in an equilibrium situation in which the rate of sea-level rise (*RSLR*, dimensions LT^{-1}, dimensions henceforth reported in [M]ass, [L]ength and [T]ime in square brackets) is matched by marsh accretion:

$$RSLR = \frac{1}{\phi}\left(\frac{R_{ref}}{\rho_0} + \frac{R_s}{\rho_s} \right) \tag{1}$$

where ϕ [dimensionless] is the porosity of the marsh sediment at a depth below which porosity does not change, ρ_o [ML^{-3}] is the density of organic material, ρ_s [ML^{-3}] is the density of the inorganic material, R_{ref} [$MT^{-1}L^{-2}$] is the mass supply rate per unit area of refractory organic matter, and R_s [$MT^{-1}L^{-2}$] is the mass supply rate per unit area of inorganic sedimentation. These mass supply rates are net supply rates (i.e. deposition minus erosion).

2.1 Accumulation and storage of organic and inorganic mass

Simple rearrangement of Eq. (1) shows that in the equilibrium situation any decrease in the supply of inorganic sediment must be compensated by an increase in refractory organic matter:

$$R_{ref} = \rho_0 \phi RSLR - R_s \frac{\rho_0}{\rho_s} \tag{2}$$

In general, organic matter is thought to exist in a number of pools [*e.g., Baisden and Amundson*, 2003; *Jenkinson and Coleman*, 2008] with different decay rates; we account for a 'fast' and 'slow' and refractory pool of organic matter in the OIMAS-A model. The total mass supply rate per unit area at which organic material is added to the marsh (R_{org}) is:

$$R_{org} = R_{ref} + R_{lsl} + R_{lfa} , \tag{3}$$

where the subscripts lsl and lfa represent slow labile and fast labile pools, respectively. Suppose that the relative proportions of refractory and labile organic matter in organic sediment are constant such that:

$$R_{lsl} = R_{org}\chi_{lsl} , \tag{4a}$$

$$R_{lfa} = R_{org}\chi_{lfa} , \tag{4b}$$

$$R_{ref} = R_{org}\left(1 - \chi_{lsl} - \chi_{lfa}\right) = R_{org}\chi_{ref} , \tag{4c}$$

where χ_{lsl} [dimensionless] is the fraction of deposited organic matter that goes into the slow labile pool, χ_{lfa} [dimensionless] is the fraction of deposited organic mater that goes into the fast labile pool, and χ_{ref} [dimensionless] is the fraction of deposited organic matter that goes into the refractory pool. The total supply of mass to the marsh surface per unit area, R_{tot} [$MT^{-1}L^{-2}$], is $R_s + R_{org}$. When marsh accretion keeps pace with sea-level rise, this is equal to:

$$R_{tot} = R_s + \frac{R_{ref}}{\chi_{ref}} = R_s + \frac{1}{\chi_{ref}}\left(\rho_o \phi RSLR - R_s \frac{\rho_o}{\rho_s}\right) . \tag{5}$$

Although the labile fractions do not contribute to carbon sequestration (due to decay), there is some finite amount of labile organic matter stored in the marsh column. The mass of labile organic matter above a layer deposited at time *T* before present is:

$$M_{lsl} = \int_0^T R_{lsl} e^{-k_{lsl} t}\, dt = \frac{\chi_{lsl} R_{ref}}{\chi_{ref} k_{lsl}} \left(1 - e^{-k_{lsl} T}\right), \tag{6}$$

where k_{lsl} [dimension T^{-1}] is the decay coefficient of the slow labile organic matter. We omit the equation for fast labile organic matter because it takes the same form as (6). As T becomes large (*e.g.*, $T \gg 1/k_{lsl}$), the exponential term in (6) goes to zero and we find that the labile organic matter stored in the marsh column is linearly proportional to the rate of mass accumulation of refractory organic material. We can similarly find the total sediment above a layer deposited at time T:

$$\begin{aligned} M_{tot} &= \int_0^T R_s + R_{ref} + R_{lfa} e^{-k_{lfa} t} + R_{lsl} e^{-k_{lsl} t}\, dt \\ &= R_s T + \left(RSLR - \frac{R_s}{\rho_s \phi} \right) \left[T + \frac{\chi_{lfa}}{\chi_{ref} k_{lfa}} \left(1 - e^{-k_{lfa} T}\right) + \frac{\chi_{lsl}}{\chi_{ref} k_{lsl}} \left(1 - e^{-k_{lsl} T}\right) \right] \end{aligned} \tag{7}$$

Eq. (7) may be used in conjunction with the density and porosity of the respective sediments to find the depth, d [dimensions L], of a layer of age T:

$$d = \frac{R_s T}{\rho_s \phi} + \left(RSLR - \frac{R_s}{\rho_s \phi} \right) \left(T + \frac{\chi_{lsl} \left[1 - e^{-k_{lsl} T}\right]}{k_{lsl} \chi_{ref}} + \frac{\chi_{lfa} \left[1 - e^{-k_{lfa} T}\right]}{k_{lfa} \chi_{ref}} \right). \tag{8}$$

If there is no decomposition of carbon and the marsh is steadily accreting, the relationship between depth and age is linear. This relationship is more complex in near-surface sediments where labile material is still present; the presence of this labile material may convolute the interpretation of marsh accretion rates using fallout radioisotopes, as we shall demonstrate below.

2.2 Interpretation of accretion rates

The use of ^{210}Pb and ^{137}Cs has become widespread in the analysis of marsh sedimentation, and we can use the OIMAS-A model to illustrate the biases of these methods under the idealized conditions of the model. If the radioisotopes ^{210}Pb and ^{137}Cs are used to determine accretion rates, a number of factors can lead to uncertainty in the results. The OIMAS-A model can illustrate the effects of two of these factors, namely the enrichment of the radioisotopes due to loss of organic matter and the nonlinear relationship between depth in the marsh column and age of the sediments at a given depth, also caused by organic decay. We neglect the effects of autocompaction; this added complexity is later introduced into the OIMAS-N model.

Two scenarios are often considered for the deposition of ^{210}Pb [*e.g. Appleby and Oldfield*, 1992]: the constant initial concentration (CIC) scenario, wherein sediment bing deposited on the surface of the marsh contains a constant concentration of ^{210}Pb, and the constant rate of supply (CRS), wherein ^{210}Pb is deposited at some fixed rate such that its concentration in surface sediments is inversely proportional to the accretion rate. For the simple steady-state accretion scenarios investigated in this section, these two scenarios of ^{210}Pb deposition yield the same results.

The concentration of lead that remains in the marsh column after some time T is enriched due to the decay of organic sediment. Following *Appleby and Oldfield* [1992], we define an enrichment factor, η, that can be determined for a given time after deposition as

$$\eta = \frac{RSLR\,\phi\,\rho_0\,\rho_s - R_s\left(\rho_0 - \rho_s\,\chi_{ref}\right)}{R_s\rho_s\chi_{ref} + \rho_0\left(\rho_s\phi\,RSLR - R_s\right)\left(\chi_{ref} + \chi_{lsl}\,e^{-k_{lsl}T} + \chi_{lfa}\,e^{-k_{lfa}}\right)} \tag{9}$$

For a given supply of ^{210}Pb, one can calculate the age of a sediment using the relationship $T_{app} = -\ln(C/C_0)/\kappa$, where κ [dimensions T^{-1}] is the ^{210}Pb decay constant. This age, however, is an apparent age because it does not account for enrichment of the sediment due to organic decay. The ratio of the true age of a sediment layer and the apparent age is:

$$\frac{T_{app}}{T} = 1 - \frac{\ln(\eta)}{T\kappa} . \quad (10)$$

Thus, a layer dated by comparing its excess ^{210}Pb content with the excess ^{210}Pb concentration of a surface layer will be older than its apparent age.

In contrast to ^{210}Pb, dating of layers using ^{137}Cs is performed by identifying a peak in the ^{137}Cs concentration. It is typically assumed that the peak ^{137}Cs concentration represents approximately the year 1963, so the apparent accretion rate would be the depth of the layer deposited in 1963 divided by the time since the year 1963. If the age of the layer were calculated using ^{210}Pb, the apparent age would be less than the true age so the apparent accretion rate as measured by ^{210}Pb will always be greater than the accretion rate measured by ^{137}Cs. This is the opposite of the trend found by *Turner et al.* [2006], who compiled a large number of studies that estimated marsh accretion using ^{210}Pb and ^{137}Cs. Accretion rates determined by ^{210}Pb, are not, however, typically calculated by dividing the depth of a layer by its apparent time of deposition; rather ^{210}Pb accretion rates are generally determined by the slope of the relationship between the logarithm of the ^{210}Pb activity and depth [*e.g., Lynch et al.*, 1989; *Orson et al.*, 1998; *Anisfeld et al.*, 1999; *Donnelly and Bertness*, 2001; *Turner et al.*, 2006]. Thus, organic decay affects the accretion rate as estimated by ^{210}Pb not only by

enriching the concentration of ^{210}Pb in a given layer, as described by *Appleby and Oldfield* [1992], but also by influencing a layer's depth below the surface as a function of its age (i.e., Eq. (8)).

The decay of carbon, through both of the above mechanisms, leads to overestimation of the accretion rate when using ^{210}Pb and ^{137}Cs. Because the rate of carbon loss is greatest near the surface, the overestimation of accretion rates using the two radioisotopes is most severe near the surface. We demonstrate the effect of decomposition by plotting the logarithm of ^{210}Pb concentration in an idealized core that contains labile carbon (Fig. 1). The accretion rate on the marshes shown in Fig. 1 is 2.5 mm yr^{-1}, whereas the accretion rates estimated from the predicted profiles (each representing 150 years of deposition) range from

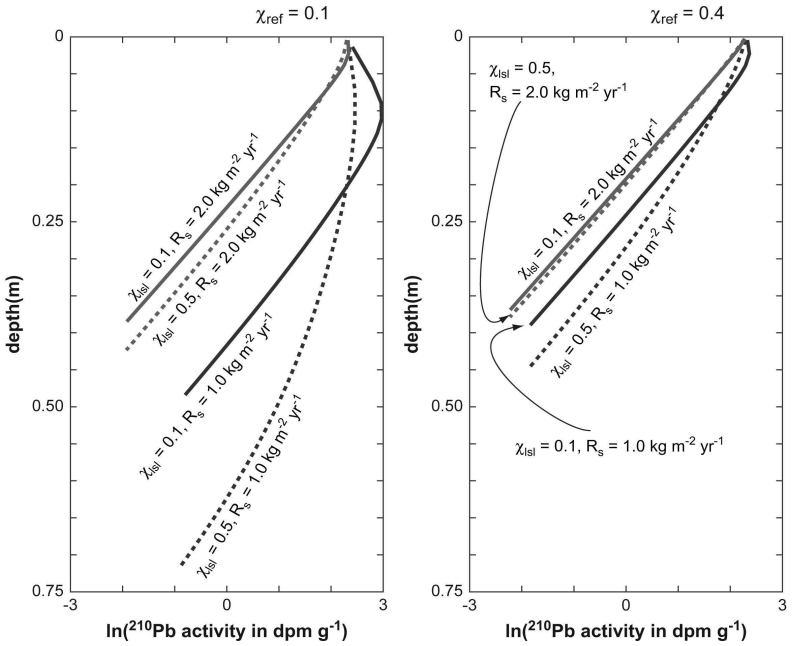

Figure 1. Activity plots of ^{210}Pb in a marsh accreting at 2.5 mm yr^{-1} for different rates of inorganic sediment supply and different proportions of deposited labile carbon. The decay constant for the fast labile pool is 0.2 yr^{-1}, based on the measurements of *Conn and Day* [1997]. The slow labile pool is set an order of magnitude slower than the fast labile pool for simplicity. Parameter values not shown on plot are selected to be typical of marsh sediments: ϕ=0.4, ρ_0=1200/kgm^3, ρ_s=2200 kg/m^3.

2.53 mm yr^{-1} (for R_s=2.0 kg $m^{-2}yr^{-1}$, χ_{ref}=0.4, and χ_{lsl}=0.1) to 6.16 mm yr^{-1} (for R_s=1.0 kg $m^{-2}yr^{-1}$, χ_{ref}=0.1, and χ_{lsl}=0.5). In extreme cases the concentration of ^{210}Pb will increase with depth near the surface, this is because the decay of organic carbon outpaces the decay of ^{210}Pb near the surface of the marsh. Deeper in the column the decrease in ^{210}Pb activity with depth better represents the true accretion rate because much of the labile carbon has been removed via decay.

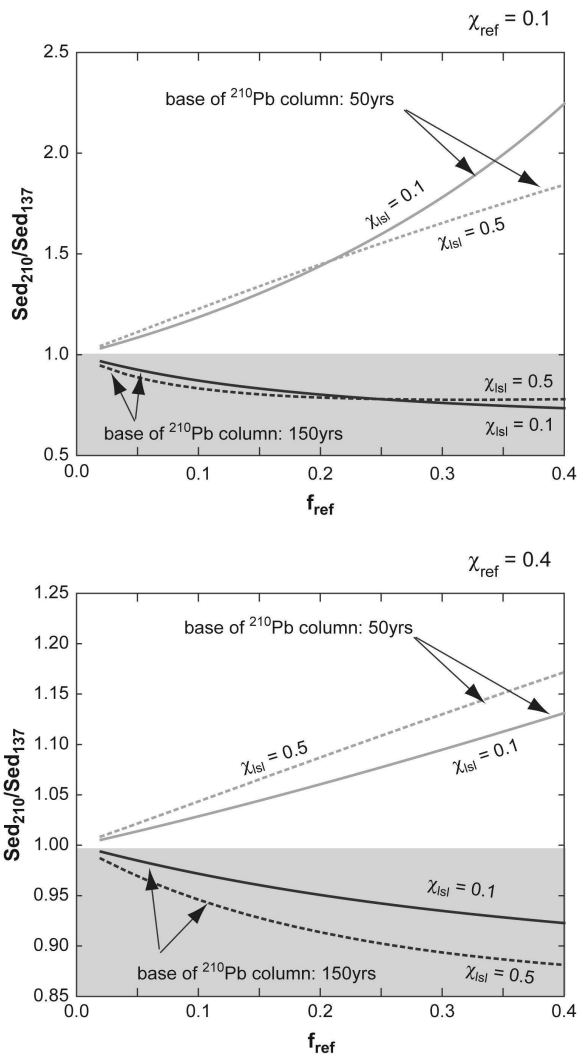

Figure 2. The ratio between the accretion rate estimated by ^{210}Pb (Sed_{210}) and by ^{137}Cs (Sed_{137}) as a function of the fraction of the deep sediments that are refractory carbon (i.e., $f_{ref}=R_{ref}/(R_{ref}+R_s)$). The ^{137}Cs peak is 45 years old in these columns, and ^{210}Pb accretion rate is estimated by regression of the ^{210}Pb activities using sediment representing 50 and 150 years of sedimentation. Parameter values are the same as in Fig. 1 unless noted in the plot. The grey region demarcates where $Sed_{210}/Sed_{137}<1$.

An important implication of the effect of organic decay on radioisotope decay profiles is that if the marsh core sampled for ^{210}Pb data extend below the ^{137}Cs peak, then the accretion rate estimated by ^{137}Cs will be greater than that estimated using ^{210}Pb (Fig. 2). This is the case for nearly all of the cores compiled by *Turner et al*. [2006]. The reason for this bias in most cases is that ^{210}Pb can be measured in sediments up to ~ 150 years in age [*e.g., Appleby and Oldfield*, 1992], whereas the ^{137}Cs peak is much younger and the sediment above the peak has yet to fully undergo organic matter decomposition and attendant loss of

volume near the surface. These results do not necessarily mean that the trends in the data compiled by *Turner et al*. [2006] are due solely to decomposition; the studies cited by *Turner et al*.[2006] were in marshes that may not adhere to the strict assumptions of the OIMAS-A model. Nonetheless, the results presented here show that a discrepancy in accretion rates determined by the two radioisotopes do not necessarily indicate a change in accretion rate; indeed such discrepancies can occur in steadily accreting marshes. Interestingly the ratio between accretion rates estimated by the two isotopes predicted by the OIMAS-A model is independent of the rate of sea-level rise. Instead the ratio in apparent accretion rates is most sensitive to both the percent of refractory carbon and the relative proportions of labile carbon in the depositing sediment (Fig. 2).

3. OIMAS-N: the numerical model

Although the OIMAS-A model can yield insights into the basic feedbacks between organic and inorganic sedimentation, and the effects of decomposition on the estimation of marsh accretion rates, it contains by necessity restrictive assumptions. Relaxing these assumptions precludes analytical solution of the governing equations, and we have therefore constructed a more flexible numerical model that can account for a rich array of evolving salt marshes called OIMAS-N.

The OIMAS-N model simulates the transient evolution of a sediment column situated within a salt marsh. Similar to the OIMAS-A model, this column of sediment may accrete through both organic and inorganic sedimentation. Unlike the OIMAS-A model, the

numerical model includes the additional processes of depth-dependent root growth, plant growth and mortality, and sediment compaction. In addition, the OIMAS-N is fully transient. Organic material is added to the column through growth of belowground biomass and the deposition of litter on the column's surface, and is lost due to decomposition. Inorganic material is added due to particles settling from tidally induced floods, and trapping of particles by salt marsh macrophytes; this sediment is deposited at the surface of the column. Erosion by storms can also be simulated by removing material from the surface of the column. The elevation of the surface changes due to erosion, sedimentation, and compaction, and OIMAS-N tracks the composition of the marsh sediments as a function of depth below the surface.

3.1 Organic component

Live macrophytes on salt marshes produce biomass. This biomass may be deposited both above and below the marsh surface. This material can be lost due to either erosion or decomposition. The amount of organic material that is added to the column at any time is a function of the biomass present on the marsh surface [*e.g., Morris et al.*, 2002; *Nyman et al.*, 2006].

3.1.1 Growth of macrophytes

A number of studies have investigated the relationship between the biomass and the edaphic factors controlling biomass of salt marsh macrophytes. For example, *Valiela et al* [1978] found that fertilization could induce short form *Spartina alterniflora* to grow to

resemble the tall form, and hypothesized that increased nutrient availability near marsh creeks could induce greater biomass on marsh platforms. *King et al*. [982] found that increased sulfide concentrations in marsh interstitial water could inhibit macrophyte growth, and attributed spatial variations in biomass to the flushing frequency of marsh sediment. Both nutrient supply and flushing of sulfides are related to the inundation frequency of a given location on a salt marsh. Using biomass measurements collected on a natural salt marsh, *Morris et al*. [2002] found that biomass of *S. Alterniflora* could be described as a function of the depth below mean high high water (MHHW), which controls inundation frequency and duration (i.e., the hydroperiod). Here we follow the findings of *Morris et al*. [2002] and calculate biomass as a function of depth below MHHW:

$$\begin{aligned} B_p &= 0 \quad D < D_{\min} \\ B_p &= \frac{B_{\max}}{D_{\max} - D_{\min}} \left(D - D_{\min}\right) \quad D_{\min} \le D \le D_{\max}, \\ B_p &= 0 \quad D > D_{\max} \end{aligned} \tag{11}$$

where B_p [dimensions ML^{-2}] is the peak biomass, B_{max} [ML^{-2}] is the biomass at the optimal depth below MHHW, D is the depth of the marsh surface below MHHW, and D_{min} and D_{max} are the minimum and maximum depths below MHHW that define the limits of macrophyte survival. The peak biomass is calculated once per year; the MHHW and depth below MHHW at the time of peak biomass from the previous year are used to determine the current year's peak biomass. This approach assumes a rapid adjustment of biomass to local factors such as the depth below MHHW based on a long-term record of biomass dynamics from the North Inlet Estuary in South Carolina [*Morris and Haskin*, 1990], and this assumption has been shown reasonable for other marshes [*e.g. Marani et al*., 2007].

The aboveground live biomass per unit area, B_{ag} [ML^{-2}], varies through the seasons, peaking in the summer months [*Morris and Haskin*, 1990]. This effect can be approximated by

$$B_{ag} = \frac{1}{2}\left[B_{\min} + B_p + \left(B_p - B_{\min}\right)\cos\left(\frac{2\pi[jd - jd_{ps}]}{365}\right)\right], \tag{12}$$

where B_{ag} is the aboveground biomass [ML^{-2}], jd is the julian day (e.g., Jan 1st = 1, Dec 31st = 365), jd_{ps} is the day of the year when aboveground biomass is at its peak and B_{min} [ML^{-2}] is the minimum aboveground biomass.

Belowground biomass is related to aboveground biomass [*e.g., Darby and Turner*, 2008]. Over 3 years, the ratio between above and belowground biomass was measured using a 'marsh organ' (Fib. 3b) at North Inlet (Fig. 3a); descriptions of the methods and apparatus involved may be found in *Morris* [2007a]. Although the data exhibit a high degree of variability (Fig. 3c), both the mean values of the root:shoot ratio and the extremal values of this ratio decline monotonically with depth over the 3 years of field seasons. We thus approximate the ratio of root:shoot of *Spartina alterniflora* at North Inlet as a linearly decreasing function of the depth below MHHW:

$$\frac{B_{bg}}{B_{ag}} = \theta_{bg} D + D_{mbm}, \tag{13}$$

where θ_{bg} and D_{mbm} are the slope [L^{-1}] and the intercept [dimensionless] of the relationship between the roots:shoots ratio and the depth below MHHW.

We have based Eqs. (11)-(13) on measurements at North Inlet because of the comprehensive nature of the data set available (16 years of monthly standing biomass and

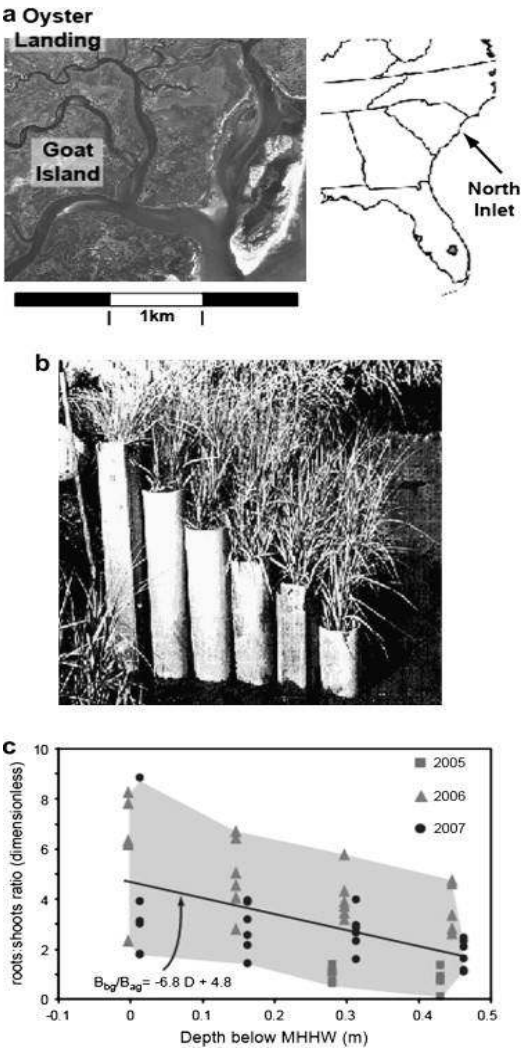

Figure 3. (a) Location map of the North Inlet estuary ad the Goat Island and Oyster Landing within the estuary. (b) Photograph of the 'marsh organ' apparatus. (c) Roots:shoots ratio as a function of depth below MHHW at North Inlet. Data were collected following the methodology of *Morris* [2007a]. Rows of tubes are spaced ~15 vertical centimeters. The small variations in elevation for given rows (*e.g.*, at ~0.3 m depth below MHHW) are due to sea-level rise over the period of data retrieval (the marsh organ was not moved over this interval). One outlier (at depth below MHHW=0.46 m, root:shoot ratio = 13.1, taken 2006) was removed because, although this had a root mass consistent with the other samples, the surface vegetation died, giving an anomalously high root:shoot ratio. If included in the analysis the regressed values of θ_{bg} and D_{mbm} change to -5.4 and 4.7, respectively.

growth rate measurements on a number of sites). Because we do not have similar data at other field locations, we cannot rule out the possibility that other species in other locations behave differently. Preliminary data in North Carolina and Louisiana [*Morris*, 2007b and unpublished data], however, suggest that these relationships are broadly applicable to widely distributed *Spartina alterniflora* communities, as well as *Juncus roemerianus* communities on the Atlantic coast of the United States. That salt marsh macrophytes likely have the highest potential for growth in an optimum intertidal elevation has been recognized for many decades [*e.g.*, *Redfield*, 1972], and more recent work using remote sensing has confirmed this prior work that numerous marsh species are confined to narrow elevation bands within salt marshes [*ie.g.*, *Silvestri and Marani*, 2004; *Morris et al.*, 2005]. Further, simple models suggest that competition between species with different optimal marsh elevations can strongly influence marsh zonation

[*Morris*, 2006, 2007c].

Following the approach of *Morris and Bowden* [1986] and *Rybczyk et al*. [1998], we describe the growth of belowground biomass being greatest near the surface, and decreasing exponentially with depth:

$$b_{bg} = b_0 e^{-d/\gamma} , \tag{14}$$

where b_{bg} [ML^{-3}] is the belowground biomass per unit volume, b_0 [ML^{-3}] is the belowground biomass per unit volume at the surface of the marsh, and γ [L] is the depth over which the root growth is reduced by a factor of e^{-1}. The total belowground biomass per unit area, B_{bg} [ML^{-2}], is related to the local biomass by:

$$B_{bg} = \int_0^\infty b_{bg} d \tag{15}$$

Using (15), the biomass at the surface may be calculated for a given total biomass:

$$b_0 = \frac{B_{bg}}{\gamma} . \tag{16}$$

During each time step, the total growth of belowground biomass is calculated based on B_p and (12) and (13); this total biomass is then converted to depth-dependent biomass by combining (14) and (16).

Throughout the year, both aboveground and belowground biomass are produced through plant growth. The change in live biomass is due to both growth and mortality of marsh macrophytes:

$$\frac{\partial B_{ag}}{\partial t} = G - M. \tag{17}$$

Based on a long-term record of biomass dynamics from the North Inlet estuary in South Carolina [*Morris and Haskin*, 1990], we assume that the growth of above ground biomass can be approximated by:

$$G_{ag} = \frac{1}{2}\left[G_{\min} + G_p + \left(G_p - G_{\min}\right)\cos\left(\frac{2\pi\left[jd - jd_{ps} + \phi\right]}{P}\right)\right] \tag{18}$$

where G_{ag} [$ML^{-2}T^{-1}$] is the rate of aboveground biomass production per unit area, G_{min} [$ML^{-2}T^{-1}$] is the minimum growth rate, G_p [$ML^{-2}T^{-1}$] is the peak growth rate, ϕ is the phase shift (in days) and P is the period of the cycle, assumed to b 365 days. The phase shift term occurs because the peak growth rate occurs some days before the date of peak biomass. The mortality rate is therefore calculated by subtracting the derivative of Eq. (12) from (18). The ratio of aboveground to belowground mortality is assumed to scale with the ratio of aboveground to belowground biomass. Both belowground growth and mortality are assumed to decrease exponentially with depth (*e.g.*, similar to root mass as described in (14)); the local belowground mortality rate is quantified using a relationship equivalent to (15) and (16). The minimum aboveground biomass, peak growth rate, and minimum growth rate are all proportional to the peak aboveground biomass:

$$B_{\min} = \theta_{B_{\min}} B_p\,, \tag{19a}$$

$$G_p = \upsilon_{G_p} B_p\,, \tag{19b}$$

$$G_{\min} = \upsilon_{G_{\min}} B_p\,, \tag{19c}$$

where $\theta_{B_{min}}$ is dimensionless and υ_{G_p} and $\upsilon_{G_{min}}$ are of dimension T^{-1}. In order to quantify the mass of carbon deposited in the soil, the mortality must be integrated with respect to time. Upon integration over an entire year we find that the total mass deposited in the marsh column is:

$$AMC = \frac{P}{2} B_p \left(\upsilon_{G_p} + \upsilon_{G_{min}} \right), \tag{20}$$

where *AMC* is the annual mass of carbon deposited. Eq. (20) is included for reference; during simulations the deposition rate varies throughout the year (Eq. (17)).

3.1.2 Decay of organic carbon

Each year, both roots and shoots die and are subject to decomposition. We separate the organic carbon into labile and refractory pools. Here we model the decay of labile pools with a linear model, and the production of the pools is controlled by the mortality of both roots and stems:

$$\frac{\partial C_{lfa}}{\partial t} = -\kappa_{lfa} C_{lfa} + m\chi_{lfa} \tag{21a}$$

$$\frac{\partial C_{lsl}}{\partial t} = -\kappa_{lsl} C_{lsl} + m\chi_{lsl} \tag{21b}$$

$$\frac{\partial C_{ref}}{\partial t} = m\chi_{ref} \tag{21c}$$

where C [ML^{-3}] is the organic carbon per unit volume, m [$ML^{-3}T^{-1}$] is the mortality rate per

unit volume and is related to the total mortality rate (M) using a relationship of the same form as (15), and the subscripts lfa, lsl, and ref refer to the two labile pools and the refractory pool, as in Section 2. Decay rates depend on a number of factors, including (possibly) sulfate concentration and oxygen supply [*e.g., Silver and Miya*, 2001]; many of the factors proposed to control the rate of organic matter decay vary with the depth below the sediment surface. Some authors have suggested depth-dependent decay coefficients [*Conn and Day*, 1997; *Rybczyk et al.*, 1998]. Others, however, have conducted measurements of decay in marsh sediment that show no depth dependence [*e.g., Blum*, 1993]. Here we describe the decay coefficients as

$$\kappa_{lsl} = \kappa_{lsl,0} e^{-d/\mu_{lsl}} \tag{22a}$$

and

$$\kappa_{lfa} = \kappa_{lfa,0} e^{-d/\mu_{lfa}} \tag{22b}$$

where $\kappa_{lsl,0}$ and $\kappa_{lfa,0}$ [T^{-1}] are the decay coefficients at the surface and μ [L] is a length scale over which the decomposition rate decreases with depth. In the case of decomposition that does not depend on depth, μ approaches infinity.

3.2 Inorganic sedimentation

During tidally induced floods, suspended matter can be advected from marsh creeks onto the marsh platform. This sediment may subsequently be deposited through either settling or trapping by marsh vegetation. Inorganic sedimentation due to both settling and trapping is a function of the depth of the marsh surface below mean high tide because with increasing depth the marsh surface is inundated and exposed to sediment laden water for

greater periods. In the OIMAS-N model, a linear relationship between the time the marsh is inundated and the sedimentation rate is used. Sedimentation also varies linearly with the concentration of suspended sediment in the waters that flood the marsh [e.g., *Mudd et al*., 2004]. Trapping is calculated using the methodology of *Palmer et al*. [2004] as implemented by *D'Alpaos et al*. [2006]. For trapping, we use a reference velocity of 1cm s^{-1}. Preliminary numerical experiments have demonstrated that flow velocity has little impact on the inorganic sedimentation rate; accretion rates due to trapping are approximately two orders of magnitude less than rates due to settling unless the reference velocity is unrealistically high ($e.g., > 0.5$ ms^{-1}). During each time step the total inundation time is calculated based on the tidal amplitude and the elevation of the marsh surface. This inundation time is then multiplied by the settling velocity and the concentration of the suspended sediment in the water above the sediment column.

The OIMAS-N model is intended to be flexible and can accommodate storm erosion by removing sediment from the top of the marsh column. For example, storm erosion could be calculated using a formulation based on excess shear stress [*e.g., D'Alpaos et al*., 2007; *Marani et al*., 2007]. In this manuscript, however, we focus on depositional processes. Storm erosion is typically focused near open water and the banks of the marsh creeks [*e.g., van de Plassche et al*., 2006], and due to the damping effect of vegetation on storm waves [*e.g., Moller*, 2006], storms typically result in deposition in the interiors of coastal salt marshes [*e.g., Goodbred and Hine*, 1995; *Leonard et al*., 1995; *Yang et al*., 2003; *Cahoon*, 2006].

3.3 Compaction

The sediments that make up salt marsh platforms are compressible. Compaction may play a significant role in determining the absolute elevation of marsh surfaces [*e.g., Cahoon et al.*, 1995; *Long et al.*, 2006; *Turner et al.*, 2006]. Here we use a constitutive equation verified by numerous laboratory compaction tests [*e.g., Gutierrez and Wangen*, 2005]:

$$E = E_0 - CI\log\left(\frac{\sigma_{eff}}{\sigma_0}\right) \tag{23}$$

Here E [dimensionless] is the void ration, CI [dimensionless] is the compression index, E_0 [dimensionless] is the void ratio at the reference stress, σ_0 [$MT^{-2}L^{-1}$], and σ_{eff} [$MT^{-2}L^{-1}$] is the effective stress. It is assumed the column is under hydrostatic pressure; because the modeled columns are on the order of meters in depth it is assumed excess pore pressure diffuses rapidly relative to the rate of sedimentation. Because of the hydrostatic assumption, the effective stress at any depth below the surface is simply the buoyant weight of the material above it. The compression index and reference void ratio depend on the substrate. For sand we set CI=0.1, σ_0=10^5 pa, and E_0=0.6 and for silt we set CI=0.2, σ_0=10^5 pa, and E_0=0.4. These values lie within the range of natural variability for these substrates. Organic material has been found to be far more compressible than inorganic material [*e.g., Mesri et al.*, 1997]. Thus for organic matter we set CI=1.0, σ_0=10^4 pa, and E_0=0.25.

4. Simulations

Both field studies [*e.g., Delaune et al.*, 1989; *Temmerman et al.*, 2003; *Chmura and Hung*, 2004] and modelling studies [*e.g., Mudd et al.*, 2004; *Temmerman et al.*, 2005; *D'Alpaos et al.*, 2007; *Kirwan and Murray*, 2007] have demonstrated that the supply of inorganic sediment decreases as a function of distance from marsh creeks. Thus the spatial distribution of inorganic sediment supply to the marsh surface should be expected to be heterogeneous. At the same time, if a marsh is to remain in equilibrium with sea-level rise the entire marsh must accrete at the same rate, by definition. Thus to maintain accretion that keeps pace with sea-level rise the preservation of inorganic material in the marsh column, through the increased deposition of refractory carbon, must offset the reduction in inorganic sedimentation as one moves away from the marsh creek.

In this section we perform a series of numerical simulations in order to explore the adjustment of marsh stratigraphy to changing rates of sea-level rise and changing rates of inorganic sediment supply. In order to perform this analysis, parameters for the simulations must be chosen. Each parameter in the OIMAS-N model can be quantified independently, but we know of no marsh where such data exist. In order to test the model, we examine its ability to reproduce marsh stratigraphy that has been measured in the field. We have chosen to test the model using data from the North Inlet Estuary, in South Carolina, USA. We choose this location to test the model because it has, to our knowledge, the most comprehensive set of data that is required to run the OIMAS-N model. At North Inlet, all but four of the required OIMAS-N model parameters have been measured independently; we use

core data from North Inlet to calibrate these four unknown parameters. We then use the calibrated parameters to run simulations used to examine the relationship between sediment supply, the rate of sea-level rise, and organic carbon accumulation on salt marshes.

4.1 Growth characteristics at North Inlet

North Inlet is a Long Term Ecological Research (LTER) site, and the stand characteristics of *Spartina alterniflora*, including standing biomass and growth rates have been monitored for a number of years. The methodology and location of these measurements is described in *Morris and Haskin* [1990]. Here we present a long-term record for the growth rate as a function of peak annual biomass for eight individual plots located at two unfertilized low marsh sites at North Inlet: Oyster Landing and Goat Island (Fig. 3a). The eight plots have data spanning either 1986-2002 or 1987-2002, and there are 195 measurements in total. From these data we have determined υ_{G_p} and $\upsilon_{G_{\min}}$ (Fig. 4a). For each year we also recorded the date of both the peak standing biomass and the peak growth rate, and from these data we determined the average phase shift, ϕ. Due to both natural variability and the fact that sampling occurred, on average, once a month in each of the eight plots, there is a high degree of variability in the phase shift data (Fig. 4b). For this reason our value for phase shift should be considered an approximation. We regard this uncertainty as tractable however, as the annually averaged organic deposition is more strongly dependent on the maximum growth rate than on the phase shift, and maximum growth rate is reasonably well constrained by the field measurements (Fig. 4a).

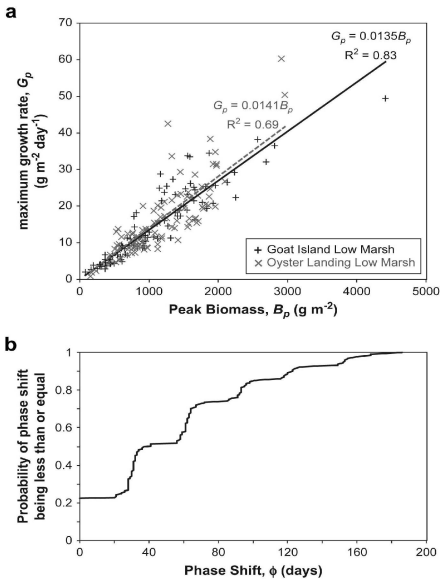

Figure 4. (a) The growth rate as a function of peak biomass for Goat Island (N=99) and Oyster Landing (N=96) low marsh sites. Each site consists of four separate plots. Linear regressions for each site are shown on the chart, there is no statistical difference between plots at the same site. Regression of all the data has ν_{Gp} = 0.0138 day^{-1} with R^2=0.76. (b) Cumulative probability plot of the phase shift ϕ. Stepped nature of the figure is due to the field sampling on a monthly interval. The average phase shift is 56 days.

Table 1. Parameter values used in simulations

Parameter	Value	Source
Tidal amplitude	0.7 m	Morris et al. (2002)
D_{max}	0.55 m	Based on data from Morris et al. (2002)
D_{min}	0.0 m	Based on data from Morris et al. (2002)
B_{max}	2500 g m^{-2}	Based on data from Morris et al. (2002)
B_{min}	0 g m^{-2}	Based on data from Morris et al. (2002)
ν	0.0138 day^{-1}	This study (Fig. 4a)
ν	0.0 day^{-1}	This study (Fig. 4a)
ϕ	56 days	This study (Fig. 4b)
θ_{bg}	-6.8 m^{-1}	This study (Fig. 3c)
D_{mbm}	4.8 (dimensionless)	This study (Fig. 3c)
Total suspended sediment concentration	30 mg l^{-1}	Gardner et al. (2006) note: value rounded from 28.47

4.2 Calibration of parameters at North Inlet

A large number of the parameters for the OIMAS-N model have been measured independently (that is, not calibrated using the model) at North Inlet (Table 1). We do, however, find it necessary to calibrate several parameters that have not been independently measured at the site. The parameters needing calibration are the settling characteristics of the suspended sediment, the e-folding depth of root growth (γ, *i.e.*, the depth at which the root growth declines by a factor of $1/e$), the decay rate of labile organic carbon, and the percentage of organic matter deposited on the marsh that is labile carbon versus refractory carbon. Of these parameters, we expect several of them to fall within a relatively tight range. For example, measured carbon decay rates on salt marshes tend to fall within a relatively narrow band between 0.2 and 0.8 yr^{-1} [*e.g., Morris and Bowden*, 1986; *Blum*, 1993; *Conn and Day*, 1997; *Rybczyk et al.*, 1998], and root depth tends to be on the order of several decimeters [*e.g., Morris and Bowden*, 1986]. We also vary the effective settling velocity, ν_{eff}, of the sediment during the simulations.

Our calibration uses published data on organic matter percentage as a function of depth for a core taken at North Inlet by *Sharma et al.* [1987]. We use the parameter values listed in Table 1, and vary the four unknown parameters. The carbon profiles generated by the OIMAS-N model are then compared to published data by quantifying the root mean square error (RMSE) between the measured and predicted organic carbon percentage:

$$RMSE = \left[\frac{1}{n} \sum_{i=1}^{n} \left(O_{measured,i} - O_{modelied,i} \right)^2 \right]^{1/2} \tag{24}$$

where O is the percent organic matter, and n is the number of samples in the core. To produce the modeled cores, we allow a sediment column to develop at an accretion rate of 0.27 cm yr^{-1}, the long-term rate determined by *Vogel et al*. [1996]. There is some indication that accretion rates have been variable over the last 150 years [*Sharma et al*., 1987], but we do not attempt to capture this variability. Because of this, our simulations are not able to exactly reproduce the ^{210}Pb profiles measured by *Sharma et al*. [1987], but the rate of sea-level rise we use is the best-fitting rate if constant sea-level rise is assumed. It is not our purpose to exactly reproduce the data of *Sharma et al*. [1987], but rather to find physically realistic approximations of the unknown parameters that can be used to test the sensitivity of coastal salt marsh stratigraphy to sediment supply and the rate of sea-level rise. We find, upon visual inspection of predicted profiles, that a number of parameter combinations can be dismissed as unrealistic (see below), whereas our best estimate of the four parameter values results in an *RMSE* of less than 1% organic matter in the core. The minimum *RMSE* for the core has been quantified based on a large number of simulations (N=1554). We are thus confident that the calibrated parameter values lie within the range of natural variability at North Inlet.

The best-fit estimate of the calibrated parameters is shown in Fig. 5, plotted with the data of *Sharma et al*. [1987]. Modification of these parameters can lead to large changes in the predicted pattern of organic composition as a function of depth. We demonstrate the effect of changing the four parameters in Fig. 6; a range of parameter combinations produce predicted organic matter profiles that clearly diverge from the patterns measured by *Sharma*

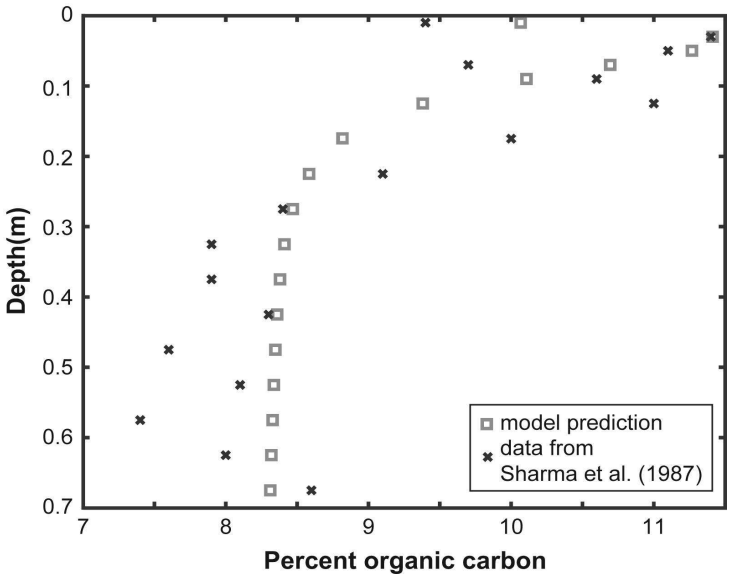

Figure 5. Best-fit prediction of % organic matter as a function of depth (grey squares) using the OIMAS-N model plotted with data collected by *Sharma et al*. [1987] at Bread and Butter Creek, North Inlet, SC (black crosses). The *RMSE* of the organic carbon % is 0.68.

et al. [1987]. When roots die, the fraction of the root mass that becomes refractory carbon is χ_{ref} (21c). Varying this parameter changes the organic carbon content in the profile at depth, but does not affect the near-surface peak in organic content (Fig. 6a). Varying the effective settling velocity ν_{eff} changes the distribution of percent carbon in the column (Fig. 6b). Varying both the *e*-folding depth of root growth (γ) and the labile carbon decay coefficient (κ) changes the near-surface peak of carbon content but not the carbon content at depth (Fig. 6c,d). In general, the carbon content approaches a constant value at depth. This is because all labile carbon is consumed by decay processes. Thus there is a layer of sediment, near the surface, where labile carbon is still present. We find that the variation in the four calibrated parameters does not lead to differences in the depth of the sediment in

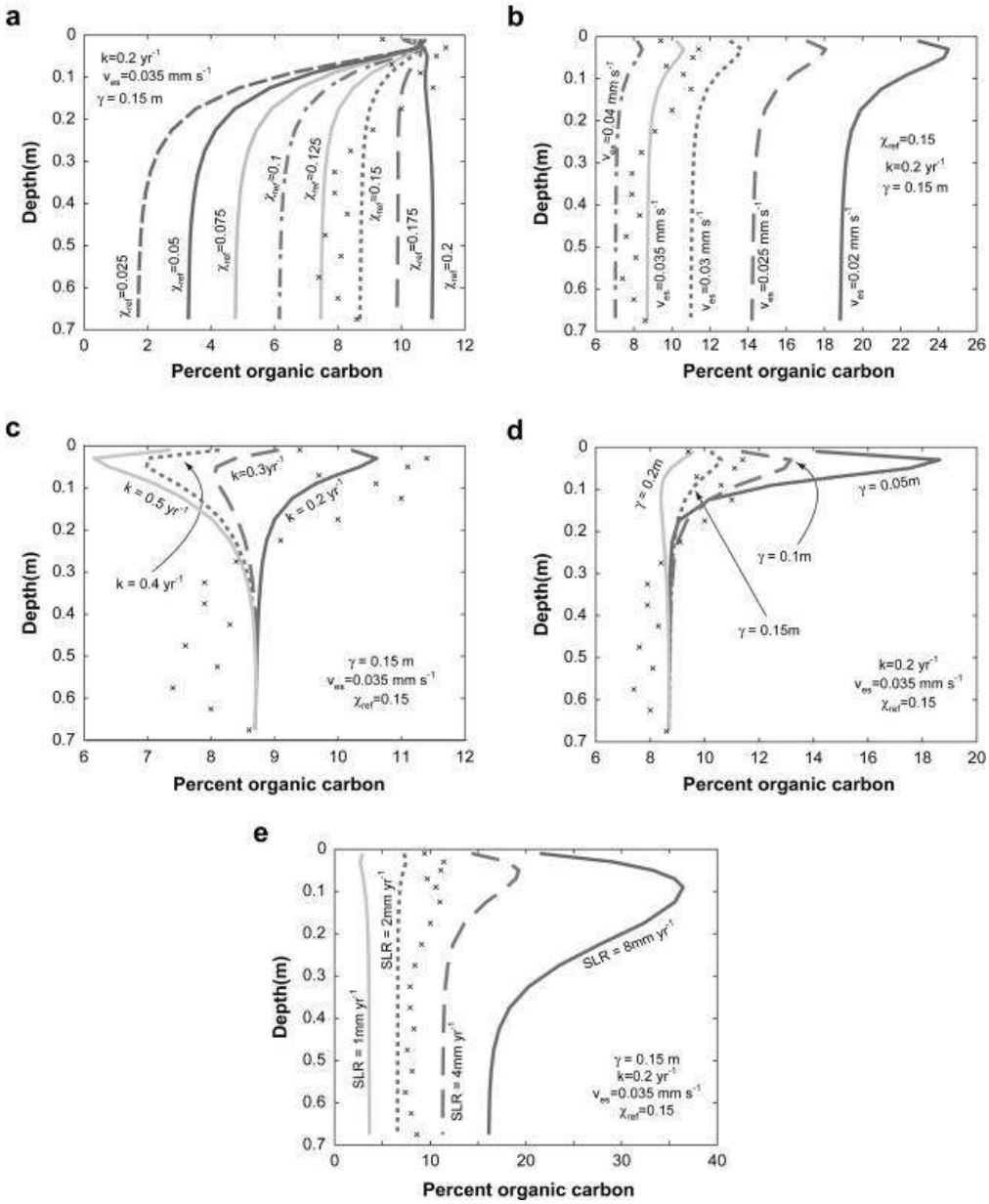

Figure 6. A series of simulated profiles of % organic matter demonstrating the effect of varying the calibrated model parameters. (a) Variable initial fraction refractory carbon, all else held constant. (b) Variable effective settling velocity. (c) Variable rate coefficient of labile carbon decay. (d) Variable e-folding depth of root growth. (e) Variable rate of sea-level rise.

which labile carbon was still present. This includes variation in the *e*-folding depth of root growth. Five simulations were performed to examine the sensitivity of the carbon profile to

changes in the rate of SLR (Fig. 6e). We find that changing the rate of SLR can change both the carbon content of the profile and the depth over which labile carbon is present.

Table 2. Best-fit of parameters to profile at Bread and Butter Creek collected by *Sharma et al.* [1987].

Parameter	Value
γ	0.11 m
k_l	0.2 yr^{-1}
v_{eff}	0.037 mm s^{-1}
χ_{ref}	0.158

4.3 Effect of the rate of sea-level rise and sediment supply on marsh stratigraphy

Using the parameters both measured independently (Table 1) and calibrated using a core from North Inlet (Table 2), we have performed a series of simulations examining the effect of changing rates of sea-level rise and sediment supply on the stratigraphy and carbon accumulation in a coastal marsh with characteristics similar to North Inlet. While the model is generally applicable, we use the parameters tested for North Inlet because we know, based on model testing, that they lie within the range of natural variability of coastal salt marshes.

At low rates of sea-level rise, the rate of refractory carbon accumulation increases with a rise in rate of sea-level rise, the total labile stored in the marsh increases (the accumulation of this carbon is zero because it all must decay), and the percent of deposited sediments that are made of organic material also increases. Carbon accumulation does not increase indefinitely with increasing sea-level rise, however. As described by *Morris et al.* [2002], for a given sediment supply there is a maximum rate of sea-level rise that marsh can

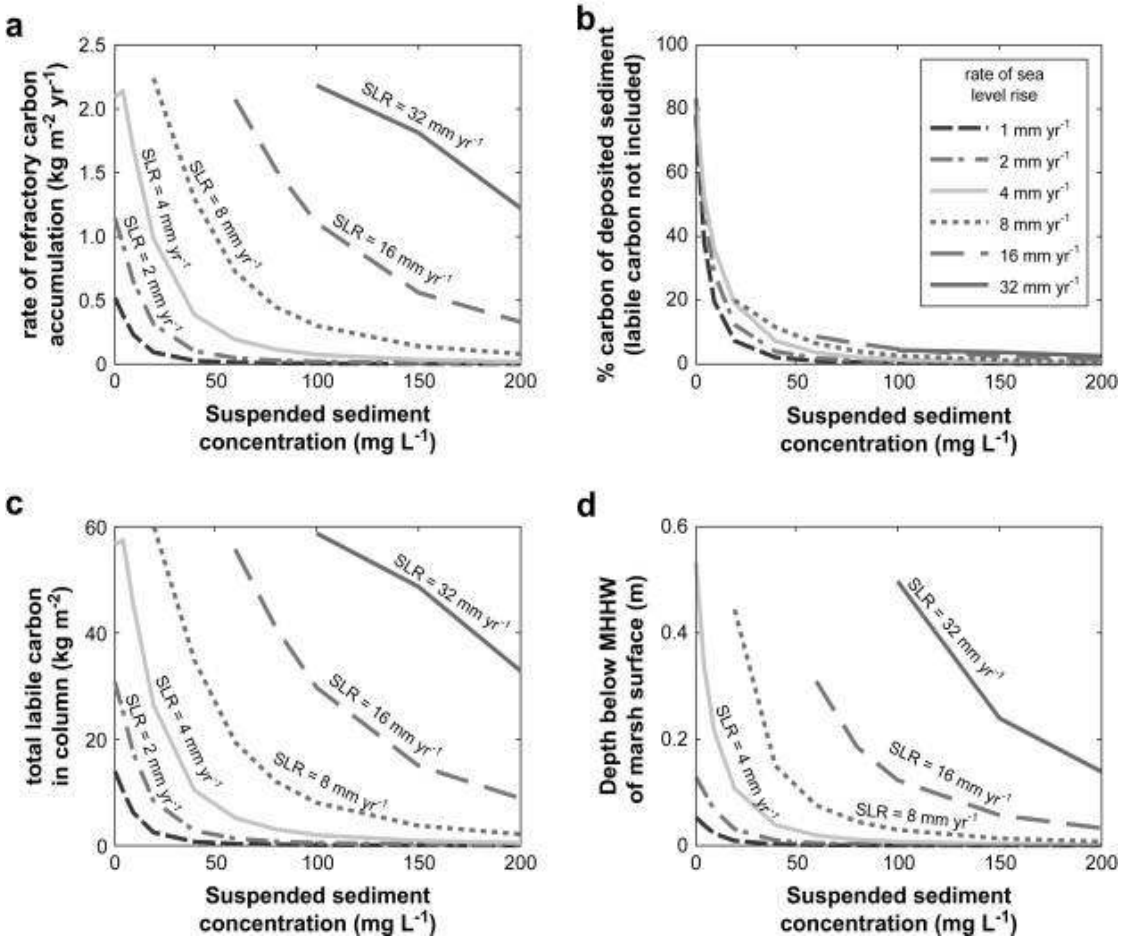

Figure 7. Supply of refractory carbon (a), carbon content of accumulating sediment (b), total labile carbon (c), and the equilibrium depth below MHHW of the marsh surface (d) under a range of rates of sea-level rise and inorganic sediment supply rates. Parameter values for simulations are shown in Tables 1 and 2.

keep pace with before it drowns (that is, the marsh surface becomes too deep relative to MHHW for plant survival). A number of our OIMAS-N model runs resulted in drowned marshes; this is why data corresponding to rapid sea-level rise ($\geq$ 8 mm yr^{-1}) are confined to relatively high suspended sediment concentrations (Fig. 7). For example, marshes with a rate of SLR of 8 mm yr^{-1} and a suspended sediment concentration of 10 mg l^{-1} will drown.

Carbon dynamics are also sensitive to inorganic sediment supply (Fig. 7). As the supply of suspended sediment decreases, the rate of refractory carbon accumulation

increases, the total labile carbon stored in the marsh increases, and the percent of deposited sediments that are mode of organic material also increases. For example, increasing the sediment supply from 1 to 10 mg per liter reduces the total labile carbon stored in the marsh sediment from 80 to 30 kg per square meter of surface area. This effect is particularly strong in marshes with relatively low sediment supply. Thus, carbon dynamics of marshes in sediment poor regions are especially sensitive to a disturbance in sediment supply, be it due to anthropogenic or other factors. We also note that suspended sediment should decrease rapidly as a function of distance from the marsh creek [*e.g., Leonard et al*., 2002; *Temmerman et al*., 2003; *Chmura and Hung*, 2004]. So it is likely that the percentage of carbon in sediment stored near marsh creeks will be lower than at locations in the interior of the marsh, as will perhaps the absolute storage of carbon, depending on the rate of sea-level rise and equilibrium marsh elevation.

The OIMAS-N model predicts rates of carbon accumulation that are consistent with those reported by *Chmura et al*. [2003], *Choi and Wang* [2004] and *Neubauer et al*. [2002] for a range of sites. *Chmura et al*. [2003], using data compiled from a number of sources, reported carbon accumulation rates of marshes with mean annual temperatures between 15°C and 20°C (the approximate annual temperature of North Inlet is 17°C) that ranged between 0 and 0.8 kg $m^{-2}yr^{-1}$, with one outlier at 1.7 kg $m^{-2}yr^{-1}$. *Morris et al*. [2002] reported an acceleration in the rate of sea-level rise at North Inlet from 2.7 mm yr^{-1} prior to 1984, to 4.0 mm yr^{-1} from 1984 to 1996, and again to 16.4 mm yr^{-1} since 1996. With these rates of sea-level rise the OIMAS-N model predicts carbon accumulation rates of 0.4 kg $m^{-2}yr^{-1}$ and 0.7 kg $m^{-2}yr^{-1}$, respectively. The OIMAS-N model also predicts that the marsh will drown at

current rates of sea-level rise (16.4 mm yr^{-1}), consistent with the findings of *Morris et al.* [2002].

We also performed exploratory simulations that included depth dependent decay of labile carbon. Studies of carbon decay rates at different depths have been inconclusive in coastal environments [*e.g., Conn and Day*, 1997], yet depth-dependent decay is common in terrestrial environments and has been incorporated into many models of soil carbon turnover [*e.g. Baisden and Amundson*, 2003; *Jenkinson and Coleman*, 2008]. A reduction in carbon decay rates with depth is likely related to, amongst other factors, the saturation state of the sediments, so we selected an *e*-folding depth in the reduction of carbon decay rates that is of the same order as the tidal amplitude: μ=0.4 m. Introducing depth-dependent decay, common in terrestrial soils but unconstrained in marsh sediment, has a significant effect on the amount of labile carbon stored in the marsh (Fig. 8). If one takes the frame of reference of deposited organic carbon, this carbon moves downward in the marsh column as sediment is deposited above it. The faster the rate of marsh accretion, the more rapidly this carbon moves to greater depth. If the rate of sea-level rise is rapid and carbon experiences depth-dependent decay, labile carbon can be preserved by advecting it below the zone where decay is most intense (Fig. 8).

5. Conclusions

Organic sedimentation can play an important role in maintaining the elevation of coastal salt marshes. Feedbacks exist between marsh elevation and sedimentation, both for inorganic sediment (higher elevation results in less flooding and exposure to suspended

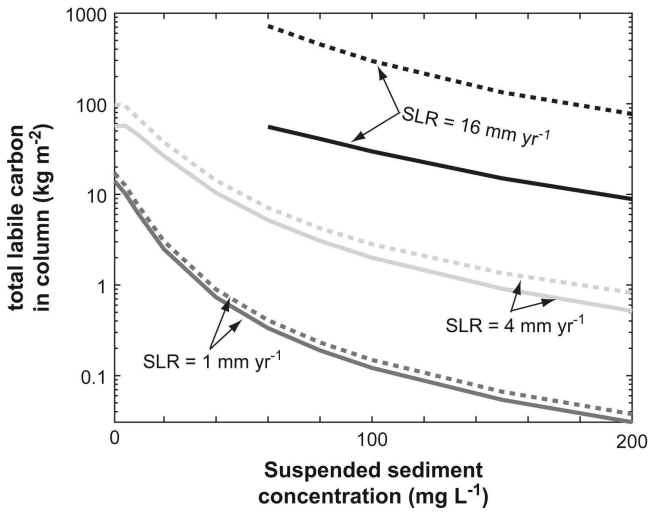

Figure 8. Effect of depth-dependent decay on the amount of labile carbon stored in the sediment column as a function of suspended sediment concentration. Solid lines are for marsh columns with no depth-dependent decay, dotted lines are for marshes with depth-dependent decay.

sediment) and organic sediment (higher elevation results in lower biomass and less root growth, but a higher root:shoot ratio). We have explored the tension between organic and inorganic sedimentation in salt marshes experiencing sea-level rise using both an analytical and numerical model. The analytical model, OIMAS-A, demonstrates the importance of understanding the organic fraction of marsh sediments when using isotope dating methods (^{137}Cs and ^{210}Pb) to estimate marsh accretion. *Turner et al*. [2006] observed that in a large number of reported marsh cores, the accretion rate determined by ^{137}Cs outpaced the accretion rate estimated by ^{210}Pb. We have demonstrated how this effect is potentially a result of organic decomposition. A key component of the difference in estimated accretion rates using these two radioisotopes is the relative depth over which they are measured; organic decomposition most strongly affects radioisotope concentrations near the marsh surface.

These results emphasize the need to report the concentrations of organic matter in profiles that are subject to radioisotope analysis.

The numerical model (OIMAS-N) has been constructed to capture a richer array of belowground processes than the OIMAS-A model. A large fraction of this model's subcomponents are general. One subcomponent that requires more study is the relationship between biomass and depth below MHHW. We have tested the OIMAS-N model at North Inlet Estuary, in South Carolina, USA, because at this location there exists a continuous, 16-year data set of monthly measurements of macrophyte growth rates and standing biomass on a number of sites, in addition to a wide range of other measurements of OIMAS-N model parameters. We expect parameter values of (11) and (13) to vary between species and geographic locations, but we cannot rule out that different species have different functional relationships between biomass, growth and depth below MHHW. Several lines of evidence, including the preliminary data from marsh organ experiments [*Morris*, 2007b] and the well-defined elevation bands of many marsh species [*e.g. Silvestri and Marani*, 2004; *Morris et al.*, 2005] do suggest that the model may be extended to other species. Thus, we urge more research in this area.

The OIMAS-N model was then used to investigate how sediment supply and sea-level rise affect marsh stratigraphy, and in particular, carbon storage. The model predicts rates of carbon accumulation in the marsh that are consistent with field measurements of carbon accumulation rates reported by others. On a marsh with characteristics similar to North Inlet, the model predicts an increase in carbon accumulation from 0.4 to 0.7 kg $m^{-2}yr^{-1}$ in response to accelerated sea-level rise from 2.7 to 4.0 mm yr^{-1}. On marshes with low

sediment supplies or high rates of sea-level rise, carbon accumulation could exceed 2 kg m^{-2} yr^{-1}. Carbon accumulation on marshes that are sediment poor are more sensitive to changes in sediment supply than sediment-rich marshes. Thus anthropogenic disturbances to sediment supplies in sediment poor marshes could dramatically change carbon accumulation rates.

6. References

Allen, J.R.L. (1995), Salt-marsh growth and fluctuating sea level: Implications of a simulation model for Flandrian coastal stratigraphy and peat-based sea-level curves, *Sedimentary Geology*, *100*:1-4, 21-45.

Anisfeld, S.C., M. Tobin, and G. Benoit (1999), Sedimentation rates in flow-restricted and restored salt marshes in Long Island Sound, *Estuaries, 22*:2A, 231-244.

Appleby, P.G., and F. Oldfield (1992), Application of lead-210 to sedimentation studies, in *Uranium Series Disequilibrium: Application to Earth, Marine and Environmental Sciences*, edited by M. Ivanovich, and R.S. Harmon, Clarendon Press, Oxford.

Baisden, W.T. and R. Amundson (2003), An analytical approach to ecosystem biogeochemistry modeling, *Ecological Applications, 13*:3, 649-663.

Blum, L.K. (1993), Spartina-Alterniflora Root Dynamics in a Virginia Marsh, *Marine Ecology-Progress Series*, *102*:1-2, 169-178.

Cahoon, D.R., D.J. Reed, and J.W. Day (1995), Estimating shallow subsidence in microtidal salt marshes of the southeastern United States: Kaye and Barghoorn revisited, *Marine Geology*, *128*, 1-9.

Chmura, G.L., R. Costanza, and E.C. Kosters (1992), Modelling coastal marsh stability in response to sea level rise: a caste study in coastal Louisiana, USA, *Ecological Modelling 64,* 47-64.

Chmura, G.L., S.C. Anisfeld, D.R. Cahoon, and J.C. Lynch (2003), Global carbon sequestration in tidal, saline wetland soils, *Global Biogeochemical Cycles*, *17*:4, doi:10.1029/2002GB001917.

Chmura, G.L. and G.A. Hung (2004), Controls on salt marsh accretion: A test in salt marshes of Eastern Canada, *Estuaries, 27*:1, 70-81.

Choi, Y.H. and Y. Wang (2004), Dynamics of carbon sequestration in a coastal wetland using radiocarbon measurements, *Global Biogeochemical Cycles, 18*(4), GB3016, doi:10.1029/2004GB002261.

Conn, C.E., and F.P. Day (1997), Root decomposition across a barrier island chronosequence: Litter quality and environmental controls, *Plant and Soil*, *195*:2, 351-364.

.

D'Alpaos, A., S. Lanzoni, S.M. Mudd, and S. Fagherazzi (2006), Modeling the influence of hydroperiod and vegetation on the cross-sectional formation of tidal channels, *Estuarine Coastal and Shelf Science*, *69*:3-4, 311-324.

D'Alpaos, A., S. Lanzoni, M. Marani, and A. Rinaldo (2007), Landscape evolution in tidal embayments: Modeling the interplay of erosion, sedimentation, and vegetation dynamics, *Journal of Geophysical Research-Earth Surface*, *112*:F1, F01008, doi: 10.1029/2006JF000537.

Darby, F.A. and R.E. Turner (2008), Effects of eutrophication on salt marsh root and rhizome biomass accumulation, *Marine Ecology Progress Series 363*, 63-70, doi:10.3354/meps07423.

Day, J.W., J. Rybczyk, F. Scarton, A. Rismondo, D. Are, and G. Cecconi (1999), Soil accretionary dynamics, sea-level rise and the survival of wetlands in Venice lagoon: a field and modelling approach, Estuarine, Coastal and Shelf Science *49*:5, 607-628.

Delaune, R.D., J.H. Whitcomb, W.H., Patrick, J.H., Pardue, and S.R. Pezeshki. (1989), Accretion and canal impacts in a rapidly subsiding wetland .1. Cs-137 and Pb-210 Techniques, *Estuaries, 12*:4, 247-259.

Donnelly, J.P. and M.D. Bertness (2001), Rapid shoreward encroachment of salt marsh cordgrass in response to accelerated sea-level rise, *Proceedings of the National Academy of Sciences of the United States of America, 98:25*, 14218-14223.

French, J.R. (1993), Numerical-simulation of vertical marsh growth and adjustment to accelerated sea-level rise, North Norfolk, UK, *Earth Surface Processes and Landforms*, *18*:1, 63-81.

Friedrichs, C.T. and J.E. Perry (2001), Tidal salt marsh morphodynamics: a synthesis, *Journal of Coastal Research 27*, 7-37.

Gardner, L.R., B. Kjerfve, and D.M. Petrecca (2006), Tidal fluxes of dissolved oxygen at the North Inlet-Winyah Bay National Estuarine Research Reserve, *Estuarine Coastal and Shelf Science, 67:3*, 450-460.

Goodbred, S.L. and A.C. Hine (1995), Coastal storm deposition — salt marsh response to a severe extratoprical storm, March 1993, West-Central Florida, Geology 23:8, 679-682.

Gutierrez, M., and M. Wangen (2005), Modeling of compaction and overpressuring in sedimentary basins, *Marine and Petroleum Geology*, *22* (3), 351-363.

Holgate, S.J., and P.L. Woodworth (2004), Evidence for enhance coastal sea level rise during the 1990s, *Geophysical Research Letters 31*, L07305, doi:10.1029/2004GL019626.

Hussein, A.H., M.C. Rabenhorst, and M.L. Tucker (2004), Modeling of carbon sequestration in coastal salt marsh soils, *Soil Science Society of America Journal 68*:5, 1786-1795.

Jenkinson, D.S. and K. Coleman (2008), The turnover of organic carbon in subsoils. Part 2. Modelling carbon turnover, *European Journal of Soil Science*, 59:2, 400-413.

Kirwan, M.L. and A.B. Murray (2007), A coupled geomorphic and ecological model of tidal marsh evolution, *Proceedings of the National Academy of Sciences of the United States of America, 104:15*, 6118-6122.

King, G.M., M.J. Klug, R.G. Wiegert, and A.G. Chalmers (1982), Relation of soil-water movement and sulfide concentration to *Spartina alterniflora* production in a Georgia salt-marsh, *Science 218*:4567, 61-63.

Krone, R.B. (1987), A method for simulating historic marsh elevations, in *Coastal Sediments '87*, edited by N.C. Krause, pp. 316-323, American Society of Civil Engineers, New York.

Leonard, L.A., A.C. Hine, M.E. Luther, R.P. Stumpf, and E.E. Wright (1995), Sediment transport processes in a West-Central Florida Open Marine Marsh Tidal Creek — the role of tides and extra-tropical storms, *Estuarine, Coastal and Shelf Science 41*:2, 225-248.

Leonard, L.A., P.A. Wren, and R.L. Beavers (2002), Flow dynamics and sedimentation in *Spartina alterniflora* and *Phragmites australis* marshes of Chesapeake Bay, *Wetlands 22*:2, 415-424.

Long, A.J., M.P. Waller, and P. Stupples (2006), Driving mechanisms of coastal change: Peat compaction and the destruction of late Holocene coastal wetlands, *Marine Geology*,

225:1-4, 63-84.

Lynch, J.C., J.R. Meriwether, B.A. Mckee, F. Veraherrera, and R.R. Twilley (1989), Recent accretion in mangrove ecosystems based on Cs-137 and Pb-210, *Estuaries, 12*:4, 284-299.

Marani, M., A. D'Alpaos, S. Lanzoni, L. Carniello, and A. Rinaldo (2007), Biologically-controlled multiple equilibria of tidal landforms and the fate of the Venice lagoon, *Geophysical Research Letters, 34*:11, L11302, doi:10.1029/2007GL030178.

Mckee, K.L., D.R. Cahoon, and I.C. Feller (2007), Caribbean mangroves adjust to rising sea level through biotic controls on change ins oil elevation, *Global Ecology and Biogeography, 16*:5, 545-556.

Mesri, G., T.D. Stark, M.A. Ajlouni, C.S. Chen (1997), Secondary compression of peat with or without surcharging, *Journal of Geothechnical and Geoenvironmental Engineering*, 123:5, 411-421.

Morris, J.T., and W.B. Bowden (1986), A Mechanistic, numerical-Model of Sedimentation, Mineralization, and Decomposition for Marsh Sediments, *Soil Science Society of America Journal*, *50*:1, 96-105.

Morris, J.T., and B. Haskin (1990), A 5-yr record of aerial primary production and stand characteristics of *Spartina alterniflora*, *Ecology*, *7*:16, 2209-2217.

Morris, J.T., P.V. Sundareshwar, C.T. Nietch, B. Kjerfve, and D.R. Cahoon (2002), Responses of coastal wetlands to rising sea level, *Ecology*, *83*, 2869-2877.

Morris, J.T., D. Porter, M. Neet, P.A. Noble, L. Schmidt, L.A. Lapine, and J. Jensen (2005), Integrating LIDAR elevation data, multi-spectral imagery and neural network modelling for marsh characterization, *International Journal of Remote Sensing, 26*:23, 5221-5234.

Morris, J.T. (2006), Competition among marsh macrophytes by means of geomorphological displacement in the intertidal zone, *Estuarine, Coastal and Shelf Science 69*:3-4, 395-402.

Morris, J.T. (2007a), Estimating net primary production of salt-marsh macrophytes, *In*: Fahey, T.J., Knapp, A.K. (Eds), *Principles and Standards for Measuring Primary Production*, Oxford University Press, pp. 106-119.

Morris, J.T. (2007b), The relative importance of mineral and organic matter accumulation in maintaining marsh elevation, Abstract, *Estuarine Research Federation Meeting*,

Providence, RI.

Morris, J.T. (2007c), Ecological engineering in intertidal saltmarshes, *Hydobiologia 577*, 161-168.

Mudd, S.M., S. Fagherazzi, J.T. Morris, and D.J. Furbish (2004), Flow, sedimentation, and biomass production on a vegetated salt marsh in South Carolina: toward a predictive model of marsh morphologic and ecologic evolution, in *The Ecogeomorphology of Tidal Marshes*, edited by S. Fagherazzi, A. Marani, and L.K. Blum, pp. 165-187, American Geophysical Union, Washington, D.C.

Neubauer, S.C., I.C. Anderson, J.A. Constantine, and S.A. Kuehl (2002), Sediment deposition and accretion in a mid-Atlantic (USA) tidal freshwater marsh, *Estuarine, Coastal and Shelf Science 54*:4, 713-727.

Neubauer, S.C., (2008), Contributions of mineral and organic components to tidal freshwater marsh accretion, *Estuarine Coastal and Shelf Science, 78*:1, 78-88.

Nyman, J.A., R.J. Walters, R.D. Delaune, and W.H. Patrick (2006), Marsh vertical accretion via vegetative growth, *Estuarine Coastal and Shelf Science*, *69* (3-4), 370-380.

Orson, R.A., W. Panageotou, and S.P. Leatherman (1985), Response of tidal salt marshes of the United States Atlantic and Gulf Coasts to rising sea levels, *Journal of Coastal Research, 1*:1, 29-37.

Orson, R.A., R.S. Warren, and W.A. Niering (1998), Interpreting sea level rise and rates of vertical marsh accretion in a southern New England tidal salt marsh, *Estuarine Coastal and Shelf Science, 47*:4, 419-429.

Palmer, M.R., H.M. Nepf, and T.J.R. Pettersson (2004), Observations of particle capture on a cylindrical collector: Implications for particle accumulation and removal in aquatic systems, *Limnology and Oceanography*, *49*:1, 76-85.

Pethick, J.S. (1981), Long-term accretion rates on tidal salt marshes, *Journal of Sedimentary Petrology, 51*:2, 571-577.

Van de Plassche, O., G. Erkens, F. Van Vliet, J. Brandsma, K. Van der Borg, and A.F.M. de Jong (2006), Salt-marsh erosion associated with hurricane landfall in southern New England in the fifteenth and seventeenth centuries, *Geology, 34*:10, 829-832.

Redfield, A.C. (1972), Development of a New England salt marsh, *Ecological Monographs 42*:2, 201-237.

Rybczyk, J.M., J.C. Callaway, and J.W. Day (1998), A relative elevation model for a subsiding coastal forested wetland receiving wastewater effluent, *Ecological Modelling*, *112*:1, 23-44.

Rybczyk, J.M. and D.R. Cahoon (2002), Estimating the potential for submergence for two wetlands in the Mississippi River Delta, *Estuaries 25*:5, 985-998.

Silver, W.L. and R.K. Miya (2001), Global patterns in root decomposition: comparisons of climate and litter quality effects, *Oecologia, 129*:3, 407-419.

Silvestri, S. and M. Marani (2004), Salt marsh vegetarian and morphology: modelling and remote sensing observations, *In:* Fagherazzi, S., Marani, A., Blum, L.K. (Eds.), *The Ecogeomorphology of Tidal Marshes*, American Geophysical Union, Washington, DC, pp. 165-87.

Sharma, P., L.R. Gardner, W.S. Moore, and M.S. Bollinger (1987), Sedimentation and bioturbationin a salt-marsh as revealed by Pb-210, Cs-137, and Be-7 studies, *Limnology and Oceanography 31*:2, 313-326.

Temmerman, S., G. Govers, S. Wartel, and P. Meire (2003), Spatial and temporal factors controlling short-term sedimentation in a salt and freshwater tidal marsh, Scheldt estuary, Belgium, SW Netherlands, *Earth Surface Processes and Landforms 28*, 739-755.

Temmerman, S., T.J. Bouma, G. Govers, Z.B. Wang, M.B. DeVries, and P.M.J. Herman (2005), Impact of vegetation on flow routing and sedimentation patterns: Three-dimensional modelling for a tidal marsh, *Journal of Geophysical Research-Earth Surface, 110:*F4, F04019, doi:10.1029/2005JF000301.

Turner, R.E., E.M. Swenson, and C.S. Milan (2001), Organic and inorganic contributions to vertical accretion in salt marsh sediments, *In:* Weinstein, M., Kreeger, K. (Eds.), *Concepts and Controversies in Tidal Marsh Ecology*, Kluwer Academic Press, Dorrecht, Netherlands, pp. 583-595.

Turner, R.E., C.S. Milan, and E.M. Swenson (2006), Recent volumetric changes in salt marsh soils, *Estuarine Coastal and Shelf Science*, *69*:3-4, 352-359.

Valiela, I., J.M. Teal, and W.G. Deuser (1978), Nature of growth forms in salt-marsh grass *Spartina alterniflora*, *American Naturalist 112*:985, 461-470.

Vogel, R.L., B. Kjerfve, and L.R. Gardner, (1996), Inorganic sediment budget for the North Inlet salt marsh, South Carolina, U.S.A, *Mangroves and Salt Marshes, 1*, 23-35.

Westrich, J.T. and R.A. Berner (1984), The role of sedimentary organic-matter in

bacterial sulfate reduction — the G model tested, *Limnology and Oceanography, 29*:2, 236-249.

Yang, S.L., C.T. Friedrichs, Z. Shi, P.X. Ding, J. Zhu, and Q.Y. Zhao (2003), Morphological response of tidal marshes, flats and channels of the outer Yangtze River mouth to a major storm, *Estuaries 26*:6, 1416-1425.

CHAPTER VI

CARBON PART II: ORGANIC DECOMPOSITION AND SEDIMENT ACCUMULATION ON SALT MARSH PLATFORMS

Abstract

Preservation and accumulation of organic carbon on salt marsh platforms is recognized as an important mechanism for maintaining coastal salt marsh elevation. The accumulation of carbon in sediments is a function of the organic carbon balance between net primary production and decomposition. Despite the importance of wetlands for carbon sequestration, little is known about the transformation rates of belowground biomass and models have yet to explore carbon sequestration with salt marsh platform evolution. *Mudd et al*. [2009] presented the first attempt at coupling the feedback between biomass production, sedimentation and sea-level rise with an explicit representation of belowground processes. The two models presented in Chapter 5 explore the influence of organic deposition on the interpretation of dating methods and the relative balance between organic and inorganic sedimentation of coastal salt marshes. This chapter builds on the previous work of *Mudd et al*. [2009] and Chapter 5, focusing on the ability of the model to reproduce marsh stratigraphy measured in the field and quantifying the mass fraction of deposited organic matter that goes into the refractory pool of carbon. Comprehensive field and laboratory data from Pine Knolls Shores, North Carolina, presented here includes biological demographics, organic matter content, grain size, sediment accretion rate, ^{210}Pb and ^{137}Cs concentrations,

and organic carbon profiles. Simulations consist of scanning across a range of sea-level rise rates and the mass supply rate of inorganic sediment for five cores, using values within a range of those observed. The effect of decomposition on the interpretation of radioisotope dating methods is demonstrated by comparing predicted ^{210}Pb based on the analytical model to the observed Lead concentrations. This analysis is used to describe the geomorphic conditions at the Pine Knolls Shore field site.

1. Introduction

Wetlands comprise approximately six percent of the Earth's land surface, yet may significantly influence the global carbon budget [*Reddy and DeLaune*, 2008]. Accumulation and preservation of organic carbon on salt marsh platforms is recognized to be an important mechanism for wetlands to keep pace with sea-level rise [*e.g. Morris and Bradley*, 1998; *Duarte et al.*, 2005; *Langley et al.,* 2009; *Mudd et al.*, 2009], especially in microtidal regimes (tidal amplitudes less than 0.3 m) that accumulate primarily by organic sedimentation. The accumulation of carbon in sediments is a function of the organic carbon balance between net primary production and decomposition. Much work has focused on the aerobic decomposition of aboveground *Spartina alterniflora*, but relatively little is known about transformation rates of belowground biomass in salt marsh sediments. Organic carbon is thought to accumulate in wetland soils because anaerobic microorganisms appear limited in their ability to attack lignocellulose [*Morris and Bradley*, 1998]. However, wetlands with anoxic sediments display a wide range of soil organic matter concentrations, suggesting that

carbon storage is far more complex than can be explained by the availability of oxygen [*Morris and Bradley*, 1998]. Sources of organic carbon in wetlands include organic matter from the C_4 macrophyte *Spartina alterniflora*, material derived from C_3 macrophytes (*e.g. Juncus roemarianus)*, allochthonous contributions from terrestrial C_3 upland plants, and organic matter from phytoplankton [*Gebrehiwet et al.*, 2008]. Although significant amounts of organic carbon are present in the soil, some of the material is relatively inert. Soil organic matter is made up of two pools that vary in their rate of decomposition or turnover. The labile pool turns over relatively rapid (less than 5 years) whereas the refractory pool time scale is 20 to 40 years [*Hoyle and Murphy*, 2006]. The labile pool results from the addition of fresh residues, including plant roots and organisms. Unlike the refractory pool, which has physical or chemical attributes making it resistant to decay, the labile fraction does not significantly contribute to carbon sequestration.

Studies have recently focused on wetland soil carbon dynamics and the influence on the global carbon cycle. Despite the importance of wetlands for carbon sequestration, few studies have explored the biogeochemical transformations of organic carbon and carbon sequestration with salt marsh platform evolution. A number of modeling studies have incorporated feedbacks between vegetation and sedimentation [*e.g.*, *Mudd et al.*, 2004; *D'Alpaos et al.*, 2007; *Kirwan and Murray*, 2007] to understand the sensitivity of wetlands to sea-level change. *Kirwan et al.* [2010] recently demonstrated that under conservative sea-level rise estimates, wetlands with low sediment availability and low tidal ranges are vulnerable and may drown, whereas wetlands with higher sediment availability are more likely to survive. Many of these studies and modeling efforts, however, neglect to incorporate

belowground organic processes, including belowground biomass production and organic matter decay. Belowground carbon decay can influence the interpretation of ^{210}Pb and ^{137}Cs, two radioisotopes commonly used to date the age of marsh sediments. Marsh sediment age can be used to constrain accretion rates, which has implications for assessing the ability of a marsh platform to keep up with changes in sea level. *Turner et al*. [2006] observed that in a large number of reported marsh age and sedimentation rates, the accretion rate based on ^{137}Cs outpaced the accretion rate estimated by ^{210}Pb. *Mudd et al*. [2009] demonstrated how this difference in estimated accretion rates is likely a result of organic decomposition.

Coastal marshes have been shown to expand landward in response to sea-level rise, resulting in the conversion of high marsh to low marsh [*e.g. Warren and Niering*, 1993]. Studies also suggest that carbon storage is greater in low marshes due to a larger quantity of soil organic matter [*Craft et al*., 1991], increasing marsh age, and hydroperiod [*e.g. Craft et al.,* 1988]. This suggests that sea-level rise and the associated shifts in plant communities could have important consequences for overall wetland contributions to the global carbon cycle. Field data from Pine Knolls Shore, North Carolina were collected and analyzed for this study to further test the models developed in *Chapter 5*, focusing on the ability of the models to reproduce marsh stratigraphy measured in the field. *Chapter 5* was recently published [*Mudd et al*., 2009], wherein two models are presented that examine the influence of organic deposition on the interpretation of dating methods and examine the relative balance and feedbacks between organic and inorganic sedimentation on coastal salt marshes. We call these models OIMAS-A and OIMAS-N (Organic-Inorganic Marsh Accretion and Stratigraphy-Analytical and Numerical, respectively). The models were initially developed

and calibrated using data from North Inlet, South Carolina, where data have been collected for more than 15 years. Here, sediment deposition based on ^{210}Pb and organic carbon content with depth for five marsh sediment profiles are used to further examine how organic deposition may influence the interpretation of radioisotope dating methods. In particular, we examine the mass fraction of deposited organic matter that goes into the refractory pool of carbon and possible enrichment of ^{210}Pb using the OIMAS-A. This approach of detailed field data analysis and model parameterization is used to further understand the process of carbon sequestration on salt marsh platforms.

2. Field Setting and Geomorphology

The study area is located at Pine Knolls Shore (PKS), North Carolina, USA. PKS is located on the back bay of Bogue Banks, an east-west trending barrier island ranging from 0.1 to 1.5 km in width, and separated from the mainland by a shallow sound (1 to 2 m deep). The PKS section of Bogue Banks is amongst the widest along the island, and contains a ridge and swale topography, characteristic of a regressive barrier. The PKS site is sediment starved because the wide and high-elevation ridge and swale morphology separates it from the open ocean, preventing overwash of beach sediments (Fig. 1). The landward margins at the site are therefore stalled, and the marshes are shrinking [*pers. comm D. Kunz*]. This is exacerbated by the low inorganic sediment budgets of North Carolina estuaries [*e.g. Wells and Kim*, 1989; *Phillips*, 1992]. The study site is dominated by the macrophytes *Spartina alterniflora, Spartina patens,* and *Juncus roemarianus*. *S. alterniflora* is a low marsh grass

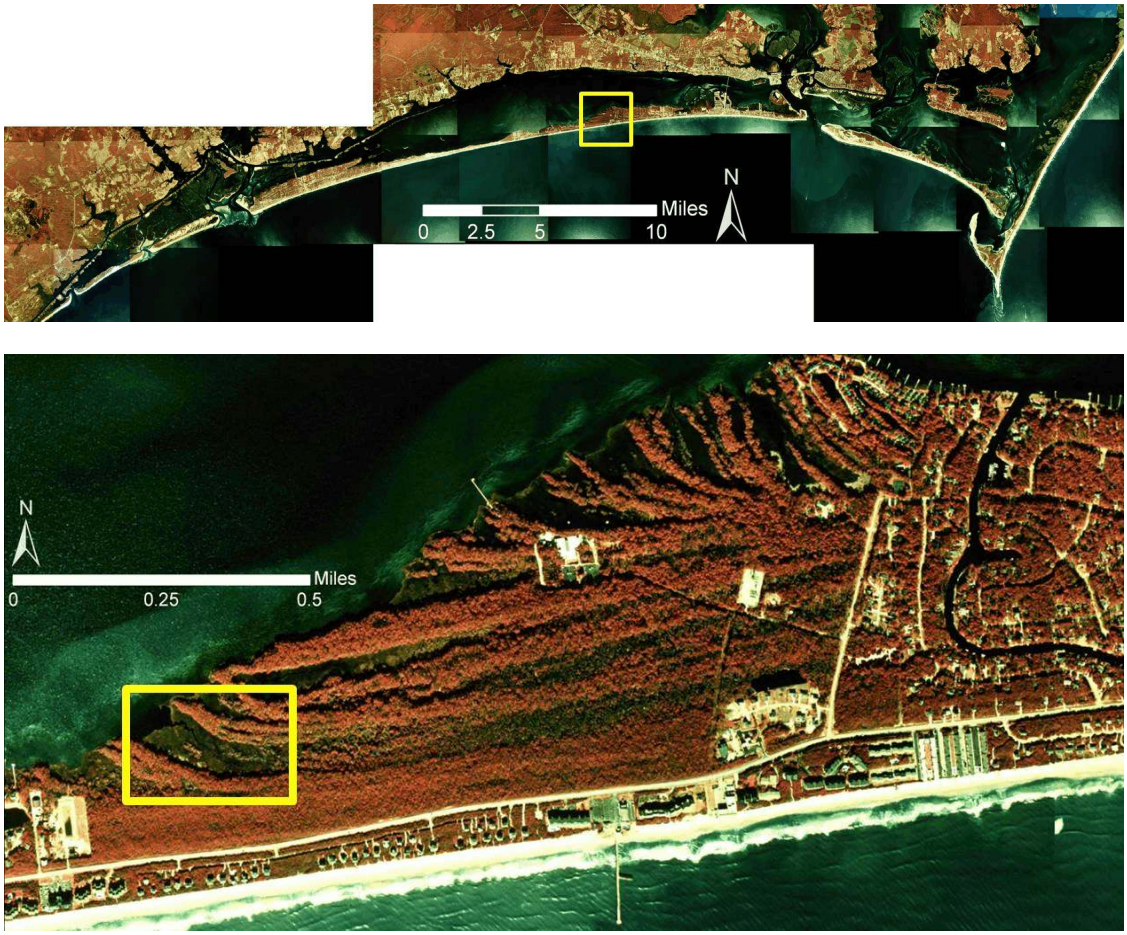

Figure 1. Overview of the PKS study site location located at the northern Outer Banks, on the east-west trending barrier Bogue Banks (*top*). The back barrier of the island is characterized by ridge and swale topography. The study area is outlined in the yellow box (*bottom*).

able to tolerate prolonged tidal inundation due to extensive aerenchymatous tissue that supplies oxygen to the roots. The upper flat surface of the high marsh, subject to less inundation, is colonized by *S. patens*. *J. roemerianus* is a high marsh rush that grows tall and occurs as dense patches restricted to elevations close to spring high tide and occasionally as monotypic stands along creek banks. The PKS marshes are relatively young and dynamic, and are likely a consequence of sea-level rise and recolonization. Aerial photographs dating

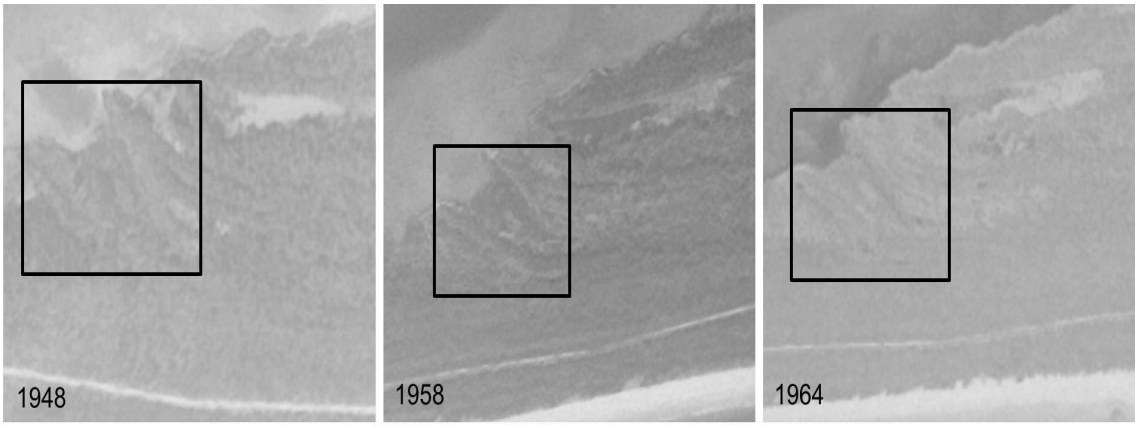

Figure 2. Aerial photographs of the PKS site used to assist with characterization of the geomorphic setting. The tidal creek that runs through the study area is located within the black box in each image.

back to 1942 were obtained from the USGS Earth Explorer; the black and white aerials are poor resolution, such that marsh extent is difficult to decipher. Nonetheless, the photographs reveal the presence of a much narrower tidal channel that runs through the study site (Fig 2).

Five cores were collected along a transect on the marsh platform with a bisecting tidal creek (Table 1). The marshes are natural and underlain by mineral soils. The depths from surface to sand for the cores collected at the site range from 31 to 43 cm, with the *Juncus* site containing the greatest extent of organic matter. Decomposing plant stems were observed in the sand layer for all cores (Fig. 3). Cores 1 and 2 from *Spartina* plots contained dense root mass to approximately 8 cm, with less dense roots to approximately 30 cm. Core 1 transitions to predominantly clean and sorted sand at approximately 30 cm, which is indicative of relict beach sand. Core 5 from the *Juncus* site contained dense root mass to 6 cm, followed by large woody stems to 16 cm and unconsolidated sediment to 30 cm. Core 3, located at a mudflat adjacent to the creek, contains root mass under the sediment surface, with decreasing plant matter at 15 cm. This is underlain by medium to fine sand and woody

debris from 20 to 40 cm. Organic matter for all cores was analyzed by loss-on-ignition (LOI, described below). Organic matter at the surface is lowest at the tidal creek and high elevation *Juncus* site (Fig. 4a). We attribute the low organic matter at the surface of the *Juncus* sites as resulting from removal of the woody plant stems before laboratory analysis. Grain size analysis was performed using a Malvern Mastersizer at Vanderbilt University. The percent of sand at the surface decreases with distance from the creek (Fig. 4b) and the percent of sand increases with depth for Cores 1,3, and 5.

Table 1. Notation and location of cores collected at PKS. Cores are analyzed for radioisotope dates (sediment accretion rates) and organic carbon.

Core	Macrophyte	Depth to Sand [cm]	Location
C1	*Spartina*	36	Near forest, 60 m north of creek
C2	*Spartina*	31	Mid platform, 50 m north of creek
C3	Mud	39	Adjacent to the creek (~7 m)
C4	*Spartina-Juncus* Boundary	40	Higher elevation, 22 m south of creek
C5	*Juncus*	63	Near *Distichlis* and woods, higher elevation, 60 m south of creek

In addition to the cores, five Surface Elevation Tables (SET) were installed at PKS. The SETs were installed at plots with macrophyte species and densities representative of the field site— *Spartina alterniflora* fertilized and unfertilized low vegetation density, *Spartina alterniflora* unfertilized tall, dense vegetation, and *Juncus roemerianus* fertilized and unfertilized. The "fertilized" test plots consist of plots with nitrogen fertilization (2 kg of Miracle Gro), used to understand the influence of increased biomass and sediment deposition. *Voss* [2010] collected soil profiles from each SET using cores 7.4 cm in diameter and 30 cm in length for her dissertation research.

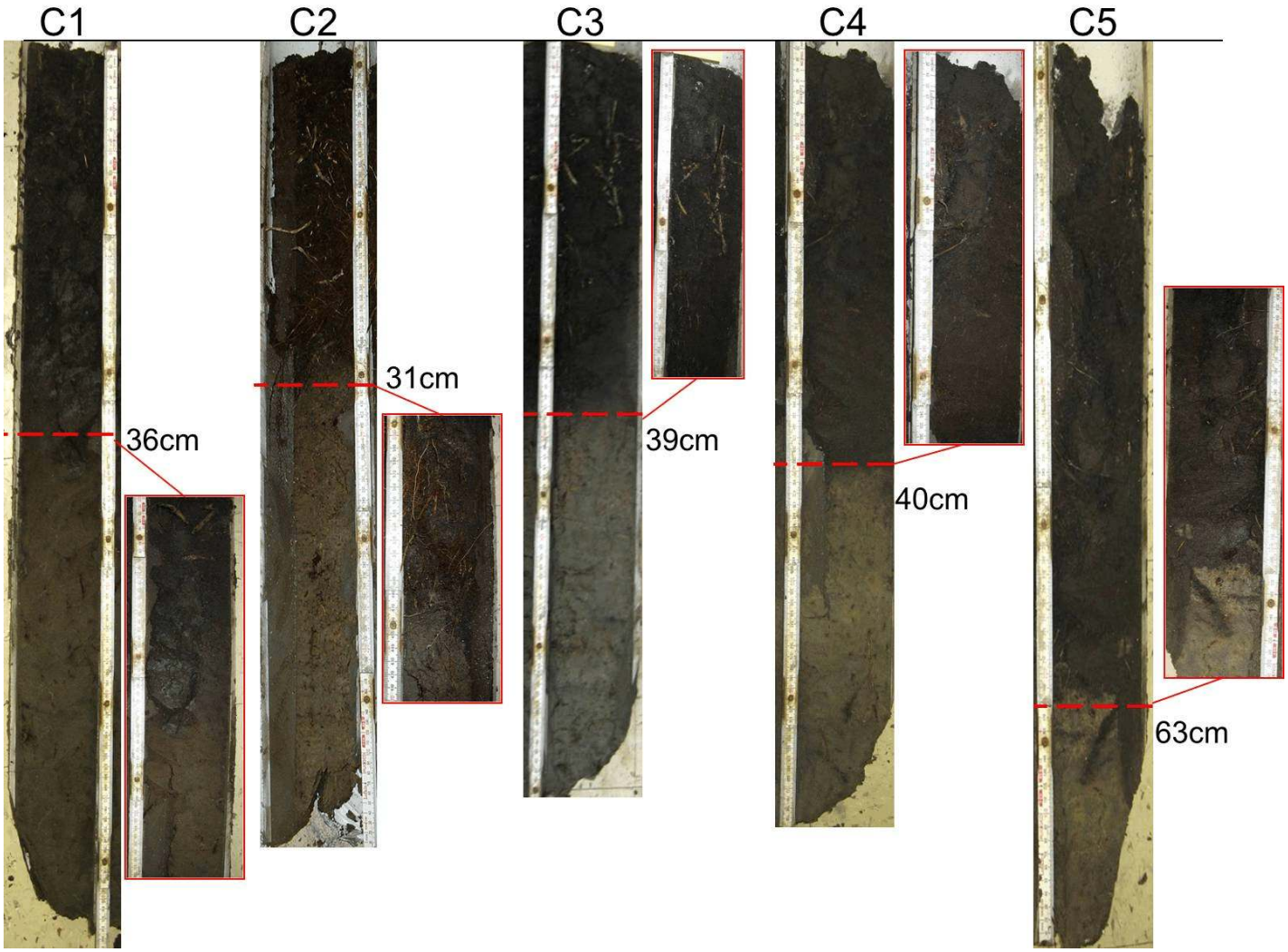

Figure 3. Profiles of each core showing the depth to sand from the marsh surface. Adjacent images show the mud-sand contact or organic matter.

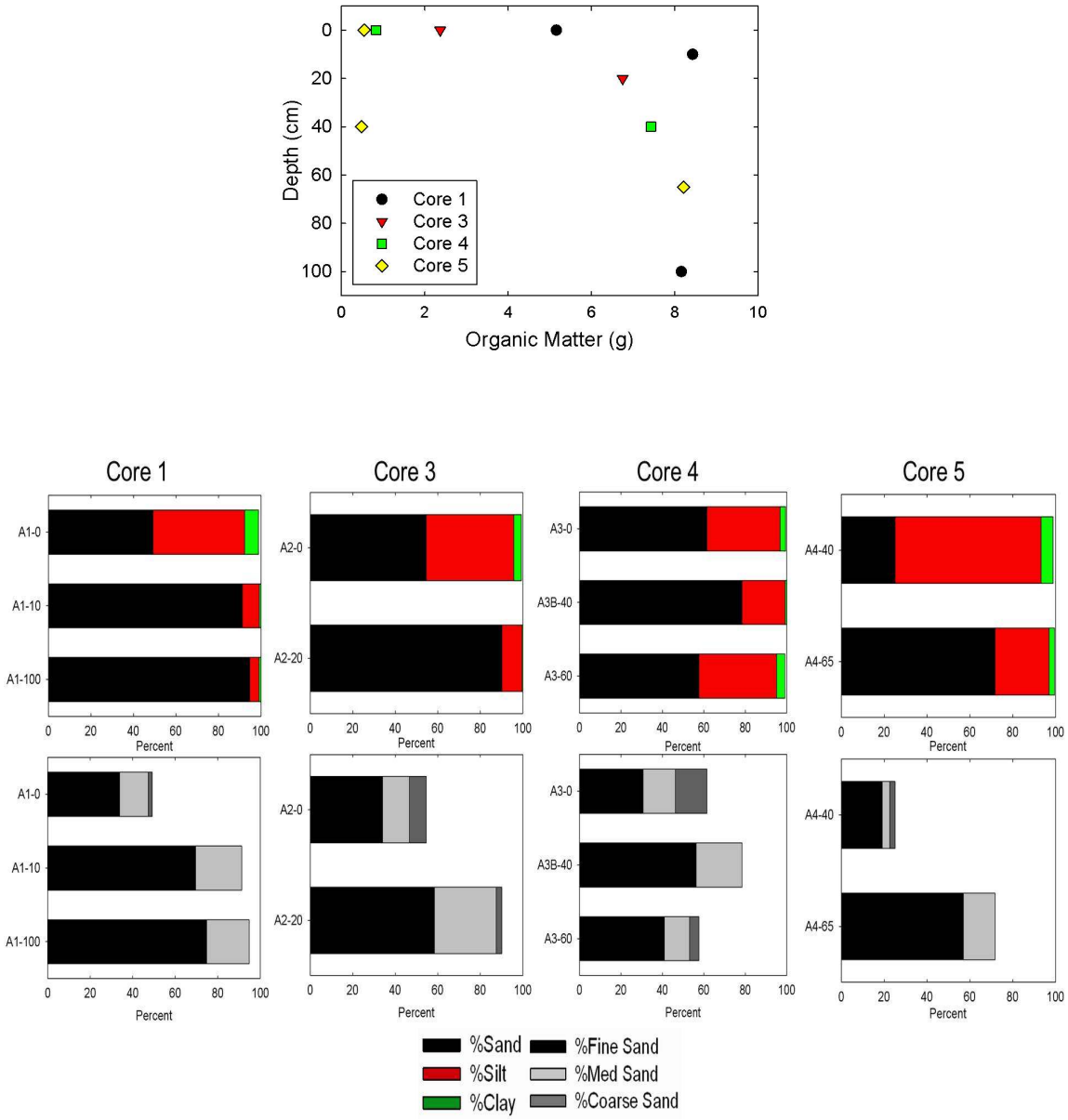

Figure 4. (a) *Top*, organic matter from loss-on-ignition sampled at depth; (b) *Bottom*, grain size analysis with depth (n = 3). Results are reported as percentage sand-silt-clay (top) and percentage sand size (bottom).

3. Methodology

Field campaigns were conducted from the 2006 growing season to the end of 2009. Five PVC cores with dimensions of 10 cm diameter and 127 cm length were collected along a transect at PKS (Fig. 5). The cores were split in half by cutting horizontally down each side, and slicing the cores with a thin wire. Subsamples were taken at 2 cm increments for Carbon-Hydrogen-Nitrogen (CHN) measurements, ^{210}Pb and ^{137}Cs radioisotope dating, and organic content using LOI. A measured volume of material from each 2 cm section of known diameter and thickness was sampled for bulk density. The samples were dried at 105° C to constant weight to calculate the moisture content. Samples for radioisotope and carbon analysis were dried and homogenized in a mortar. Sediment deposition and accretion rates were measured using sediment tiles and SETs. Biomass was measured along the core transect, including stem counts per unit area in the field and LOI determined in the laboratory.

3.1 Carbon-Hydrogen-Nitrogen Analysis

Organic matter in sediments is commonly measured via bulk organic matter using loss-on-ignition (LOI) or wet oxidation [*e.g. Dean*, 1974; *Byers et al.,* 1978; *Dankers & Laane,* 1983]. Thermal methods (*e.g.* LOI) aim to separate organic carbon from inorganic carbon; when sediment samples are heated, the combustion of organic carbon typically occurs at temperatures less than 550° C, whereas inorganic carbon is combusted at temperatures greater than 400°C. Acids commonly used in the wet oxidation approach are

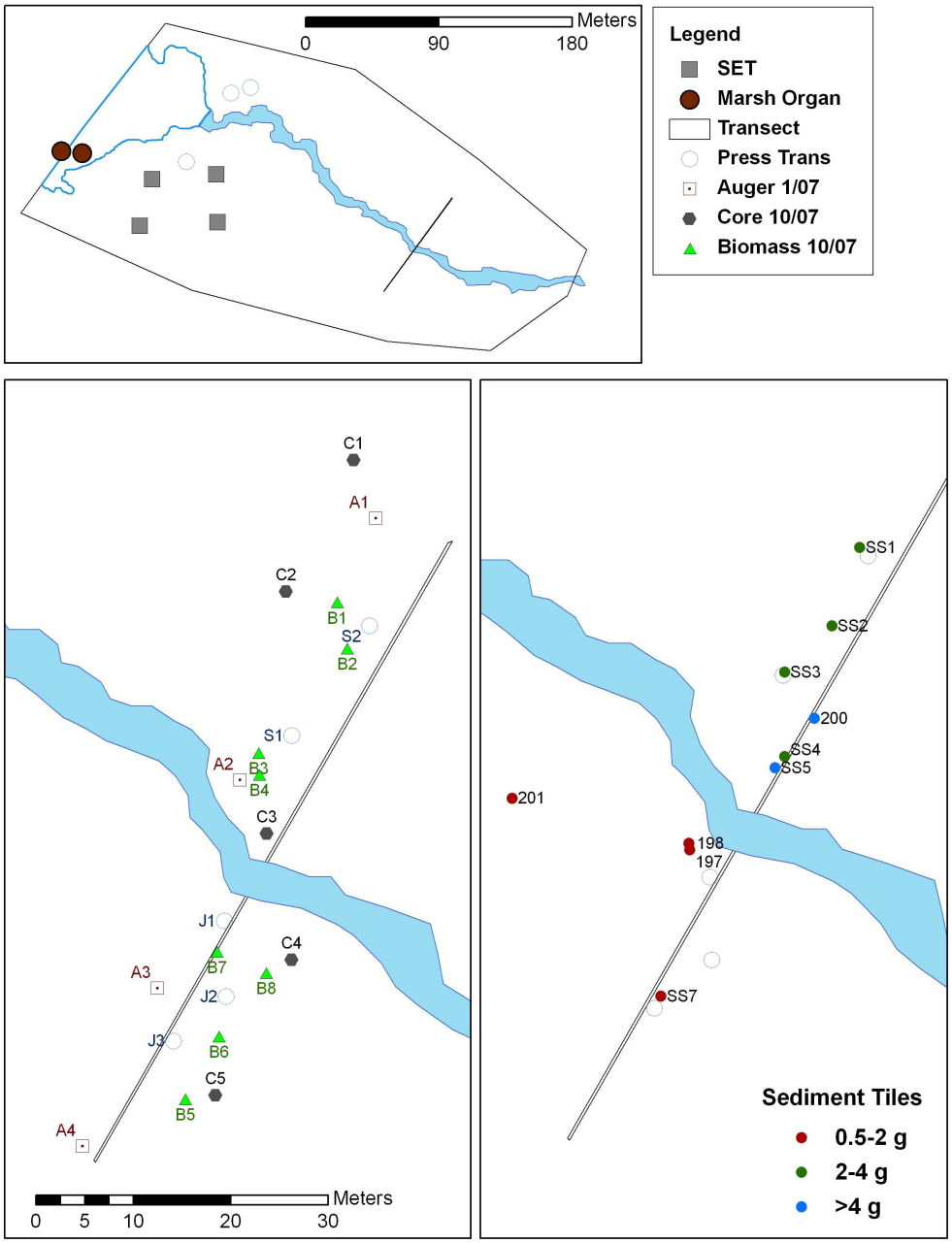

Figure 5. Map of the field data sampling locations and date of collection. The SETs and marsh organs are located closer to the sound than the sampling along the transect, positioned at the interior marsh. Data reported here were acquired along a transect that spans *Spartina alterniflora* and *Juncus roemarianus* on the other side. The sediment tile figure reports the measured weight of sediment accrued over one year.

non-oxidizing, such as hydrochloric [*Hedges and Stern*, 1984], phosphoric [*Froelich*, 1980], and sulphurous [*Verardo et al*., 1990]. Another method to measure carbon content is the automated Carbon-Hydrogen-Nitrogen analyzer (CHN), which detects the gaschromatic combustion products CO_2, N_2, and H_2O. Whereas this method requires only a small sample (less than 100 mg) and provides for simultaneous analysis of carbon and nitrogen, all carbons forms are combusted and measured as total carbon by CHN-analyzers. However, samples can be pretreated and run separately (*e.g*. LOI and wet oxidation)[*e.g*. *King et al*., 2008].

Laboratory analysis of organic carbon and nitrogen in this study follows the technique described by *Verardo et al*., [1990]. Samples were analyzed at Hancock Biological Station, KY with the Perkin Elmer Series II CHNS/O 2400. This method analyzes total carbon, nitrogen, and sulfur in solid samples by flash combustion. Organic and inorganic forms of carbon were separated prior to analysis without the loss of nitrogen via removal of carbonate carbon by acidification with sulfurous acid in situ within aluminum sample cups (pipet 20 µl 6% sulfurous acid diluted to 3%). Sulfurous acid is used in decarboxylation because it eliminates the need for drying and re-weighing residuals and it is a non-oxidizing acid which breaks down to H_2O and SO_2 upon drying. The holding block of samples was placed on a heated pad until dry. The response of the Perkin Elmer Series II CHNS/O 2400 is calibrated for each set of samples using three blank aluminum cups, one Conditioning Agent (2.852 mg), and one Acetanilide standard (0.5 to 1.5 mg). The known standard is used to calibrate the analyzer to micrograms, and the calibration factor is then used to calculate the unknowns. The table of data output is provided in Appendix E.

3.2 Macrophyte Stem Density

Stem densities were measured in August 2007, near the end of the peak growing season. Stem density was measured using 625 cm^2 quadrants thrown at the point of sampling, and all grass within the quadrant was counted and clipped. Upon returning to the lab, vegetation was rinsed, recounted and separated into dead and living groups. The living group was further sorted into short (0 to 40 cm) and tall (greater than 40 cm) subgroups, and all vegetation was dried and weighed to determine the biomass within each group. Heights were recorded so that the average weight per stem and weight per linear centimeter may be calculated. Each subgroup was placed into a pre-weighed aluminum foil pouch and dried at 80° C for 48 hours. Biologic demographic results are reported in Appendix F. Stem density is used in this contribution to understand sediment deposition, and is used explicitly in the numerical analysis.

3.3 Sedimentation Measures

3.3.1 Sediment Collection Tiles

Net rates of marsh sediment deposition were measured using 20×20 cm ceramic tiles flush with the marsh surface [*e.g. Pasternack and Brush*, 1998]. Sediment tile measurements include biannual measurements of sediment thickness on tiles and annual scraping of tiles for laboratory analysis (*e.g.* grain size, LOI, and sedimentation rates). Sediments were scraped and washed with deionized water into clean, pre-weighed Nalgen plastic specimen cups. Samples were dried at 50° C and weighed to calculate mass sedimentation rates.

3.3.2 Loss on Ignition

Loss on ignition is a quick and inexpensive method for measuring organic matter. Organic matter is indicative of the relative role of in situ biomass contributing to sediment accretion, which in turn provides an indication of the sedimentation rate. Samples were obtained from the marsh surface, cores, and sediment tiles. Samples were dried at 100° C, and the difference between the dried and weighed sample yields the water content. Samples were then placed in a muffle furnace at 450° C for 8 hours to yield the organic content (*see* Appendix G) [*e.g. Craft et al.*, 1991].

3.3.3 Surface Elevation Tables (SET)

A concurrent collaborative study, led by Don Cahoon at the USGS, established five Surface Elevation Tables (SETs) at PKS in June 2006. Because subsurface processes can exert significant influence over sediment elevation in wetland systems, SETs are used to quantify elevation change over different portions of a sediment profile (Fig. 6) [*e.g. Cahoon et al.,* 1999 and 2000]. Feldspar marker horizons were applied to the marsh surface and may be used in conjunction with the SETs to provide information on belowground processes that influence elevation change. Field and laboratory SET analysis was conducted by *Voss* [2010], a collaborator teamed with the study, and relevant results are summarized here.

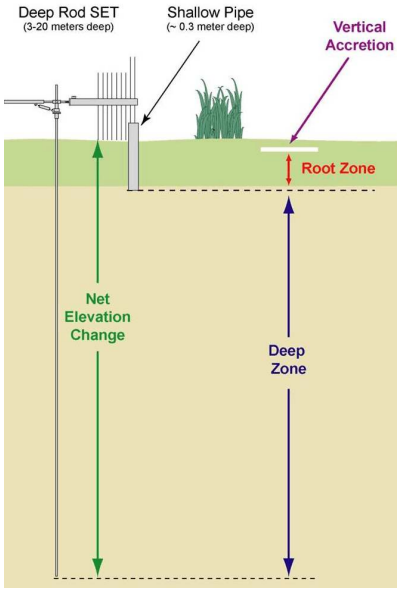

Figure 6. Surface Elevation Table measurement capabilities as developed by Don Cahoon [*e.g. Cahoon et al.,* 1999 and 2000]. Elevation change is determined from the sum of calculated vertical accretion, root zone and deep zone.

3.4 Radioisotopes

Lead-210 (^{210}Pb, half life = 22.6 y) and Cesium-137 (^{137}Cs, half life = 30 y) are often used to date sediments up to 150 years old. Lead-210 occurs naturally as one of the radioisotopes in the ^{238}U decay series, and is removed from the atmosphere by precipitation. This unstable isotope accumulates in sediments and subsequently decays to a stable form of lead (^{206}Pb). Cesium-137 is a radioactive isotope of Cesium formed as a fission product during nuclear fission, and was introduced into the environment with the start of nuclear weapons testing. Dating is determined by locating the peak in ^{137}Cs with depth along a sediment profile, which correlates with the 1963 peak release of atmospheric ^{137}Cs concentration. The ^{137}Cs profile in a sediment column can be used to determine sediment accretion rates over the past 50 years. Isotopic analysis of cores was performed at Vanderbilt University using a high purity germanium planar gamma detector. Samples were analyzed at 2 cm intervals, from the surface to the mud-sand contact; each sample was processed in the detector for 24 hours. The total activity of ^{210}Pb was measured directly from the 46.5 kV gamma peak. Excess ^{210}Pb activity (unsupported ^{210}Pb) was determined for each sample by subtracting background activity (supported ^{210}Pb), calculated by proxy for effective parent ^{226}Ra, from total ^{210}Pb activity. Logarithmic plots of excess ^{210}Pb activity versus depth are used to determine variations in sedimentation rates and as input into the OIMAS-A model.

Two scenarios are often considered for the deposition of ^{210}Pb [*e.g. Appleby and Oldfield*, 1992]— the constant initial concentration (CIC) model and the constant rate of supply (CRS) model. The CRS scenario is based on the assumptions that ^{210}Pb is deposited at some fixed rate through time, the initial ^{210}Pb concentration in the sediment may vary, and

the influx rate of sediment may vary. With these assumptions, the concentration C of unsupported ^{210}Pb at depth x is

$$C(x) = C_0(t)e^{-\lambda_{210}T} \tag{1}$$

where

$$\lambda_{210} = \frac{\ln 2}{22.26} = 0.3114 \tag{2}$$

C_0 is the initial concentration, assumed to be the average surface sample activity, and T is time. Eq. (2) is the radioactive decay constant of ^{210}Pb. The excess ^{210}Pb inventory I [dpm cm^{-2}] is the product $Ax\rho_b$, where A is the activity [dpm g^{-1}] and ρ_b is the bulk density [g cm^{-3}]. It follows that the age at a given depth is determined from the inventory difference as

$$I(x) = I(0)e^{-\lambda_{210}T} = \frac{1}{\lambda_{210}} \ln \left(\frac{\sum_{x=0}^{n} I}{\sum_{x=0}^{I} I} \right) + \frac{I}{2} \tag{3}$$

where the summation in the numerator consists of the total unsupported ^{210}Pb in the sediment column (for sample size n) and the summation in the denominator is the total unsupported ^{210}Pb activity in the sediment column beneath depth x.

Conversely, the CIC model assumes that the vertical sediment accumulation rate will not affect the ^{210}Pb concentration and that the concentration is constant. The CIC model results in a monotonic decline of ^{210}Pb concentrations with depth. According to *Appleby and Oldfield* [1983], the age of sediment layers with ^{210}Pb concentration is

$$T = \frac{1}{\lambda_{210}} \ln \frac{C(0)}{C} \tag{4}$$

4. Results

4.1 Sedimentation

Accretion rates from sediment tiles along the core sampling transect are reported here (Table 2). Cores 1 and 2 are located in *Spartina alterniflora* and Cores 4 and 5 in *Juncus roemarianus*. Sedimentation is greatest at Core 3, the mudflat adjacent to the creek, and surface sedimentation rates decrease away from the creek. Accretion rates are low at the high elevation *Juncus* site (Core 5), attributed to the irregular flooding (see *Chapter 2*). Our results agree with field studies that have demonstrated that the supply of inorganic sediment decreases with distance from marsh creeks [*e.g. Temmerman et al.*, 2003; *Chmura and Hung*, 2004].

Voss [2010] measured the PKS SETs for her dissertation and analyzed sedimentation, bioaccretion at the surface and root zone, decomposition, erosion, shallow and deep subsidence, and compaction of soils. Relevant data used in the sections below are summarized in Figure 7. For example, the shallow SET data inform the role of soil organic matter accumulation with regard to elevation change. Accretion rates, organic matter, stem density, and elevations from the SETs are shown in Table 3. The LOI from each SET is reported as the average from three cores each with two replicate samples. The fertilized plot with sparse *Spartina alterniflora* contained the greatest organic matter and the unfertilized *Juncus roemerianus* had the least organic matter. Average accretion rates determined from the feldspar marker horizons were 8.90 mm yr^{-1} for the fertilized plots and 4.80 mm yr^{-1} for the unfertilized plots. The SET data suggest that the PKS marshes are net erosional.

Table 2. Accretion rates and LOI from sediment tiles and biomass and live aboveground biomass per unit area. Samples collected adjacent to core sampling locations.

Sample	Biomass (stems m^{-2})	Accretion Rate (mm/yr)	LOI	Bio Wt (g/m^2)
C1	416-560	0.29	6.63	260.14
C2	270-320	0.44		155.84-198.85
C3	--	1.27-5.50	8.92-11.23	--
C4	144-272	0.66		351.55
C5	320	0.12	30.27	450.45

Table 3. Results from the SET core LOI (g) analysis, with the mean percent organic matter as a proportion of 1.0 in parenthesis. The five samples are denoted below as *Sp* (*Spartina*), *Ju* (*Juncus*), UF (Unfertilized), F (Fertilized), S (Sparse stem density), and D (Dense stem density). The upper 1 cm is reported as the top, the next 14 cm as middle, and the third fragment consisted of remains and generally included 16 to 20 cm depth. Stem density is also reported for the five SET plots. Accretion rates are from 2006 to 2008 measurements.

	***Sp*-UF-S**	***Sp*-UF-D**	***Sp*-F-S**	***Ju*-UF**	***Ju*-F**
Top	1.026 (0.240)	0.758 (0.309)	1.160 (0.235)	0.450 (0.060)	0.638 (0.199)
Middle	1.451 (0.470)	1.228 (0.476)	1.240 (0.360)	0.753 (0.095)	0.757 (0.234)
Bottom	1.404 (0.484)	1.844 (0.475)	2.170 (0.473)	0.546 (0.068)	1.071 (0.275)
Biomass (stems m^{-2})	450-600	690-975	460-750	735-2500	2600-3440
Accretion (mm/yr)	12.578	2.505	11.22	4.802	6.756
Elevation (mm)	4.75	-6.17	9.61	6.71	3.54

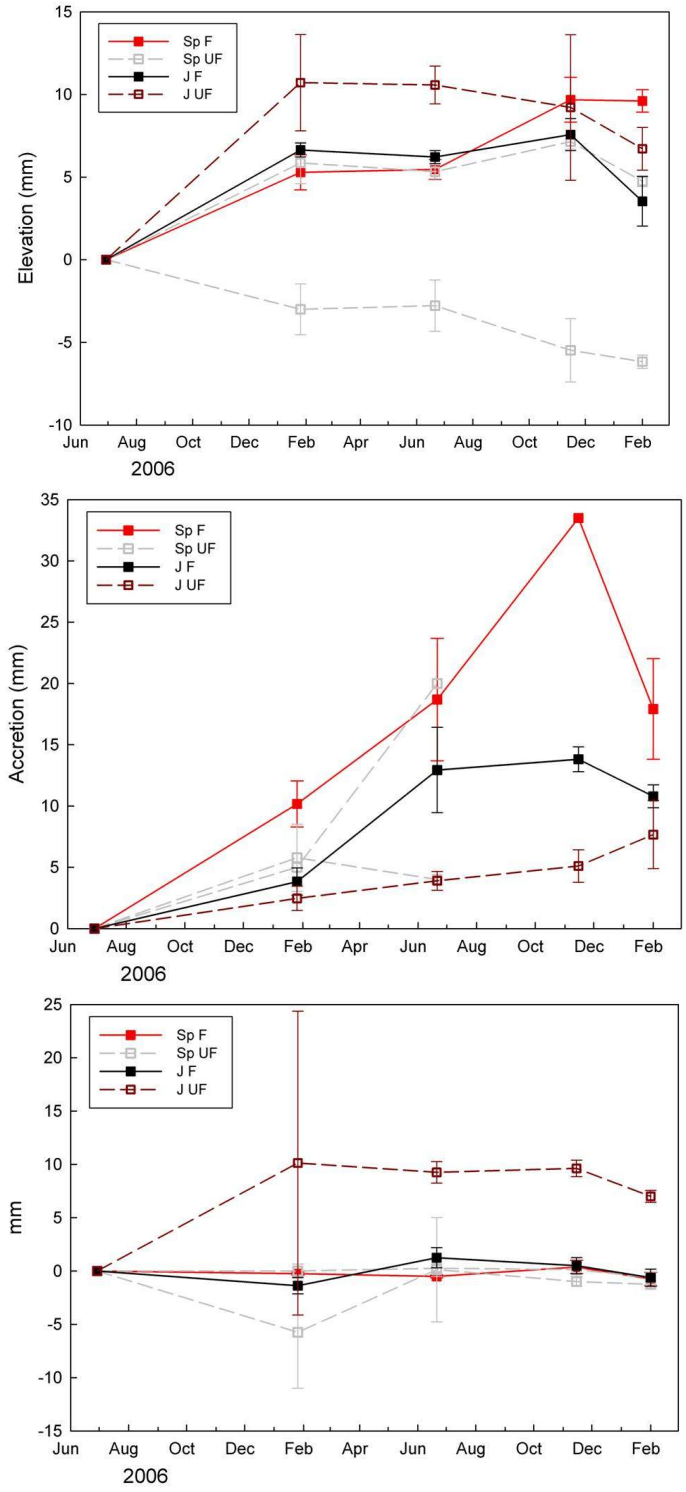

Figure 7. SET accretion data from *Voss* [2010]. (*top*) SET elevation shows deposition and erosion on the surface; (*middle*) feldspar marker horizon shows vertical accretion; (*bottom*) deep rod SET used to determine if subsidence is occurring.

4.2 Radioisotopes

Vertical profiles of the measured activities of ^{210}Pb and ^{137}Cs are shown in Figure 8 and provided in tabular form in Appendix H. The inflections in Cores 2 and 3, where Lead concentrations increase with depth at approximately 20 and 12 cm, respectively, may result from a change in the sedimentation rate. The accretion rates differ with inclusion and exclusion of these points; results reported here refer to these data values being excluded in the accretion calculations and the OIMAS-A model since the model assumes that sediment is accreting at a constant rate. The concentration of ^{210}Pb and ^{137}Cs with depth follow a similar pattern, appearing to increase and decrease in concentration at similar depths in Cores 1, 2, and 3. The concentration of ^{210}Pb and ^{137}Cs do not appear related, however, for Cores 4 and 5. Furthermore, the maximum concentration of ^{210}Pb inventories can be separated by plant species and location (Table 4), wherein the *Juncus* and higher elevation cores contain greater maximum concentrations of ^{210}Pb. These observations suggest differing ^{210}Pb inputs between Cores 1-3 and Cores 4 and 5. Because the ^{210}Pb and ^{137}Cs increase and decrease following a similar pattern with depth, these sediments were likely homogenized over the past 100 years. The source of Lead for Cores 1-3 is not likely atmospheric fallout onto the platform, but sediment exposed to water subject to atmospheric input and later resuspended from the bay. Cores 4 and 5, however, suggest atmospheric input and decay.

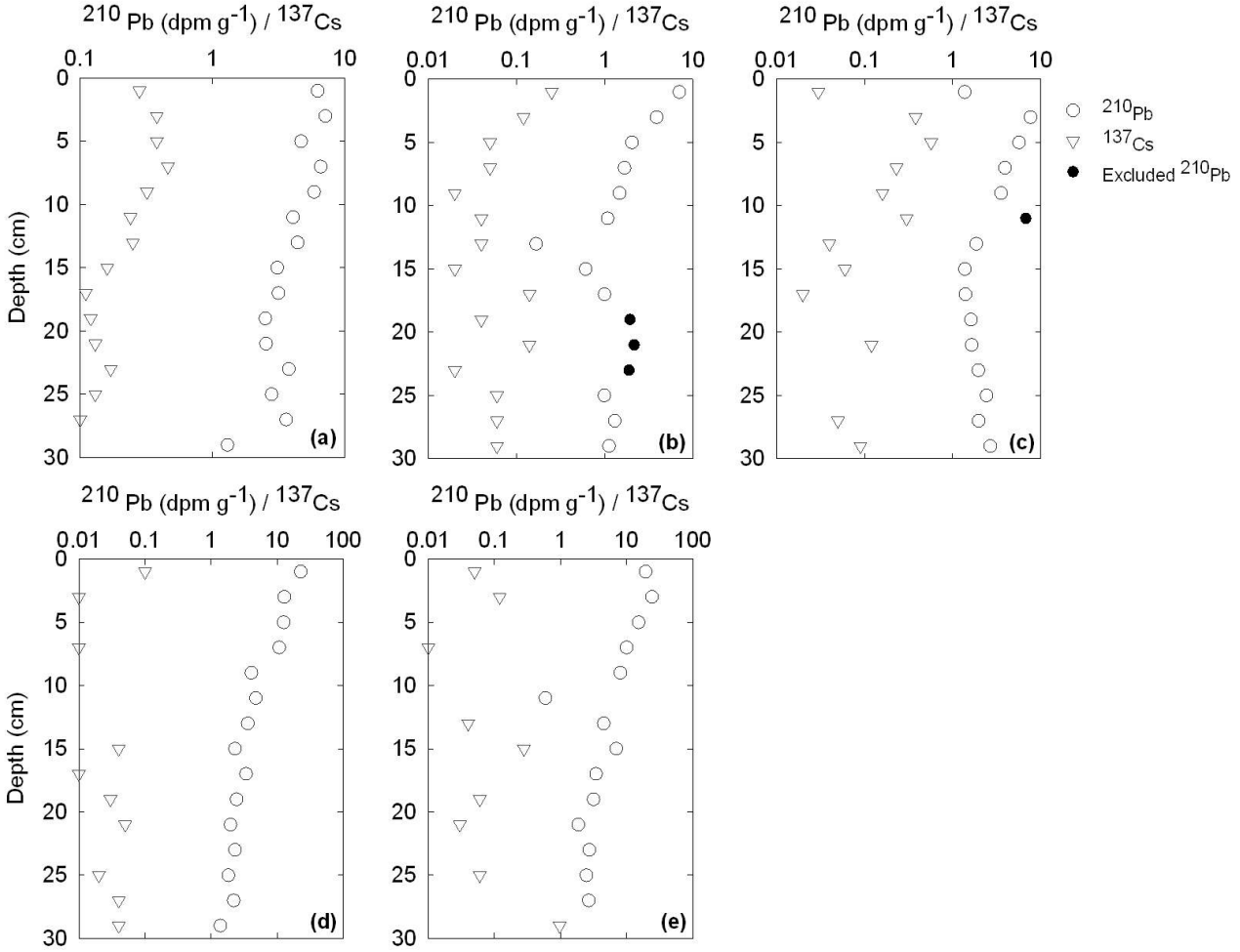

Figure 8. Radioisotope plots with units of disintegrations per minute per gram, (a) Core 1, (b) Core 2, (c) Core 3, (d) Core 4, and (e) Core 5. The data points noted as excluded indicate a change in the sedimentation rate, and were removed for OIMAS-A analysis.

Table 4. Radioisotope activity (dpm/g) and accretion rates. The ^{210}Pb accretion rates are determined from Eqs (3) and (4), and the ^{137}Cs peak from an apparent peak or at the maximum depth when a peak is not present.

Sample	Maximum Concentration (dpm/g)	Pb CIC Rate mm/yr	Pb CRS Rate mm/yr	Cs Rate mm/yr
C1	7.1	0.510	0.460	1.489
C2	7.0	0.150	0.281	0.212
C3	7.6	0.222	0.211	1.063
C4	22.5	0.305	0.337	0.212
C5	24.2	0.178	0.417	6.17

The CRS model assumes that ^{210}Pb is deposited at a fixed rate such that the concentration in surface sediments is inversely proportional to the accretion rate. The increase and decrease in ^{210}Pb concentration with depth for Cores 1-3 may result from differential rates of sediment accumulation. Greater accumulations in ^{210}Pb result from slow sedimentation rates or resuspension of an upper layer with younger atmospheric fallout, and less accumulation of ^{210}Pb may represent diluted concentrations resulting from fast sedimentation or resuspension of lower layers where the ^{210}Pb has decayed. However, neither the CRS or CIC models can be justified for Cores 1-3 because the source does not appear to be atmospheric. Nonetheless, because ^{210}Pb and ^{137}Cs track one another with depth the concentrations are not a result of dilution due to pore water diffusion. Accretion rates calculated using the CIC and CRS models for Core 3 are much lower than those measured from the sediment tiles. Cores 4 and 5 are organic rich, and suggest atmospheric input and atmospheric decay. These cores are closest to the CIC model. Accretion rates from the CIC model correlate well with those determined from the sediment tiles for Cores 4 and 5 (Table

3).

All cores contain measurable ^{137}Cs at depth, suggesting a possible age of 1950 or younger; however, an obvious ^{137}Cs peak is not present in any of the cores. Accretion rates from ^{137}Cs are calculated here from an apparent peak or at the maximum depth when a peak is not present (Table 4). Where ^{137}Cs is present at the surface, the source of Cesium is likely anthropogenic, possibly resulting from upland erosion. *Kim et al*. [1997] suggests that sedimentation rates from ^{137}Cs present in sediments older than 50 years may be compromised by the post depositional mobility of ^{137}Cs in salt marsh sediments. Although the degree of ^{137}Cs mobility is contested, it is likely that distributions of ^{137}Cs can be affected significantly by the marsh hydrology and presence of vegetation (*e.g*. salinity changes and pore fluid movement). Further, *Davis et al*. [1984] suggest that ^{137}Cs may become mobile upon decomposition of the organic phase. Small but detectable activities of ^{137}Cs in sediment intervals older than 1940 have also been attributed to a low abundance of clays [*Schottler and Engstrom*, 2006] and high input of sediment from tidal waters that dilute the concentration of atmospherically derived nuclides [*e.g. Conner et al.,* 2001]. The penetration of ^{137}Cs beyond the length of the core can also be attributed to the detection of very low ^{137}Cs, which is often at or below the limits of analytical detection [*e.g. Swarzenski et al.,* 2006]. The authors define the detection limit for ^{137}Cs as 2 times the average of background counts at ±5 kev from the limits of integration centered at 661.62 kev.

4.3 Carbon Analysis

Organic carbon was measured in a sediment profile to assist with interpretation of the OIMAS-A model output and for input into the OIMAS-N model. The greatest organic carbon concentrations are present in a layer of sediment near the surface where labile carbon is present. The peak in each core corresponds to the bottom depth of dense root mass. Below this peak and at the contact with the underlying sand layer, the carbon content diminishes with depth (Fig. 9). The peak is much deeper for Cores 4 and 5, located at the *Juncus site*, where the cores contain organic matter over a greater depth. The percent organic carbon content decreases because all labile carbon is consumed by decay processes (*e.g.* aerobic and anaerobic microbial decomposition) [*Jørgensen*, 1983]. An exception to the peaks observed is Core 5, where no clear peak exists yet values do approach zero at depth. The sediment profile shows dense root mass from the surface to 60 mm, roots and large woody stems to 160 mm, and increasingly consolidated sediment from 180 to 300 mm.

The greatest peaks in the percent organic carbon (35%) occur at the mudflat (Core 3) and *Juncus roemarianus* site (Core 4), at a depth of 28 cm and 34 cm, respectively. In contrast, the peak in organic carbon at the adjacent *Spartina alterniflora* site is less (19%), with the peak at 10 cm depth. *Craft et al.* [1991] suggest that the proportion of organic carbon increases with soil organic matter, which is attributed to aging and the accumulation of reduced organic compounds, regardless of the organic carbon source. As a marsh ages, interaction of water saturated soils and net primary productivity deposition result in accumulation of soil organic matter. Over time, anaerobic decomposition produces reduced compounds that contain a higher carbon content than "fresh" plant tissue.

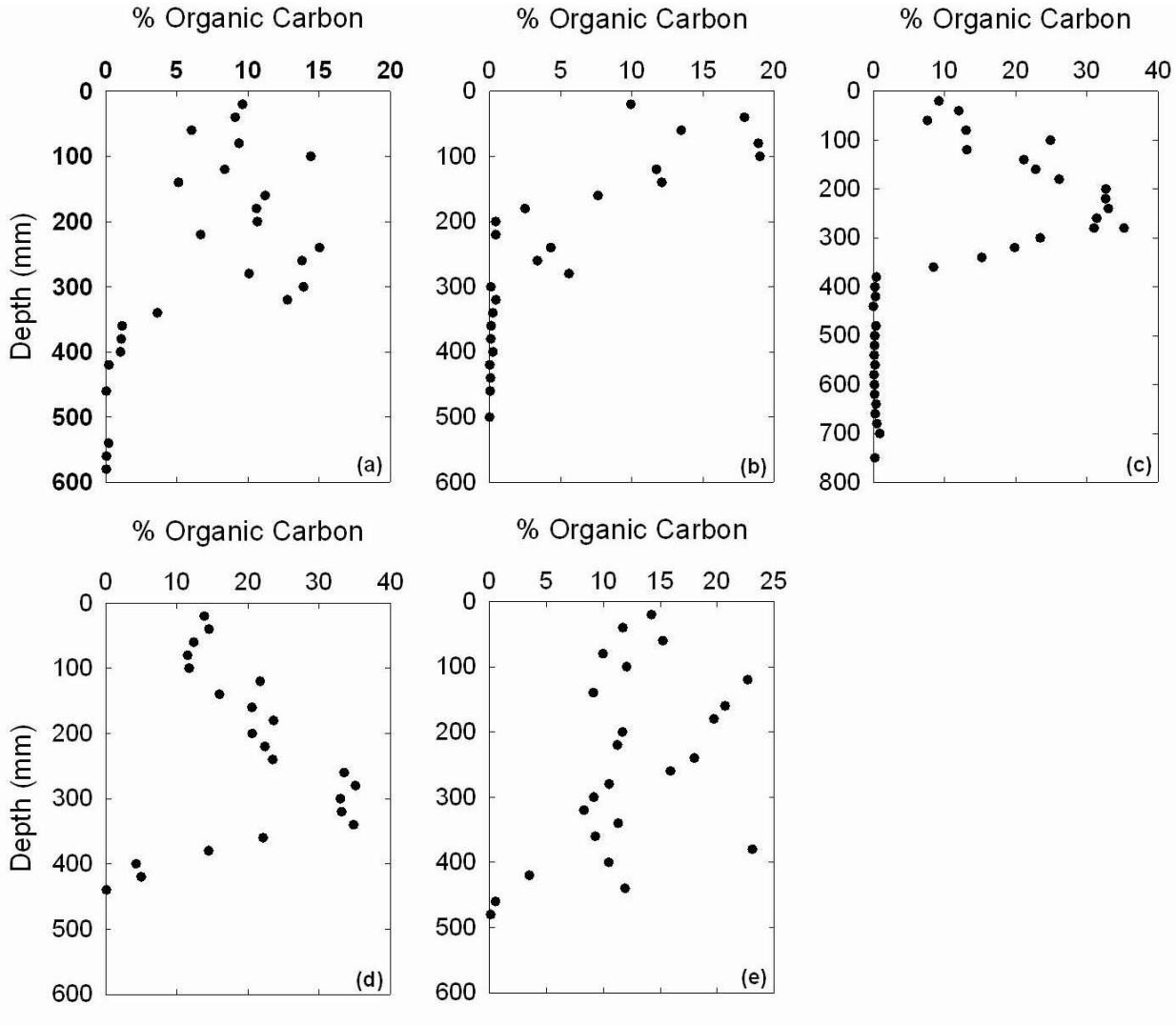

Figure 9. Profiles of percent soil organic carbon with depth for (a) Core 1, (b) Core 2, (c) Core 3, (d) Core 4, and (e) Core 5. Comparison of the above results to terrestrial soil organic carbon, where carbon content is less than 5 % at the surface [*e.g. Roseberry*, 2009], suggests that wetlands may exert a significant contribution to the global carbon budget.

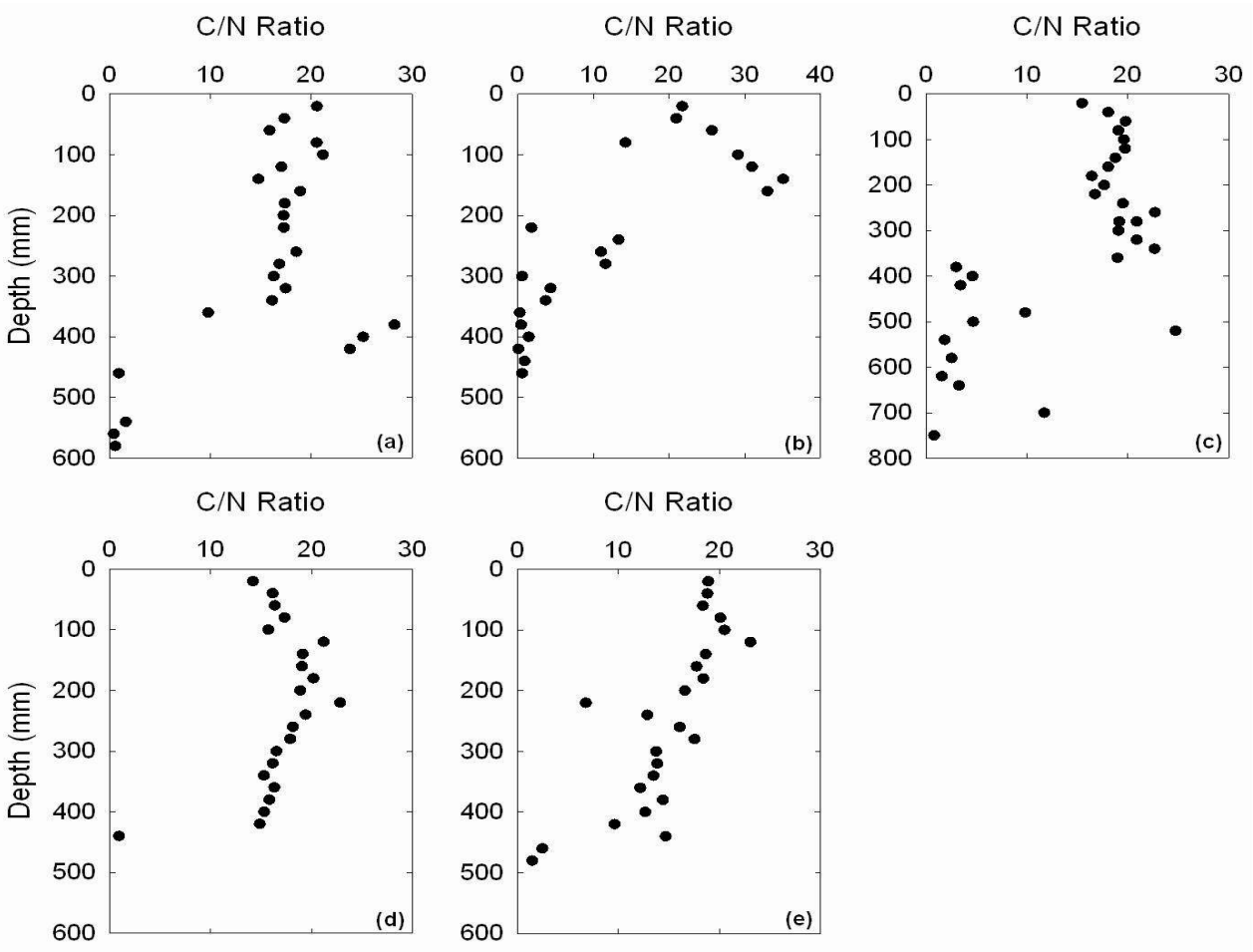

Figure 10. Carbon to Nitrogen ratio output from the CHN analysis, for (a) Core 1, (b) Core 2, (c) Core 3, (d) Core 4, and (e) Core 5. C:N provides an indication of organic matter decomposition and stabilization, where C:N decreases with an increase in decomposition. High input of recalcitrant residues increase C:N in the labile fraction, approximately C:N > 30, resulting in immobilization of nitrogen and making it unavailable for plant intake.

The Carbon-Nitrogen ratio (C:N) provides an indication of organic matter decomposition and stabilization. The amount of labile carbon influences both the activity and mass of micro-organisms in soil, which is important for the release of plant available nitrogen. The net release of nitrogen from the labile soil organic matter occurs at a C:N below approximately 22:1 [*Hoyle and Murphey*, 2006]. High inputs of more recalcitrant residues can increase the ratio of carbon to nitrogen in the labile fraction and can result in net immobilization of nitrogen, making it unavailable for plant uptake. Conversely, C:N decreases with an increase in decomposition. Typical C:N for soil organic matter range from 15 to 25 [*Nair et al*., 2001]. Plots of C:N from PKS are shown in Figure 10. The C:N indicate net mineralization (C:N < 20) of organic N or an equilibrium (C:N = 20-30) between mineralization and immobilization (microbial immobilization at C:N > 30). Likewise, C:N previously measured at PKS by *Craft et al*. [1991] ranged from 14.0 to 23.3.

5. Analytical Analysis

The analytical analysis examines the influence of organic deposition on the interpretation of ^{210}Pb and the relative balance and feedbacks between organic versus inorganic sedimentation on coastal salt marshes. In *Mudd et al*. [2009] we demonstrate factors that can lead to uncertainty in the interpretation of accretion rates using ^{210}Pb and ^{137}Cs, namely the enrichment of radioisotopes due to the loss of organic matter and the nonlinear relationship between depth in the marsh column and age of the sediments. If there is no decomposition of carbon and the marsh is steadily accreting, the relationship between

depth and age is linear. The radioisotope and sedimentation results presented above are used here to quantify the carbon and sediment accumulation rates. We begin with the assumption that the marsh platform is in equilibrium with sea-level rise. Therefore, the rate of sea-level rise *RSLR* [dimensions LT^{-1}] is the accretion rate at a given point on the platform. A decrease in the supply of inorganic sediment must be compensated by an increase in refractory organic matter R_{ref} [$MT^{-1}L^{-2}$]. We assume that sediment is accreting at a constant rate and the decay rate of labile organic matter does not depend on its depth below the marsh surface. The mass supply rate per unit area at which inorganic material is added to the marsh R_S [$MT^{-1}L^{-2}$] is also constant and is based on data from the SETs and sediment tiles. The total supply of mass to the marsh surface per unit area [$MT^{-1}L^{-2}$] is

$$R_{tot} = R_S + \frac{R_{ref}}{\chi_{ref}} \tag{5}$$

where χ_{ref} [dimensionless] is the fraction of deposited organic matter that goes into the refractory pool. Although the labile fractions do not contribute to carbon sequestration, there is some finite amount of labile organic matter stored in the marsh column. We solve for the mass of labile organic matter M_{lab} as well as the total sediment M_{tot} above a layer deposited at a given time. Used in conjunction with the density and porosity of sediments, M_{tot} can be used to find the depth x of layer for a given age,

$$x = \frac{R_s T}{\rho_s \phi} + \left(RSLR - \frac{R_s}{\rho_s \phi} \right) \left(T + \frac{\chi_{lab}[1 - e^{-k_{lab}T}]}{k_{lab}\chi_{ref}} \right) \tag{6}$$

where ρ_s is the density of the inorganic material [ML^{-3}], ϕ is the porosity of the marsh sediment [dimensionless], χ_{lab} is the fraction of deposited organic matter that goes into the

labile pool [dimensionless], and k_{lab} is the decay coefficient of labile organic matter [T^{-1}]. The percent of refractory material is backcalculated using Eq (6) since it can not be measured in the field because the marsh platform is relatively young, observed by the shallow organic matter profile underlain by sand, wherein carbon is detected throughout the extent of the organic material.

Simulations consist of varying combinations of the rate of sea-level rise, mass supply rate of inorganic sediment, and the fraction of deposited organic matter that enters the refractory pool. Parameters that remain constant are reported in Table 5. Simulations begin by scanning across a range of *RSLR*, R_s, and χ_{ref} for each core, relative to values observed from modern data. The effect of decomposition is demonstrated by plotting predicted ^{210}Pb concentrations for each of the PKS cores. The logarithmic ^{210}Pb profiles generated by the OIMAS-A model are compared to the measured data by quantifying the root mean square error (RMSE) between the measured and predicted Lead concentrations:

$$RMSE = \left[\frac{1}{n} \sum_{i=1}^{n} \left(\log Pb_{measured,i} - \log Pb_{modeled,i} \right) 2 \right]^{1/2} \quad (7)$$

where *Pb* has units of dpm g^{-1} and *n* is the number of samples in the core.

Table 5. Parameter values used in simulations.

Parameter	Definition	Value
κ	the decay coefficient of ^{210}Pb	0.0315 [y^{-1}]
ρ_O	density of organic matter	1200 [kg m^{-3}]
ρ_S	density of inorganic matter	2200 [kg m^{-3}]
ϕ	porosity	0.4
k_{lab}	decay coefficient of labile pool	0.2 [y^{-1}]

The best fit of the three parameters ($RSLR$, R_s, χ_{ref}) for each core are plotted in Figure 11. The parameter combinations producing the lowest RMSE for each core are listed in Table 6. The mass supply rates per unit area of inorganic sediment are based on field sampling over two years, yet the model spans a range of quantities to explore sensitivity. The R_s values reported in Table 6 translate to a thickness ranging from 0.5 mm to 10 mm. The best fit R_s from each core corresponds with observations from the field, namely the decrease of inorganic sediment with distance from the creek. The best fit sea-level rise rates also correspond with local North Carolina sea-level rise observations reported in the literature. For example, regional assessments of sea-level trends in North Carolina suggest a 4.3 to 4.7 mm yr^{-1} rate of rise for the 20th century [*Poulter*, 2005; *Kemp et al.*, 2011]. Accretion rates from the predicted curves were determined by the slope of the relationship between the logarithm of the ^{210}Pb activity and depth (Fig 11). Varying χ_{ref} is observed to change the organic carbon content in the profile at depth, but does not affect the near-surface peak in organic content. When little material enters the refractory pool, the concentration of ^{210}Pb increases with depth near the surface because the decay of organic carbon outpaces the decay of ^{210}Pb near the surface of the marsh.

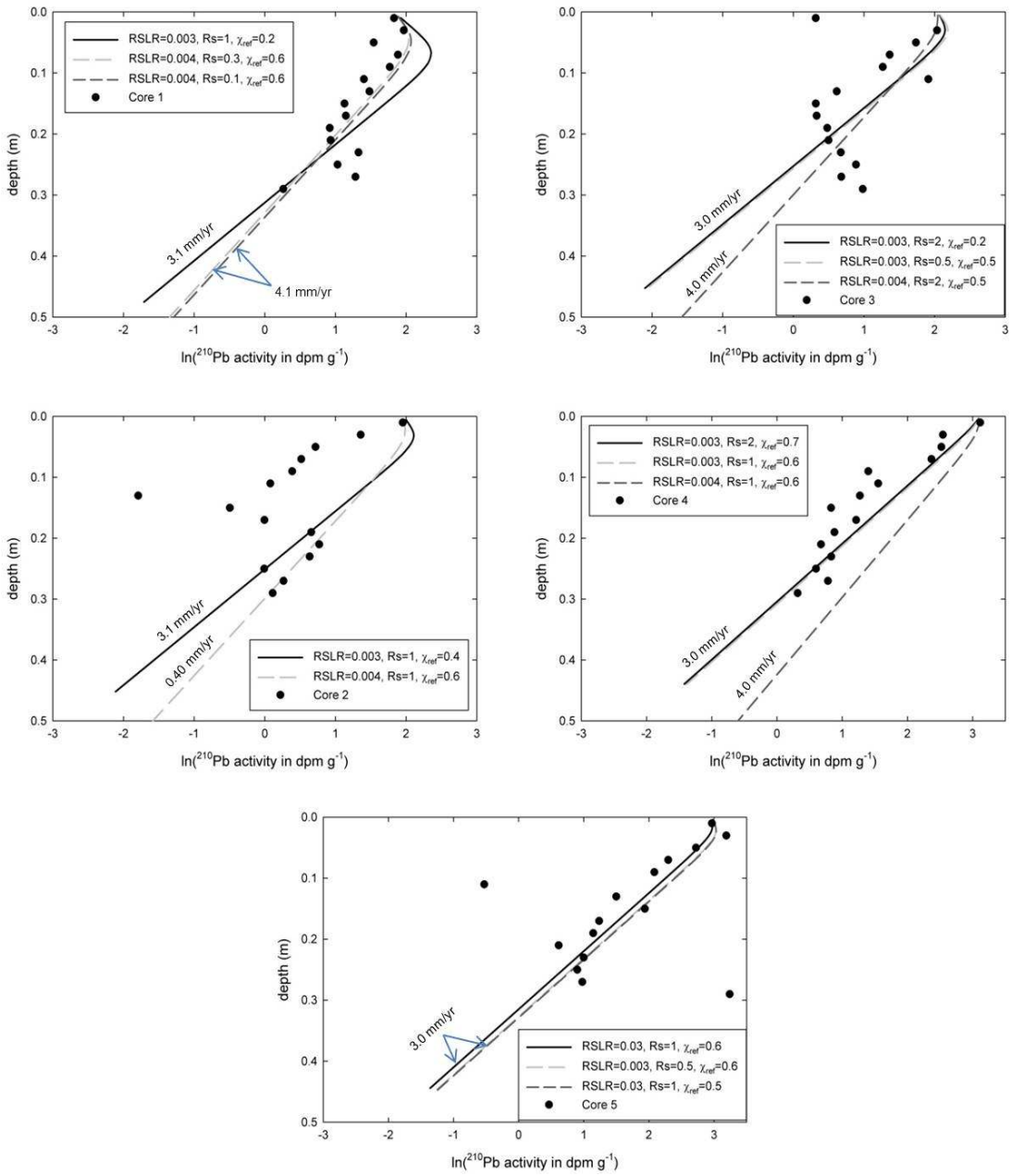

Figure 11. Activity plots of ^{210}Pb for different rates of inorganic sediment supply and different proportions of deposited labile carbon. The predicted profiles shown provide the lowest RMSE for each core. Accretion rates determined from the slope of ^{210}Pb and depth are shown on each figure.

Table 6. Best global fit parameters and calculated accretion rates.

Core	SLR (m/yr)	χ_{ref}	R_s (kg y^{-1} m^{-2})	Accretion (mm/yr)	% Refractory
C1	0.004	0.6	0.1	0.41	0.950
C2	0.004	0.6	1	0.04	0.579
C3	0.004	0.5	2	0.40	0.293
C4	0.003	0.7	2	0.30	0.350
C5	0.003	0.5	2	0.30	0.350

6. Discussion

The analytical approach introduced in *Mudd et al*. [2009] and modified for use with the field data collected at PKS provides a more advanced model to interpret ^{210}Pb dates and sediment accretion compared to the CRS and CIC models. Because the rate of carbon loss is greatest near the surface, the overestimation of accretion rates using the two radioisotopes is most severe near the surface. In extreme cases the concentration of ^{210}Pb increases with depth near the surface because the decay of organic carbon outpaces the decay of ^{210}Pb near the surface of the marsh. Such an increase was observed in the organic carbon profiles for Cores 3 and 5. The decrease in ^{210}Pb activity with depth better represents the true accretion rate because much of the labile carbon has been removed via decay. The carbon and predicted profiles suggest that the model assumptions are not satisfied throughout the depositional history for the *Spartina* sites. This is a limit of the OIMAS-A model assumption of constant sediment accretion, and can be addressed with further modeling using the

OIMAS-N model.

Accretion rates in this study are quantified from sediment tiles, radioisotope data, and analytical modeling (Tables 2, 4, and 6). The differences between the tile and SET sedimentation rates likely results from the distance of the sampling sites from the estuary. The SETs are located near the platform edge, which offers more favorable edaphic conditions than inland areas due to increased available oxygenation and greater exchange rate of waters. Such processes likely influence the primary productivity, and stem densities at the SETs were observed to be two to three times greater than the interior sampling sites. Additionally, *Mudd et al*. [2010] recently demonstrated that increased accretion rates can be attributed to enhanced settling brought about by reduced turbulent kinetic energy associated with greater stem densities. However, such a correlation is not observed at the interior marsh adjacent to the tidal creek. This may result from the low stem densities at PKS or the substantially different slopes of the *Spartina* and *Juncus* platforms, 0.01 and 0.005 respectively; the varying elevation of the *Spartina* and *Juncus* platforms renders comparison of suspended sediment unfeasible.

The CIC model is most appropriate for the organic rich Cores 4 and 5. For Cores 1, 2, and 3, the sediment source is likely resuspension of shallow bay sediments, and thus neither the CRS nor CIC model can be applied. Accretion rates are greatest at Core 3 (1.27 mm yr^{-1} to 5.50 mm yr^{-1}), the core obtained closest to the tidal creek, and decrease with distance from the tidal creek. The OIMAS-A model underestimates accretion rates for this core; however, if the three outlier points at approximately 20 cm depth are assumed to reflect a change in sedimentation rate and texcluded from the model, then the model is consistent

with measured accretion rates. Accretion rates from the radioisotopes suggest that this marsh platform can not maintain equilibrium with sea level. That is, accretion is less than the rate of sea-level rise, which ranges from 2 to 4 mm yr^{-1} based on tide gage estimates. Radioisotope data support the SET results from *Voss* [2010], where the marshes at PKS are concluded to be net erosional, although net elevation change was not statistically significant. Cesium concentrations are low across the transect, likely because oceanic radioisotope sources tend to have nondetectable ^{137}Cs. Because ^{137}Cs is measurable at depth, we suggest the marsh platform is likely younger than 1940 to 1950s.

7. Conclusions

Elevated CO_2 contributes to global warming, which is largely responsible for the accelerating rate of sea-level rise through thermal expansion and ice melt [*Bindoff et al.*, 2007]. However, elevated CO_2 may have important biologically mediated effects on coastal wetland ecosystems, including, for example, stimulating plant productivity and elevation gain [*Langely et al.,* 2009]. Carbon sequestration in estuarine wetlands is linked to sediment accumulation. The rate of carbon sequestration may be determined as the product of soil organic carbon density and the rate of soil vertical accretion [*e.g. Chmura et al.*, 2003].

This study presents detailed field and laboratory sampling to explore carbon with depth, organic decomposition, and sediment accumulation. The analytical analysis provides baseline parameters for future carbon sequestration studies, including the mass fraction of organic matter that goes into the refractory pool (χ_{ref}), which was previously calibrated in

Mudd et al. [2009]. Although biological data are only used here to evaluate the role of stem density and sediment accumulation, analysis of biological parameters was performed to later characterize the growth of macrophytes using the OIMAS-N. Organic carbon profiles were measured using CHN, which also provides an indication of organic matter decomposition and stabilization via C:N ratios. Sedimentation was measured using surface deposition rates from sediment tiles, radioisotope data, and SETs. Nonetheless, each analytical approach provides a different accretion rate. Similar to core data summarized by *Turner et al*. [2006], the accretion rate determined by ^{137}Cs is greater than that estimated by ^{210}Pb. This likely results from the diluted Cesium concentration at the marsh platform, organic decomposition, or a combination of both. The accretion rates for each of the methods are, however, less than the rate of sea-level rise at the site. The SET analysis from 2006 to 2008 shows that the marshes are net erosional, although little elevation change was observed.

The radioisotope date provide a unique description of the depositional environments on the *Spartina alterniflora* and *Juncus roemarianus* marshes, separated by a tidal creek. The elevation of the *Juncus* marsh is much greater than the *Spartina* marsh, and the carbon analysis supports greater accumulation of organic matter at the *Juncus* site. *Craft et al*. [1991] suggest that the proportion of organic carbon increases with soil organic matter, which is attributed to aging and the accumulation of reduced organic compounds, regardless of the organic carbon source. As a marsh ages, interaction of water saturated soils and net primary productivity deposition result in accumulation of soil organic matter. Over time, anaerobic decomposition produces reduced compounds that contain a higher carbon content than "fresh" plant tissue. The radioisotope analysis suggests that the *Spartina* marsh consists

of sediment exposed to water subject to atmospheric input, which is supported by the greater inorganic sediment. The analytical model is used to examine the influence of organic decay, where the effect of decomposition is demonstrated by plotting predicted lead concentrations for a sediment column. Simulations reveal that organic decay affects a layer's depth below the surface as a function of age. For example, greater amounts of deposited organic matter that become refractory result in a reduced lead peak. Organic decomposition most strongly affects radioisotope concentrations near the marsh surface. The basic concept and assumptions of the OIMAS-A model, namely that sediment is accreting at a constant rate, is not the best approach for cores located at the *Spartina* sites; instead, this site further shows the importance of quantifying the decomposition regime of the marsh to understand transient marsh accretion.

8. References

Appleby, P.G., and F. Oldfield (1983), The assessment of ^{210}Pb data from sites with varying sediment accumulation rates, *Hydrobiologia, 103*, 29-35.

Appleby, P.G., and F. Oldfield (1992), Application of lead-210 to sedimentation studies, *in: Uranium Series Disequilbrium: Application to Earth, Marine and Environmental Sciences*, eds. M. Ivanovich and R.S. Harmon, Clarendon Press, Oxford.

Bindoff, N.L. (2007), *Climate Change 2007: The Physical Science. Basis Contribution of Working Group 1 to the Fourth Assessment Report of the Intergovernmental Panel on Climate Change*, eds. S. Solomon et al., Cambridge Univ Press, New York, pp 387-429.

Byers, S.C., E.L. Mills, and P.L. Stewart (1978), A comparison of methods of determining organic carbon in marine sediments, with suggestions for a standard method, *Hydrobiologia, 58:1*, 43-47.

Cahoon, D.R., J.W. Day, Jr., and D.J. Reed (1999), The influence of surface and shallow

subsurface soil processes on wetland elevation: a synthesis, *Current Topics in Wetland Biogeochemistry, 3*, 72-88.

Cahoon, D.R., J. French, T. Spencer, D.J. Reed, and I. Moller (2000), Vertical accretion versus elevational adjustment in UK salt marshes: an evaluation of alternative methodologies, in *Coastal and Estuarine Environments: Sedimentology, geomorphology and geoarchaeology*, eds. K. Pye and J.R. Allen, Geological Society, London, Special Publications, 175, 223-238.

Chmura, G.L., S.C. Anisfeld, D.R. Cahoon, and J.C. Lynch (2003), Global carbon sequestration in tidal, saline wetland soils, *Global Biogeochemical Cycles, 17:4*, doi:10.1029/2002GB001917.

Chmura, G.L. and G.A. Hung (2004), Controls on salt marsh accretion: A test in salt marshes of Eastern Canada, *Estuaries 27:1*, 70-81.

Conner, R.F., G.L. Chmura, and C.B. Beecher (2001), Carbon accumulation in Bay of Fundy salt marshes: Implications for restoration of reclaimed marshes, *Global Biogeochemical Cycles 15:4*, 943-954.

Craft, C.B., S.W. Broome, and E.D. Seneca (1988), Nitrogen, Phosphorus and Organic Carbon pools in natural and transplanted marsh soils, *Estuaries, 11:4*, 272-280.

Craft, C.B., E.D. Seneca, and S.W. Broome (1991), Loss on ignition and Kjeldahl digestion for estimating organic carbon and total nitrogen in estuarine marsh soils: Calibration with dry combustion, *Estuaries, 14:2*, 175-179.

D'Alpaos, A., S. Lanzoni, M. Marani, and A. Rinaldo (2007), Landscape evolution in tidal embayments: modeling the interplay of erosion, sedimentation, and vegetation dynamics, *Journal of Geophysical Research-Earth Surface, 112*, F1, F01008, doi:10.1029/2006JF000537.

Dankers, N., and R. Laane (1983), A comparison of wet oxidation and loss on ignition of organic material in suspended matter, *Sci. Technol. Letters, 4*, 283-290.

Davis, R.B. (1984), ^{137}Cs and ^{210}Pb dating of sediments from soft-water lakes in New England (USA) and Scandinavia— A failure of ^{137}Cs dating, *Chem. Geol.*, 44, 151-195.

Dean, W.E. (1974), Determination of carbonate and organic matter in calcareous sediments and sedimentary rocks by loss on ignition: comparison with other methods, *Journal of Sedimentary Petrology, 44:1*, 242-248.

Duarte, C.M., J.J. Middelburg, and N. Caraco (2005), Major role of marine vegetation on the

oceanic carbon cycle, *Biogeosciences, 2*, 1-8.

Froelich, P.N. (1980), Analysis of organic carbon in marine sediments, *Limnology and Oceanography, 25,* 564-572.

Gebrehiwet, T., C.M. Koretsky, and R.V. Krishnamurthy (2008), Influence of *Spartina* and *Juncus* on saltmarsh sediments, III Organic geochemistry, *Chemical Geology, 255,* 114-119.

Heges, J.I., and J.H. Stern (1984), Carbon and nitrogen determinations of carbonate-containing solids, *Limnonology and Oceanography, 29*, 657-663.

Hoyle, F., and D. Murphy (2006), Seasonal changes in microbial function and diversity associated with stubble retention versus burning, *Australian Journal of Soil Research 44*, 407-423.

Jørgensen, B.B. (1983), Processes at the sediment-water interface, *In* B. Bolin and R.B. Cook, eds. *The major biogeochemical cycles and their interactions*, Wiley, 477-509

Kemp, A.C., B.P. Horton, J.P Donnelly, and M.E. Mann (2011), Climate related sea-level variations over the past two millennia, *Proceedings of the National Academy of Sciences*, 108, 11017-11022.

Kim, G., N. Hussain, T.M. Church, and W.L. Carey (1997), The fallout isotope ^{207}Bi in a Delaware salt marsh: a comparison with ^{210}Pb and ^{137}Cs as a geochronological tool, *The Science of the Total Environment, 196*, 31-41.

King, J., J.B. Hubeny, C. Gibson, E. Laliberte, K. Ford, and M. Cantwell (2008) Anthropogenic eutrophication of Narragansett Bay: evidence from dated sediment cores, *In: Science for Ecosystem-Based management: Narragansett Bay in the 21st Century*, eds. A. Desbonnet and B.A. Costa-Pierce, New York: Springer, 211-232.

Kirwan, M.L., and A.B. Murray (2007), A coupled geomorphic and ecological model of tidal marsh evolution, *Proc. Natl. Acad. Sci. U.S.A., 104*, 6118-6112, doi:10.1029/2009JF001400.

Kirwan, M.L., G. R. Guntenspergen, A. D'Alpaos, J.T. Morris, S.M. Mudd, S. Temmerman (2010), Limits on the adaptability of coastal marshes to rising sea level, *Geophysical Research Letters, 37*, L23401, DOI:10.1029/2010gl045489.

Langley, JA, K.L. McKee, D.R. Cahoon, J.A. Cherry, and J.P. Megonigal (2009), Elevated CO_2 stimulates marsh elevation gain, counterbalancing sea-level rise, *Proc. Natl. Acad. Sci*, doi 10.1073.

Morris, J.T., and P.M. Bradley (1999), Effects of nutrient loading on the preservation of

organic carbon in wetland sediments, *Limnology and Oceanography, 44,* 699-702.

Mudd, S.M., S. Fagherazzi, J.T. Morris, and D.J. Furbish (2004), Flow, sedimentation, and biomass production on a vegetated salt marsh in South Carolina: Toward a predictive model of marsh morphologic and ecologic evolution, in *the Ecogeomorphology of Tidal Marshes, Coastal Estuarine Stud*., vol. 59, edited by S Fagherazzi, M. Marani, and L.K. Blum, pp. 165-187, AGU, Washington, D.C.

Mudd, S.M., S.M. Howell, and J.T. Morris (2009), Impact of dynamic feedbacks between sedimentation, sea-level rise, and biomass production on near-surface marsh stratigraphy and carbon accumulation, *Estuarine, Coastal and Shelf Science, 82:*3, 377-389.

Mudd, S.M., A. D'Alpaos, and J.T. Morris (2010), How does vegetation affect sedimentation on tidal marshes? Investigating particle capture and hydrodynamic controls on biologically mediated sedimentation, *Journal of Geophysical Research-Earth Surface, 115*, F03029, doi:10.1029/2009JF001566.

Nair, V.D., D. Graetz, K.R. Reddy, and O.G. Olila, (2001), Soil Development in Phosphate-mined Created Wetlands of Florida, USA, *Wetlands, 21:2*, 232-239.

Pasternack, G.B. and G.S. Brush (1998), Sedimentation cycles in a river-mouth tidal freshwater marsh, *Estuaries, 21:3*, 407-415.

Phillips, J.D. (1992), The source of alluvium in large rivers in the lower coastal plan of North Carolina, *Catena 19:*59-75.

Reddy, K.R., and R.D. DeLaune, (2008), *Biogeochemistry of Wetlands: Science and Applications*, CRC Press Taylor and Francis Group, Boca Raton, FL.

Roseberry, J.C. (2009), Effects of soil transport processes on organic carbon storage in forested hillslope soils, MS Thesis, Vanderbilt University, 82p.

Schottler, S.P., and D.R. Engstrom (2006), A chronological assessment of Lake Okeechobee (Florida) sediments using multiple dating parkers, *J. Paleolimnol., 36*, 19-36.

Swarzenski, P.W., M. Baskaran, R.J. Rosenbauer, and W.H. Orem (2006), Historical trace element distribution in sediments from the Mississippi River Delta, *Estuaries and Coasts, 29:6B*, 1094-1107.

Temmerman, S., G. Govers, S. Wartel, and P. Meire (2003), Spatial and temporal factors controlling short-term sedimentation in a salt and freshwater tidal marsh, Scheldt estuary, Belgium, SW Netherlands, *Earth Surface Processes and Landforms 28*, 739-755.

Turner, R.E., C.S. Milan, and E.M. Swenson (2006), Recent volumetric changes in salt marsh soils, *Estuarine, Coastal and Shelf Science, 69:3-4*, 352-359.

Verardo, D.J., P.N. Froelich, and A. McIntyre (1990), Determination of organic carbon and nitrogen in marine sediments using the Carlo Erba NA-1500 Analyzer, *Deep-Sea Research, 37:1*, 157-165.

Voss, C. (2010), Responses of dominant marsh macrophytes to inundation and disturbance and assessing marsh ecosystem services, *PhD Dissertation*, East Carolina University.

Warren, R.S. and W. A. Niering (1993), Vegetation change on a northeast tidal marsh: interaction of sea-level rise and marsh accretion, *Ecology 74*, 96-103.

Wells, J.T. and S-Y. Kim (1989), Sedimentation in the Albemarle-Pamlico lagoonal system: synthesis and hypothesis, *Marine Geology 88:* 263-284.

CHAPTER VII

CONCLUSION AND FUTURE DIRECTIONS

The five manuscripts that comprise this dissertation demonstrate the relations between inundation, biomass, and elevation on salt marsh platforms. This work constitutes important advances in eco-geomorphology and the framework upon which my work in the future will be based. In chapters II and III, I have derived statements of mass conservation for wetland hydrodynamics that can be modified to suit a wide variety of salt marsh platform conditions. This approach differs from previous studies because: (i) the drag coefficient is dynamically solved as function of the Reynolds number for drag forces produced by macrophyte stems, (ii) the model is based on transitional to laminar flow conditions, (iii) the total drag is the sum of the drag on individual stems, and (iv) the contribution from bed stress is considered important at low biomass and water-depth conditions, and is incorporated in the model. The hydrodynamic model characterizes platform length-scale and stem density ranges for bath-tub versus wave-like flooding behavior. This model will allow geomorphologists and resource managers to better understand the flow regime and primary productivity response on salt marsh platforms.

I examined the change in inundation duration and flow routing with barrier design (Chapter III). This study provides the first step to determining if shoreline structures facilitate macrophyte degradation or platform erosion, the former resulting from either pooling of water or lack of inundation, or promote marsh platform stability. I suggest that the ideal

barrier design should be informed by the principles of ecology and sedimentology. An important next step is to pursue field studies to monitor inundation, productivity, and sedimentation in relation to various barrier designs.

In addition, I demonstrate that the mixed tidal record does not consist of a wind-driven component superimposed on the astronomical signal. Rather, low-frequency wind-driven variations in the water level constitute a significant part of the total variance of the observed record, the effect of which is to set the average water level about which the semi-diurnal and diurnal signals fluctuate. This work has important implications for elucidating macrophyte productivity in relation to elevation of the marsh platform and inundation.

I also investigated the influence of organic deposition on the interpretation of dating methods, as well as the balance and feedbacks between organic versus inorganic sedimentation on coastal salt marshes (Chapters V and VI). This work is the first to couple the feedback between biomass production, sedimentation and sea-level rise with an explicit representation of belowground processes.

My future research direction involves three primary goals. The first is the addition of sedimentation in the two-dimensional hydrodynamic model, as well as refining the code for better efficiency. An important next step is to include the marsh topography and detailed measurements of marsh biomass and sedimentation. By better constraining the low and high marsh habitats for a range of marsh health and tidal regimes, I hope to be able to refine length-scale and stem density relations in regards to the flow geometry. The living shoreline concept should be further tested because natural structures are generally porous and permit some amount of water and sediment through during the flood and ebb. Understanding how

barriers modify the flow and sedimentation will allow me to further explore advantageous barrier designs.

The methods developed for this thesis will also be used to understand platform response to sea-level rise. This work is currently in progress and involves collaboration with Jim Morris at the University of South Carolina. As an initial step, we are using high resolution digital elevation models and site-specific biomass, sedimentation, tidal range, and fetch to examine habitat change in response to sea-level rise from present day to 2100. The field studies and response to engineered structures will be used to further forecast climate change effects, including the ability of shorelines and platforms to keep pace with sea-level rise.

APPENDIX A

Literature review of resistance coefficients and experimental data available (*Chapter II*). The main parameters listed below include: depth y, velocity V, slope S, width W, discharge Q, vegetation height h; Manning's roughness coefficient n; spacing s; diameter d; effective drag coefficient C_{de}; frictional resistance force F_v; vegetation porosity η, Mach number M; and kinematic viscosity υ.

Study by	Study	Flow State	Vegetation	C_D	F or F_D	Main Results and Conclusions
Li and Shen (1973)	Field	Subcritical	Emergent, cylinder, d=15.25cm, *s*: square, triangular	assumed $C_D'=1.2$		Determine sediment yields for plant configurations; superposition technique for wakes generated behind isolated elements as proposed by Petryk (1969); Staggered: $\overline{C_D}=1.1$, independent of N_A and decreases with increasing stem density; $\overline{C_D}$ increases with density for parallel configurations.
Petryk and Bosmajian (1975)	Numerical	Turbulent	Emergent	$C_D=(1+1.9\frac{d}{a_z}C_\infty)\left(\frac{V_*}{V}\right)^2 +\Delta C_D'$	$f_v=\frac{4yd}{a_{xa_z}}C_D$	Estimate n as a function of hydraulic radius and emergent stem density.
Chen (1976)	Lab	Laminar	Emergent, Kentucky Blue Grass, Bermuda Grass		$f=(510{,}000S^{0.662})/Re$	Estimate f for channel given bed slope and Re; friction factor decreases with Re in laminar flow range.

Study by	Study	Flow State	Vegetation	C_D	F or F_D	Main Results and Conclusions
Linder (1982)	Lab		Emergent, 50 stems/m^2	$C_{De}=\left(1+1.9\frac{d_p}{a_z}C_D\right)\left(0.2025(\frac{a_x}{d})^{0.46}C_D\right)+\left(\frac{2a_y}{a_y-d}-2\right)$	$f=\frac{4dh}{a_x a_y}C_D$	Extend the work of Li and Shen (1973) to compute C_D for single plant in a group and the friction factor for vegetation. First term on the RHS is the resistance due to the narrowing effect of neighboring elements and the second term is resistance due to gravitational force. Suggest effects of turbulence and non-uniform velocity profile can be neglected.
Shih and Rahi (1982)	Field	Trans.	Emergent hyacinth, pickerel weed, buttonbrush		$(n/n_i)=(y_i/y)^{\zeta}$	n increases as y decreases and n is related to the square root of vegetation density and $R^{2/3}$. Sparse vegetation: ζ may vary from 0.33 to 0.5. At smaller flow depths, ζ may range from 1.0 to 2.0
Burke and Stolzenbach (1983)	Field, Numerical		Emergent, Submergent, 0.1cm	Model: $C_D=bRe_d^c$ Specify C_D and then adjust stem density (function of height); assume 2.5		Turbulent eddy scales 1-3% of the water depth, and turbulent stresses 2% of the drag for aH=0.1. Alternative approach to closing momentum equations. Parameterize turbulent stress with k-ε low Re model.
Kadlec (1990)	Field	Laminar to Trans.	Emergent, sedges, Isolated submerged, 1000stem/m^2	$C_D a=\hat{X}=\frac{2gS}{V^2}$	$S=C_D a\frac{v^2}{2g}$	X= resistence coefficient; K, β, α determined for each site. Densely vegetated marshes and laminar flow: K (roughness)=1*10^7/86400 $s^{-1}m^{-1}$, β=3, α=1. Sparsely vegetated marshes and laminar flow: K=5*10^7/86400$s^{-1}m^{-1}$. Stem data from Valiela et al (1978).

Study by	Study	Flow State	Vegetation	C_D	F or F_D	Main Results and Conclusions
White (1991)	Numerical	$1<Re_d<10^5$		$C_D = 1 + \frac{10}{Re_d^{2/3}}$		From Tritton (1959) cylinder data; Empirical expression for C_D of isolated cylinder, curve-fit, dependent on Re_d.
Tsujimoto and Kitamura (1991)	Lab	Subcritical	Emergent, cylinders, *s*: square			Focus on development of trends and not empirical relations.
Roig (1994)	Lab	Trans. to Turbulent Re_h=5440-5820	Emergent, Rigid, *d*=9.5mm, *s/d*: 4-12 *Salicornia virginica*		$F_V = -0.0909\rho u^2(1-\eta) Re_s^{1/2}\left(\frac{h}{s}\right)^{1/2}$	Estimate bulk vegetative resistence force to emergent or submerged flow; frictional resistance force obtained from depth, velocity, and stem spacing.
Dunn et al (1996)	Lab		Emergent, Submergent	$\overline{C_{DH}} = \frac{\int_0^H C_D u_h^2 dy}{\int_0^H u_h^2 dy}$	$F_D = \rho\frac{A\overline{C_D}U^2}{2}$	Four equations given for C_D; C_D max values: 1.32 to 1.86– not dependent on any flow values. Plant density determines shape of the velocity profile.

Study by	Study	Flow State	Vegetation	C_D	F or F_D	Main Results and Conclusions
Koch and Ladd (1997)	Numerical	Re_d 0-180	Periodic & Random arrays	C_D increases with ϕ for $Re_p \leq O(100)$	$F/(\mu U) = c_1 + c_2 Re$	Lattice-Boltzmann simulation; restriction to low M bypassed by use of large d and/or small υ to obtain large Re_d. Mean drag transitions from quadratic Re dependence ($Re_d \leq 5$) to linear dependence ($Re_d > 5$) Square: cylinder spacing characterizes dynamics of ϕ=0.0125 to 0.1 Random: c_1/c_2 decreases with increasing ϕ, indicating inertial effects are weaker with density.
Hodges (1997)	Lab		Emergent and Submergent, d=0.95cm	C_D=0.5 assumed F_{d2}, C_D=1.1 assumed F_{d3}	$F_{d1} = \frac{1}{2}\rho U^2 (0.24d)^2$ $F_{d2} = \frac{1}{2}\rho U^2 d(1 + \frac{gh_c}{U^2})h_c C_D$ $F_{d3} = \frac{1}{2}\rho U^2 d(y_n - h)C_D$	Drag force based on Blevins (1992), summation of: (1) spray/wave drag (formation of wave upstream of dowel), (2) ventilation drag (within height of depression downstream of dowel), (3) hydrodynamic drag.
Fathi-Moghadam and Kouwen (1997)	Lab	Trans. to Turbulent	Emergent, flexible pine/cedar		$f = \frac{4y}{h}\left[C_d\left(\frac{A_v}{\forall}\right)h\right]$	Emergent: vegetation density is always dominant parameter regardless of species or foliage shape and distribution.
Wu et al (1999)	Lab	Laminar	Emergent and Submergent	$C_D = (3.44 * 10^6 S^{0.50})/Re_w$	$n_b = \left[\frac{(3.4\times 10^6) S^{0.5} \upsilon}{2g}\right] D^{-\frac{1}{3}}$	Estimated C_D converted to n_b. n_b decreases with velocity increase and dependent on depth. Regression indicates Re, slope, and height of vegetation important.

Study by	Study	Flow State	Vegetation	C_D	F or F_D	Main Results and Conclusions
Nepf (1999)	Numerical	$Re_d > \approx 200$	Two-cylinder, random array	$(1-ad)C_B U^2 + \frac{1}{2}\overline{C_D} ad (\frac{h}{d}) U^2 = gh\frac{\partial h}{\partial x}$	$F_T = \frac{1}{2}\overline{C_D} a U^2$	Constant $\overline{C_D}$ up to ad=0.01; steady decline beyond this density. $\overline{C_D}$ suppression described by wake shelter $Re_d < \approx 200$ wake production negligible
Nepf and Vivoni (2000)	Lab	$Re_h = 4x10^3$ to $4x10^4$	Plastic blades	$0 = -g\frac{\partial H}{\partial x} - \frac{\partial \langle \overline{uw} \rangle}{\partial z} - \frac{1}{2} C_D a \langle U \rangle^2$	$f_D = \rho U_h^2 h^3 w$	$C_D(z)$ increases towards the bed, emergent canopy constant $C_D \approx 1$. C_D estimated from surface slope and profiles of Re stress.
Tsihrintzis (2001)				$C_D = \gamma R_h^{-k}$		k depends on biomechanical properties of the vegetation (density); γ related to the stem spacing and/or friction slope.
James et al (2001)	Field and Lab	Re_d=246-4838	Emergent, Submergent, Flexible, Rigid, reeds, cylinders	$F_D = C_D A \frac{1}{2} \rho V^2$	Determined from moment equilibrium and weight of water in container	Resistance to flow affected by stem shape; C_D increases for foliage on natural stems; C_D for natural stems may be dependent on Re at higher values of Re than cylinders.
Thompson (2001)	Lab	Re_d=4636-23880		$C_d = \frac{2F}{\rho U^2 A}$	$\frac{\sum F}{m^2}$	C_D constant with flow depth; resistance measured for individual stems.

Study by	Study	Flow State	Vegetation	C_D	F or F_D	Main Results and Conclusions
Lee et al (2004)	Field and Lab	$0<R_d<200$ $0<R_h<10000$ $0<R_s<1000$	Sawgrass	Observed F'_{xvb} used to find C_D from $F'_{xvb}=\frac{C'_D\rho U^2}{2}$	Observed resistence $F'_{xvb}=\rho g S_h$ $S_h\equiv\left(\frac{\partial z_b}{\partial x}+\frac{\partial h}{\partial x}\right)$	Multiple regression of dim. analysis to relate Re_h and s. C'_D inverse function of Re_h, valid for emergent sawgrass, $Re_h<10{,}000$ and $0.05<s/h<0.2$. Drag expression in terms of a and 1/s, where $s=(d/a)^{-0.5}$; when rearranged results in $\overline{C_D}$ scaling with $(ad)^{-0.5}$
Jarvelo (2002)	Lab	Re_h=24,200-177,00		$C'_D=\frac{4}{4R}$		C'_D function of Darcy-Weisbach (1/m); Leaves increase friction factor, dependent on flow velocity.
Tanino and Nepf (2008)	Lab	Re_d=25 to 685	Wooden dowels, ϕ=0.091 to 0.35	Depth-averaged C_D $\frac{C_D\langle u\rangle_H^2}{2}md\equiv -1(1-\phi)g\frac{d\eta}{dx}$ From Ergun (1952) $C_D=2\left(\frac{\alpha_0}{Re_d}+\alpha_1\right)$	$\langle f_D\rangle_H m=-(1-\phi)\rho g\frac{d\eta}{dx}$ From Ergun (1952) $\frac{\langle f_D\rangle_H}{\mu\langle\bar{u}\rangle}=\alpha_0+\alpha_1 Re_d$	Array averaged for Re_d dependence. C_D and normalized drag increase with ϕ; coefficients estimated from linear regression; valid for $O(30)\le Re_d\le O(700)$ C_D decreases as Re_d increases for all ϕ investigated and C_D in a random array is larger than the isolated cylinder for $O(30)\le Red\le O(700)$ for $\phi\le 0.35$
Harvey et al 2009	Field	0.02 to 0.79 cms^{-1}	Emergent	$\overline{C_D}=2K_0Re_{d,h}^{-k}(ad)^{-0.5}$ $F^*=\frac{gS}{U^2a(ad)^{-0.5}}=K_0Re_{d,h}^{-k}$		Rewrite Lee et al (2004), eliminate s since wake sheltering at higher densities reduces bulk drag. K_0 and k empirical constants related to drag's dependence on Re, estimated by linear regression of F* and Re. Derived expression for $\overline{C_D}$, substitute into force balance for dimensionless drag coefficient F*

APPENDIX B

Shear stress partitioning from *Thompson* [2001] and the calculated values from this study (Chapter 2, Eq. (10)), where *Thompson* [2001] uses the notation, water depth $h = 0.007$ and total ground surface area m^2 $As = 0.144$. *Thompson's* [2001] data is used in total resistance calculations.

Samp	Q (m^3s^{-1})	U_{avg} (ms^{-1})	H_{avg} (m)	Re_d	N_A (m^{-2})	λ	Δ^2	d (m)	t_P (Pa)	t_R (Pa)	t_P/t	C_D	t_P (N/V)	t_R (N/V)	t (N/V)	Calc C_D	Calc t_P	Calc F_v
C1A	0.0045	0.48	0.025	12143	6.9	0.0043	0.07	0.0254	0.80	0.40	0.664	0.822	32	16	48.193	1.104	44.390	22.247
C1B	0.0105	0.78	0.035	19733	6.9	0.0062	0.07	0.0254	2.27	1.27	0.642	0.667	64.857	36.286	101.024	1.211	74.843	64.438
C4A	0.0045	0.46	0.026	11637	27.6	0.0181	0.13	0.0254	0.83	1.21	0.407	0.609	31.923	46.538	78.435	1.096	38.690	81.146
C4B	0.0105	0.60	0.046	15179	27.6	0.3190	0.13	0.0254	0.99	4.52	0.179	0.774	21.522	98.261	120.233	1.149	30.762	144.720
C9A	0.0045	0.39	0.030	9867	62.1	0.0476	0.20	0.0254	0.78	1.99	0.282	0.557	26	66.333	92.199	1.068	22.980	127.839
C9B	0.0105	0.47	0.058	11890	62.1	0.0912	0.20	0.0254	1.19	7.94	0.130	0.787	20.517	136.897	157.825	1.100	13.857	191.289
SC4A	0.0045	0.54	0.022	5110	27.6	0.0058	0.05	0.0095	0.73	0.64	0.535	0.740	33.182	29.091	62.022	0.984	66.621	37.553
SC4B	0.0105	0.76	0.036	7191	27.6	0.0095	0.05	0.0095	1.24	2.35	0.346	0.888	34.444	65.278	99.550	1.022	68.435	77.242
SC9A	0.0045	0.49	0.024	4636	62.1	0.0143	0.08	0.0095	0.76	1.84	0.293	1.058	31.667	76.667	108.077	0.976	48.846	68.955
SC9B	0.0105	0.67	0.041	6340	62.1	0.0244	0.08	0.0095	0.97	5.22	0.156	0.828	23.659	127.317	151.657	1.007	44.719	133.051
TL1A	0.0045	0.48	0.025	17259	6.9	0.0061	0.10	0.0361	0.99	0.12	0.889	0.193	39.600	4.800	44.544	1.178	44.390	33.741
TL1B	0.0105	0.72	0.038	23880	6.9	0.0088	0.09	0.0333	1.72	2.61	0.397	1.161	45.263	68.684	114.013	1.263	57.149	75.059
TS1A	0.0045	0.48	0.025	7028	6.9	0.0025	0.04	0.0147	1.25	0.16	0.888	0.473	50	6.400	56.306	1.019	44.390	11.885
TS1B	0.0105	0.77	0.036	12961	6.9	0.0042	0.04	0.0169	2.05	1.49	0.582	1.222	56.944	41.389	97.843	1.117	70.247	38.522

APPENDIX C

The two-dimensional hydrodynamic model domain (*Chapter III*) is illustrated below in Figure C1 for a one-structure barrier configuration. The barrier exists at $i = 1$ for $j = 1$ to "*open*" (denoted with a bold black line). Water surface elevation ζ and water depth h are set at $i = 1$ to 2 for $j >$ *open* to j_{max}, and driven by a sinusoidal tidal forcing. The value of h is examined at the start of each time step; if $\zeta <$ sinusoidal tide elevation, then ζ is set to the η + "*lag depth*." The lag depth or depth of residual water always present on the marsh platform is set to 0.001 m for model stability. The resistence and velocity constituents are also calculated at these nodes, where values other than depth are obtained from the previous time-step.

To implement reflections and thus an infinite model domain, no-flow boundaries are constructed at $j = 1$, $j = j_{max}$, and $i = i_{max}$. Therefore, calculations after the initialization are performed from $j = 2$ to j_{max-1} and $i = 2$ to i_{max-1}. Nodes operated on are shown in the yellow box in Figure C1. Central finite differencing is first performed for nodes i =2 to i_{max-1} behind the barrier, wherein the total resistance is calculated to solve for the new water depth and water surface elevation,

$$\eta = h_{0_{i,j}} + \frac{\partial}{\partial x_2}\left[\eta_{0_{i,j}} \zeta_{i,j} + \right] \frac{\partial}{\partial y_2}\left[\eta_{0_{i,j}} \zeta_{i,j}\right] \qquad (1)$$

Central finite differencing for the total stress and new water surface elevation then operate on nodes $j >$ *open* to j_{max-1}. Water depths and elevations are reflected across the j and i boundaries, wherein node $j = 1$ takes the value of j =3 for $j = 2$, j_{max-1}, and the value

at j_{max} takes the value of node $j_{max - 2}$ for [illegible] . Likewise, values are reflected across the barrier such that node $i = 1$ takes the value at $i = 3$. The node structure and reflections are similar for the two-structure scheme (Figure C2). The sinusoidal tide is forced at the nodes outlined in red.

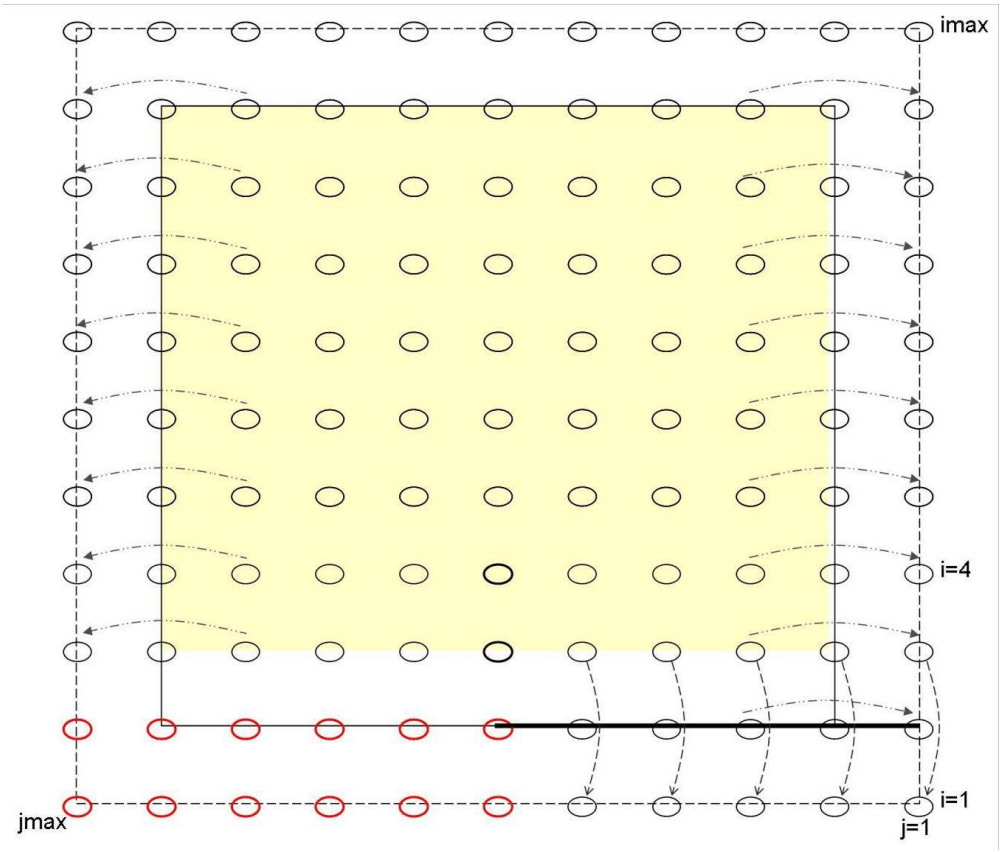

Figure C1. One-structure barrier reflection schema.

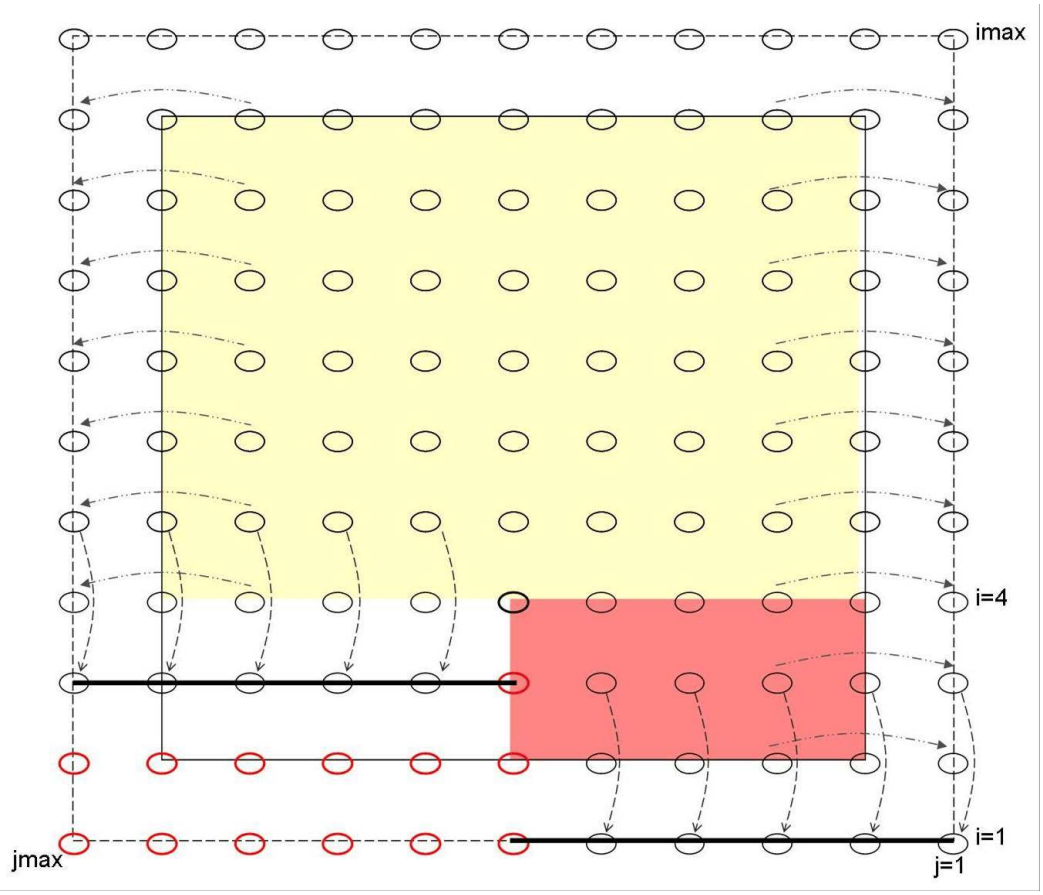

Figure C2. Node and reflection scheme for the two barrier configuration. The inside frame consists of nodes subject to inundation operation. The central differencing scheme requires that calculations are first performed in the pink box, followed by the remaining nodes in the yellow box.

APPENDIX D

The following section outlines the two-dimensional hydrodynamic simulations (*Chapter III*).

Model runs with no barriers consider N_A = 50, 100, and 500 stems m^{-2}, slope of 0.01, 0.004, and 0.002.

For one structure simulations, the barrier lengths are < Half (12 m, 28 m), = Half (20 m,44 m), and > Half (28 m, 60m) [short length-scale, long length-scale].

Structure Length [m]	Biomass	*x*-length scale [m]	*y*-length scale [m]
short	100	120	40
short	500	150	40
short	100	150	40
short	500	150	40
long	100	150	80
long	500	150	80

The two structure configuration is run with the following barrier designs:
(1) < Half: lower structure 12 m and upper structure 28 m, and lower 28 m and upper 56 m for long length-scale.
(2) = Half: both lower and upper structures equal to 20 m and increased to 44 m for long length-scales
(3) > Half: lower structure 28 m and upper structure 12m, and lower structure 60 m and upper 20 m for long length-scale.

Structure Length [m]	Biomass	*x*-length scale [m]	*y*-length scale [m]
short	100	150	40
short	500	150	40
short	100	150	40
short	500	150	40
long	100	150	80
long	500	150	80

APPENDIX E

Carbon-Hydrogen-Nitrogen (CHN) output for Cores 1-5 (*Chapter VI*).

Core 1

Depth Interval	ORGANIC CARBON				TOTAL CARBON			
(mm)	C	H	N	C/N	C	H	N	C/N
0-20	9.62	1.41	0.55	20.55	7.14	0.93	0.54	15.41
20-40	9.11	1.25	0.61	17.34	7.15	0.89	0.50	16.70
40-60	6.04	0.81	0.44	15.87	5.55	0.60	0.51	12.66
60-80	9.37	1.32	0.53	20.55	10.79	1.34	0.81	15.46
80-100	14.41	1.97	0.79	21.15	11.92	1.44	0.78	17.83
100-120	8.36	1.17	0.57	17.05	11.12	1.42	0.74	17.55
120-140	5.12	0.71	0.40	14.77	16.21	2.12	1.26	15.03
140-160	11.21	1.54	0.69	18.92	10.21	1.37	0.85	13.97
160-180	10.60	1.55	0.71	17.38	13.12	1.85	0.69	22.21
180-200	10.66	1.52	0.72	17.24	4.60	0.50	0.32	16.54
200-220	6.67	0.97	0.45	17.29	13.57	1.81	0.86	18.32
220-240	15.02	2.07	0.97	N/V	21.82	2.92	1.31	19.39
240-260	13.79	1.98	0.87	18.51	13.74	1.87	0.91	17.60
260-280	10.08	1.77	0.70	16.85	10.67	1.44	0.71	17.52
280-300	13.90	2.04	1.00	16.28	16.08	2.15	1.07	17.48
300-320	12.77	1.80	0.85	17.47	5.52	0.67	0.36	18.07
320-340	3.64	0.56	0.26	16.13	4.28	0.39	0.34	14.62
340-360	1.16	0.24	0.14	9.78	1.32	-0.02	0.11	13.96
360-380	1.10	0.29	0.02	28.24	0.98	-0.07	0.08	15.21
380-400	1.05	0.23	0.02	25.13	1.67	0.01	0.10	18.72
400-420	0.23	0.12	0.00	23.82	0.05	-0.04	-0.06	N/V
420-440	N/V	N/V	N/V	N/V	0.45	-0.07	-0.01	N/V
440-460	0.05	0.08	0.07	0.94	0.06	-0.13	-0.02	N/V
460-480	-0.19	0.10	0.11	N/V	0.03	-0.16	-0.22	N/V
480-500	-0.48	0.21	0.12	N/V	0.33	-0.11	0.13	3.01
500-520	-0.03	0.11	0.16	N/V	-0.11	-0.17	0.05	N/V
520-540	0.21	0.11	0.15	1.62	-0.27	-0.07	0.13	N/V
540-560	0.06	0.08	0.16	0.44	-0.18	-0.16	0.02	N/V
560-580	0.05	0.07	0.09	0.60	-0.03	-0.13	-0.04	N/V
580-600	N/V	N/V	N/V	N/V	-0.12	-0.16	0.00	N/V
600-620	N/V	N/V	N/V	N/V	-0.14	-0.14	-0.03	N/V
620-640	N/V	N/V	N/V	N/V	-0.22	-0.13	-0.08	N/V
640-660	N/V	N/V	N/V	N/V	-0.17	-0.16	-0.05	N/V
660-680	N/V	N/V	N/V	N/V	-0.26	-0.18	-0.05	N/V
680-700	N/V	N/V	N/V	N/V	-0.27	-0.18	0.07	N/V
700-750	N/V	N/V	N/V	N/V	0.10	-0.11	0.07	1.53

Core 2					Core 3			
Depth Interval	ORGANIC CARBON				ORGANIC CARBON			
(mm)	C	H	N	C/N	C	H	N	C/N
0-20	15.66	2.08	0.91	20.18	9.22	1.57	0.70	15.46
20-40	20.83	2.86	1.34	18.07	12.02	1.85	0.78	18.06
40-60	26.58	3.36	1.52	20.42	7.62	1.06	0.45	19.78
60-80	24.95	3.29	1.39	21.01	13.04	1.77	0.80	19.07
80-100	19.02	2.61	1.23	17.97	24.90	3.18	1.48	19.61
100-120	4.82	0.73	0.40	13.96	13.15	1.82	0.78	19.74
120-140	11.89	1.61	0.79	17.48	21.16	2.77	1.31	18.78
140-160	9.93	1.48	0.53	21.73	22.83	3.06	1.47	18.07
160-180	17.91	2.56	1.00	20.97	26.11	3.49	1.85	16.44
180-200	13.47	1.96	0.61	25.67	32.69	4.44	2.16	17.65
200-220	N/V	N/V	N/V	N/V	32.64	4.56	2.27	16.74
220-240	18.88	2.54	1.55	14.25	33.02	4.20	1.97	19.52
240-260	19.00	3.00	0.76	29.11	31.39	4.28	1.61	22.69
260-280	11.73	1.48	0.44	30.94	31.01	4.25	1.73	20.89
260-280	N/V	N/V	N/V	N/V	35.23	5.04	2.15	19.15
280-300	12.11	1.51	0.18	35.08	23.45	3.45	1.43	19.07
300-320	7.63	0.88	0.06	32.99	19.87	3.10	1.11	20.89
320-340	2.51	0.14	-0.44	N/V	15.26	2.16	0.79	22.64
340-360	0.44	-0.17	-0.61	N/V	8.46	1.25	0.52	18.98
340-360	0.44	0.30	0.28	1.84	N/V	N/V	N/V	N/V
360-380	4.31	0.74	0.38	13.32	0.44	0.03	0.17	2.99
380-400	3.37	0.60	0.36	11.01	0.25	-0.03	0.06	4.61
400-420	5.59	0.98	0.56	11.60	0.31	-0.01	0.11	3.42
420-440	0.10	0.01	0.20	0.59	0.03	-0.05	-0.03	N/V
440-460	0.45	0.11	0.12	4.36	-0.10	-0.13	0.05	N/V
460-480	0.24	0.09	0.08	3.69	0.38	0.15	0.05	9.85
480-500	0.12	0.07	0.47	0.29	0.23	0.11	0.06	4.69
500-520	0.09	0.04	0.22	0.46	0.19	0.10	0.01	24.75
520-540	0.25	0.06	0.20	1.48	0.14	0.07	0.09	1.86
540-560	0.02	0.01	0.24	0.11	0.26	0.03	-0.77	N/V
560-580	0.08	0.11	0.10	0.93	0.12	0.04	0.06	2.54
580-600	0.05	0.08	0.11	0.58	0.17	0.06	-0.07	N/V
600-620	-0.03	0.04	0.12	N/V	0.19	0.06	0.14	1.59
620-640	0.00	0.54	0.45	N/V	0.40	0.11	0.14	3.28
640-660	N/V	N/V	N/V	N/V	0.27	0.03	-0.01	N/V
660-680	N/V	N/V	N/V	N/V	0.52	0.02	-0.01	N/V
680-700	N/V	N/V	N/V	N/V	0.93	0.35	0.09	11.74
700-750	N/V	N/V	N/V	N/V	0.23	0.11	0.33	0.81

Core 4					Core 5			
Depth Interval	**ORGANIC CARBON**				**ORGANIC CARBON**			
(mm)	C	H	N	C/N	C	H	N	C/N
0-20	13.87	2.89	1.14	14.20	14.22	2.23	0.88	18.89
20-40	14.51	2.85	1.05	16.14	11.71	1.85	0.73	18.81
40-60	12.38	2.39	0.88	16.36	15.23	2.36	0.97	18.35
60-80	11.51	2.00	0.78	17.32	9.97	1.42	0.58	20.08
80-100	11.73	2.14	0.87	15.72	12.05	1.62	0.69	20.51
100-120	21.72	3.14	1.19	21.21	22.67	2.87	1.15	23.06
120-140	15.99	2.53	0.98	19.12	9.12	1.31	0.57	18.63
140-160	20.56	3.31	1.26	19.04	20.68	2.65	1.36	17.73
160-180	23.58	3.51	1.36	20.17	19.71	2.60	1.25	18.40
180-200	20.61	3.18	1.32	18.88	11.67	1.63	0.82	16.57
200-220	22.37	3.51	1.14	22.84	11.24	2.07	1.94	6.76
220-240	23.47	3.52	1.41	19.42	17.99	2.78	1.63	12.85
240-260	33.51	4.97	2.15	18.15	15.89	2.33	1.15	16.06
260-280	35.10	5.20	2.29	17.89	10.51	1.55	0.7	17.53
280-300	32.99	5.12	2.33	16.52	9.16	1.31	0.78	13.73
300-320	33.15	5.27	2.39	16.15	8.30	1.14	0.70	13.83
320-340	34.83	5.44	2.66	15.30	11.31	1.54	0.98	13.46
340-360	22.12	3.70	1.58	16.31	9.30	1.30	0.89	12.16
360-380	14.48	2.68	1.07	15.82	23.09	3.01	1.87	14.38
380-400	4.28	0.80	0.33	15.31	10.48	1.45	0.97	12.63
400-420	5.00	0.85	0.39	14.87	3.51	0.49	0.43	9.61
420-440	0.11	0.09	0.14	0.93	11.90	1.52	0.95	14.67
440-460	N/V	N/V	N/V	N/V	0.53	0.18	0.25	2.46
460-480	N/V	N/V	N/V	N/V	0.11	0.06	0.09	1.46

APPENDIX F

Biology samples and laboratory analysis from Pine Knolls Shore, North Carolina (*Chapter VI*).

Core	Sample	Field Count Total	Lab Count	Height (mm)	Dry Wt (g)	g/ m^2
1	B1 Live	x	16	250-400	9.74	300
	B1 Dead		10	170-500	6.25	
	B1 Loose		--	--	2.74	
2	B2 Live	35	17	170-400	12.42	304.1
	B2 Dead		5	280-400	5.13	
	B2 Loose		--	--	1.44	
3	B3 Live	17	17	300-450	16.25	332.62
	B3 Dead		3	300-420	2.24	
	B3 Loose		--	--	1.18	
3	B4 Live Short	17	3	< 400	2.46	324.3
	B4 Live Tall		8	400-600	14.28	
	B4 Dead		6	270-450	3.52	
5	B5 Juncus	20	15	1300	23.91	450.44
	B5 Lose		--	--	4.23	
5	B6 Juncus	x	9	1200	21.97	351.55
4	B7 Live	17	14	800	51.02	816.35
4	B8 Juncus	x	15	630-1200	33.63	
	B8 Lose		--	--	8.78	1495.1

APPENDIX G

Loss-on-ignition report for samples collected at Pine Knoll Shore Site, North Carolina (*Chapter VI*).

Core	Sample - Depth (cm)	Location	Weight of Sediment after 6 hrs at 450 C (g)	Weight of Sediment after 900 C (g)
1	A1-0	Spartina, higher elevation	5.16	5.1
	A1-10		8.43	8.4
	A1-100		8.16	8.14
3	A2-0	Mudflat	2.37	2.29
	A2-20		6.75	6.7
4	A3-0	Juncus	0.83	0.71
	A3-40		7.43	7.42
5	A4-0	High elevation, woods-edge	0.54	0.47
	A4-40		0.48	0.43
	A4-65		8.21	8.19

APPENDIX H

Radioisotope data for cores collected at Pine Knolls Shore, NC, used to determine accretion rates (*Chapter VI*).

Core 1

Depth (cm)	Bulk density (g cm-3)	xs Pb-210 (dpm g-1)	Cs-137 (Count)	Inventory (dpm cm-2)	Age (yr)	Accretion Rate (cm yr-1)
1	0.19	6.23	0.28	2.42	1.45	0.69
3	0.23	7.15	0.38	3.35	5.18	0.58
5	0.26	4.67	0.38	2.47	9.44	0.53
7	0.20	6.58	0.46	2.62	13.68	0.51
9	0.21	5.87	0.32	2.43	18.52	0.49
11	0.23	4.07	0.24	1.88	23.30	0.47
13	0.22	4.4	0.25	1.90	28.15	0.46
15	0.26	3.09	0.16	1.61	33.42	0.45
17	0.20	3.15	0.11	1.27	38.49	0.44
19	0.26	2.51	0.12	1.28	43.75	0.43
21	0.27	2.54	0.13	1.36	50.29	0.42
23	0.22	3.77	0.17	1.65	59.79	0.38
25	0.25	2.8	0.13	1.38	73.34	0.34
27	0.25	3.61	0.1	1.79	98.58	0.27
29	0.18	1.3		0.46	---	---

Core 2

Depth (cm)	Bulk density (g cm-3)	xs Pb-210 (dpm g-1)	Cs-137 (Count)	Inventory (dpm cm-2)	Age (yr)	Accretion Rate (cm yr-1)
1	0.25	7.05	0.25	3.59	3.90	0.26
3	0.25	3.89	0.12	1.92	11.00	0.27
5	0.35	2.05	0.05	1.42	16.21	0.31
7	0.29	1.68	0.05	0.96	20.52	0.34
9	0.29	1.47	0.02	0.87	24.27	0.37
11	0.29	1.08	0.04	0.62	27.68	0.40
13	0.30	0.17	0.04	0.10	29.46	0.44
15	0.35	0.61	0.02	0.42	30.82	0.49
17	0.25	1.00	0.14	0.49	33.35	0.51
19	0.34	1.93	0.04	1.31	39.01	0.49
21	0.30	2.16	0.14	1.29	49.52	0.42
23	0.26	1.89	0.02	0.97	62.68	0.37
25	0.26	0.99	0.06	0.52	75.65	0.33
27	0.28	1.30	0.06	0.73	92.95	0.29
29	0.23	1.12	0.06	0.51	97.28	0.30

Core 3

Depth (cm)	Bulk density ($g\ cm^{-3}$)	xs Pb-210 ($dpm\ g^{-1}$)	Cs-137 (Count)	Inventory ($dpm\ cm^{-2}$)	Age (yr)	Accretion Rate ($cm\ yr^{-1}$)
1	0.07	1.37	0.03	0.21	0.15	6.67
3	0.22	7.65	0.38	3.37	2.88	1.04
5	0.25	5.67	0.57	2.80	8.22	0.61
7	0.24	3.91	0.23	1.88	12.95	0.54
9	0.25	3.55	0.16	1.76	17.18	0.52
11	0.26	6.76	0.30	3.53	24.53	0.45
13	0.27	1.85	0.04	0.98	32.50	0.40
15	0.31	1.37	0.06	0.86	36.41	0.41
17	0.18	1.39	0.02	0.51	39.64	0.43
19	0.29	1.62	0.00	0.92	43.42	0.44
21	0.27	1.65	0.12	0.90	49.01	0.43
23	0.28	1.96	0.00	1.11	56.57	0.41
25	0.24	2.43	0.00	1.14	67.91	0.37
27	0.19	1.97	0.05	0.76	82.06	0.33
29	0.25	2.67	0.09	1.34	77.01	0.38

Core 4

Depth (cm)	Bulk density ($g\ cm^{-3}$)	xs Pb-210 ($dpm\ g^{-1}$)	Cs-137 (Count)	Inventory ($dpm\ cm^{-2}$)	Age (yr)	Accretion Rate ($cm\ yr^{-1}$)
1	0.13	22.56	0.10	5.67	2.29	0.44
3	0.28	12.73	0.01	7.17	8.19	0.37
5	0.23	12.44	0.00	5.65	15.40	0.32
7	0.17	10.68	0.01	3.69	21.90	0.32
9	0.34	4.05	0.00	2.75	27.30	0.33
11	0.31	4.72	0.00	2.93	32.96	0.33
13	0.29	3.56	0.00	2.09	38.96	0.33
15	0.32	2.29	0.04	1.48	44.02	0.34
17	0.25	3.37	0.01	1.71	49.33	0.34
19	0.27	2.41	0.03	1.30	55.30	0.34
21	0.32	1.96	0.05	1.27	61.46	0.34
23	0.34	2.30	0.00	1.55	69.93	0.33
25	0.34	1.82	0.02	1.24	81.29	0.31
27	0.37	2.18	0.04	1.60	99.44	0.27
29	0.39	1.37	0.04	1.07	104.33	0.28

Core 5

Depth (cm)	Bulk density ($g\ cm^{-3}$)	xs Pb-210 ($dpm\ g^{-1}$)	Cs-137 (Count)	Inventory ($dpm\ cm^{-2}$)	Age (yr)	Accretion Rate ($cm\ yr^{-1}$)
1	0.06	19.44	0.05	2.23	0.80	1.26
3	0.07	24.26	0.12	3.62	2.98	1.01
5	0.14	15.22	0.00	4.33	6.21	0.81
7	0.20	9.94	0.01	3.89	9.93	0.70
9	0.24	8.03	0.00	3.93	13.92	0.65
11	0.27	0.59	0.00	0.31	16.32	0.67
13	0.21	4.48	0.04	1.85	17.61	0.74
15	0.23	6.94	0.28	3.26	20.88	0.72
17	0.28	3.44	0.00	1.94	24.59	0.69
19	0.22	3.14	0.06	1.38	27.21	0.70
21	0.24	1.85	0.03	0.90	29.13	0.72
23	0.22	2.72	0.00	1.18	30.99	0.74
25	0.21	2.46	0.06	1.02	33.09	0.76
27	0.24	2.66	0.00	1.26	35.42	0.76
29	0.28	25.54	0.97	14.54	23.74	1.22

APPENDIX I

Matlab code for the one-dimensional hydrodynamic model. Functions for efficiency and output writting are demonstrated for one node, noted as comments below.

(1) One-dimensional hydrodynamic code for uniform stem density

```
% created July 3 2007, SMHOWELL
% Na constant-linear slope
% a and b from Pine Knolls Shore Spartina
% Parameters
clear all;
tic % used to calculate the total run time and for efficiency testing
a = 0.001;
dx = 2;
imax = 171; % set maximum number of index values
Na = 500; % #stems per unit area
dt = 1; % seconds
end_time = 1209600;%403200;
end_j = end_time/dt;
b = 0; %-.1277;
A1 = 0.5; % M2 tidal amplitude
A2 = 0.08; % K1
g = 9.8; %  m/s2
d = 0.005; % stem diameter, m
lagdepth = 0.02;
rho = 1020; % kg/m3
mu = 0.001; % kg/ms
Mn = 0.02;
%Mn = 0.1;
% nframes = 100;
% framespacing = end_j/nframes; %conditional for taking frames
countspacing = 2400;%1200;%2400;%1200; % every 20 minutes
countsize = 504;%336; % # events recorded

%% Initial conditions
for i=1:imax
    eta(i) = b + a*(i-1)*dx;
    zold(i) = eta(i) + lagdepth;   %initial water surface
    x(i) = (i-1)*dx;
    Hold(i) = zold(i) - eta(i);
    Uold(i) = 0.001;
    Reold(i) = (rho*d*(abs(Uold(i))))/mu;
    Cdold(i) = 10^(0.9914-(0.6341*log10(Reold(i))) + ...
               (0.0984*log10(Reold(i))^2));
    Cold(i) = (Hold(i)^(1/6))/Mn;
    Cfold(i) = (2*g)/(Cold(i)^2);
    Kold(i) = ((2*g)/((Cdold(i)*Na*d)+(Cfold(i)/Hold(i))))^1/2;
    Fold(i) = Hold(i)*Kold(i);
end
% V = 0;  %movie frame counter
count = 0;
%% Time Loop
for j = 1:end_time
    time(j) = j*dt; %updates the time elapsed
```

```
    % tidal forcing (sec) sinusoid with 12hr period
    zold(1) = b + A1*sin(2*pi*time(j)/44640) + ...
              A2*sin(2*pi*time(j)/86040) + lagdepth;
          if zold(1) <= (b + lagdepth)
              zold(1) = b + lagdepth;
          end
    Hold(1) = zold(1) - eta(1);
    Cold(1) = (Hold(1)^(1/6))/Mn;
    Cfold(1) = (2*g)/(Cold(1)^2);
    Kold(1) = ((2*g)/((Cdold(1)*Na*d)+(Cfold(1)/Hold(1))))^1/2;
    Uold(1) = -(Kold(1))*sign(zold(2)-zold(1))*...
            (abs((zold(2)-zold(1))/dx))^1/2;
    Fold(1) = Hold(1)*Kold(1);
    for i = 2:imax-1
         B1 = (Fold(i+1)+Fold(i))/2*...
              sign(zold(i+1)-zold(i))*...
              (abs((zold(i+1)-zold(i))/dx))^1/2;
         B2 = (Fold(i)+Fold(i-1))/2*...
              sign(zold(i)-zold(i-1))*...
              (abs((zold(i)-zold(i-1))/dx))^1/2;
         Hnew(i) = Hold(i) + (dt/dx) * (B1-B2);
            if Hnew(i) <= lagdepth
                Hnew(i) = lagdepth;
            end
         znew(i) = eta(i) + Hnew(i);
    end
      for i = 2:imax-1
          Unew(i) = -Kold(i)*sign(znew(i+1)-znew(i))*...
                    (abs((znew(i+1)-znew(i))/(dx)))^1/2;
      end
      for i = 2:imax-1
          Renew(i) = (rho*d*(abs(Unew(i))))/mu;
          if Renew(i) < 0.1
           Renew(i) = 0.1;
          end
      end
      for i = 2:imax-1
          Cdnew(i) = 10^(0.9914-(0.6341*log10(Renew(i))) + ...
                     (0.0984*log10(Renew(i))^2));
          Cnew(i) = (Hnew(i)^(1/6))/Mn;
          Cfnew(i) = (2*g)/(Cnew(i)^2);
          Knew(i) = ((2*g)/((Cdnew(i)*Na*d)+(Cfnew(i)/Hnew(i))))^1/2;
          Fnew(i) = Hnew(i)*Knew(i);
      end
      for i=2:imax-1
        zold(i) = znew(i);
        Uold(i) = Unew(i);
        Reold(i) = Renew(i);
        Cdold(i) = Cdnew(i);
        Cold(i) = Cnew(i);
        Cfold(i) = Cfnew(i);
        Kold(i) = Knew(i);
        Hold(i) = Hnew(i);
        Fold(i) = Fnew(i);
      end
%% store output
        temp2 = mod(j,countspacing);
        if temp2 == 0
```

```
            count = count + 1;
            depth4(count) = Hold(3);
            depth8(count) = Hold(5);
            depth16(count) = Hold(9);
            depth20(count) = Hold(11);
            depth40(count) = Hold(21);
            depth60(count) = Hold(31);
            depth80(count) = Hold(41);
            depth100(count) = Hold(51);
            T(count) = time(j)/60;

           velocity4(count) = Uold(3);% shown for 4, repeat as above
           Reynolds4(count) = Reold(3);
           Cd4(count) = Cdold(3);
         end
% Use plot below or animation function
% Plot
%axis tight;
set(gca,'nextplot','replacechildren');
temp = mod(j,framespacing);
count_file =0;
if temp == 0
     V = V + 1;
     %subplot(2,1,1)
     plot(x,eta,x,zold);
     title(['time is ' num2str(time(j)/3600) ' hrs'])
     axis([-1,500,0,1]);
     %subplot(2,1,2)
     %plot(x,Uold)
     %axis([-1,50,-0.05,0.1]);
     M(V) = getframe(gcf);
     %{
     if (mod(V,20) == 0)
        eval(['save Mlog_',num2str(count_file),' M']);
        clear M;
        V = 0;
        count_file = count_file + 1;
     end
     %}
 end
%}
end
%movie2avi(Mov,'movie2')
%% save output
trdepth4 = depth4';
save depth4m.txt trdepth4 -ASCII
% shown for 4; repeat for 8, 16, 20, 40, 60, 80, 100 for velocity, Re,
Cd
trT = T';
save Tmin.txt trT -ASCII
trvelocity4 = velocity4';
save velocity4.txt trvelocity4 -ASCII
trReynolds4 = Reynolds4';
trCd4 = Cd4';
save Cd4.txt trCd4 -ASCII
%
toc
```

(2) One-dimensional hydrodynamic Matlab code for biomass that has a parabolic distribution over the distance of the marsh platform

```
% created July 3 2007, SMHOWELL
% last modified 4.20.10
% Na constant-linear slope
% Parameters
clear all;
tic
a = 0.01;
dx = 3;
Yp = 500; % max Na
Zo = 0.08; % Sea level where Sp Grows
Zp = 0.4; % elevation max Na
imax = 21; % set maximum number of index values
dt = 0.5; % seconds
end_time = 403200;% also run to 1209600;%
end_j = end_time/dt;
b = 0; %-.1277;
A1 = 0.5; % M2 tidal amplitude
A2 = 0.08; % K1
g = 9.8; %  m/s2
d = 0.005; % stem diameter, m
lagdepth = 0.02;
rho = 1020; % kg/m3
mu = 0.001; % kg/ms
Mn = 0.02;
nframes = 336;
framespacing = end_j/nframes; %conditional for taking frames
%countspacing = 2400; %1200;%2400;%1200; % every 20 minutes
%countsize = 504; %336; % # events recorded
%% Preallocate memory, example of several variable shown below
eta = zeros(1,imax);
x = zeros(1,imax);
zold = zeros(1,imax);
%% Saved variables
depth3 = zeros(1,countsize);
% below same as depth3, repeat for 9,15,21,39,60,81
T = zeros(1,countsize);
velocity3 = zeros(1,countsize);
Reynolds3 = zeros(1,countsize);
Cd3 = zeros(1,countsize);
%% Initial conditions
for i=1:imax
    eta(i) = b + a*(i-1)*dx;
    zold(i) = eta(i) + lagdepth;   % initial water surface
    x(i) = (i-1)*dx;
    Na(i) = (-Yp/((Zo-Zp)^2))*((eta(i)-Zp)^2)+Yp;
    if Na(i) < 20
        Na(i) = 20;
    end
    Hold(i) = zold(i) - eta(i);
    Uold(i) = 0.001;
    Reold(i) = (rho*d*(abs(Uold(i))))/mu;
    Cdold(i) = 10^(0.9914-(0.6341*log10(Reold(i))) + ...
              (0.0984*log10(Reold(i))^2));
    Cold(i) = (Hold(i)^(1/6))/Mn;
    Cfold(i) = (2*g)/(Cold(i)^2);
```

```
    Kold(i) = ((2*g)/((Cdold(i)*Na(i)*d)+(Cfold(i)/Hold(i))))^1/2;
    Fold(i) = Hold(i)*Kold(i);
end
V = 0;  % movie frame counter
% count = 0;
%% Time Loop
for j = 1:end_time
    time(j) = j*dt; % updates the time elapsed
    % tidal forcing (sec) sinusoid with 12hr period
    zold(1) = b + A1*sin(2*pi*time(j)/44640) + ...
              A2*sin(2*pi*time(j)/86040) + lagdepth;
          if zold(1) <= (b + lagdepth)
              zold(1) = b + lagdepth;
          end
    Hold(1) = zold(1) - eta(1);
    Cold(1) = (Hold(1)^(1/6))/Mn;
    Cfold(1) = (2*g)/(Cold(1)^2);
    Kold(1) = ((2*g)/((Cdold(1)*Na(i)*d)+(Cfold(1)/Hold(1))))^1/2;
    Uold(1) = -(Kold(1))*sign(zold(2)-zold(1))*...
            (abs((zold(2)-zold(1))/dx))^1/2;
    Fold(1) = Hold(1)*Kold(1);
    for i = 2:imax-1
         B1 = (Fold(i+1)+Fold(i))/2*...
              sign(zold(i+1)-zold(i))*...
              (abs((zold(i+1)-zold(i))/dx))^1/2;
         B2 = (Fold(i)+Fold(i-1))/2*...
              sign(zold(i)-zold(i-1))*...
              (abs((zold(i)-zold(i-1))/dx))^1/2;
         Hnew(i) = Hold(i) + (dt/dx) * (B1-B2);
            if Hnew(i) <= lagdepth
                Hnew(i) = lagdepth;
            end
         znew(i) = eta(i) + Hnew(i);
    end
      for i = 2:imax-1
          Unew(i) = -Kold(i)*sign(znew(i+1)-znew(i))*...
                    (abs((znew(i+1)-znew(i))/(dx)))^1/2;
      end
      for i = 2:imax-1
          Renew(i) = (rho*d*(abs(Unew(i))))/mu;
          if Renew(i) < 0.1
           Renew(i) = 0.1;
          end
      end
      for i = 2:imax-1
          Cdnew(i) = 10^(0.9914-(0.6341*log10(Renew(i))) + ...
                     (0.0984*log10(Renew(i))^2));
          Cnew(i) = (Hnew(i)^(1/6))/Mn;
          Cfnew(i) = (2*g)/(Cnew(i)^2);
          Knew(i) = ((2*g)/((Cdnew(i)*Na(i)*d)+(Cfnew(i)/Hnew(i))))^1/2;
          Fnew(i) = Hnew(i)*Knew(i);
      end
      for i=2:imax-1
        zold(i) = znew(i);
        Uold(i) = Unew(i);
        Reold(i) = Renew(i);
        Cdold(i) = Cdnew(i);
        Cold(i) = Cnew(i);
```

```
        Cfold(i) = Cfnew(i);
        Kold(i) = Knew(i);
        Hold(i) = Hnew(i);
        Fold(i) = Fnew(i);
      end
 end
end
toc
```

APPENDIX J

Two-dimensional hydrodynamic model Matlab code. Functions for efficiency and writing output are demonstrated for one node, which is noted as a comment below.

(1) Two-dimensional hydrodynamic code for no structures

```
clear all;
%% Paramterers
dt = 0.05; % seconds
end_time = 7200000;% endtime in seconds
b = 0; % component of eta, the linear slope below
a = 0.001; % component of eta, the linear slope below
lagdepth = 0.01; % assume small amount of water on platform
Mn = 0.02;
dx = 10; % x: marsh platform width (from creek to woods)
dy = 10; % y: marsh platform length
A1 = 0.5; % M2 tidal amplitude
A2 = 0.08; % K1 tidal amplitude
g = 9.8; % grav accel, m/s2
r = 1020; % rho, kg/m3
mu = 0.001; % mu, kg/ms
ups = mu/r; % kinematic viscosity, m2s-1
imax = 11; % set max # of (x) index values
jmax = 11; % set max # of (y) index values
%nframes = 36;
%framespacing = end_time/nframes;
countspacing = 24000;
countsize = 300;
%% Constant Biomass, so diffusivity is D = (r*g)/(Na*5*m)
Na = 500;
%% Preallocate memory
% several examples shown below
eta = zeros(imax,jmax);
zold = zeros(imax,jmax);
znew = zeros(imax,jmax);
x = zeros(imax,jmax);
y = zeros(imax,jmax);
Hold = zeros(imax,jmax);
%
%% Store Output, several examples shown below, continue for all
variables
% depthij
%{
depth23 = zeros(1,countsize);

%% Initial conditions; create vectors
for i=1:imax
    for j=1:jmax
    eta(i,j) = b + a*(i-1)*dx;
    zold(i,j) = eta(i,j) + lagdepth; %initial water surface
    x(i,j) = (i-1)*dx;
    y(i,j) = (j-1)*dy;
    Hold(i,j) = zold(i,j) - eta(i,j); % q is depth h
```

```
    Uold(i,j) = 0.001;
    Vold(i,j) = 0.001;
    Cold(i,j) = (Hold(i,j)^(1/6))/Mn;
    Cfold(i,j) = (2*g)/(Cold(i,j)^2);
    Kold(i,j) = (2*g)/((Na*10*ups)+((Cfold(i,j)/Hold(i,j))*...
        (abs(Uold(i,j)^2 + Vold(i,j)^2))^1/2*sign(Uold(i,j)^2+...
        Vold(i,j)^2)));
    Fold(i,j) = Hold(i,j)*Kold(i,j);
    end
end
%V = 0;  % movie frame  counter
count = 0;
%% Time
tic
for n = 1:end_time
    %count = count + 1;
    time(n) = n*dt; % updates time elapsed
    for j=2:jmax-1
          for i=2:imax-1
              B1 = (Fold(i+1,j)+Fold(i,j))/2*...
              (zold(i+1,j)-zold(i,j));
              B2 = (Fold(i-1,j)+Fold(i,j))/2*...
              (zold(i,j)-zold(i-1,j));
              B3 = (Fold(i,j+1)+Fold(i,j))/2*...
              (zold(i,j+1)-zold(i,j));
              B4 = (Fold(i,j-1)+Fold(i,j))/2*...
              (zold(i,j)-zold(i,j-1));
          % Hnew constant biomass
              znew(i,j) = zold(i,j) + ((dt/dx^2)*(B1-B2))+...
                        ((dt/dy^2)*(B3-B4));
                if znew(i,j) <= eta(i,j) + lagdepth
                     znew(i,j) = eta(i,j) + lagdepth;
                end
              Hnew(i,j) = znew(i,j) - eta(i,j);
          end
    end
    % next 2 for loops:reflections across i&j boundaries
    for i=2:imax-1 % Set Boundaries
        Hnew(i,1) = Hnew(i,3);
        znew(i,1) = znew(i,3);
        Hnew(i,jmax) = Hnew(i,jmax-2);
        znew(i,jmax) = znew(i,jmax-2);
    end
    for j=1:jmax
        Hnew(1,j) = Hnew(3,j);
        znew(1,j) = znew(3,j);
    end
    % replace olds with new before moving to next time step
    for i=1:imax-1
        for j = 1:jmax % changed from jmax-1 to correct jmax node
            zold(i,j) = znew(i,j);
            Hold(i,j) = Hnew(i,j);
        end
    end
    % Set the water surface & depth for i=1 and i=2,
    % which is driven by sinusoidal tidal forcing
    temp = b + A1*sin(2*pi*time(n)/44640)+ ...
           A2*sin(2*pi*time(n)/86040) + lagdepth;
```

```
    for j = 1:jmax
        zold(2,j) = temp + eta(2,j) +lagdepth;
        zold(1,j) = temp + eta(1,j) +lagdepth;
        Hold(2,j) = zold(2,j) - eta(2,j);
        Hold(1,j) = zold(1,j) - eta(1,j);
    temp2 = b + eta(2,j) + lagdepth;
        if temp <= temp2
        zold(2,j) = temp2;
        Hold(2,j) = zold(2,j) - eta(2,j);
        end
    temp3 = b + eta(1,j) + lagdepth;
        if temp <= temp3
        zold(1,j) = temp3;
        Hold(1,j) = zold(1,j) - eta(1,j);
        end
    end
    for j=1:jmax-1
        for i=1:imax-1
            Unew(i,j) = -Kold(i,j)*((zold(i+1,j)-zold(i,j))/(dx));
            Vnew(i,j) = -Kold(i,j)*((zold(i,j+1)-zold(i,j))/(dy));
            Cnew(i,j) = (Hold(i,j)^(1/6))/Mn;
            Cfnew(i,j) = (2*g)/(Cnew(i,j)^2);
            Knew(i,j) = (2*g)/((Na*10*ups)+((Cfnew(i,j)/Hold(i,j))*...
            (abs(Unew(i,j)^2 + Vnew(i,j)^2))^1/2*sign(Unew(i,j)^2+...
            Vnew(i,j)^2)));
            Fnew(i,j) = Knew(i,j)*Hold(i,j);
        end
    end
    for j=1:jmax-1
        for i=1:imax-1
            Uold(i,j) = Unew(i,j);
            Vold(i,j) = Vnew(i,j);
            %Cold(i,j) = Cnew(i,j);
            %Cfold(i,j) = Cfnew(i,j);
            Kold(i,j) = Knew(i,j);
            Fold(i,j) = Fnew(i,j);
        end
    end
%% Save Data (save depths to evaluate frequency of qold)
%
%depth1(count) = qold(i,j);
temp7 = mod(n,countspacing);
if temp7 == 0
count = count + 1;
    T(count) = time(n)/60;
    %{
    depth23(count) = Hold(2,3);
    depth25(count) = Hold(2,5);
    %}

end
end
%
%% save point output
 %
 trT = T';
 save T.txt trT -ASCII
 %{
```

```
 trdepth23 = depth23';
 save d23.txt trdepth23 -ASCII
 trdepth25 = depth25';
 save d25.txt trdepth25 -ASCII
 trdepth27 = depth27';
 save d27.txt trdepth27 -ASCII
 trdepth210 = depth210';
 save d210.txt trdepth210 -ASCII
toc
```

(2) Two-dimensional hydrodynamic code for one structure

```
% two-dimensional hydrodynamics of salt-marsh platform
% smh
% modified 6.29.10
% set-up to solve 2-D, plot 1-D & 2-D
% includes bed stress

clear all;
%% Paramterers
dt = 0.01; % seconds
end_time = 36000000;%4320000; % endtime in seconds
b = 0; % component of eta, the linear slope below
a = 0.002; % component of eta, the linear slope below
lagdepth = 0.01; % assume small amount of water on platform
Mn = 0.02;
dx = 10; % x: marsh platform width (from creek to woods)
dy = 10; % y: marsh platform length
A1 = 0.5; % M2 tidal amplitude
A2 = 0.08; % K1 tidal amplitude
g = 9.8; % grav accel, m/s2
r = 1020; % rho, kg/m3
mu = 0.001; % mu, kg/ms
ups = mu/r; % kinematic viscosity, m2s-1
imax = 11; % set max # of (x) index values
jmax = 11; % set max # of (y) index values
% open/close: boundary cond for j's; j=1:open-1 is no flow bound
% j=open:jmax is where water enters
open = 6;
close = jmax;
%nframes = 48;%896;%344;
%framespacing = end_time/nframes; % conditional for taking frames
countspacing = 120000;
countsize = 300;
%% Changing Biomass
%Na_max = 1000; % # stems per unit area
%beta = 1000; % rate constant for Na(z)
%% Uniform Biomass
Na = 300;
)-1
%% Preallocate memory
% to include eta, zold, znew, x, y, time, and new/old for H, U, V, C,
Cf, K, F
eta = zeros(imax,jmax);
%Na = cell(imax,jmax);
%
%% Store Output
```

```
% variable ij
T = zeros(1,countsize);
depth23 = zeros(1,countsize);
depth25 = zeros(1,countsize);
depth27 = zeros(1,countsize);
depth210 = zeros(1,countsize);
%% Initial conditions; create vectors
for i=1:imax
    for j=1:jmax
    eta(i,j) = b + a*(i-1)*dx;
    zold(i,j) = eta(i,j) + lagdepth; %initial water surface
    x(i,j) = (i-1)*dx;
    y(i,j) = (j-1)*dy;
    %Na(i,j) = Na_max - (beta*(a*(i-1)*dx));
    Hold(i,j) = zold(i,j) - eta(i,j); % q is depth h
    Uold(i,j) = 0.001;
    Vold(i,j) = 0.001;
    Cold(i,j) = (Hold(i,j)^(1/6))/Mn;
    Cfold(i,j) = (2*g)/(Cold(i,j)^2);
    Kold(i,j) = (2*g)/((Na*10*ups)+((Cfold(i,j)/Hold(i,j))*...
        (abs(Uold(i,j)^2 + Vold(i,j)^2))^1/2*sign(Uold(i,j)^2+...
        Vold(i,j)^2)));
    Fold(i,j) = Hold(i,j)*Kold(i,j);
    end
end
%V = 0;  % movie frame  counter
count = 0;
%% Time
tic
for n = 1:end_time
    time(n) = n*dt; % updates time elapsed
    %count = count + 1;
    for j=2:jmax-1
        if j < open % no flow region
          for i=2:imax-1
              B1 = (Fold(i+1,j)+Fold(i,j))/2*...
              (zold(i+1,j)-zold(i,j));
              B2 = (Fold(i-1,j)+Fold(i,j))/2*...
              (zold(i,j)-zold(i-1,j));
              B3 = (Fold(i,j+1)+Fold(i,j))/2*...
              (zold(i,j+1)-zold(i,j));
              B4 = (Fold(i,j-1)+Fold(i,j))/2*...
              (zold(i,j)-zold(i,j-1));
          % Hnew constant biomass
              znew(i,j) = zold(i,j) + ((dt/dx^2)*(B1-B2))+...
                        ((dt/dy^2)*(B3-B4));
                if znew(i,j) <= eta(i,j) + lagdepth
                     znew(i,j) = eta(i,j) + lagdepth;
                end
              Hnew(i,j) = znew(i,j) - eta(i,j);
          end
        end
        if j >= open % flow region
          for i=3:imax-1
              B1 = (Fold(i+1,j)+Fold(i,j))/2*...
              (zold(i+1,j)-zold(i,j));
              B2 = (Fold(i-1,j)+Fold(i,j))/2*...
              (zold(i,j)-zold(i-1,j));
```

```
            B3 = (Fold(i,j+1)+Fold(i,j))/2*...
            (zold(i,j+1)-zold(i,j));
            B4 = (Fold(i,j-1)+Fold(i,j))/2*...
            (zold(i,j)-zold(i,j-1));
            znew(i,j) = zold(i,j) + ((dt/dx^2)*(B1-B2))+...
                      ((dt/dy^2)*(B3-B4));
              if znew(i,j) <= eta(i,j) + lagdepth
                   znew(i,j) = eta(i,j) + lagdepth;
              end
            Hnew(i,j) = znew(i,j) - eta(i,j);
        end
    end
end
% next 2 for loops:reflections across i&j boundaries
for i=2:imax-1 % Set Boundaries
    Hnew(i,1) = Hnew(i,3);
    Hnew(i,jmax) = Hnew(i,jmax-2);
    znew(i,1) = znew(i,3);
    znew(i,jmax) = znew(i,jmax-2);
end
for j=1:open-1
    Hnew(1,j) = Hnew(3,j);
    znew(1,j) = znew(3,j);
end
% replace olds with new before moving to next time step
for i=1:imax-1
    for j = 1:jmax % changed from jmax-1 to correct jmax node
        zold(i,j) = znew(i,j);
        Hold(i,j) = Hnew(i,j);
    end
end
% Set the water surface & depth for i=1 and i=2,
% which is driven by sinusoidal tidal forcing
temp = b + A1*sin(2*pi*time(n)/44640)+ ...
       A2*sin(2*pi*time(n)/86040) + lagdepth;
for j = open:close
    zold(2,j) = temp + eta(2,j) +lagdepth;
    zold(1,j) = temp + eta(1,j) +lagdepth;
    Hold(2,j) = zold(2,j) - eta(2,j);
    Hold(1,j) = zold(1,j) - eta(1,j);
temp2 = b + eta(2,j) + lagdepth;
    if temp <= temp2
    zold(2,j) = temp2;
    Hold(2,j) = zold(2,j) - eta(2,j);
    end
temp3 = b + eta(1,j) + lagdepth;
    if temp <= temp3
    zold(1,j) = temp3;
    Hold(1,j) = zold(1,j) - eta(1,j);
    end
end
for j=1:jmax-1
    for i=1:imax-1
        Unew(i,j) = -Kold(i,j)*((zold(i+1,j)-zold(i,j))/(dx));
        Vnew(i,j) = -Kold(i,j)*((zold(i,j+1)-zold(i,j))/(dy));
        Cnew(i,j) = (Hold(i,j)^(1/6))/Mn;
        Cfnew(i,j) = (2*g)/(Cnew(i,j)^2);
        Knew(i,j) = (2*g)/((Na*10*ups)+((Cfnew(i,j)/Hold(i,j))*...
```

```
            (abs(Unew(i,j)^2 + Vnew(i,j)^2))^1/2*sign(Unew(i,j)^2+...
            Vnew(i,j)^2)));
            Fnew(i,j) = Knew(i,j)*Hold(i,j);
        end
    end
    for j=1:jmax-1
        for i=1:imax-1
            Uold(i,j) = Unew(i,j);
            Vold(i,j) = Vnew(i,j);
            %Cold(i,j) = Cnew(i,j);
            %Cfold(i,j) = Cfnew(i,j);
            Kold(i,j) = Knew(i,j);
            Fold(i,j) = Fnew(i,j);
        end
    end
%% Save Data (save depths to evaluate frequency of qold)
temp7 = mod(n,countspacing);
if temp7 == 0
    count = count + 1;
    T(count) = time(n)/60;
    %
    depth23(count) = Hold(2,3);
    depth25(count) = Hold(2,5);
    depth27(count) = Hold(2,7);
    end
end
%% 2D Plot
%{
axis tight;
set(gca,'nextplot','replacechildren');
temp4 = mod(n,framespacing);
%count_file =0;
if temp4 == 0
     V = V + 1;
     surf(x,y,zold,Hold)
     title(['time is ' num2str(time(n)/3600) ' hrs'])
     colormap jet
     colorbar
     caxis ([0 .8])
     axis ([0 91 0 91 0 1])
     %axis ([1 imax-1 1 jmax 0 3])
     M(V) = getframe(gcf);
     %{
     if (mod(V,20) == 0)
        eval(['save Mlog_',num2str(count_file),' M']);
        clear M;
        V = 0;
        count_file = count_file + 1;
     end
     %}
end
end
%}
%% Plot 1 D
%{
 for i=1:imax-1
     temp2 = x(i,90);
     xplot(i) = temp2;
```

```
     temp3 = zold(i,90);
     zoldplot(i) = temp3;
     temp4 = eta(i,90);
     etaplot(i) = temp4;
 end
      temp5 = mod(n,framespacing);
      if temp5 == 0
        V = V + 1;
        plot(xplot,etaplot,xplot,zoldplot);
        title(['time is ' num2str(time(n)) ' sec'])
        axis([-1,500,-1,2]);
        Mov(V) = getframe;
      end
 %}
%% save point output
 trT = T';
 save T.txt trT -ASCII

 trdepth23 = depth23';
 save d23.txt trdepth23 -ASCII
 trdepth25 = depth25';
 save d25.txt trdepth25 -ASCII
 trdepth27 = depth27';
 save d27.txt trdepth27 -ASCII
 trdepth210 = depth210';
 save d210.txt trdepth210 -ASCII
%save movieA4B_4.mat M
%movie2avi(M,'movieA6B_short.avi','fps',2);
toc
```

(3) Two-dimensional hydrodynamic code for two structures

```
clear all;
%% Paramterers
dt = 0.005; % seconds
end_time = 72000000;%36000000;%7200000;%1209600;%4320000; % endtime in
seconds
%end_n = end_time/dt;
b = 0; % component of eta, the linear slope below
a = 0.001; % component of eta, the linear slope below
lagdepth = 0.01; % assume small amount of water on platform
Mn = 0.02;
dx = 10; % x: marsh platform width (from creek to woods)
dy = 10; % y: marsh platform length
A1 = 0.5; % M2 tidal amplitude
A2 = 0.08; % K1 tidal amplitude
g = 9.8; % grav accel, m/s2
r = 1020; % rho, kg/m3
mu = 0.001; % mu, kg/ms
ups = mu/r; % kinematic viscosity, m2s-1
imax = 11; % set max # of (x) index values
jmax = 11; % set max # of (y) index values
% open/close: boundary cond for j's; j=1:open-1 is no flow bound
% j=open:jmax is where water enters
openB = 9;
closeB = jmax;
closeT = 9;
%nframes = 48;
```

```
%framespacing = end_time/nframes;
countspacing = 240000;%120000;%24000;
countsize = 300;
%% Constant Biomass, so diffusivity is D = (r*g)/(Na*5*m)
Na = 400;
%% Preallocate memory
%% Initial conditions; create vectors
for i=1:imax
    for j=1:jmax
    eta(i,j) = b + a*(i-1)*dx;
    zold(i,j) = eta(i,j) + lagdepth; %initial water surface
    x(i,j) = (i-1)*dx;
    y(i,j) = (j-1)*dy;
    Hold(i,j) = zold(i,j) - eta(i,j); % q is depth h
    Uold(i,j) = 0.001;
    Vold(i,j) = 0.001;
    Cold(i,j) = (Hold(i,j)^(1/6))/Mn;
    Cfold(i,j) = (2*g)/(Cold(i,j)^2);
    Kold(i,j) = (2*g)/((Na*10*ups)+((Cfold(i,j)/Hold(i,j))*...
        (abs(Uold(i,j)^2 + Vold(i,j)^2))^1/2*sign(Uold(i,j)^2+...
        Vold(i,j)^2)));
    Fold(i,j) = Hold(i,j)*Kold(i,j);
    end
end
%V = 0;  % movie frame  counter
count = 0;
%% Time
tic
for n = 1:end_time
    time(n) = n*dt; % updates time elapsed
    for j=2:jmax-1
        if j < openB % no flow region
          for i=2:4
              B1 = (Fold(i+1,j)+Fold(i,j))/2*...
              (zold(i+1,j)-zold(i,j));
              B2 = (Fold(i-1,j)+Fold(i,j))/2*...
              (zold(i,j)-zold(i-1,j));
              B3 = (Fold(i,j+1)+Fold(i,j))/2*...
              (zold(i,j+1)-zold(i,j));
              B4 = (Fold(i,j-1)+Fold(i,j))/2*...
              (zold(i,j)-zold(i,j-1));
          % Hnew constant biomass
              znew(i,j) = zold(i,j) + ((dt/dx^2)*(B1-B2))+...
                        ((dt/dy^2)*(B3-B4));
                if znew(i,j) <= eta(i,j) + lagdepth
                     znew(i,j) = eta(i,j) + lagdepth;
                end
              Hnew(i,j) = znew(i,j) - eta(i,j);
          end
        end
          for i=4:imax-1
              B1 = (Fold(i+1,j)+Fold(i,j))/2*...
              (zold(i+1,j)-zold(i,j));
              B2 = (Fold(i-1,j)+Fold(i,j))/2*...
              (zold(i,j)-zold(i-1,j));
              B3 = (Fold(i,j+1)+Fold(i,j))/2*...
              (zold(i,j+1)-zold(i,j));
              B4 = (Fold(i,j-1)+Fold(i,j))/2*...
```

```
          (zold(i,j)-zold(i,j-1));
          znew(i,j) = zold(i,j) + ((dt/dx^2)*(B1-B2))+...
                    ((dt/dy^2)*(B3-B4));
            if znew(i,j) <= eta(i,j) + lagdepth
                 znew(i,j) = eta(i,j) + lagdepth;
            end
          Hnew(i,j) = znew(i,j) - eta(i,j);
      end
end
% next 2 for loops:reflections across i&j boundaries
for i=2:imax-1 % Set Boundaries
    Hnew(i,1) = Hnew(i,3);
    znew(i,1) = znew(i,3);
end
for i = 4:imax-1
    Hnew(i,jmax) = Hnew(i,jmax-2);
    znew(i,jmax) = znew(i,jmax-2);
end
for j=1:openB-1
    Hnew(1,j) = Hnew(3,j);
    znew(1,j) = znew(3,j);
end
for j = closeT+1:jmax
    Hnew(3,j) = Hnew(5,j);
    znew(3,j) = znew(5,j);
end
% replace olds with new before moving to next time step
for i=1:imax-1
    for j = 1:jmax % changed from jmax-1 to correct jmax node
        zold(i,j) = znew(i,j);
        Hold(i,j) = Hnew(i,j);
    end
end
% Set the water surface & depth for i=1 and i=2,
% which is driven by sinusoidal tidal forcing
temp = b + A1*sin(2*pi*time(n)/44640)+ ...
       A2*sin(2*pi*time(n)/86040) + lagdepth;
for j = openB:jmax
    zold(2,j) = temp + eta(2,j) +lagdepth;
    zold(1,j) = temp + eta(1,j) +lagdepth;
    zold(3,closeT) = temp + eta(3,closeT) +lagdepth;
    zold(4,closeT) = temp + eta(4,closeT) +lagdepth;
    Hold(2,j) = zold(2,j) - eta(2,j);
    Hold(1,j) = zold(1,j) - eta(1,j);
    Hold(3,closeT) = zold(3,closeT) - eta(3,closeT);
    Hold(4,closeT) = zold(4,closeT) - eta(4,closeT);

temp2 = b + eta(2,j) + lagdepth;
    if temp <= temp2
    zold(2,j) = temp2;
    Hold(2,j) = zold(2,j) - eta(2,j);
    end
temp3 = b + eta(1,j) + lagdepth;
    if temp <= temp3
    zold(1,j) = temp3;
    Hold(1,j) = zold(1,j) - eta(1,j);
    end
temp4 = b + eta(3,closeT) + lagdepth;
```

```
        if temp <= temp4
        zold(3,closeT) = temp4;
        Hold(3,closeT) = zold(3,closeT) - eta(3,closeT);
        end
    temp5 = b + eta(4,closeT) + lagdepth;
        if temp <= temp5
        zold(4,closeT) = temp5;
        Hold(4,closeT) = zold(4,closeT) - eta(4,closeT);
        end
    end
    for j=1:jmax-1
        for i=1:imax-1
            Unew(i,j) = -Kold(i,j)*((zold(i+1,j)-zold(i,j))/(dx));
            Vnew(i,j) = -Kold(i,j)*((zold(i,j+1)-zold(i,j))/(dy));
            Cnew(i,j) = (Hold(i,j)^(1/6))/Mn;
            Cfnew(i,j) = (2*g)/(Cnew(i,j)^2);
            Knew(i,j) = (2*g)/((Na*10*ups)+((Cfnew(i,j)/Hold(i,j))*...
            (abs(Unew(i,j)^2 + Vnew(i,j)^2))^1/2*sign(Unew(i,j)^2+...
            Vnew(i,j)^2)));
            Fnew(i,j) = Knew(i,j)*Hold(i,j);
        end
    end
    for j=1:jmax-1
        for i=1:imax-1
            Uold(i,j) = Unew(i,j);
            Vold(i,j) = Vnew(i,j);
            %Cold(i,j) = Cnew(i,j);
            %Cfold(i,j) = Cfnew(i,j);
            Kold(i,j) = Knew(i,j);
            Fold(i,j) = Fnew(i,j);
        end
    end

%% Save Data (save depths to evaluate frequency of qold)
%depth1(count) = qold(i,j);
temp7 = mod(n,countspacing);
if temp7 == 0
count = count + 1;
    depth23(count) = Hold(2,3);
    depth25(count) = Hold(2,5);
    depth27(count) = Hold(2,7);
    end
end
%% save point output
 %
 trT = T';
 save T.txt trT -ASCII
toc
```